

**DEVELOPMENT AND EXPERIMENTAL VALIDATION
OF COMPUTATION MODEL FOR RE-FLOOD
CONDITIONS IN A PARTIALLY DEGRADED REACTOR
CORE**

By
ONKAR SURESH GOKHALE
ENGG01201004016

Bhabha Atomic Research Centre, Mumbai

A thesis submitted to the
Board of Studies in Engineering Sciences
In partial fulfillment of requirements
for the Degree of
DOCTOR OF PHILOSOPHY
of
HOMI BHABHA NATIONAL INSTITUTE



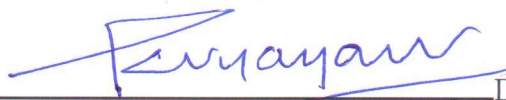
August 2017

HOMI BHABHA NATIONAL INSTITUTE

Recommendations of the Viva Voce Board

As members of Viva Voce board, we certify that we have read the dissertation prepared by Onkar Suresh Gokhale, enrollment number ENGG01201004016 titled "Development and Experimental Validation of Computational Model for Re-flood Conditions in a Partially Degraded Reactor Core" and recommend that it may be accepted as fulfilling the dissertation requirement for the degree of Doctor of Philosophy.

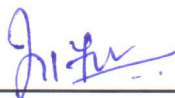
Dr. P. K. Vijayan
Chairman



Date:

3/3/18

Prof. B. P. Puranik
Guide/Convener



Date:

3/3/18

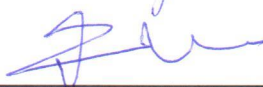
Dr. A. K. Nayak
Member



Date:

3/3/18

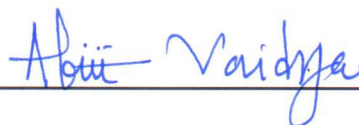
Prof. Atul Sharma
Member



Date:

3/3/18

Dr. A. M. Vaidya
Member



Date:

3/3/18

Prof. R. P. Vedula
Examiner



Date:

3/3/18

Final approval and acceptance of this dissertation is contingent upon the candidate's submission of the final copies of the dissertation to HBNI.

I hereby certify that I have read this dissertation prepared under my direction and recommend that it may be accepted as fulfilling the dissertation requirements.

Guide:



Date:

3/3/18

Place:

BARC

STATEMENT BY AUTHOR

This dissertation has been submitted in partial fulfillment of requirements for an advanced degree at Homi Bhabha National Institute (HBNI) and is deposited in the Library to be made available to the borrowers under the rule of HBNI.

Brief quotations from this dissertation are allowable without special permission, provided that accurate acknowledgement of the source is made. Requests for permission for extended quotation from or re-production of this manuscript in whole or in part may be granted by Competent Authority of HBNI when in his or her judgement the proposed use of material is in the interest of scholarship. In all other instances, however, permission must be obtained from author.



Onkar Suresh Gokhale

DECLARATION

I, hereby declare that the investigation presented in the dissertation has been carried out by me. The work is original and has not been submitted earlier as a whole or in part for a degree / diploma at or any other institution / university.



Onkar Suresh Gokhale

Dedicated to my parents and my family.

ACKNOWLEDGEMENTS

I would take this opportunity to express my sincere gratitude towards my guide, Prof. B. P. Puranik for his continuous guidance and support. This quality of work could be achieved only because of technical understanding evolved during long discussions with him.

I would like to thank Dr. A. K. Ghosh, former Director, Health, Safety & Environment Group and Shri. H. G. Lele, former Section Head, Core Safety Studies Section, for giving me an opportunity to pursue my research interest and the guidance they provided during initial stages of this work. I am highly grateful to Dr. D. Mukhopadhyay, whom I have been associated with since the first day of my professional career, for all the support and motivation he has always been providing to me. I would also like to thank Prof. K. Iyer, IITB, who extended his support by offering infra-structural facilities for conducting the experiments.

This work involved designing, fabricating, erecting and operating DRCRE experimental facility. I would like to thank Shri. D. G. Belokar for his help during design, fabrication and mechanical testing of the experimental setup and Smt S Ambokar, for readily incorporating several changes in the fabrication drawing of the setup from time to time. I also appreciate significant efforts put in by all the staff from Hall 7 Workshop and Instrumentation Lab who carried out very intricate job of fabricating the experimental setup. I am extremely thankful to Shri. Subhash Shirsat for helping me during erection of the facility. Bringing numbers onto the data recorder would not have been possible without the long hours put in by my colleague Shri Dharmanshu Mittal. I am thankful to him for all the support during instrumentation and operation of the DRCRE facility.

I gratefully acknowledge contributions of the doctoral committee members Dr. P. K. Vijayan, Dr. R. K. Singh, Dr. A. K. Nayak, Prof. Atul Sharma, Dr. K. Velusamy, Prof. J. C. Mandal and Dr. A. M. Vaidya for sparing their valuable time for critical critical assessment of my work. Incorporation of their constructive

suggestions has helped in improving quality of this work. I am highly grateful to Prof. R. P. Vedula (IITB) and Prof. Munshi (IITK) for their invaluable comments during review of this thesis.

I thank all those who have also contributed towards this work but whose mention has been missed out inadvertently.



Onkar Suresh Gokhale

PUBLICATIONS

Journals

1. O. S. Gokhale, B. P. Puranik and A. K. Ghosh, "Analytical Study on Degraded Core Quenching", Kerntechnik, Volume 78, Issue 3, April 2013.
2. O. S. Gokhale and B. P. Puranik, "Performance of Two Fluid Model based Numeric Tool with Pressure and Enthalpy as Independent Variables for Two Phase Flow in Axial and Radial Direction", Kerntechnik, Volume 9, Issue 2, March 2014.
3. O. S. Gokhale and B. P. Puranik, "Investigation of Effect of Ballooned Fuel Pins on Quenching Behaviour: Design of Experiments and Preliminary Analysis", Nuclear Technology, Volume 190, April 2015.
4. O. S. Gokhale and B. P. Puranik, "Experimental Investigation of Partially Ballooned Fuel Pins under Low Injection Flow Rates", Submitted to Nuclear Engineering and Design in August 2017.

International Conferences

1. O. S. Gokhale, B. P. Puranik, "Design of Experimental Setup for Investigation of Reflooding of Moderately Degraded Reactor Core: Scaling Analysis and Pretest Calculations", 22nd National and 11th International ISHMT-ASME Heat and Mass Transfer Conference, December 28-31, IIT Kharagpur, India, 2013.
2. O. S. Gokhale, B. P. Puranik, "New Water packing Mitigation Scheme for Two Fluid Model based Numeric Tool for Simulation of Two Phase Flow", 23rd National Heat and Mass Transfer Conference and 1st International ISHMT-ASTFE Heat and Mass Transfer Conference, December 17-20, Tiruvananthapuram, India, 2015.

Contents

Synopsis	vii
List of Figures	xiii
List of Tables	xxii
Nomenclature	xxiv
1 Introduction	1
1.1 Introduction	1
1.2 Severe Accident and SAMG Action of Re-flooding	2
1.3 Objective	3
1.4 Organisation of the Thesis	4
2 Reactor Systems and Physics of Re-wetting	6
2.1 Reactor Systems	6
2.2 Evolution of In-Vessel Accident	7
2.3 Physics of Re-wetting	10
2.3.1 Effect of Surface Temperature	11
2.3.2 Effect of Flow Rate	12
2.3.3 Difference between Re-wetting and Quenching	16
3 Literature Review	17
3.1 Evolution of Analytical and Numerical Techniques	18

3.1.1	Solutions with Assumed Fluid Conditions	18
3.1.2	Solutions with Coupled Fluid Flow and Heat Conduction Equations	30
3.2	Scaling Methodologies for Degraded Core Quenching	31
3.2.1	Two Phase Flow Scaling Laws by Graff	32
3.3	Evolution of Experimental Methods	34
3.3.1	Experiments with Intact Rod Geometry	34
3.3.2	Experiments with Deformed Rod Geometry	39
3.4	Conclusions of Literature Survey	49
4	Feasibility Analysis	53
4.1	Brief Description of the VVER-1000 (V320) Reactor and Plant Model	53
4.2	Evolution of Core Degradation without SAMG Action	55
4.3	Effectiveness of SAMG Action of Water Injection into RPV	57
4.3.1	Injection into Localized Ballooned Core Condition	57
4.3.2	Injection into Large Scale Ballooned Core Condition	58
4.3.3	Injection into Core Assuming Steam Starved Initial Condition	61
4.4	Consequences of SAMG Action	61
4.5	Estimation of Scaled Injection Rates for Experimental Setup	64
4.6	Conclusions of Feasibility Analysis	65
5	Non-Dimensionalization and Pre-Test Analysis for the Experi- mental Setup	66
5.1	Introduction	66
5.2	Non-Dimensionalization of Governing Equations	67
5.2.1	Non-Dimensionalization of Fluid Energy Equation	67
5.2.2	Non-Dimensionalization of Fuel Energy Equation	76
5.2.3	Non-Dimensionalization of Clad Energy Equation	78

5.3	Conservation of Non-Dimensional II Terms	83
5.3.1	Fluid Energy II Terms	84
5.3.2	Fuel Energy II Terms	89
5.3.3	Clad Energy II Terms	89
5.3.4	Selection of II Terms for Conservation	90
5.4	Pre-test Analysis of the Experimental Setup	91
5.4.1	Quenching of Upstream Non-ballooned Region (Node 1) . .	93
5.4.2	Quenching of Ballooned Region (Nodes 2, 3, and 4)	93
5.4.3	Quenching of Downstream Non-ballooned Region (Nodes 5 and 6)	95
5.5	Conclusions of Pre-Test Analysis	95
6	Design and Fabrication of Experimental Setup	97
6.1	Approach for Scaling	97
6.2	Description of Experimental Setup	98
6.2.1	Fuel Pin Simulator (FPS)	98
6.2.2	Fuel Pin Simulator Assembly	103
6.2.3	Test Section	104
6.2.4	Sealing Flange Sliding Pin Assembly	106
6.2.5	Steam Supply Assembly	107
6.2.6	Water Supply Assembly	107
6.2.7	Exhaust Assembly	107
6.2.8	Power Supply Assembly	107
6.2.9	Instrumentation	110
6.3	Fabrication of the Experimental Setup	114
7	Experimental Results and Discussion	117
7.1	Matrix of Experimental Parameters	117
7.2	Experimental Procedure	118

7.3	Characterization Experiments	119
7.3.1	Heat Loss Experiments	119
7.3.2	FPS Characterization Experiments	121
7.4	Initial Conditions for Experiments	121
7.5	Discussion of a typical Quenching Experiment	124
7.5.1	Assessment of Heat Transfer Coefficient	131
7.5.2	Assessment of Quench Front Location and Quench Front Velocity	134
7.5.3	Effect of Initial Average FPS Temperature	136
7.5.4	Effect of Water Injection Flow Rate	138
7.5.5	Effect of Input Power	144
7.6	Discussion on High Temperature Experiment	145
7.7	Development of Correlations	148
7.7.1	Correlation for Peak Heat Transfer Coefficient	148
7.7.2	Correlation for Average Quench Front Velocity	150
7.8	Salient Observations from Experiments	152
8	Development of Numeric Tool and Validation	153
8.1	Introduction to the code PDRCR	153
8.2	PDRCR Architecture and Modules	154
8.2.1	Discretization of Fluid Flow path (Module FLOW)	155
8.2.2	Conservation Equations for Fluid Flow	156
8.2.3	Solution of Conservation Equations for Fluid Flow (Module FLOW)	167
8.2.4	Solution of Conservation Equation for Fuel (Module FUEL)	171
8.2.5	Module for Heat Transfer Coefficients (Module HTC)	174
8.2.6	Module for Steam Water Properties (Module PROP)	178
8.3	Solution Algorithm	178
8.4	New Water Packing Mitigation Scheme	179

8.5	Treatment of Cross-Flow	181
8.6	Treatment of Heat Transfer with Cross-Flow	183
8.7	Treatment of Large Axial Temperature Gradients in FUEL	184
8.8	Validation Results for PDRCR	185
8.8.1	Test Case 01: Radial Heat Conduction with Internal Heat Generation	188
8.8.2	Test Case 02: Axial Heat Conduction with Internal Heat Generation	188
8.8.3	Test Case 03: 1D Single Phase Water Flow (Isothermal Con- dition)	189
8.8.4	Test Case 04: 1D Single Phase Water Flow (Non-Isothermal Condition)	189
8.8.5	Test Case 05: 1D Single Phase Steam Flow (Isothermal Con- dition)	190
8.8.6	Test Case 06: 1D Single Phase Steam Flow (Non-Isothermal Condition)	191
8.8.7	Test Case 07: Water Fill Test	192
8.8.8	Test Case 08: 2D Single Phase Water Flow with Cross-Flow	193
8.8.9	Test Case 09: Property Values at Different States of System	194
8.8.10	Test Case 10: Performance of New Water Packing Mitigation Scheme	195
8.9	Simulations of Reactor Core Quenching Experiments	197
8.9.1	Comparison with Intact Rod Experiments - Single Flow Path simulation in PDRCR	198
8.9.2	Comparison with Intact Rod Experiments - Parallel Flow Path Simulation in PDRCR	210
8.9.3	Comparison with Ballooned Rod Experiments	214

8.10 Comparison of DRCRE Experimental Results with PDRCR Predictions	217
8.11 Development of Quenching Map	221
9 Conclusions	223
9.1 Conclusions of Present Study	223
9.2 Scope for Future Work	226
A Calibration of Measuring Instruments	236
A.1 Calibration of K-type Thermocouples	236
A.2 Calibration of Flowmeter	237
A.3 Calibration of Level Transmitter	239
B Uncertainty Analysis	241
B.1 Uncertainties in Measured Parameters	241
B.2 Uncertainties in the Derived Quantities	242
B.2.1 Uncertainty of Input Power Measurement	242
B.2.2 Uncertainty in Heat Transfer Coefficient	242
B.2.3 Uncertainty in Quench Front Velocity	243
C Thermocouple Installation Details	244
D Use of Developed Correlations	249
D.1 Correlation for Peak Heat Transfer Coefficient	249
D.2 Correlation for Average Quench Front Velocity	250
E Sample Calculations for the Pi-Terms	251
F Comparison of PDRCR Prediction with DRCRE Experimental Results	255

Synopsis

Continued development of Nuclear Power Plants (NPPs) has led to life extension of existing NPPs and new designs are being adopted for new plants plants. However, public perceptions of the safety of these plants will continue to have an important impact on the future of these plants due to the potential for occurrence of Severe Accident (SA). Safety enhancement is ensured by providing engineered features which become functional under Severe Accident Management Guidelines (SAMG) to arrest core degradation. Verification of such features feature is essential for an effective SAMG prescription.

SA leads to heatup of fuel pins beyond operating temperature. The fuel pin gets ballooned at multiple locations and the length of ballooned portion progressively increases in the axial direction. This state of reactor core is known as partially degraded core condition. Injection of fire fighting water into the reactor core is one of the SAMG actions. The success of such injection depends on the time of execution because the blockages in the core tend to increase as the accident progresses. A detailed literature review was carried out pertaining to experimental and analytical studies for water injection in reactor core. The following knowledge gap areas were identified:

1. Several studies investigate quenching of intact as well as blocked core ranging upto 90% blockage and extending upto 6% of length. However, no information is available on quenching of blocked core with blockages extending beyond 6% of length.

2. Unlike flow rates expected under SA conditions the flow rates considered for most of the quenching studies are equal to or higher than typical SAMG values.
3. The existing numerical tools are not adequate to simulate quenching with low injection flow rates in which flow re-distribution is expected to be dominant.

The present work involves an experimental investigation of quenching of core with 45% flow area blockages extending upto 60% of total length. The experiments are performed in the Degraded Reactor Core Reflood Experimental (DRCRE) facility with an objective to understand quenching patterns for a range of water injection rates, input power and temperature. A numerical tool Partially Degraded Reactor Core Reflooding (PDRCR) has been developed that can address specific issues pertaining to flow blockages and low injection flow rate conditions.

Scaling Analysis and Design of Experimental Setup

Non-dimensionalization of mass, momentum and energy conservation equations was performed to arrive at the geometrical parameters and the process parameters for a scaled down experimental setup. The Pi-terms important for quenching phenomena, are preserved in the scaled down setup with respect to the actual PWR configuration. The geometry and the operating parameters were identified from this analysis.

The DRCRE test section consists of Fuel Pin Simulator (FPS) matrix enclosed in SS shroud representing a PWR reactor core with central high power region with ballooned FPS (25 nos) and peripheral low power region with non-ballooned FPS (20 nos) and dummy FPS (12 nos). Each FPS consists of a tungsten heater rod enveloped in alumina pellets (surrogate material simulating fuel), encased in SS clad. Each of this FPS is instrumented with K-type thermocouples (TC) along its length and circumference.

Experimental Investigation

Several experiments were performed in the DRCRE as per test matrix. In each of the experiments performed, the FPS is heated electrically to a temperature as mentioned in the test matrix. The setup is filled with superheated steam to drive out air. After achieving steady state, the decay power and the water injection are started simultaneously. The injection flow rate is found to determine the type of rewetting. For the higher flow rate case, the quench front is located at the water level suggesting that the rewetting is fluid-controlled. As the flow rate is reduced, the quench front moves ahead of the water level suggesting conduction controlled rewetting. It was observed that typically the peak HTC is minimum near the beginning of the ballooned region because of flow re-distribution taking place and in the ballooned region the peak HTC rises monotonically. A correlation has been developed for the peak HTC as a function of injection flow rate, peak FPS temperature, input power and location in the ballooned region. The correlation is able to predict the HTC ratio within $\pm 10\%$. An empirical correlation has also been developed for the quench front velocity as a function of injection flow rate, average FPS Temperature and input power. The correlation is able to predict the quench front velocity ratio within $\pm 10\%$. With increase in injection flow rate, the quench front velocity approaches cold reflood condition (reflood at ambient temperature without any power input) in the conduction controlled rewetting region. In the fluid controlled rewetting region the quench front velocity appears to diverge from the cold reflood condition with increase in flow rate.

PDRCR Code Development

A code Partially Degraded Reactor Core Reflood (PDRCR) has been developed to simulate reflood behaviour of partially degraded core. The code includes several modules such as FUEL (radial & axial conduction), FLOW (6-equation 2-fluid

model for steam water flow), HTC (for coupled heat transfer between fuel & fluid channel), PROP (steam-water properties subroutine based on IAPWS-97 formulation) and DROP (pressure drop calculation). PDRCR facilitates modeling of parallel flow paths with flow across two flow paths using cross flow junction. All modules of PDRCR employ fully-explicit formulation. The code also incorporates special models specific for core reflood conditions.

Existing thermal-hydraulics codes make use of velocity dependent numeric multipliers to reduce water packing. Such schemes are known to be ineffective for low flow rate conditions. A novel water packing mitigation scheme has been developed that identifies the cell that is expected to experience water packing and then creates a dummy cell at the boundary of this cell. This scheme helps in eliminating the artificial pressure spikes created due to water packing.

Presence of sharp temperature gradients in the FUEL domain are addressed by discretizing the domain in finer sub-cells only in the fuel cell in the vicinity of water level. This scheme reduces computational requirements by using coarse cells in the region away from the water front.

All modules of PDRCR are individually benchmarked against analytical solutions or by comparison with other numeric tools. Validation of the PDRCR code has been done against the data available in published literature such as SEFLEX experiments as well as for the data generated from the DRCRE facility. The PDRCR code prediction of quenching behaviour for SEFLEX as well as DRCRE experiments is satisfactory. It can be concluded that PDRCR is able to predict quenching behaviour for a wide range of core blockages ranging from 90% blockage for 6% length in case of SEFLEX to 45% blockage for 60% length in case of DRCRE facility. Cross-flow velocity magnitudes are negligible for 0% blockage, whereas for blockages ranging from 62% to 90% the cross-flow magnitudes are comparable to injection velocities. Thus, it is evident that cross-flow effects and the consequent flow re-distribution plays a significant role in quenching of partially degraded core

condition.

Conclusions

Following conclusions were drawn from the study:

1. Water injection in DRCRE, with 45% flow blockages extending over 60% of FPS length is found to be successful for decay power levels up to 1% of full power and injection flow rates of 0.11 - 0.45 g/s/m/pin for all initial average temperatures of FPS up to 650⁰C.
2. The clad temperature remains below 1000C for all cases except for initial temperature of 650⁰C and injection rate less than 25 g/s.
3. The development of various modules of PDRCR code and the water packing mitigation scheme and cross-flow models in particular, are found to be satisfactory for the simulation of partially degraded reactor core reflood conditions.
4. PDRCR code is found to be capable of simulating degraded core reflood conditions with flow blockages ranging from 45% to 90% and axial blockages ranging from 6% to 60% for low flow rate conditions.

Contributions from Present Work

The following are the key contributions of the present work:

1. A scaled down experimental facility DRCRE is designed and built that can simulate reflooding under partially degraded reactor core conditions.
2. Reflooding of FPS representing a scaled down degraded reactor core with 45% flow area blockage extending up to 60% of the length is investigated for the first time.

3. Correlations are proposed for the peak HTC, average HTC and quench front velocity in the ballooned region with 45% flow area blockage extending up to 60% of the length.
4. A numerical tool PDRCR is developed that can simulate quenching of partially degraded reactor core and employs a novel water packing mitigation scheme for low flow rate conditions.

List of Figures

1.1	Various Stages of Core Degradation under Severe Accident Condition	3
1.2	Scope of Work	4
2.1	Fuel Assembly of PWR (Courtesy Westinghouse)	7
2.2	Schematic of PWR Core	7
2.3	Ballooned Fuel Pin	9
2.4	Schematic of Various Stages of Core Degradation in Phase II of Accident	9
2.5	Pool Boiling Curve for Water at Atmospheric Pressure	11
2.6	Clad Temperature for Bottom Re-flooding	12
2.7	Bottom Re-flooding with High Injection Rate	14
2.8	Bottom Re-flooding with Low Injection Rate	14
2.9	Top Re-flooding in Single Rod Geometry	15
3.1	Heat Transfer Modes during Re-flooding	23
3.2	Clad Temperature Evolution	23
3.3	Effect of Heat Flux on Quench Front Velocity	24
3.4	Effect of Inlet Velocity on Quench Front Velocity	24
3.5	Typical Flow Channel of PWR	25
3.6	Effect of Initial Uncovered Height on Fuel Temperature Distribution	26
3.7	Effect of Hydrogen Distribution on Fuel Temperature Distribution .	26
3.8	Effect of Zr Oxidation on Fuel Temperature Distribution	26

3.9	Effect of Steam Dissociation on Fuel Temperature Distribution . . .	26
3.10	Flow Regimes and Heat Transfer Modes in Schutzle’s Code	28
3.11	Schematic of Moving Mesh in Schutzle’s Code	28
3.12	Comparison of Cladding Temperature with FLECHT Experiments .	28
3.13	Quench Front Tracking Scheme	29
3.14	Variation of Thermodynamic and Flow Quality along the Channel .	33
3.15	Cladding Temperature for FEBA and SEFLEX Experiments . . .	35
3.16	Quench Front Propagation for FEBA and SEFLEX	35
3.17	Cross-sectional View of Rod Bundles for Experiments by Tuzla et al.	36
3.18	Schematic of Test Section for Experiments by Tuzla et al.	36
3.19	Variation of Wall Superheat along Flow Channel	36
3.20	Effect of Inlet Quality on Quench Front Velocity	37
3.21	Effect of Inlet Mass Flow Rate on Quench Front Velocity	37
3.22	Onset of Cooling for Different Elevations in the Test Section	38
3.23	Variation of Core Temperature along the Test Section Length . . .	39
3.24	Variation of Quench Rate along the Test Section Length	39
3.25	Schematic of FEBA Test Matrix and Ballooned Fuel Pins	41
3.26	FEBA Fuel Matrix Configurations depicting Position of Blockages .	41
3.27	Clad Temperature Transient for SEFLEX Experiments	44
3.28	Clad Temperature Variation in THETIS Experiments	46
3.29	Variation of Steam and Droplet Speed along Channel Length	47
3.30	Central Rod Temperatures in FLECHT-SEASET Experiments . . .	48
3.31	Peripheral Rod Temperatures in FLECHT-SEASET Experiments .	48
3.32	Range of Radial and Axial Blockages considered for Quenching Studies	50
3.33	Injection Flow Rates considered for Quenching Studies	52
4.1	Nodalization of VVER Reactor Core	54
4.2	Stages of Core Degradation	55
4.3	Evolution of VVER Core Degradation under LOCA Conditions . .	56

4.4	Temperature Variation of Fuel for Injection under Localized Ballooned Condition (Steam Rich Condition)	58
4.5	Temperature Variation of Fuel for Injection under Gross Ballooned Condition (Steam Rich Condition)	59
4.6	Temperature Variation of Fuel Ring 3 for Injection under Gross Ballooned Condition (Steam Rich Condition)	59
4.7	Peak Cross-Flow Rate under Different Core Configurations	60
4.8	Temperature Variation of Fuel for Injection under Localized Ballooned Condition (Steam Starved Condition)	62
4.9	Temperature Variation of Fuel for Injection under Gross Ballooned Condition (Steam Starved Condition)	62
4.10	Temperature Variation of Fuel for Injection under Localized Clad Burst Condition (Steam Starved Condition)	62
4.11	Temperature Variation of Fuel for Injection under Gross Clad Burst Condition (Steam Starved Condition)	62
5.1	Representation of Zones under Quenching Process	68
5.2	Nodalization of Model of Experimental Setup developed in RELAP5	92
5.3	Temperature Variation of Node 1	94
5.4	Temperature Variation of Node 2	94
5.5	Temperature Variation of Node 4	95
5.6	Temperature Variation of Node 6	95
6.1	Schematic of the Experimental Setup	98
6.2	Straight FPS and Ballooned FPS	101
6.3	FPS Assembly Configuration Map	104
6.4	3D Schematic of the Test Section	105
6.5	Drawing of Sealing Flange Sliding Pin Assembly	106
6.6	Configuration of Copper Discs used as Connecting Bus Bars indicating Current Flow Direction	108

6.7	Electrical Configuration of Heated FPS	109
6.8	Thermocouple Locations Map	111
6.9	Thermocouple Location Planes	112
6.10	Thermocouple Plug	114
6.11	Stages of Test Section Fabrication	115
6.12	Photograph of the DRCRE Test Section	116
7.1	Internal FPS Resistance	121
7.2	Power Input to the Test Section	124
7.3	Radial Temperature Profile	125
7.4	Axial Temperature Profile	125
7.5	Water Injection Rate	126
7.6	Temperature Transient at Different Planes along the Test Section Length	128
7.7	Pressure Transient	129
7.8	Inlet and Outlet Fluid Temperature Transient	130
7.9	Carryover Measured at the Exit of the Setup	130
7.10	Variation of Heat Transfer Coefficient	132
7.11	Variation of Peak Heat Transfer Coefficient	133
7.12	Water Level and Quench Front Location Transient	134
7.13	Quench Front Velocity along the Test Section	135
7.14	Effect of Initial Avg. FPS Temp on Quenching Behavior	137
7.15	Effect of Initial Avg. FPS Temp. on Quench Front Velocity	138
7.16	Effect of Water Injection Rate on Quenching Behavior	139
7.17	Effect of Water Injection Rate on Quench Front Behavior	140
7.18	Evolution of Water Level and Location of Quench Front for different Water Injection Rates	141
7.19	Variation of Quench Front Velocity with Injection Rate at 1% Decay Power	142

7.20	Variation of Quench Front Velocity with Injection Rate at 0.5% Decay Power	142
7.21	Comparative Carryover Measurements for Experiments with differ- ent Water Injection Rates	143
7.22	Effect of Input Power on Quenching Behavior	144
7.23	Comparative Carryover measurements for experiments with differ- ent power input	145
7.24	Maximum Temperature Transient for different Injection Rates . . .	146
7.25	Water Level and Quench Front Location for different Injection Rates	147
7.26	FPS Axial Temperature Variation	148
7.27	Peak Heat Transfer Correlation	151
7.28	Quench Front Velocity Correlation	151
8.1	PDRCR Code Structure	154
8.2	Flow Path discretized into Control Volumes	155
8.3	Solution Process for FLOW Module	171
8.4	Heat Conduction in Radial Direction	172
8.5	Heat Transfer Regime Identification Map	176
8.6	PDRCR Algorithm	179
8.7	Creation and Deletion of Dummy Cell	181
8.8	Conceptual Representation of Cross-Flow	183
8.9	Discretization of Cross-Flow Path	183
8.10	FUEL and FLOW Nodalization	185
8.11	Temperature Profile for Radial Heat Conduction	188
8.12	Temperature Profile for Axial Heat Conduction	189
8.13	Fluid Pressure Transient for Isothermal Water Injection	190
8.14	Fluid Temperature Transient for Water Injection at 363 K at 0.1m/s	190
8.15	Fluid Temperature Transient for Water Injection at 292.2 K at 0.1m/s	190
8.16	Fluid Pressure Transient for Isothermal Steam Injection	191

8.17 Fluid Temperature Transient for Water Injection at 930 K at 0.1m/s	191
8.18 Fluid Temperature Transient for Water Injection at 430 K at 0.1m/s	191
8.19 Void Fraction Transient for Water Injection into Steam Filled Pipe	192
8.20 Pressure Transient for Water Injection into Steam Filled Pipe . . .	192
8.21 Nodalization of Flow Path for Cross-Flow of Water (Simulation with FLOW)	193
8.22 COMSOL Domain for Simulation of Cross-Flow of Water	193
8.23 Velocities at Cross-Flow Junctions in FLOW and comparison with COMSOL	194
8.24 Pressure Prediction without any Water Packing Mitigation Scheme	196
8.25 Pressure Prediction with Water Packing Mitigation Scheme of TRACE	196
8.26 Pressure Prediction with New Water Packing Mitigation Scheme of PDRCR	197
8.27 Input Power Curve (Comparison of SEFLEX Series I Test 4 and PDRCR Code)	201
8.28 Initial Axial Temperature Distribution (Comparison of SEFLEX Series I Test 4 and PDRCR Code)	202
8.29 Inlet Flow Rate (Comparison of SEFLEX Series I Test 4 and PDRCR Code)	202
8.30 Clad Temperature at various Axial Locations (Comparison of SE- FLEX Series I Test 4 and PDRCR Code)	203
8.31 Clad Temperature Variation at axial location of 2270 mm	204
8.32 Variation of Heat Transfer Coefficients at axial location of 2270 mm	204
8.33 Axial Clad Temperature Distribution at $t = 100$ s	205
8.34 Radial Temperature Distribution at $t = 100$ s	205
8.35 Evolution of Radial Temperature Distribution	206
8.36 Shroud Temperature at various Axial Locations (Comparison of SE- FLEX Series I Test 4 and PDRCR Code)	206

8.37	Clad Temperature at various Axial Locations (Comparison of SE-FLEX Series I Test 3 and PDRCR Code)	207
8.38	Shroud Temperature at various Axial Locations (Comparison of SE-FLEX Series I Test 3 and PDRCR Code)	207
8.39	Clad Temperature at various Axial Locations (Comparison of SE-FLEX Series I Test 5 and PDRCR Code)	208
8.40	Shroud Temperature at various Axial Locations (Comparison of SE-FLEX Series I Test 5 and PDRCR Code)	208
8.41	Clad Temperature at various Axial Locations (Comparison of SE-FLEX Series I Test 6 and PDRCR Code)	209
8.42	Shroud Temperature at various Axial Locations (Comparison of SE-FLEX Series I Test 6 and PDRCR Code)	209
8.43	Selection of Channels for SEFLEX Simulation	210
8.44	Clad Temperature at various Axial Locations (Comparison of SE-FLEX Series I Test 4 and PDRCR Code with two channels)	212
8.45	Shroud Temperature at various Axial Locations (Comparison of SE-FLEX Series I Test 4 and PDRCR Code with two channels)	212
8.46	Cross-Flow Water Velocity at various Axial Locations (PDRCR with two channels)	213
8.47	Cross-Flow Steam Velocity at various Axial Locations (PDRCR with two channels)	214
8.48	Clad Temperature at various Axial Locations (Comparison of SE-FLEX Series III Test 35 and PDRCR Code with two channels) . . .	215
8.49	Shroud Temperature at various Axial Locations (Comparison of SE-FLEX Series III Test 35 and PDRCR Code with two channels) . . .	216
8.50	Cross-Flow Steam Velocity at various Axial Locations (Comparison of SEFLEX Series III Test 35 and PDRCR Code with two channels)	216

8.51	Cross-Flow Liquid Velocity at various Axial Locations (Comparison of SEFLEX Series III Test 35 and PDRCR Code with two channels)	217
8.52	Selection of Channels for DRCRE Simulation	219
8.53	Clad Temperature at various Axial Locations (Comparison of DRCRE Test 31 and PDRCR Code with 2 channels)	219
8.54	Shroud Temperature at various Axial Locations (Comparison of DRCRE Test 31 and PDRCR Code with 2 channels)	220
8.55	PDRCR Prediction of Cross-flow at various Axial Locations	220
8.56	Quenching Map	221
A.1	Thermocouple Calibration Curve	237
A.2	Rotameter Calibration Curve	238
A.3	Level Transmitter Calibration Curve	240
C.1	Pin Location Map	248
F.1	Clad Temperatures at Various Axial Locations (Comparison of DRCRE Test 07 with PDRCR Predictions)	255
F.2	Shell Temperatures at Various Axial Locations (Comparison of DRCRE Test 07 with PDRCR Predictions)	256
F.3	Clad Temperatures at Various Axial Locations (Comparison of DRCRE Test 10 with PDRCR Predictions)	256
F.4	Shell Temperatures at Various Axial Locations (Comparison of DRCRE Test 10 with PDRCR Predictions)	257
F.5	Clad Temperatures at Various Axial Locations (Comparison of DRCRE Test 14 with PDRCR Predictions)	257
F.6	Shell Temperatures at Various Axial Locations (Comparison of DRCRE Test 14 with PDRCR Predictions)	258
F.7	Clad Temperatures at Various Axial Locations (Comparison of DRCRE Test 17 with PDRCR Predictions)	258

F.8	Shell Temperatures at Various Axial Locations (Comparison of DR- CRE Test 17 with PDRCR Predictions)	259
F.9	Clad Temperatures at Various Axial Locations (Comparison of DR- CRE Test 50 with PDRCR Predictions)	259
F.10	Shell Temperatures at Various Axial Locations (Comparison of DR- CRE Test 50 with PDRCR Predictions)	260
F.11	Clad Temperatures at Various Axial Locations (Comparison of DR- CRE Test 60 with PDRCR Predictions)	260
F.12	Shell Temperatures at Various Axial Locations (Comparison of DR- CRE Test 60 with PDRCR Predictions)	261

List of Tables

3.1	Heat Transfer Correlations used by Kimball and Roy	22
3.2	Heat Transfer Correlations used in Schutzle's Code	27
4.1	Core Configuration Map under Localized Clad Ballooned Condition	60
4.2	Core Configuration Map under Gross Clad Ballooned Condition . .	61
4.3	Summary of Effectiveness of Water Injections in Degraded Core . .	63
5.1	List of II Terms for Fluid Energy Equation	74
5.2	List of II Terms for Fuel Energy Equation	79
5.3	List of II Terms for Clad Energy Equation	81
5.4	Comparison of II Terms for the Experimental Setup with Typical PWR	85
5.5	Time of Quenching for Central and Peripheral Zones for Case A and Case B	92
6.1	Dimensional Details of FPS	99
6.2	Details of FPS Material	102
6.3	Power Supply Parameters	110
6.4	List of Instruments	113
7.1	Matrix of Experimental Parameters	118
7.2	Estimation of Heat Loss from DRCRE Setup	119
7.3	Input Parameters for DRCRE Experiments	121

8.1	Heat Transfer Regimes and Correlations used in PDRCR	176
8.2	Test Cases for PDRCR Modules Validation	186
8.3	Comparison of Properties cCalculated by PROP Subroutine with Reference Values in IAPWS Tables	195
8.4	Process Parameters for SEFLEX Series I Tests	200
8.5	Geometrical Parameters and Discretization Details for Simulation with PDRCR	200
8.6	Geometrical Parameters and Discretization Details for Simulation of SEFLEX with 2 Channels in PDRCR	211
8.7	Geometrical Parameters and Discretization Details for Simulation of DRCRE with 2 Channels in PDRCR	217
A.1	Calibration Table for K-type Thermocouples	236
A.2	Calibration Table for Rotameter	238
A.3	Calibration Table for Level Transmitter	239
C.1	Thermocouple Location Details	244

Nomenclature

Abbreviations

BWR Boiling Water Reactors

CHF Critical Heat Flux

CRA Control Rod Assembly

DG Diesel Generator

DRCRE Degraded Reactor Core Reflood Experiment

ECCS Emergency Core Cooling Systems

FA Fuel Assembly

FEBA Flooding Experiments with Blocked Array

FLECHT-SEASET Full Length Emergency Cooling Heat Transfer-Separate Effects and System Effects Tests

ID Inner Diameter

LF Leidenfrost

LOCA Loss of Coolant Accident

MFB Minimum Film Boiling

NPP	Nuclear Power Plant
OD	Outer Diameter
ONB	Onset of Nucleate Boiling
PDRCR	Partially Degraded Reactor Core Reflood code
PWR	Pressurized Water Reactors
RCS	Reactor Coolant System
RPV	Reactor Pressure Vessel
SA	Severe Accident
SAA	Severe Accident Analysis
SAMG	Severe Accident Management Guidelines
SEFLEX	Fuel Rod Simulator Effects in Flooding Experiments
SG	Steam Generator
TMI	Three Mile Island
UKAEA	United Kingdom Atomic Energy Authority

Greek Symbols

α	Void Fraction
δ	Film Thickness (m)
Γ	Mass Generation Rate ($kg/m^3.s$)
ϕ	Contact Angle (<i>radian</i>)
ρ	Density (kg/m^3)
σ	Surface Tension (N/m)

Roman Symbols

\dot{m}	Mass Flux ($kg/m^2.s$)
Bi	Biot Number
C_p	Specific Heat Capacity ($kJ/kg.K$)
l	Length (m)
q'''	Volumetric Heat Generation Rate (W/m^3)
A	Flow Area (m^2)
D	Diameter (m)
e	Internal Energy
f	Friction Factor
H	Enthalpy (kJ/kg)
h	Heat Transfer Coefficient ($W/m^2.K$)
j	Superficial Velocity
k	Thermal Conductivity ($W/m.K$)
P	Pressure (Pa)
Q	Energy Release Rate (W)
r	Radial Coordinate
SS	Stainless Steel
T	Temperature (K)
t	Thickness (m)
u	Velocity (m/s)

V	Volume (m^3)
W	Power (W)
x	Steam Quality
z	Axial Coordinate

Subscripts

1ϕ	Single Phase
2ϕ	Two Phase
BI	Boiling Initiation
c	Clad Parameter
CHF	Critical Heat Flux
cl	Center Line
conv	Convection
crit	Critical Parameter
dr	Droplet Parameter
dum	Dummy Fuel Parameter
e	Thermodynamic Quantity
ext	External
F	Multiplier
f	Liquid Phase
FC	Forced Convection
fg	Interphase Property

fuel	Fuel Property
g	Gaseous Phase
gap	Pellet Clad Gap
h	Hydraulic
hous	Housing (Enclosure) Property
i	Inlet Parameter
in	Input Parameter
int	Internal
inter	Interphase Parameter
LF	Leidenfrost
loss	Loss to
Max	Maximum
MFB	Minimum Film Boiling
o	Outlet Parameter
PB	Pool Boiling
PCH	Phase Change Number
q	Quenching Parameter
quench	Quench Front Parameter
r	Reduced Parameter
rad	Radiation
sat	Property at Saturation Point

sub	Subcooling
TB	Transition Boiling
TH	Thermal
ud	Parameter Upward and Downward of the Quench Front
w	Wall/Surface

Superscripts

n	Present Time Step
sat	Property at Saturation Point

Chapter 1

Introduction

1.1 Introduction

Technological developments in nuclear industry over the last few decades have helped in life extension of existing Nuclear Power Plants (NPPs) as well as in conceptualisation of better designs for new NPPs. However, public perception of the safety of these plants will continue to have an important impact on the future of these plants. One of the most critical factors in public perception is the potential for occurrence of *Severe Accidents* (SA). The safety for the NPP is ensured by using inherent safety features in the NPP design as well as by incorporation of *safety systems* in the NPP backed up by Severe Accident Analysis of postulated accident conditions. Severe Accident Analysis (SAA) aims at identifying ways and means to reduce or even eliminate the effects of such accidents, through the development of more realistic accident management strategies of more advanced reactor designs.

SA involve complex physio-chemical and radiological phenomena that take place sequentially during various stages of the accident progression. *Severe Accident Management Guidelines* (SAMG) are evolved from the SAA which aim at arresting the accident progression and mitigating its effects. The success of SAMG action depends on the evolution path the accident follows and the time of execu-

tion of the SAMG action. Verification of such accident mitigating measures is essential for the prescription of an efficient SAMG action. A numeric tool is thus necessary to study the effects of various SAMG actions. Such tools help to make an engineering judgement of the outcome of the SAMG actions.

1.2 Severe Accident and SAMG Action of Re-flooding

Although the definition of SA is specific to a reactor type, in general, *severe accidents* can be defined as the accidents which involve fuel damage and reactor core damage. Postulated Loss of Coolant Accident (LOCA) in Pressurised Water Reactors (PWR) with failure of mitigation systems and without any operator intervention is one such SA. The accident progresses with reduction in water level in the Reactor Pressure Vessel (RPV). This leads to heat up of fuel pins beyond normal operating temperature. The fuel pin gets ballooned at multiple locations and the length of ballooned portion progressively increases in the axial direction. Presence of steam and high temperature of the clad (1300-1500 K) causes accelerated oxidation in the Zr-clad. The fuel clad may melt because of heat of oxidation or may break due to reduction in mechanical strength post oxidation. Eventually the entire core is exposed and it melts due to high temperatures, if no actions are taken to limit the core temperature. The debris formed due to core melting lead to large blockages in the core region. Figure 1.1 shows different stages of core degradation under SA conditions. The core state as found in Three Mile Island unit-2 (TMI-2) accident is also shown in Figure 1.1.

Systematic injection of water into the PWR core under accident conditions is one of the SAMG actions. The success of such injection in re-flooding the reactor core depends on the time of execution. For example, late re-flooding under severely degraded core conditions with formation of debris conditions is not efficient in arresting sustained core heating. This results in the formation of molten pool, as experienced in TMI-2 [2]. This is mainly due to the reduced heat transfer area

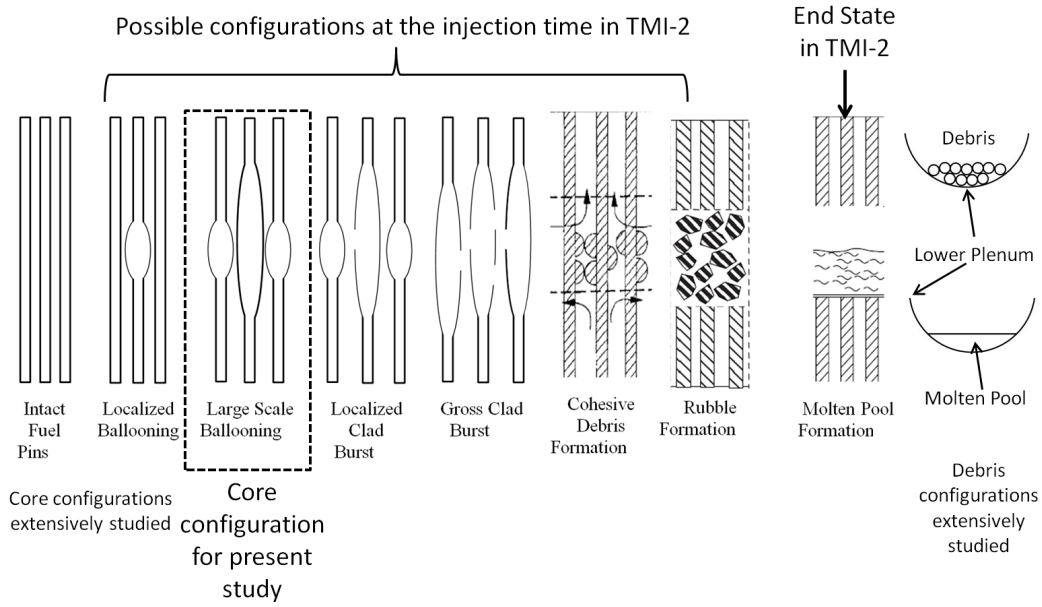


Figure 1.1: Various Stages of Core Degradation under Severe Accident Condition [1]

and low thermal conductivity of the debris crust. On the other hand, success of injection at very early stage of accidents depends significantly on the core blockage state at the time of injection. Several studies have been performed to investigate the effect of injection into in-core debris formed under re-flooding and coolability of debris formed due to flow of corium into lower plenum [3]. Injection in core with blockages extending over small length are also well studied [4]. However, scarce literature is available for the consequences of re-flooding in the case of blockages extending for large lengths of the core.

1.3 Objective

The objective of this study is to understand the evolution of quenching patterns under re-flooding conditions for a partially degraded reactor core with blockages extending for large lengths of core. Such a reactor core configuration is observed in early phase of the accident. The study involves experimental investigation of quenching of partially degraded core condition, development of numeric tool for

quenching reported in literature. The knowledge gap areas with respect to partially degraded core quenching are identified. A feasibility analysis carried out to estimate capabilities of the present system codes and to determine the range of process parameters feasible for the experimental study is presented in Chapter 4. Non-dimensionalization of governing equations to capture important physical phenomena in the experimental set up and comparison of non-dimensional Π -terms with actual plant scale are described in Chapter 5. Design of the experimental facility (DRCRE) and fabrication have been outlined in Chapter 6. Results of various experiments performed in the DRCRE facility and development of correlations are discussed in Chapter 7. Development and validation of thermal hydraulic numeric tool PDRCR, capable of simulating re-flooding under partially degraded core conditions has been discussed in Chapter 8. The comparison of results of DRCRE experiments and predictions using PDRCR code are also reported in this chapter. Chapter 9 enlists conclusions of this study.

Chapter 2

Reactor Systems and Physics of Re-wetting

The nuclear reactor systems designed, developed and constructed so far follow a definite design philosophy of ensuring very low risk to the public. Redundant and diverse safety features are employed to obviate the chances of occurrence of a severe accident. This chapter describes, in brief, general systems of a nuclear reactor, progression of an accident and fundamentals of re-wetting phenomenon.

2.1 Reactor Systems

A typical reactor core of a PWR consists of fuel rod assemblies, containing square or triangular array of fuel rods, control rods and guide tubes as shown in Figure 2.1. The core is enveloped in a Core Barrel and is housed in lower portion of the RPV as shown in Figure 2.2.

The coolant water enters the reactor core from bottom, flows upwards into the Upper Plenum and exits through the nozzles to the Steam Generators (SGs). The heat generated within the fuel pins is removed in this process and the coolant gets heated. The coolant water leaving the steam generators flows down the annular region (known as Downcomer) between the vessel wall and the core barrel. The

flow rates over the reactor core are adjusted with the help of flow holes provided in the lower core plate, allowing more flow in the central core region owing to higher power in that region. During LOCA the integrity of Reactor Coolant System (RCS) is lost. The coolant flows out through the rupture location and the core cooling is compromised. The Emergency Core Cooling Systems (ECCS) prevent the core from overheating by forcing in adequate amount of water to the core. However, un-availability or failure of such systems may lead to excessive heating of core that leads to degradation. The accident progresses through different stages of degradation as explained in next section.

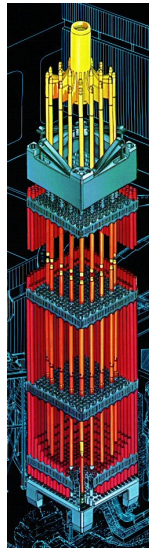


Figure 2.1: Fuel Assembly of PWR (Courtesy Westinghouse)

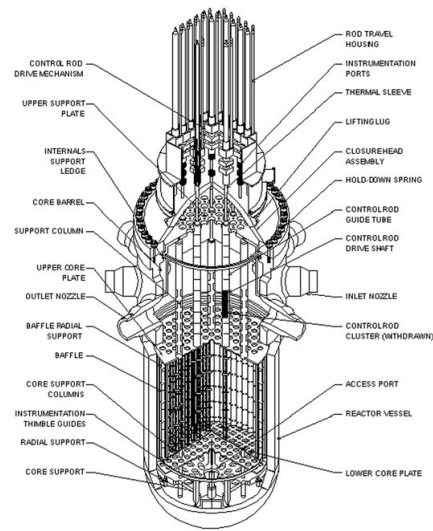


Figure 2.2: Schematic of PWR Core [5]

2.2 Evolution of In-Vessel Accident

It is perhaps instructive to delineate different stages of accident progression following an initiating event that leads to loss of cooling in the reactor core and causes overheating and degradation of fuel rods. The sequence of events can be divided into four characteristic phases [6] as:

- **Phase I:** Heating up of the core until failure of the core support structure.

It starts with certain water level in the RPV and ends with the failure of the core support structure.

- **Phase II:** The second phase is characterized by the evaporation of the water in the lower plenum of the RPV. It lasts until a molten core debris called corium is formed.
- **Phase III:** The third phase is concerned with the heat up of the pressure vessel after formation of a molten pool in the lower plenum of the RPV and RPV failure.
- **Phase IV:** After RPV failure, the molten corium will interact in the fourth phase with the concrete structure beneath the pressure vessel.

Typically with the break of largest size in RCS, the core temperature escalation due to loss of cooling starts 20 minutes beyond accident initiation. In about 35 minutes the water level drops below the upper grid plate and thus the fuel exposure begins leading to temperature rise. This is Phase I of the accident. Failure of the SAMG actions to limit the temperature rise in Phase I results in core temperatures higher than 980°C that triggers exothermic Zircoloy oxidation reaction producing heat as much as 10 times the decay heat [7]. Rapid temperature escalation of the order of $1 - 10\text{K/s}$ leads to rapid release of fission product gases within the fuel cladding. The pressure in the fuel pins builds up and at the same time the pressure outside the pins, i.e., the system pressure is reduced due to RCS break. Due to this pressure difference and high temperatures experienced by the cladding, the cladding deforms through creep to attain ballooned portions. A typical ballooned fuel pin has been shown in Figure 2.3. As accident progresses the number of ballooned locations as well as length of ballooned region starts increasing.

If unattended, 50 % of the reactor core attains failure temperature within 1.3 hours from the accident initiation [6]. The fuel pins fail because of clad rupture. Cracked fuel pellets come out of the fuel clad and form suspended rubble. Con-



Figure 2.3: Ballooned Fuel Pin [8]

tinuous decay heat generation within the fuel pellets leads to formation of debris, blocking almost all the flow area for coolant flow and results into a molten pool of fuel-clad material at the end of Phase II of accident. A schematic of these degradation stages is shown in Figure 2.4.

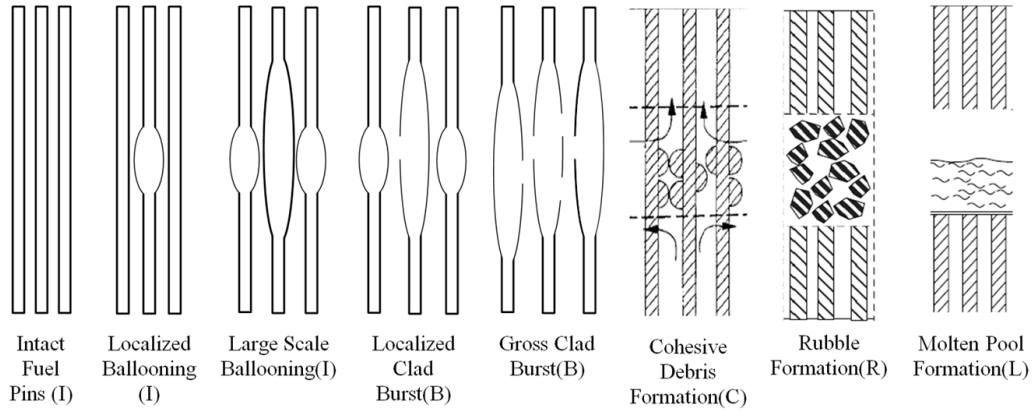


Figure 2.4: Schematic of Various Stages of Core Degradation in Phase II of Accident [1]

Formation of ballooned portions in the fuel rods results in reduction of the flow path available for the steam flow during boil-off phase and for the water injection during re-flood phase. Since the power density across the diameter of the reactor core is not uniform, the temperatures of fuel rods in the central and peripheral locations are different. The extension of ballooning along the fuel pin length and the flow blockage created because of ballooning are not uniform throughout the core cross-section. The coolability of such blocked regions along the fuel rods is governed by complex thermo-hydraulic phenomena taking place near the ballooned surface, such as [4]:

- **Flow Re-distribution:** Due to higher flow restrictions in the blocked regions, the flow gets re-distributed upstream and down-stream of the blockage. The flow through the blocked region is lower than the flow in the peripheral region. This reduces heat transfer in the central region.
- **Increase in Liquid Fraction:** Although the steam flow rates through the blocked region decrease because of flow re-distribution, the entrained droplets tend to move with the same velocity due to higher inertia. This increases the liquid fraction in coolant flow resulting in heat transfer enhancement.
- **Increased Turbulence:** Droplet impact on the ballooned surface and shattering causes increase in turbulence and reduces steam superheat, favoring cooldown.

The consequences of these effects greatly depend on the blockage characteristics such as the blockage ratio, axial extension of ballooned region and coolant conditions (flow rate, system pressure, inlet temperature). The combination of these effects can either degrade or improve cladding-coolant heat exchange in the vicinity of blocked region depending upon which of the complex thermal-hydraulic process dominates.

2.3 Physics of Re-wetting

Re-wetting can be defined as the establishment of contact between the coolant fluid and hot, dry surface [9]. In a typical accident situation in a reactor as explained in Section 2.2, re-wetting occurs due to injection of ECCS into the degraded reactor core. The surface temperature and flow rates are the primary variables that govern the re-wetting phenomena.

2.3.1 Effect of Surface Temperature

Figure 2.5 shows a typical pool boiling curve for saturated water under atmospheric pressure. With increase in the heat flux values beyond the Onset of Nucleate Boiling (ONB), marginal increase in surface temperature is observed with large increase in the heat flux. This is due to higher heat transfer coefficient in the Nucleate Boiling Region. This trend continues till the Critical Heat Flux (CHF) is attained at T_{CHF} . At this temperature, transition from nucleate boiling to film boiling begins, resulting in sharp decrease in the heat transfer coefficient. In a heat flux controlled type experiment, with initial state at point B representing stable film boiling, decrease in the heat flux traces the film boiling curve. The surface temperature is so high that the fluid is not able to establish contact with the surface irrespective of the fluid temperature. The heat transfer is essentially through the small film of vapor formed near the surface. With decrease in heat flux, the fluid establishes contact with the surface at *Minimum Film Boiling Temperature* (T_{MFB}) also known as the *Leidenfrost Temperature* (T_{LF}).

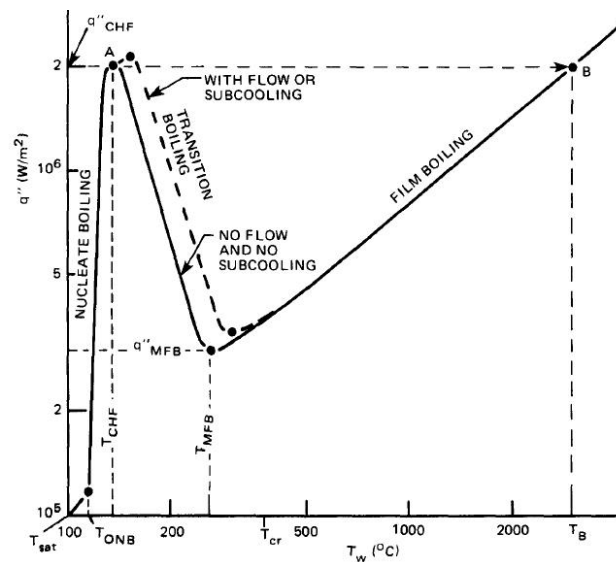


Figure 2.5: Pool Boiling Curve for Water at Atmospheric Pressure [10]

T_{LF} is equal to T_{MFB} observed for small droplets boiling on heated isother-

mal surface. However, as the droplet size increases or the surface becomes non-isothermal, the temperature measured at the point close to the liquid-droplet contact is slightly higher than the actual temperature at the contact, thus increasing the measured Leidenfrost Temperature. For a large droplet the T_{LF} would approach the pool boiling condition, i.e., T_{MFB} .

$$T_{MFB} > T_{LF, Large\ Droplets} > T_{LF, Small\ Droplets} > T_{LF, Isothermal\ Surface} \quad (2.1)$$

The Leidenfrost temperature is also called as re-wetting temperature.

2.3.2 Effect of Flow Rate

Injection of water as coolant into the degraded reactor core may lead to re-wetting of the fuel rods depending upon the flow rates of the coolant and the direction of water injection. Two strategies, namely, *Bottom Re-flooding* and *Top Re-flooding* have been adopted in the present generation reactors.

2.3.2.1 Bottom Re-flooding

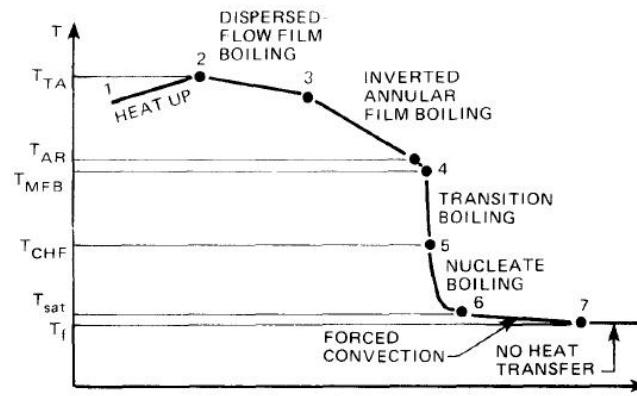


Figure 2.6: Clad Temperature for Bottom Re-flooding [10]

Bottom Re-flooding occurs when water is injected into the reactor core from

bottom. Typical cladding temperature history obtained in a *Bottom Re-flooding* is shown in Figure 2.6. For the case of high injection flow rates, initially the clad temperature rises (Point 1 to Point 2 in Figure 2.6) before cooling begins. As the coolant tries to enter the flow channel, it evaporates into fine droplets and dispersed flow film boiling begins, accompanied by fall in temperature (Point 2 to Point 3 in Figure 2.6). Since the flow rate is high, the coolant is able to enter the channel. However, since the surface temperature is higher than the re-wetting temperature, the coolant can not wet the surface and forms a film between the liquid body and the hot surface as shown in Figure 2.7. This region of flow experiences Film Boiling (Point 3 to Point 4 in Figure 2.6). Higher hydrostatic pressure in the channel forces the liquid to come in contact with the hot surface, causing transition from Film Boiling to Nucleate Boiling. The transition region is very narrow. Considerable amount of bubble formation occurs in this region. Since the surface comes in contact with bulk of liquid, this case is close to the pool boiling case and thus the re-wetting occurs essentially at T_{MFB} . The *Quench Front* is the boundary between the transition region and film boiling region. In this case the Quench Front is located at or below the water front.

For the case of *Bottom Re-flooding* with lower injection rates, liquid can not form a column above the point of contact between the liquid and solid. Hence, no hydrostatic head can force the liquid into contact with solid. The boiling region ends where the water level comes in contact with the solid surface as shown in Figure 2.8. This corresponds to the temperature T_{CHF} . The sputtering or boiling process in the boiling region produces droplets that move in the downstream direction alongwith vapor and wet the surface if the surface temperature is at or below T_{LF} . Thus quenching actually occurs at a place which is above the water level and the temperature at this location is the T_{LF} . The distance between the point at T_{CHF} and the point at T_{LF} is significant. In the sputtering region, significant axial conduction takes place from the hotter surface region to the cooler surface

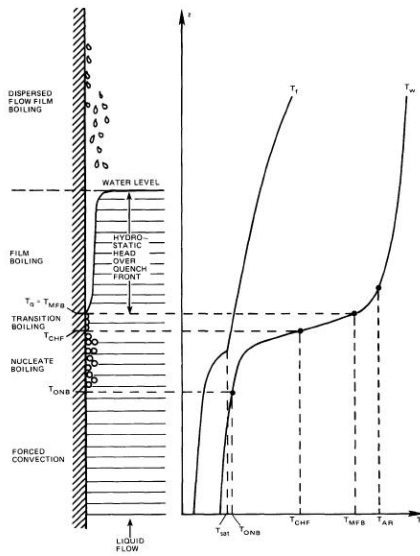


Figure 2.7: Bottom Re-flooding with High Injection Rate [10]

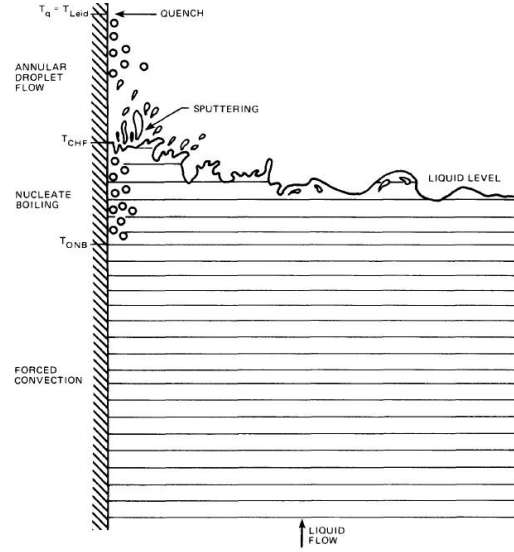


Figure 2.8: Bottom Re-flooding with Low Injection Rate [10]

region within the solid and it dictates the progress of water level in contact with solid. The *Quench Front* lies at the point downstream of the water front where temperature is T_{LF} .

Precursory Cooling, ahead of the quench front is very important in case of *Bottom Re-flooding* with high mass flow rates. Thus this type of quenching is known as Fluid Controlled Quenching. In contrast, in case of *Bottom Re-flooding* with lower mass flow rates, axial conduction within the solid surface is more significant factor and the quenching is therefore called as Solid Controlled Quenching or Conduction Controlled Quenching.

2.3.2.2 Top Re-flooding

In Boiling Water Reactors (BWR), the ECCS injects water to the top of the core via sprays. In this case, the quenching is by top flooding by a film of water. In the wet region behind the edge of the liquid film as shown in Figure 2.9, heat is removed from the surface by nucleate boiling. The bubble formation is maximum closer to the wet front. At the wet front, the wall temperature approaches T_{CHF} . The bubbles are so numerous that they interfere with each other and disrupt the edge

of the liquid film. The lateral force associated with nucleation reaches a maximum at the critical heat flux, causing the sputtering of droplets and the shearing of the film from the hot surface. The T_{CHF} is also known as the sputtering temperature, which characterizes the physical phenomenon of liquid film breakdown associated with *Top Re-flooding*. The re-wetting temperature corresponds to the T_{CHF} .

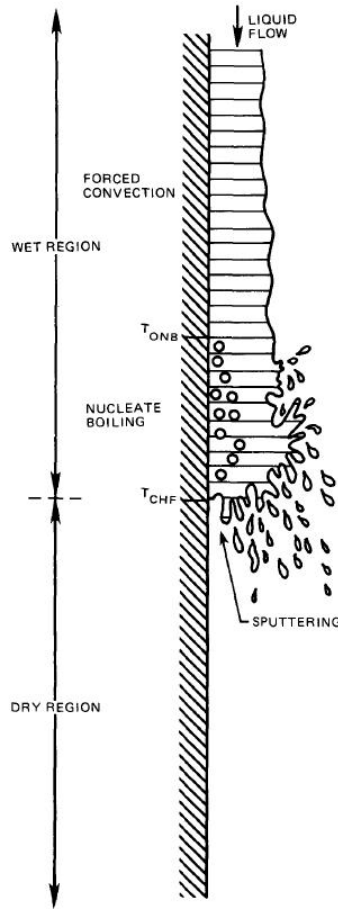


Figure 2.9: Top Re-flooding in Single Rod Geometry [10]

Once the falling film is displaced from the surface, it does not return since the only force acting on the liquid is gravity. This is only valid for the case of a single-rod geometry, for once the falling film is ejected from the rod, it will not touch the rod again. However, a nuclear reactor core has a multi-rod geometry; therefore, the liquid film displaced from the surface of one rod in the form of droplets will come in contact with another rod, cooling that part of the rod by precursory cooling.

Eventually, the rod will be re-wetted since the temperature will be at or below T_{LF} . Thus, in a multi-rod geometry the quench front for *Top Re-flooding* by a falling film will be below the sputtering front, and the quench temperature will be T_{LF} , just as in the previously discussed case of *Bottom Re-flooding* with low mass flow rate.

2.3.3 Difference between Re-wetting and Quenching

The terms re-wetting and quenching are often incorrectly assumed to be synonymous. Although re-wetting and quenching almost always take place in pair, these are distinctly different phenomena [11]. Quenching is rapid cooling of hot solid surface such as fuel cladding, caused due to heat transfer enhancement and does not necessitate a liquid-solid contact. The enhancement in heat transfer may be caused by some other mechanism other than solid-liquid contact such as sudden acceleration of steam flow. Re-wetting, however, implies establishment of direct liquid-solid contact and presence of liquid-vapour-solid triple interface. In most of the re-flooding scenarios, quenching is immediately followed by re-wetting of the surface and these two phenomena take place so quickly that it is difficult to identify end of quenching and beginning of re-wetting. The quenching temperature is higher than the re-wetting temperature.

From the reactor safety point of view, both quenching and re-wetting phenomena are important. The quenching of fuel rods helps preserve fuel rods, while the re-wetting helps in permanent, long term heat transfer enhancement on the fuel clad surface and ensures low temperatures.

Chapter 3

Literature Review

The problem of re-wetting of fuel pins has been studied experimentally by several researchers. Replication of complex geometries of core at various stages of accidents is found to be challenging, specifically when the reactor core undergoes geometrical changes during the accident. High temperatures and heat fluxes typical for nuclear fuel pins are difficult to achieve in out-of-pile experiments (experiments performed outside the reactor core). Moreover, the experimental facilities are usually scaled down keeping in focus some of the physical phenomena specific for the study and thus, the applicability of the results is limited to the phenomena. Development of analytical tools and incorporation of analytical and experimental results in numerical codes has helped in developing generic numeric tools capable of handling different reactor conditions and phenomena. This chapter briefly describes the development of significant analytical methods, numeric tools, development of scaling philosophy and experimental results pertaining to core quenching studies.

3.1 Evolution of Analytical and Numerical Techniques

A typical analysis of re-wetting phenomena involves solution of the equation of heat transfer within the fuel rod coupled to the flow equations along with different heat transfer correlations dictated by the flow regime. Several simplifying assumption have been made by several researchers in order to arrive at an analytical solution to the re-wetting problem. Some of the more prominent analytical solutions have been discussed here.

3.1.1 Solutions with Assumed Fluid Conditions

Solution of the heat conduction equation over the fuel rod, which assumes the form of a Modified Laplace Equation, involves lesser complexities as compared to the solution of flow equations in the flow channel. Thus it is imperative to obtain solution for heat conduction with closure laws for the flow (fluid parameters applied as boundary condition). Typically the simplification on the flow part has been done by using constant or known quench front velocity, quench temperatures and fixed heat transfer coefficients over different regions of the flow [12].

Based on the heat transfer coefficients, the models can be classified as Two Region Models which divide the flow channels into two parts:

1. Region behind the quench front with single phase liquid flow.
2. Region ahead of the quench front with single phase vapor flow.

The heat transfer coefficients in the two regions are defined as constants or as a function of the fluid velocities.

Multi Region Models divide the flow length into a number of regions, assigning a different heat transfer coefficient specific to each region. Some of the models have been discussed here:

3.1.1.1 Two Region Model by Duffey and Porthouse

Duffey and Porthouse [10] obtained a solution for re-wetting front velocity in one-dimensional thin clad situation as well as for the two-dimensional situation in Cartesian co-ordinate system. The model used Two Region approach with constant heat transfer coefficient in the single phase fluid domain behind the quench front and negligible heat transfer coefficient ahead of the quench front. The solution was obtained in terms of Infinite Fourier Series expansion. It was shown that the re-wetting front velocity can be approximated as Eq. (3.1) for the one-dimensional case and as in Eq. (3.2) for the two-dimensional case.

$$u_{quench}^{-1} = \rho c_p \left(\frac{t}{hk} \right)^{1/2} \frac{(T_w - T_f)^{1/2} (T_w - T_{LF})^{1/2}}{(T_{LF} - T_f)} \quad (3.1)$$

$$u_{quench}^{-1} = \left(\frac{\rho c_p}{h} \right) \frac{(T_w - T_s)}{(T_{LF} - T_s)} \left\{ \frac{Bi^2}{\gamma^2} - Bi \frac{(T_{LF} - T_s)}{(T_w - T_s)} \right\}^{1/2} \quad (3.2)$$

where

$$Bi = \frac{ht}{k} = \gamma \tan^{-1} \gamma \quad (3.3)$$

From the equations it can be seen that the re-wetting velocity does not change with time and depends on the difference between the surface and fluid temperature, geometrical parameters and material of the fuel clad. These analytical solutions compared with the experimental data within a factor of two for the Biot Number $Bi < 7$.

3.1.1.2 Two Region Model by Yeh

Yeh [13] also employed constant and zero heat transfer coefficients for the upstream and downstream zones of the quench front and obtained analytical solution for a cylindrical rod geometry in the form of an infinite series over cylindrical co-ordinate that is valid for all values of Biot Number. Based on these results, Caflisch [14]

assumed constant quench front velocity and obtained an analytical expression for the quench temperature as a function of heat transfer coefficient as:

$$\frac{2h}{u_{fg}} = \frac{2}{T_{quench}^2} \cos\left(\frac{\pi T_{quench}}{2}\right) \quad (3.4)$$

3.1.1.3 Two-Region Model by Gurcak et al.

Gurcak et al. [15] proposed the use of Isotherm Migration to solve heat conduction problem within the fuel rod in 2-dimensional cylindrical coordinate system. The general heat conduction equation can be written as:

$$\rho c_p \left(\frac{\partial T}{\partial t} \right) = \frac{1}{r} \frac{\partial}{\partial r} \left(kr \frac{\partial T}{\partial r} \right) + \frac{\partial}{\partial z} \left(k \frac{\partial T}{\partial z} \right) + q''' \quad (3.5)$$

Using the fundamental identity for isotherm migration as expressed in Eq. (3.6) the heat conduction equation can be transformed into:

$$z = z(r, T(r, z, t), t) \quad (3.6)$$

$$\rho c_p \left(\frac{\partial z}{\partial t} \right) + \frac{\partial}{\partial T} \left\{ \frac{k \left[\left(\frac{\partial z}{\partial r} \right)^2 + 1 \right]}{\frac{\partial z}{\partial T}} \right\} - \frac{1}{r} \frac{\partial}{\partial r} \left(kr \frac{\partial z}{\partial r} \right) + q''' \frac{\partial z}{\partial T} = - \frac{\partial k}{\partial z} \quad (3.7)$$

Thus the temperature T becomes the independent parameter and the axial co-ordinate z becomes the dependent parameter. The temperature being an independent parameter in Eq. (3.7), it can be solved for a particular value of temperature, say T_{quench} . Thus, the quench front position can be accurately determined. The need of using prohibitively low time steps for solving the original governing equation can be eliminated with higher time steps for the transformed governing equation.

3.1.1.4 Multi-Region Models Review by Carbajo and Seigal

Carbajo and Seigal [16] carried out comparative analysis of various models and numerical techniques reported in literature. They concluded that Two Region Model with zero heat transfer coefficient ahead of quench front is valid only for the Top Re-flooding since in case of Top Re-flooding precursory cooling due to steam ahead of quench front is absent. Three Region Models make use of correlations which are simple to use but do not take into consideration the physics of the problem. For example, assumption of adiabatic conditions ahead of quench front is not valid for fuel rod quenching situations. Multi Region Models divide the regions along the length of fuel into a number of flow regimes and assign respective heat transfer correlations of the regime. Some of the Multi-Regions Models have been discussed in subsequent sections.

3.1.1.5 Multi-Region Model by Kimball and Roy

Kimball and Roy [17] developed a time-dependent, two-dimensional conduction model in cylindrical co-ordinate system for the bottom re-flooding of a tube in an annulus using a finite integral transform. The heat transfer regions were divided as shown in Figure 3.1.

The governing heat conduction for the clad in a non-dimensional form was expressed as:

$$\frac{\partial \theta}{\partial t}(r, z, t) = \frac{D_h^2}{(R_o - R_i)^2} \left[\frac{1}{r} \frac{\partial}{\partial r} \left(r \frac{\partial \theta}{\partial r} \right) \right] + \frac{\partial^2 \theta}{\partial z^2} + \frac{D_h^2}{kT_{sat}} q'''(r, z, t) \quad (3.8)$$

where

$$\theta = \frac{T - T_f}{T_{sat}} \quad (3.9)$$

The correlations used for the T_{ONB} , T_{CHF} and T_{MFB} were as given in Eq.

(3.10) through Eq. (3.12).

$$\Delta T_{ONB} = \left[\frac{8\sigma T_{sat} q''_w}{k_f \rho_{fg} H_{fg}} \right]^{1/2} \quad (3.10)$$

$$T_{CHF} = -1.1446P^2 + 22.751P + 112.1 \quad (3.11)$$

$$T_{MFB} = T_{sat} + \left(10 \ln(q') \right) (8.49 + 2.80 \ln(P)) u^{0.029} (0.00309T_{peak} + 0.452) \quad (3.12)$$

The heat transfer coefficients used in different regions are tabulated in Table 3.1. Since the Quench Temperature depends on the coolant inlet velocity [16], the variation of the Quench Temperature with coolant inlet velocity was proposed as given in Eq. (3.13).

$$T_{quench} = 0.5 (T_{CHF} + T_{MFB}) + 0.5 (T_{MFB} - T_{CHF}) * \tanh[f(u_{in})] \quad (3.13)$$

Table 3.1: Heat Transfer Correlations used by Kimball and Roy

Region	Correlations Used
Single Phase Liquid Region	Dittus-Boelter Correlations
Nucleate Boiling Region	Modified Chen's Correlation
Inverted Annular Flow Boiling Region	Chan's Experimental Data
Convection to Steam with Entrainment	Heinemen's Correlation

The clad temperature history along the length of the fuel pin at various times is shown in Figure 3.2. The quench front velocity remains constant through the length of the fuel pin as shown in Figure 3.3.

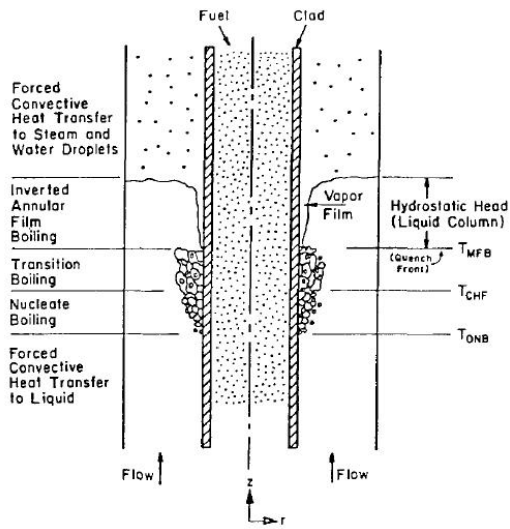


Figure 3.1: Heat Transfer Modes during Re-flooding [17]

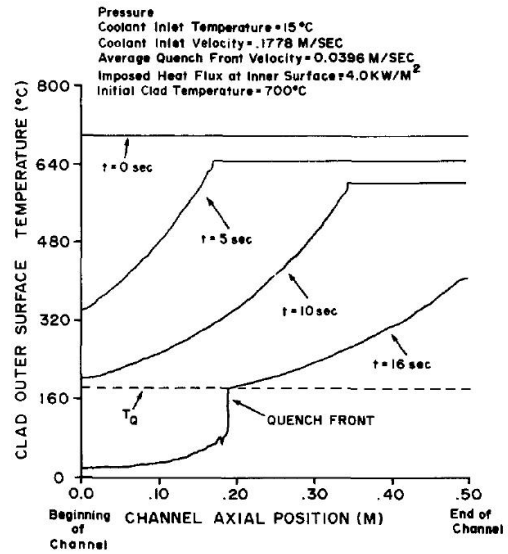


Figure 3.2: Clad Temperature Evolution [17]

It can be seen that the quench front velocity decreases with increase in the heat flux value owing to requirement of removal of higher energy from the same length. The quench front velocity increases with increase in inlet flow rate as shown in Figure 3.4. The results obtained exhibit correct trends with the imposed clad inner surface heat flux and coolant inlet velocity.

3.1.1.6 Multi-Region Model by Viskanta and Kim

Viskanta and Kim [18] developed a model to predict temperature distribution along the flow channel of a PWR ahead of the quench front. The model included one-dimensional heat conduction along the fuel, convective heat transfer between the fuel surface and coolant and also the radiation heat exchange between the fuel surfaces and between the surface and steam. A typical flow channel considered is shown in Figure 3.5.

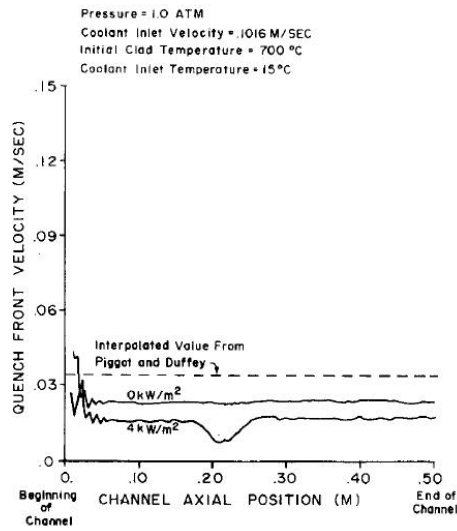


Figure 3.3: Effect of Heat Flux on Quench Front Velocity [17]

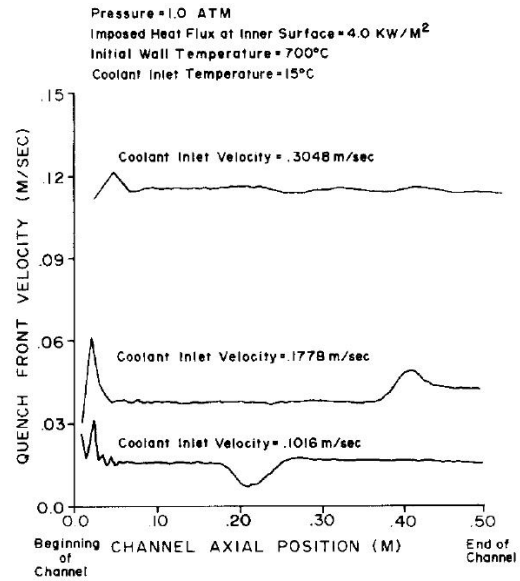


Figure 3.4: Effect of Inlet Velocity on Quench Front Velocity [17]

Two different models, one with Lumped Fuel model and other including fuel with Fuel-Clad-Gap model were considered. It was observed that the Fuel-Clad-Gap model predicts higher fuel temperature and lower clad temperatures than the respective portions in the lumped fuel model. This is due to lower effective heat transfer (convection between fuel and clad) between the fuel and the clad in the case of Fuel-Clad-Gap model than the higher effective heat transfer (conduction in fuel) in the lumped fuel model. The simulations were carried out with different values of initial uncovered height of the fuel pins. Larger initial uncovered height of fuel pins yields higher temperatures of the fuel pin and coolant as shown in Figure 3.6. Effect of presence of Hydrogen in the coolant was also studied with the assumption that some amount of Hydrogen was initially present at the quench front (this contradicts the physical situation wherein hydrogen is generated along the uncovered portion of the core). Presence of Hydrogen in the coolant decreases the fuel temperature as shown in Figure 3.7 due to higher specific heat of steam-hydrogen mixture.

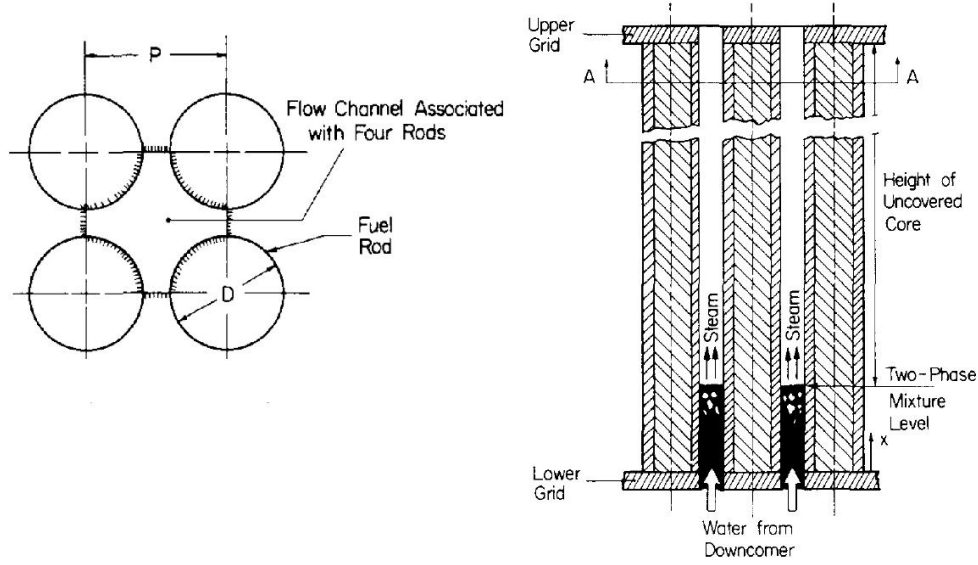


Figure 3.5: Typical Flow Channel of PWR [18]

The results obtained exhibit correct trends with the imposed clad inner surface heat flux and coolant inlet velocity. Effect of Zr-clad oxidation and steam dissociation in presence of Zr at high temperatures was reported by Viskanta and Mohanty [19]. The Zr-oxidation being an exothermic reaction increases the fuel clad temperature substantially as shown in Figure 3.8, whereas the steam dissociation being endothermic tends to reduce the fuel clad temperature as shown in Figure 3.9.

3.1.1.7 Multi-Region Model by Schutzle and Unger

A one-dimensional flow channel analysis was carried out by Schutzle and Unger [20] with the assumption that the pressure drop along the flow channel is negligible and hence momentum equation was not solved for. The continuity and energy equation for the the water and steam were given as:

$$\frac{\partial}{\partial t} [\rho_f (1 - \alpha) A] + \frac{\partial}{\partial z} (G_f A) = -\phi A \quad (3.14)$$

$$\frac{\partial}{\partial t} [\rho_g (\alpha) A] + \frac{\partial}{\partial z} (G_g A) = -\phi A \quad (3.15)$$

$$\frac{\partial}{\partial t} [\rho_f H_f (1 - \alpha) A + \rho_g H_g (\alpha) A] + \frac{\partial}{\partial z} (G_f H A + G_g H_g A) - \frac{\partial}{\partial t} (P A) = q''' A \quad (3.16)$$

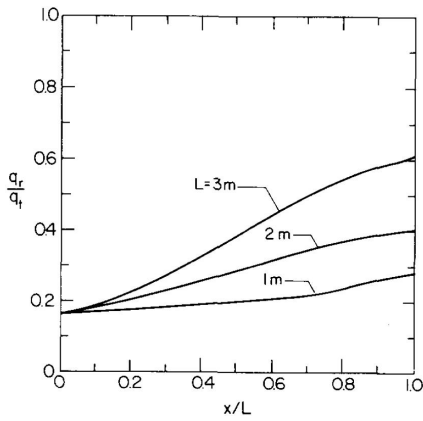


Figure 3.6: Effect of Initial Uncovered Height on Fuel Temperature Distribution [18]

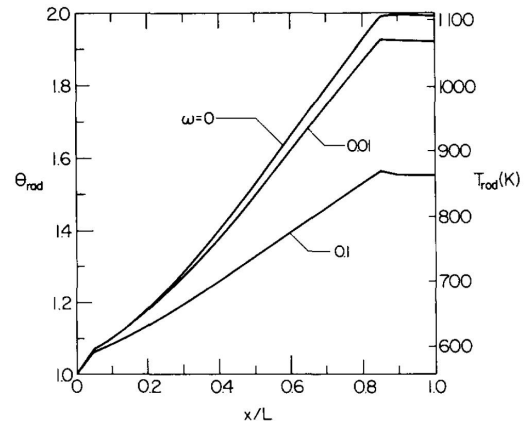


Figure 3.7: Effect of Hydrogen Distribution on Fuel Temperature Distribution [18]

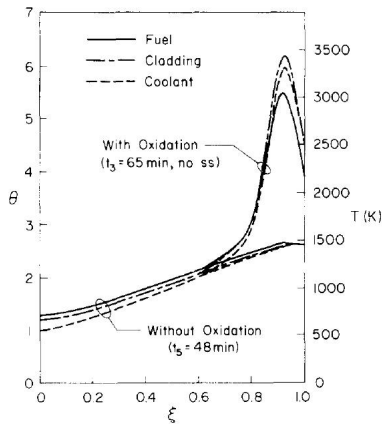


Figure 3.8: Effect of Zr Oxidation on Fuel Temperature Distribution [18]

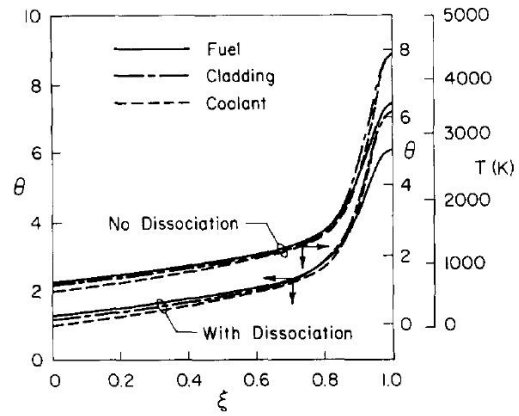


Figure 3.9: Effect of Steam Dissociation on Fuel Temperature Distribution [18]

Different flow regimes were identified based on the fluid and wall temperature

(Figure 3.10) and the vapour void fraction was modeled using drift flux relation [21]. Heat transfer correlations used by this code are tabulated in Table 3.2.

Table 3.2: Heat Transfer Correlations used in Schutzle’s Code

Region	Correlations Used
Laminar Convection	Collier’s Correlation
Turbulent Convection	Dittus-Boelter Correlation
Subcooled and Saturated Nucleate Boiling	Chen’s Correlation
Saturated Film Boiling	Bromley Correlation
Subcooled Film Boiling	Sudo and Murao Correlation
CHF	Zuber Correlation
T_{MFB}	Henry Correlation

The fuel rod temperatures were calculated by two-dimensional time dependent Fourier Equation for cylindrical geometry along with a moving grid approach in the vicinity of the quench front to capture the steep temperature gradients and higher conduction rates in the fuel in this region (Figure 3.11).

The results obtained from the simulations were compared to the experimental data obtained from FLECHT Group-I Experiments. The comparison for the clad temperature is shown in Figure 3.12. The quenching as predicted by the code occurs 13 s later than the quenching observed in the test. This is due to lower heat transfer coefficients used by the code for the precursory cooling region.

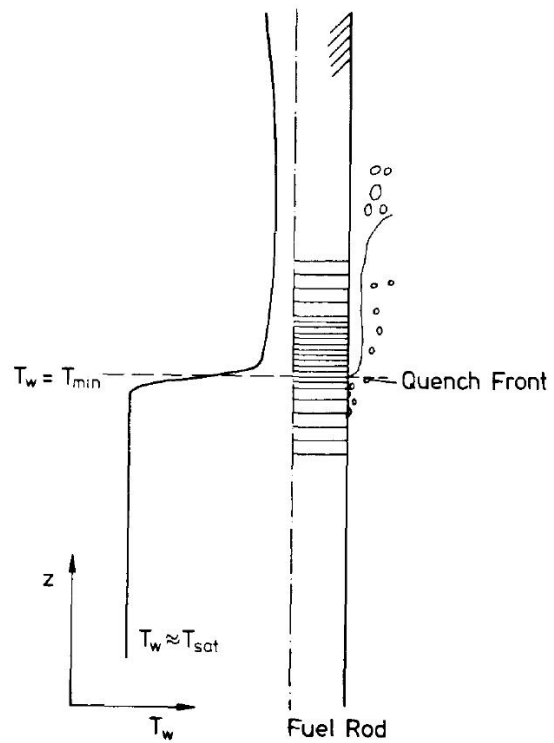
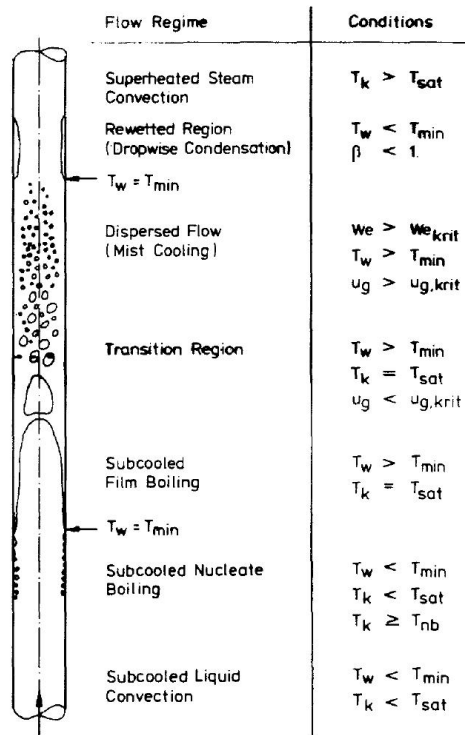


Figure 3.10: Flow Regimes and Heat Transfer Modes in Schutzle's Code [20]

Figure 3.11: Schematic of Moving Mesh in Schutzle's Code [20]

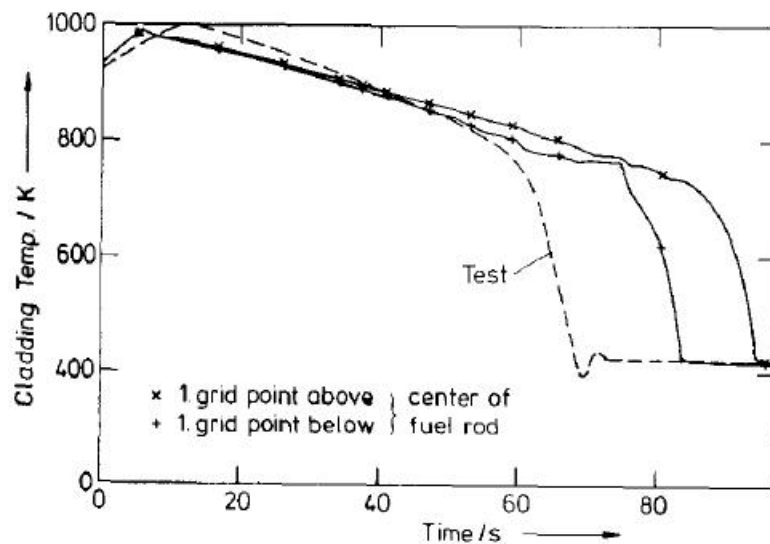


Figure 3.12: Comparison of Cladding Temperature with FLECHT Experiments [20]

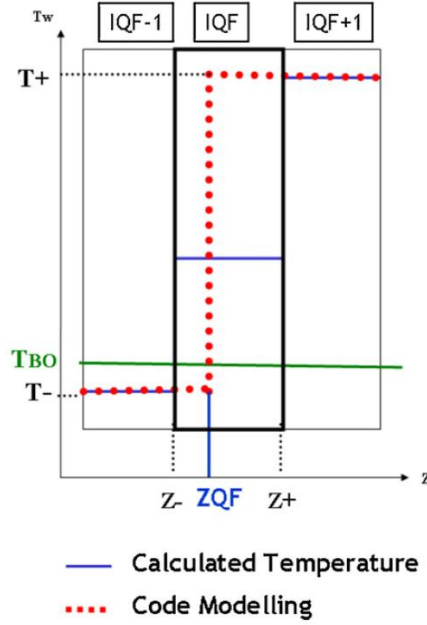


Figure 3.13: Quench Front Tracking Scheme [22]

3.1.1.8 Quench Front Tracking Model by Fichot[22]

The quench front position under bottom re-flood conditions is driven by strong axial conduction taking place in the fuel pin near the quench front. Precise estimate of the position of the quench front requires finer mesh sizes in the transition boiling region. The wall to fluid heat transfer, downstream of the quench front, is calculated as sum of two terms as given by Eq. (3.17).

$$q'' = k \frac{dT_w}{dz} + h(T_w - T_{sat}) \left(1 - \frac{z - z_{QF}}{\Delta z_0} \right) \quad (3.17)$$

where Z_0 is the droplet mean free path. The first term is the large heat flux present at the quench front due to sharp temperature gradients near the front and is limited to within CHF. The second term is the clad pre-cooling downstream of the front due to droplet entrainment. A formulation of heat flux near the quench front is not employed by the Severe Accident Analysis codes, due to very long CPU times required for refined meshes.

Consequently, such codes evaluate the heat transfer near the quench front using heat transfer coefficient. This type of modeling is valid only for high injection rates,

low heating power and low pressures. Fichot [23] developed a model for quench front tracking to overcome these deficiencies. The quench front position is detected by comparing the temperatures at mesh points with the quench front temperature given by Eq. (3.18) as shown in Figure 3.13.

$$T(Z_{QF}) = \frac{Z_{QF}}{Z_{+IQF} - Z_{-IQF}} T^- + \left(1 - \frac{Z_{QF}}{Z_{+IQF} - Z_{-IQF}}\right) T^+ \quad (3.18)$$

The results obtained were compared with the PERICLES and RBTH tests and were found to be in good agreement.

3.1.2 Solutions with Coupled Fluid Flow and Heat Conduction Equations

Several one-dimensional thermal hydraulic codes such as RELAP-SCDAP [24] have been developed to analyze the coupled Fluid Flow Heat Transfer problems. The essential focus of such *system codes* is to facilitate modeling of entire nuclear plant systems en-route making simplifying assumptions in order to preserve the important physical phenomena. For example, RELAP-SCDAP solves for mass, momentum and energy equations for water as well as steam in a single direction. These equations are coupled to heat conduction equations in the interacting structures through set of appropriate correlations. However, the treatment of cross-flow is crude; the momentum equation in the direction perpendicular to the dominant flow direction does not take into account the flux terms. The magnitude of flux terms in this direction is expected to be negligible as compared to the predominant flow flux under *normal operation* of NPP. However, as it will be shown in subsequent chapters, the flux terms in both these directions are comparable in an accident scenario, specifically for re-flooding scenario under partially degraded core. Hence, use of such codes may be justified in understanding overall characteristics of the

systems but may not be suitable in assessing a specific physical phenomena. A modification is thus required to be able to simulate such phenomenon.

3.2 Scaling Methodologies for Degraded Core Quenching

Modeling of *severe accident* situations in a reactor core requires knowledge of several interrelated complex processes such as the quench front movement and entrainment [25], corium dispersion [26], blowdown [27]. The codes developed to model such phenomena make use of numerous assumptions for simplification of these complex processes. Scaled down experimental facilities are built to verify the applicability of such codes. Scaling criteria required for design of such scaled down experimental facilities are obtained from Dimensional Analysis, Differential Equations or from Analytical Methods [28].

Dimensional Analysis involves generation of large number of parameters, encompassing all the important parameters relevant for the process. Since knowledge of relevant parameters is essential for this analysis it is applicable only to well-known processes.

Scaling of Differential Equations along with the scaled initial and boundary conditions can be used to obtain complete scaling criteria ensuring inclusion of all the process parameters. The scaling criteria evolved using this depends on the completeness of the differential equation itself. Lack of a complete governing differential equation for cases such as re-wetting and applicability of boundary conditions such as the closure relations only in the local regions makes use of this method difficult for severe accident situation.

The restriction on completeness of differential equation can be solved by using Stepwise Integral Method that converts differential equation into analytical solutions. This method not only generates integral scaling criteria but also facilitates

determination of hierarchy of these criteria by identifying its relative importance.

3.2.1 Two Phase Flow Scaling Laws by Graff

Graff [29] brought out scaling criteria for a Two Phase flow situation in a BWR using Stepwise Integral Approach from non-dimensionalisation of conservation equations for Drift Flux Model. The flow channel length was divided into two regions: Lower part of the core with sub-cooled boiling and higher part of the core with two phase region. In the sub-cooled boiling region the thermodynamic quality and flow quality are given by Eq. (3.19) and Eq. (3.20) respectively.

$$x_e(z) = \left(\frac{H(z) - H_f^{sat}}{H_{fg}} \right) \quad (3.19)$$

$$x(z) = \left(\frac{\dot{m}_g}{\dot{m}} \right) \quad (3.20)$$

Variation of these qualities along the flow channel is shown in Figure 3.14. The thermodynamic quality can also be obtained from energy balance as given in Eq. (3.21).

$$x_e(z) = \left(\frac{q''}{\dot{m}H_{fg}} \right) \left(\frac{4l}{D_h} \right) \frac{z}{l} - \left(\frac{H_f^{sat} - H_{in}}{H_{fg}} \right) \quad (3.21)$$

The two dimensional groups that are manifested in these equations are the Phase Change Number (Eq. (3.22)) and the sub-cooling number (Eq. (3.23)).

$$N_{pch} = \left(\frac{q''}{\dot{m}H_{fg}} \right) \left(\frac{4l}{D_h} \right) \quad (Phase\ Change\ Number) \quad (3.22)$$

$$N_s = \left(\frac{H_f^{sat} - H_{in}}{H_{fg}} \right) \quad (Subcooling\ Number) \quad (3.23)$$

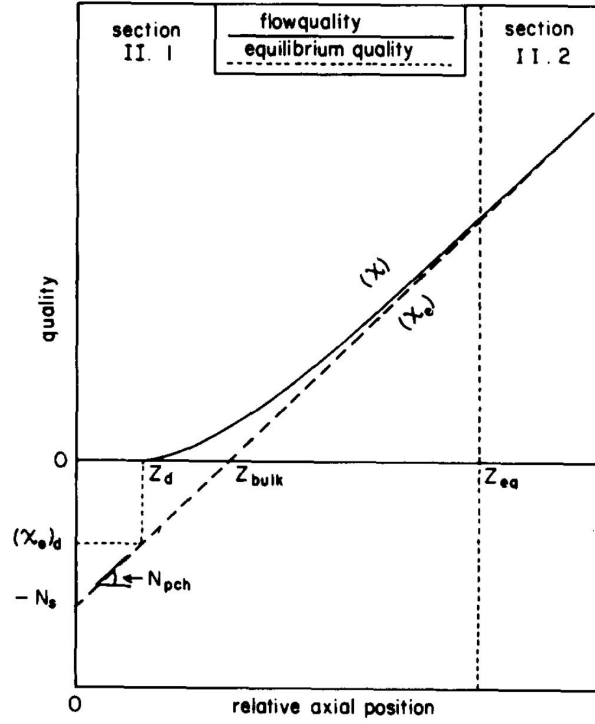


Figure 3.14: Variation of Thermodynamic and Flow Quality along the Channel [29]

Similarly from the two phase flow region the non-dimensional numbers to be conserved are given in Eq. (3.24) through Eq. (3.27)

$$N_\rho = \left(\frac{\rho_g}{\rho_f} \right) \quad (3.24)$$

$$N_g = \left(\frac{D_h}{l} \right) \quad (3.25)$$

$$N_{Fr} = \left(\frac{\dot{m}^2}{\rho_f^2 l g} \right) \quad (3.26)$$

$$N_d = \frac{(\rho_f (C_0 - 1) H_{fg})}{\dot{m}} + \frac{\rho_f u_{gj}}{\dot{m}} \quad (3.27)$$

3.3 Evolution of Experimental Methods

As mentioned in Section 2.2, the coolability of the rod bundles depends on several factors. Several experiments have been carried out by various researchers in order to study the effect of these factors on quenching patterns post LOCA scenario. Some of the experimental studies reported in literature are discussed here:

3.3.1 Experiments with Intact Rod Geometry

Although as seen in the Section 2.2, the time gap between the initiation of accident in a nuclear reactor and the beginning of deformation of fuel rods is very small, the quenching of intact rod geometry has been studied extensively to validate the quenching models developed.

3.3.1.1 Bottom Rewetting Experiments by Ihle and Rust

Ihle and Rust [30] pointed out that the experiments reported in literature to understand Bottom Re-wetting were done with solid type electrical heaters with direct contact between the heater and the cladding. However, in an actual nuclear fuel, there exists a gap between the heat generating fuel element and the clad, the gap being usually filled with inert gas such as Argon. The presence of gap has significant effect on the clad temperatures as well as the quench patterns [18]. Ihle and Rust carried out experiments (known as SEFLEX) with Tungsten electrical heater, surrounded with annular Zr pellets enclosed in Zr-clad with a gap between the pellets and the cladding and compared the results with FEBA experiments done with solid heater rods. Experiments were performed with both Intact as well as Blocked array of fuel pins.

As shown in Figure 3.15 Plot A, the effect of gap in the heater rods is not significant near the entrance of the test section. However, the effect becomes prominent at higher elevations, with gap filled fuel pins cooling at much higher rates than the solid type pins of FEBA experimental facility as shown in Figure

3.15 Plot D. The propagation of quench front has been shown in Figure 3.16. It also suggests that the quench front travels at a faster rate with SEFLEX fuel bundles than in case of FEBA fuel bundles.

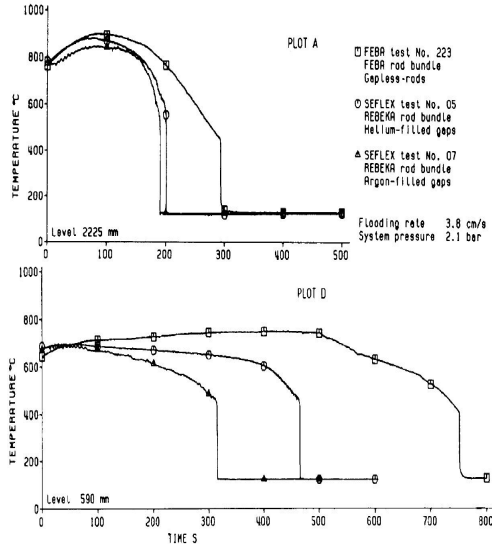


Figure 3.15: Cladding Temperature for axial level 2225 mm (Plot A) and 590 mm (Plot D) for FEBA and SEFLEX Experiments [30]

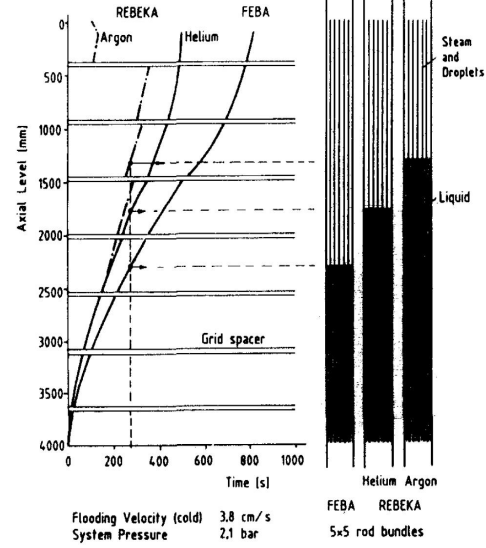


Figure 3.16: Quench Front Propagation for FEBA and SEFLEX (REBEKA) Rod Bundles [30]

3.3.1.2 Bottom Re-wetting Experiments by Tuzla et al.

Tuzla et al. [31] carried out an experimental study of bottom re-wetting phenomena in a 3X3 rod bundle assembly. Low mass fluxes were considered for this study that translate into re-wetting velocity in the range of 1 – 5 mm/s range. The cross-section of the rod bundles is shown in Figure 3.17. The rod bundle geometry consisted of nine test rods surrounded by a heated square shroud for a realistic simulation of an infinitely arrayed rod bundle assembly. The schematic of the test setup is shown in Figure 3.18. The effects of various flow parameters such as mass flux, wall heat flux, and quality on the re-wetting process were studied.

Initially the test section was heated to 450°C by passing steam through it. The electrical power to the heater rods embedded inside the fuel rod was then

switched on to achieve desired heat flux value, along with simultaneous injection of saturated coolant in the test sections at desired flow rate. The variation of wall superheat along the flow channel at two different times is shown in Figure 3.19.

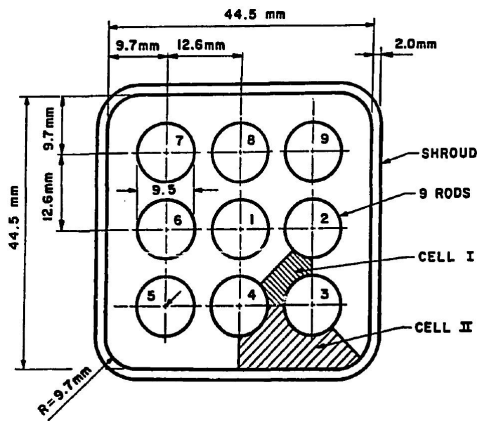


Figure 3.17: Cross-sectional View of Rod Bundles for Experiments by Tuzla et al. [31]

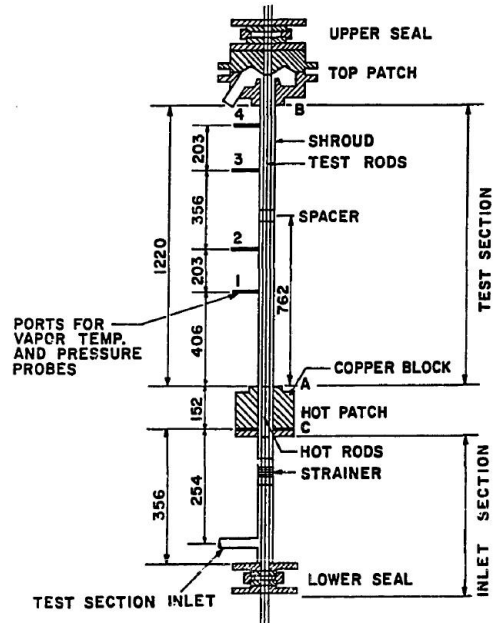


Figure 3.18: Schematic of Test Section for Experiments by Tuzla et al. [31]

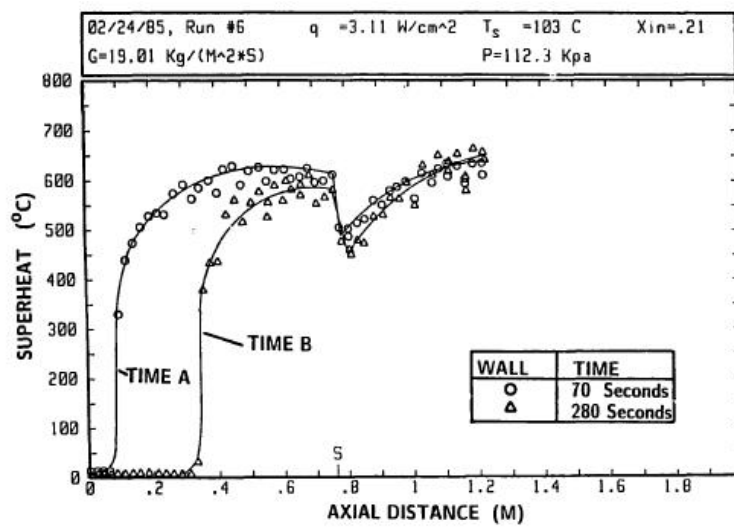


Figure 3.19: Variation of Wall Superheat along Flow Channel [31]

Upstream of the quench front the wall is essentially at saturation temperature. Wall superheat increases rapidly near the quench front. The dip in the wall superheat near point S is observed due to presence of spacer grid at that point. Figure 3.20 shows the effect of inlet quality on the quench front velocity. The quench front velocity increases with increase in inlet quality due to higher precursory cooling available at higher inlet quality. Moreover, there is increase in the quench front velocity with increase in inlet sub-cooling owing to higher sensible heat removal capacity of inlet fluid. The quench front velocity also increases with increase in inlet coolant velocity as shown in Figure 3.21.

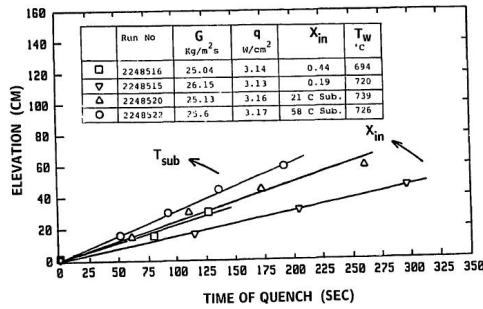


Figure 3.20: Effect of Inlet Quality on Quench Front Velocity [31]

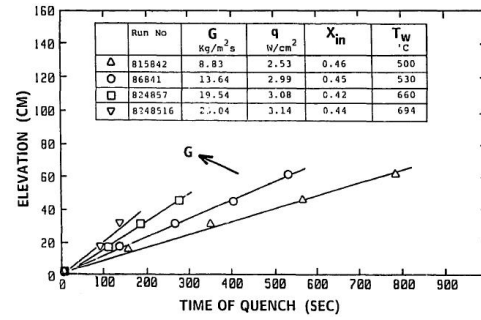


Figure 3.21: Effect of Inlet Mass Flow Rate on Quench Front Velocity [31]

3.3.1.3 Bottom Re-wetting Experiments (QUENCH) by Sepold et al.

The QUENCH Test Facility at Karlsruhe, Germany was designed to investigate the hydrogen generation during injection of water into uncovered core of a LWR [32]. The test facility consists of test section with the test bundle over which superheated steam from the steam generator flows, along with argon as a carrier gas from bottom. The test bundle is made up of 21 fuel rod simulators approximately 2.5 m long. The quench water enters the test section at 395 K, i.e., saturation temperature at 0.2 MPa. Twenty fuel rod simulators are heated using 6 mm tungsten heaters over a length of 1024 mm surrounded with ZrO₂ pellets with Zr cladding and the central fuel rod simulator is unheated. The total heating power is 70 kW.

The test bundle is surrounded by a shroud of Zircaloy with a 37 mm thick ZrO_2 fiber insulation.

The QUENCH experiments was carried out in four phases, namely, a heat-up phase, a pre-oxidation phase (to create oxide layer as is the initial condition in reactor core), a transient phase and a quenching phase. Initially the setup is heated to 1400 – 1500K by electric heaters in argon-steam environment. Quenching is initiated by stopping the steam-argon flow and injecting water in lower plenum at desired flow rates. Before the water enters the test section power is reduced from about 20 kW to 4 kW to simulate decay heat level of the fission products.

It was observed that the onset of cooling occurs simultaneously throughout the length of the fuel rod as soon as the fluid enters the test section. This is depicted in Figure 3.22.

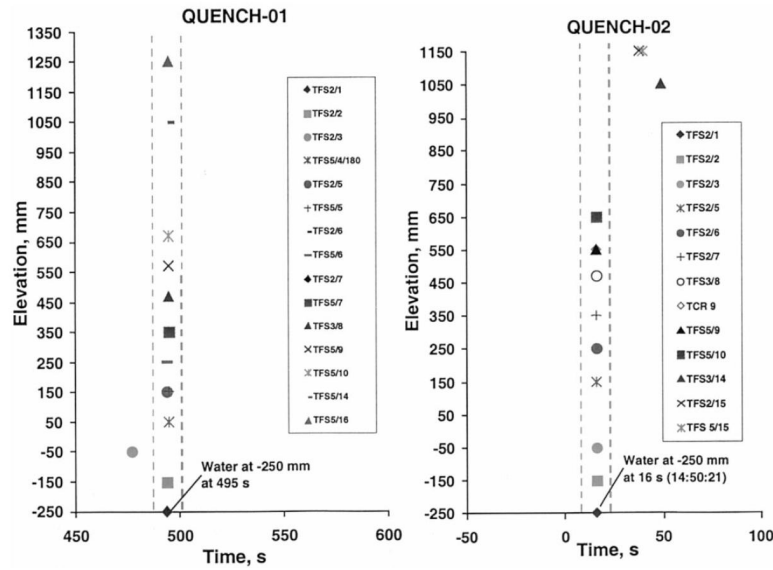


Figure 3.22: Onset of Cooling for Different Elevations in the Test Section [32]

With the entry of coolant into the test section, most part of the coolant gets converted to steam, which provides precursory cooling for the downstream portions of the test section, thus triggering cooling throughout the test section. Figure 3.23 shows variation of core temperature at different elevations. The fuel rods show

saturation temperatures up to the elevation of 250 mm, indicating that the quench front has reached up to that level. The temperatures in the upper region of test section show large fluctuations suggesting local wetting of cladding. The quench rates observed at different elevations of the test section differ as shown in Figure 3.24.

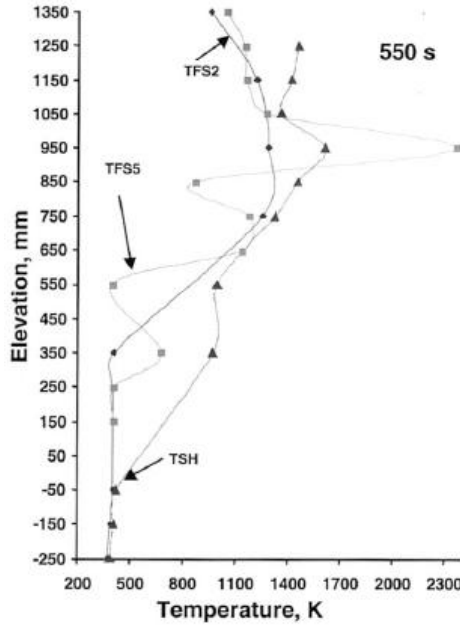


Figure 3.23: Variation of Core Temperature along the Test Section Length [32]

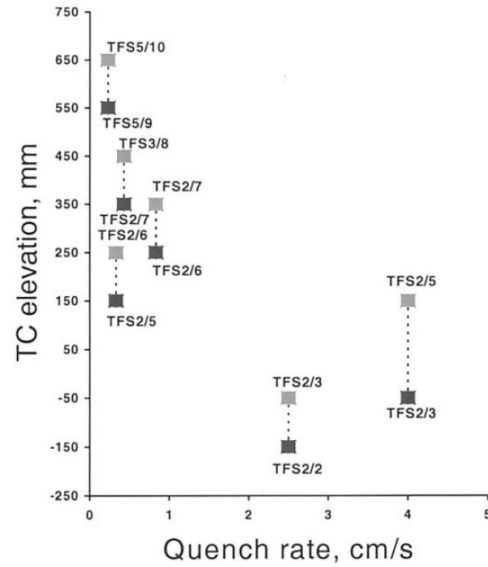


Figure 3.24: Variation of Quench Rate along the Test Section Length [32]

3.3.2 Experiments with Deformed Rod Geometry

As mentioned in Section 2.2, failure of ECCS can lead to higher temperatures in the reactor core which may trigger clad ballooning and blockage of flow path for the coolant. Experiments carried out to study the effect of flow blockages include FEBA [30], SEFLEX [33, 34, 35], THETIS [4] and FLECHT-SEASET [36] programmes. All of these experiments are out-of-pile experiments carried out with predefined deformed rod geometries. The size and length of the pre-fabricated balloons were based on the results from multi-rods ballooning experiments, mainly

from the programmes conducted in Germany (REBEKA), USA (MRBT) and Japan (JAERI). These tests (JAERI tests in particular) have shown the possibility of severe flow restriction (up to 90%) and axially extended contacts between rods over more than 20 cm [37], however, this study does not include quenching of such rods.

Grandjean [4] carried out a review of experiments studying the effect of deformed rod geometry on coolability. Main findings from these experiments are discussed here:

3.3.2.1 FEBA Experiments

The Flooding Experiments with Blocked Arrays (FEBA) programme involved separate effect tests under different re-flood rate, system pressure and quench water temperature. The heater rods used in FEBA bundle tests were solid type simulators, each composed of a heated spiral element embedded in magnesium oxide insulator, tightly encased in 1 mm thick stainless steel cladding. The 5 x 5 bundle was housed in a 6.5 mm thick stainless steel shroud whose large calorific capacity is used to partially simulate the thermal environment of the surrounding fuel rods. The Ballooned Portions were simulated by superimposing hollow sleeves onto a group or the whole bundle of rods in a coplanar manner. Two blockage ratios were chosen: 62 and 90%. The stainless steel sleeves were 180 mm long for maximum blockage lengths of 125 mm (62% blockage) and 65 mm (90% blockage), respectively as shown in Figure 3.25. These sleeves were 1 mm thick with uniform thickness for the 62% blockage and 1 mm to 2.35 mm thick for the 90% blockage. Tests were carried out with different locations of the ballooned portions in the fuel matrix as shown in Figure 3.26.

Following conclusions were drawn from the FEBA experiments:

- With a blockage ratio of 90%, sleeve temperatures in the blocked region are significantly lower than temperatures recorded in the bypass.

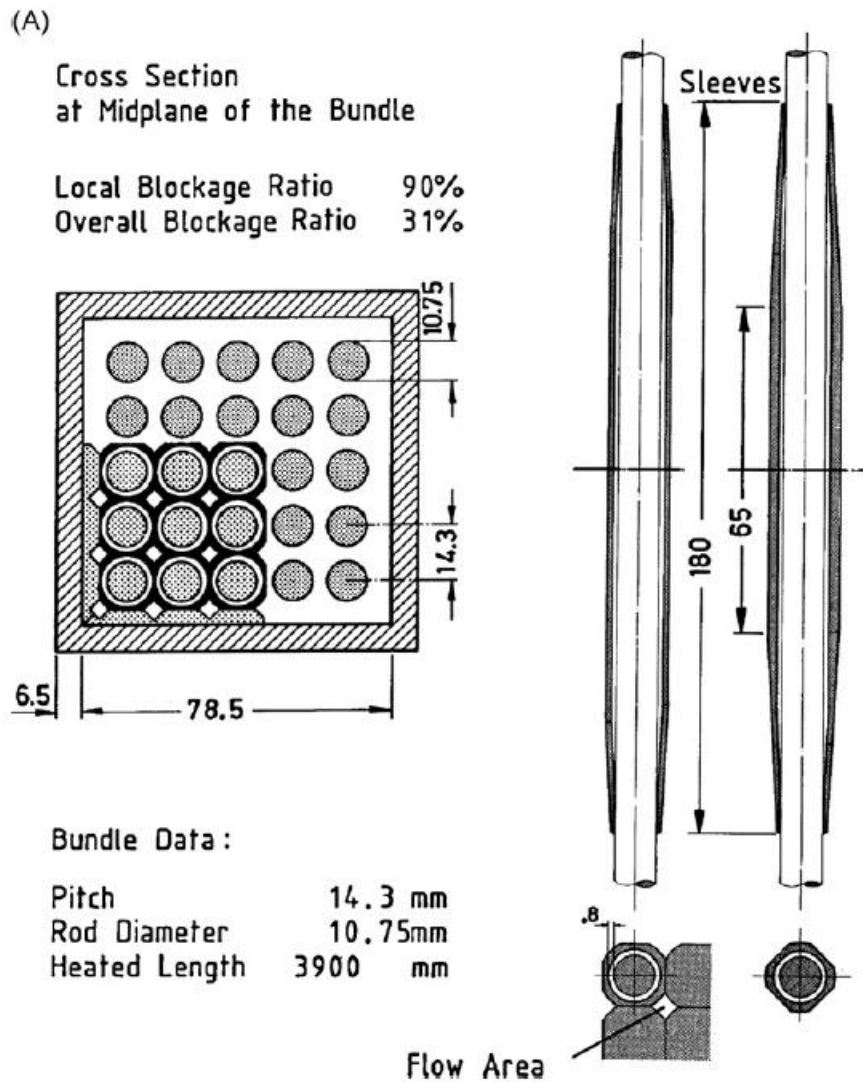


Figure 3.25: Schematic of FEBA Test Matrix and Ballooned Fuel Pins [4]

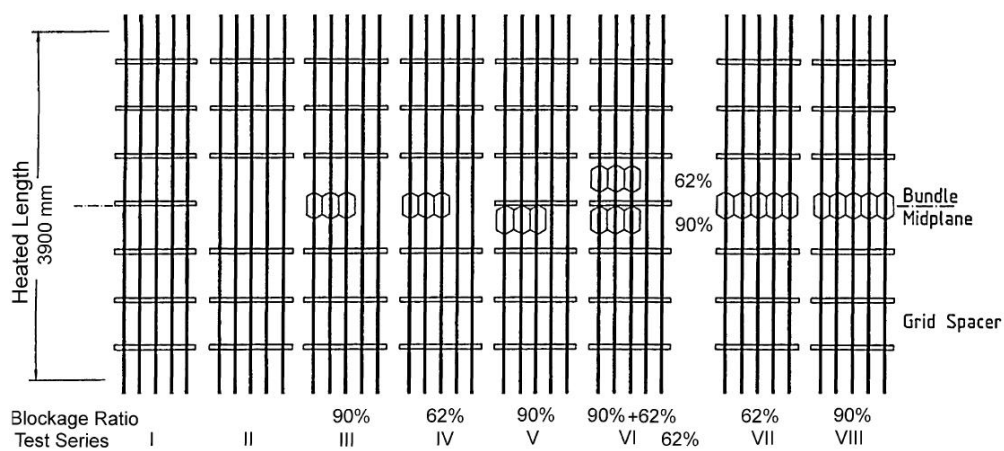


Figure 3.26: FEBA Fuel Matrix Configurations depicting Position of Blockages [4]

- Compared with a blockage-free test under the same conditions, the maximum temperature in the test with blockage is not higher, although re-wetting is delayed.
- With a blockage ratio of 62%, sleeve temperatures in the blockage are always significantly lower than cladding temperatures in the by-pass. Re-wetting also occurs earlier in the blockage.
- Downstream from the blockage, the maximum cladding temperature in the blocked region always appears lower than the maximum cladding temperature in the by-pass region.
- For a double blockage of 90 and 62%, located, respectively, upstream and downstream from the mid-plane spacer grid, behavior in the blockages appears to be similar to tests with only one blockage.
- A marked reduction in cladding temperatures is observed at 62% blockage outlet (in comparison to those recorded in the by-pass at the same level); however, this tendency reverses further downstream where blockage cladding temperatures rise above cladding temperatures in the by-pass 200 mm downstream from this second blockage. This observation may suggest a possible penalizing behavior in a blockage configuration with long balloons.
- Coolability significantly increases in the absence of a by-pass, both within and downstream from the blockage in comparison to a test with a by-pass under the same conditions.

The shortcomings of FEBA experiments are:

- In a realistic accident situation in PWR, the clad ballooning reduces the clad thickness in the ballooned region, reducing the thermal inertia of the fuel locally. However in FEBA experiments a constant uniform clad thickness was assumed over the ballooned portion.

- Superimposing sleeves on heater rods induces delay in re-wetting immediately downstream from the blockage due to axial thermal conduction from the fuel clad beneath the sleeve.

3.3.2.2 SEFLEX Experiments

To answer the questions raised against the applicability of FEBA experimental results, SEFLEX experiments were carried out with and without blocked arrays. The fuel used for SEFLEX Experiments had a gap between the annular pellets and the clad. The gap was pressurized with Argon and Helium to study the effect of gap thermal conductance on the re-flood behavior: Helium is the filling gas for fresh fuel rods whereas Argon thermal conductivity roughly simulates that of the fission gases mixed with helium found in end-of-life spent fuel rods.

Figure 3.27 compares the temperature variation measured at mid-plane of the blockage for the FEBA test and SEFLEX tests, both performed with injection rate of 3.8 cm/s at 2.1 bar .

For the FEBA test, although the sleeve temperature of ballooned rod is lower than the by-pass rod at the time of quenching, the quenching of by-pass rod is earlier than that of the ballooned rod. On the other hand, for the SEFLEX tests with Argon as well as Helium, the ballooned clads show lower temperatures than the intact clads throughout the cooling transient and quenching occurs significantly earlier than the intact rods. This is primarily due to lower thermal capacity of the balloons of SEFLEX rods as well as the greater thermal decoupling between the balloon and the heater due to larger gap. In severe blockage condition (90%), re-wetting of the central section of the balloons occurs at a very early stage due to increased turbulence and cooling from liquid droplets. Quenching progresses via secondary quench fronts upstream and downstream from the blockage, leading to earlier re-wetting of the non-deformed parts of the rods near the balloons in comparison to an unblocked bundle.

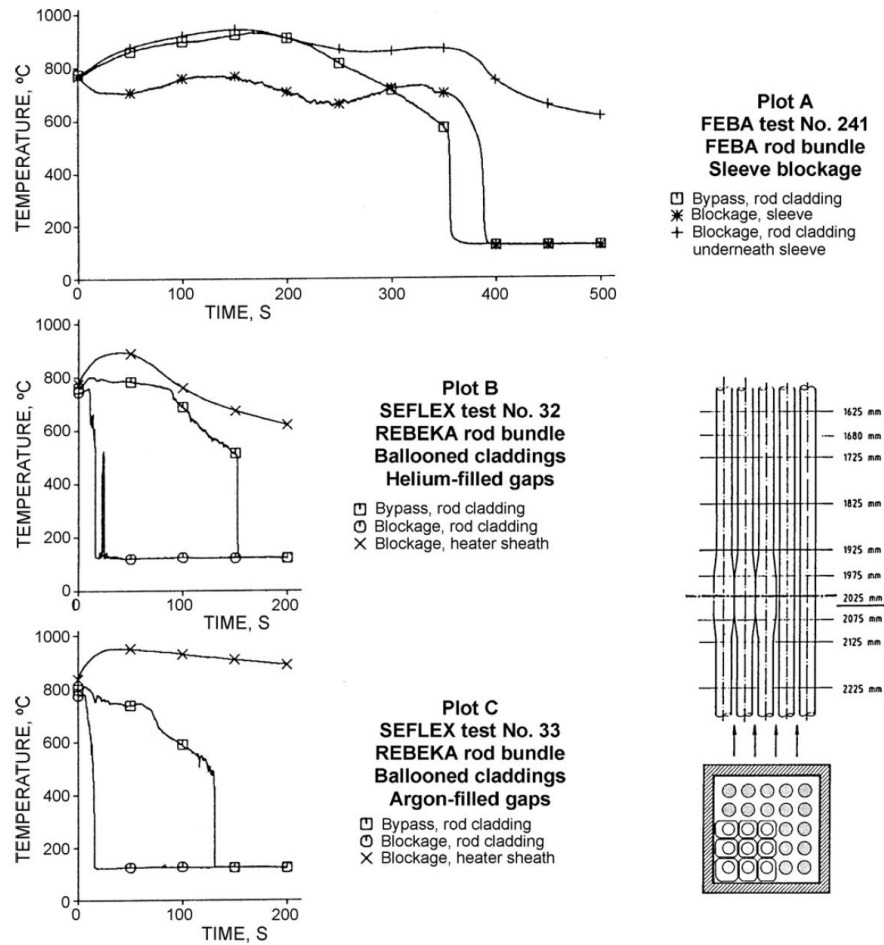


Figure 3.27: Clad Temperature Transient for SEFLEX Experiments [4]

However the SEFLEX tests employed a higher ratio of re-flood rate to input power as compared to the typical ratio for NPPs. Tests with severe re-flood conditions, i.e., with much lower re-flood rates were not performed. Also the tests did not account for peaking of power in the ballooned regions that would occur due to slumping of fuel pellets within a ballooned fuel rod in a realistic situation.

3.3.2.3 THETIS Experiments

The THETIS programme was carried out by the United Kingdom Atomic Energy Authority (UKAEA) at the Atomic Energy Establishment in Winfrith. The test assembly consisted of a 7 x 7 rod array with a 4 x 4 group of rods containing the blockage region. The assembly was enclosed in a square shroud tube. The fuel rod simulators of 12.2 mm diameter had a heated length of 3.58 m and were held in

position with a set of seven spacer grids. These fuel rod simulators were solid type electric simulators similar to FEBA test rods. The 4 x 4 rod array blocked region was separated from the shroud by one or two rows of non-deformed fuel rods. This configuration prevented thermal conduction through the direct contact between the cladding balloons and the shroud, as was the case for blockages located on the edge of the assembly in FEBA and SEFLEX tests. Ballooning of the rod cladding was simulated by superimposing a pre-fabricated Inconel sleeve. The maximum blocked region extended over 180 mm, with entry and exit tapers. The sleeve thickness in the maximum deformed region was 0.3 mm, which is comparable to that of a real cladding balloon.

Figure 3.28 shows the effect of blockage ratio on the coolability for the same re-flood flow rates. During early period of cooling, blockage cooling is improved due to onset of liquid entrainment into the blocked region. The temperature in the blocked regions for the 90% blockage are thus lower than that for 80% blockage in the early period of cooling. The peak balloon temperature for the 80% blockage reaches 880°C at about 275 s. The peak temperatures for the 90% blocked case can be expected to be higher than this. Higher peak temperatures for higher blockages that experience better cooling during early cooling phase can be explained based on the relative speeds of steam and droplets and their effect on heat transfer.

A blockage causes the coolant flow to divert into the by-pass. The mass flow rate in the blockage sub-channels is reduced approximately in proportion to the flow area for long blockage. Consequently, the steam speed in the maximum blocked section is comparable to that in the unblocked section. When the quench front is rather far upstream, the entrained droplets are accelerated by the steam flow due to the progressive acceleration of steam caused by the heating and evaporation of the liquid. The steam flow approaching a blocked section, reduces to a lower value and increases again to its original value through the blocked section as shown in Figure 3.29.

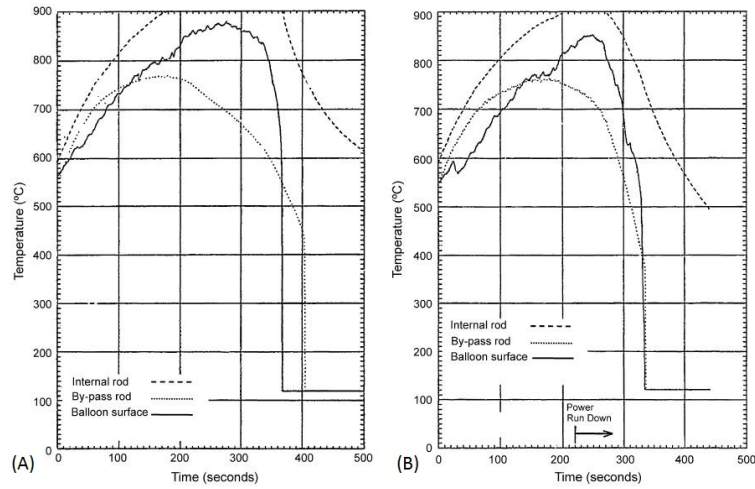


Figure 3.28: Clad Temperature Variation for 80% Blockage (Plot A) and 90% Blockage (Plot B) respectively [4]

In terms of heat transfer, with the decrease in the hydraulic diameter, the surface heat transfer coefficient increases and effective transfer surface decreases. Thus, the heat transfer per unit length remains practically the same for 80 and 90% blockages within the blocked region. Then, why do the higher blocked regions experience higher cooling during early cooling phase and lower cooling during late cooling phase? When the quench front is far upstream, the droplets get sufficient time and length to get accelerated to a speed, sufficient enough, to break through the deceleration region and enter the maximum blocked region. Once in this smaller volume, the droplets can efficiently de-superheat the steam and limit heating of the reduced flow of steam. The greater the slowdown, the longer is the transit time of the droplets in the blockage region and the greater the heat transfer from the steam to the liquid. Thus the cooldown in the early stages of re-flood is more efficient in the 90% blockage than in the 80% blockage. Later on during re-flooding, as the quench front approaches the bottom of the blockage, the droplets have smaller time and length available for getting accelerated. The speed they acquire is not sufficient enough to break through the decelerating region. Thus, the droplets fall back towards the blockage entry where they are swept aside

into the by-pass. Without cooling from the liquid droplets, steam will superheat significantly in the maximum blockage section, driving the corresponding surface temperatures at the throat outlet, making the cooldown in this late phase of cooling more efficient in 80% blockage than in case of 90% blockage.

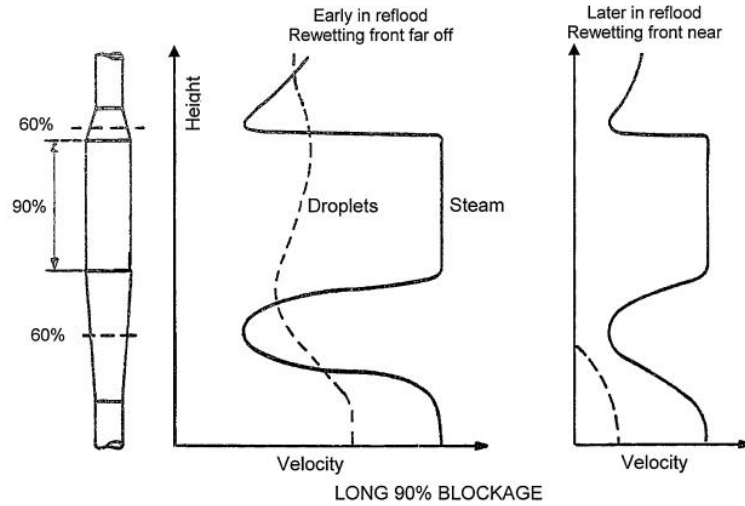


Figure 3.29: Variation of Steam and Droplet Speed along Channel Length [4]

3.3.2.4 FLECHT-SEASET Experiments

The objective of FLECHT-SEASET Programme was to perform tests on a 21-rod array to determine the effects of different blockage configurations and geometries on re-flood heat transfer and to perform tests on a 163-rod array to evaluate the effect of a large flow by-pass under the most severe heat transfer conditions observed in the 21-rod bundle test series.

Figure 3.30 shows the temperatures of the central rod for the unblocked and co-planar blockage configurations. The temperature rise slows down in blockage configurations, particularly in the configuration without bypass. This decrease in the temperature rise results from cooling generated by liquid droplets carried in the steam flow, which is even more pronounced when this flow is deprived of a bypass. However, for the configuration with bypass, the temperature after turnaround finally exceeds the temperature in the blockage free configuration and blockages

without bypass configuration. Figure 3.31 shows that the variation of temperatures of the peripheral rods are similar to that for the central rod until in the vicinity of the quench front. In configuration B, the peripheral rod is located in the by-pass region and is thus subjected to a higher flow rate than the corresponding flow rate in the blockage-free test. Therefore, this peripheral rod has a lower temperature than the corresponding rod in configuration A. In configuration C without by-pass, the peripheral rod does not benefit from this additional flow and its temperature would be expected to be higher than the corresponding rod in configuration B. However, the cooling effect of the liquid droplets upon the balloon dominates the cooling effect of the by-pass flow, thus reducing the temperatures below the bypass in configuration B.

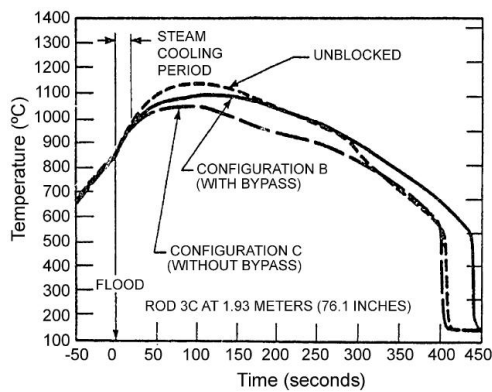


Figure 3.30: Central Rod Temperatures for Un-blocked and Co-planar Blockage Configuration [4]

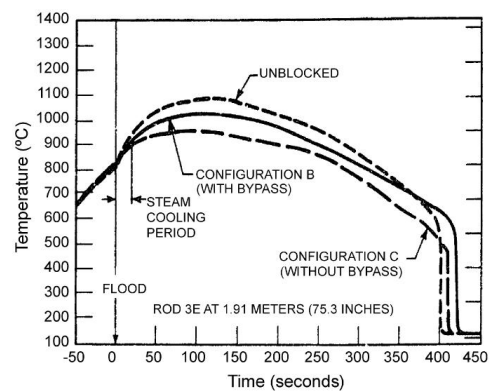


Figure 3.31: Peripheral Rod Temperatures for Un-blocked and Co-planar Blockage Configuration [4]

Similar tests were performed on a 163-rod array to conclude that the beneficial effect of the blockage upon the increase in heat transfer remains sufficiently dominant, at least at the beginning of the transient. This compensates for the detrimental effect of the flow bypass and produces lower maximum temperatures in comparison to those obtained in a blockage-free configuration.

Temperature variations in and downstream from a blockage region are generally conditioned by heat transfers taking place at the beginning of the re-flood phase

with two-phase mist flow conditions. A blockage induces antagonistic effects whose relative significance depends on the geometrical conditions of the blockage and its by-pass, as well as the thermo-hydraulic conditions of the re-flood which stem from:

- Reduction of the flow passage in the blockage that leads to flow diversion towards the by-pass, therefore reducing the mass flow in blockage sub-channels. For sufficiently long blockages (200 mm), the reduction in the steam flow is approximately proportional to the reduction in the cross-section area. This reduction in coolant flow therefore tends to restrict blockage coolability.
- However, in a two-phase flow, the inertia of droplets favors their penetration of the blockage, particularly if the quench front is sufficiently far off to have permitted their acceleration in the steam flow. Inside the blockage, the liquid droplets are dispersed due to their impact on the blockage surfaces, fragmented and re-entrained in the form of finer droplets, which significantly increases heat transfer with steam. This de-superheating of steam, associated with the increase in turbulence, improves the coolability of the blockage surfaces.
- At the blockage outlet, the deceleration of the steam flow in the widening section can cause bigger droplets to fall under gravity onto the hot blockage surfaces, thereby leading to dispersion and evaporation in steam jets, which once again leads to an accentuated cooling in the region.

3.4 Conclusions of Literature Survey

The Re-wetting Problem has been extensively studied with the help of analytical models and numerical codes developed as well as from several experiments performed on various fuel matrices. Following conclusions can be drawn from the literature reviewed:

1. The time frame available from the accident initiation up to the degradation of 50% core is just about 1.5 hours. The transition of core from intact condition to molten debris takes place within this 1.5 hours. Thus the partially degraded core under consideration for this study, exists for only a short duration of time. Such a core is expected to have ballooned, self standing fuel rods with ballooned portion of rods spanning over 50-60% of the length as observed in few in-pile experiments.
2. Figure 3.32 shows radial and axial blockages used for quenching studies in out-of-pile experiments performed in various experimental facilities.

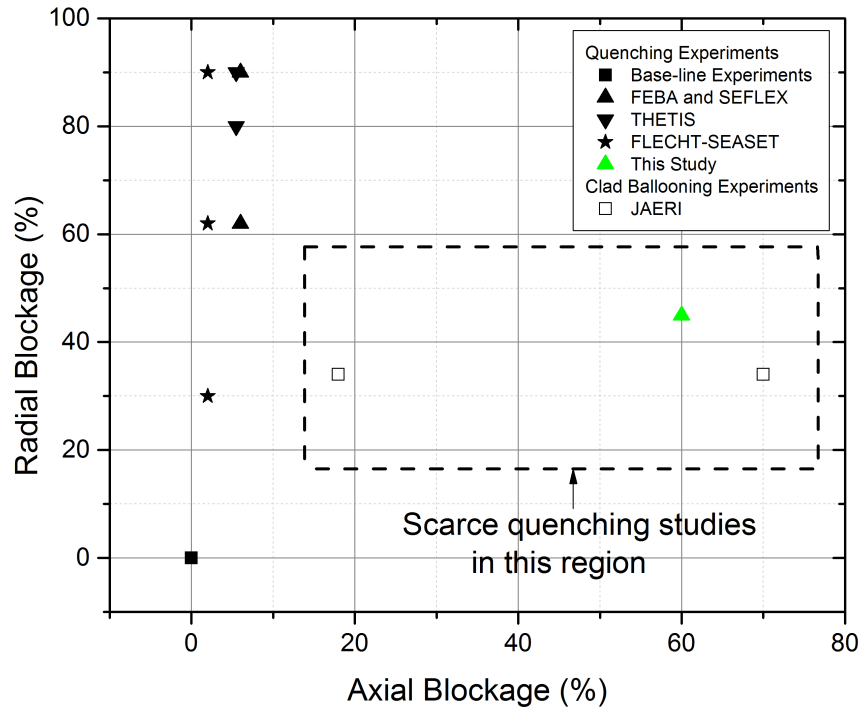


Figure 3.32: Range of Radial and Axial Blockages considered for Quenching Studies

Radial blockage is caused because of increase in diameter of the fuel pin, whereas, axial blockage refers to extent of length over which this blockage exists. The core configuration with axial blockages upto 6% with wide range of radial blockages are well studied. However, no literature is available for quenching of axial blockages more than 6%. As mentioned in Section 2.2,

the blockages can reduce heat transfer because of flow-redistribution or can assist heat transfer by providing narrow flow-path for entrained droplets, thereby increasing chances of interaction of these droplets with heated surfaces. Particularly, the later effect may be much more pronounced if the narrow flow-path extends over longer distances as against high radial blockage case, wherein, the former effect is expected to be stronger.

3. Figure 3.33 shows water injection rates considered by various experimental facilities against the flow rates considered for a typical SAMG action. These experiments are performed to arrive at a design basis for prescribing SAMG injection rate. Hence, the range of injection rates considered does not cover injection rates lower than the typical SAMG injection rates. In a severe accident condition, the flow path from the point of injection of water to the reactor core is likely to offer flow resistance either due to blockages or because of leakage paths for the water to escape. Hence, the flow rates likely to reach the reactor core are expected to be lower than the typical SAMG flow rates.
4. Although, in most of the analytical work, the quench front velocity has been assumed constant and expression have been obtained for the same, the quench front travels with different velocities along the fuel rod length depending on the thermal hydraulic condition as observed in various experiments.
5. While modeling the heat conduction problem in fuel rod, it is essential to model the gap conductance between the fuel and the clad to obtain realistic behavior. A two region or multi region approach for the heat transfer to fluids is not adequate, and it is required to solve for the fluid equations (mass, momentum, energy conservation) with appropriate closure laws in each regime.

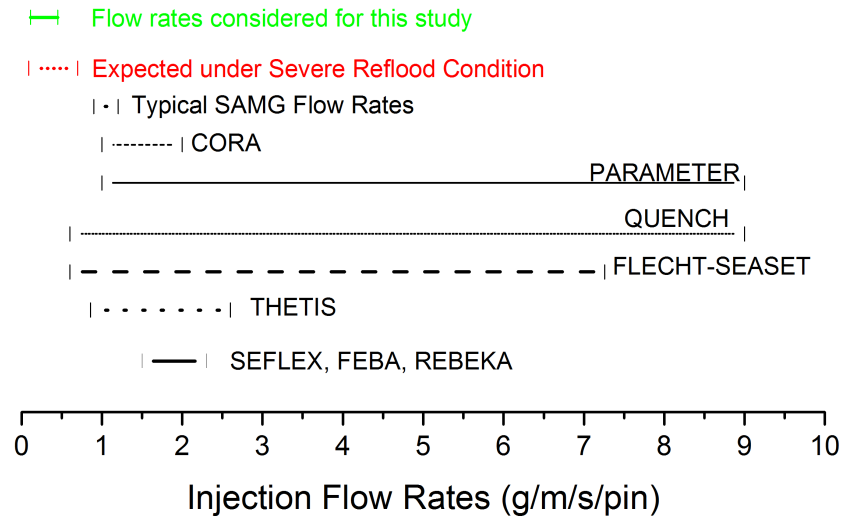


Figure 3.33: Injection Flow Rates considered for Quenching Studies

6. The two-dimensional flow effects observed in the simulation of core quenching are significant even in case of intact fuel rod geometry. The effects are found to be enhanced in the case of deformed fuel rod experiments with limited span of ballooned fuel rod portion. These effects are expected to be stronger in case of deformed fuel rods with larger span of ballooned regions, expected in partially degraded core configuration.

In conclusion, there is still a need of numerical tool that can handle the two-dimensional effects, arising inherently due to uneven deformation of fuel rods in a reactor core. Quenching experiments performed so far have focused on the validation of one-dimensional models for the quenching of intact fuel rods. The deformed rod quenching experiments have dealt with ballooning over short length of the fuel rods. The injection flow rates considered for these studies are also higher than expected injection rates. Since the quench patterns are strongly governed by the length of the blocked region as well, there is a need for studying quenching patterns for extended length blockages in reactor core.

Chapter 4

Feasibility Analysis

A feasibility analysis was carried out to understand the present code capabilities of system codes such as RELAP5/SCDAP for severe accident evolution and predictions of the code for re-flooding conditions. VVER 1000 reactor was selected as an example. This exercise has helped not only in understanding the present code capabilities but also towards identifying the range of fluid flow parameters to be used for the experimental setup.

4.1 Brief Description of the VVER-1000 (V320) Reactor and Plant Model

VVER-1000 is a 3000 MW (thermal) PWR with four-loop system with four horizontal steam generators [38]. The reactor core consists of 163 hexagonal Fuel Assemblies (FA) and each FA comprises of 312 fuel elements and 18 control rods. There are 61 Control Rods Assembly (CRA) of B_4C absorbing material. The fuel element is made up of annular UO_2 pellets with inside diameter of 2.35 mm and outside diameter of 7.72 mm enveloped in $Zr - 1\%$ clad of thickness 0.65 mm. The total length of fuel pin is 3837 mm and the active length is 3530 mm. The fuel elements have a pitch of 12.75 mm. The core is enveloped in a core shroud. During

normal operation of the reactor, water is pumped into the annular down-comer region between the core barrel and RPV. Water flows through the down-comer into the lower plenum and enters the core region through the lower plenum. It then flows over the fuel pins where it picks up heat from the fuel pins and exits the core through the upper plenum. The reactor is equipped with high and low pressure safety injections along with hydro accumulators. Under SAMG action, the high pressure safety injection pumps are an option to be utilized with the mobile Diesel Generators (DG) under Station Black Out (SBO) condition. The pumps can add water at a maximum flow rate of 200 kg/s . Provision is made to add water at 100 kg/s from top and bottom of the core, independently [39].

Figure 4.1 shows the Nodalization of core used in RELAP5/SCDAP (Mod3.2) Code specific VVER 1000 model. The VVER core is divided into six concentric zones (called as channels), five zones containing representative clubbed fuel pins (called as fuel rings) and one bypass zone. The zones are interconnected radially with the help of cross-flow junctions in RELAP. This allows solution of momentum in radial direction without considering the momentum flux terms.

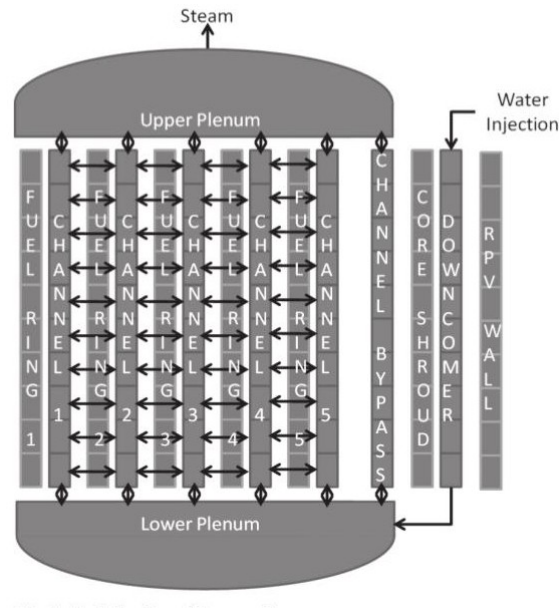


Figure 4.1: Nodalization of VVER Reactor Core

The decay heat generation within the fuel pins, convective heat transfer from

the pin surface to the corresponding core fluid and the radiation heat transfer between fuel pins and between the fuel pins and the core shroud has been accounted for. The junction form loss coefficients for the models are initially adjusted to obtain correct steady state flow rates for reactor full power operation. The same loss coefficients are then used for further simulations.

4.2 Evolution of Core Degradation without SAMG Action

The postulated LOCA situation leads to loss of inventory of the Reactor Coolant System (RCS) and fall in the water level within RPV. This leads to uncover of fuel pins. In absence of any SAMG action, continued decay heat generation within the fuel pin causes rise in the fuel pin temperature accompanied by changes in the pin geometry through ballooning. The stages of core degradation are shown in Figure 4.2. The heat up begins after the level in the RPV falls below half of the core height. Figure 4.3 shows the rise in the fuel temperature and marks different degradation stages.

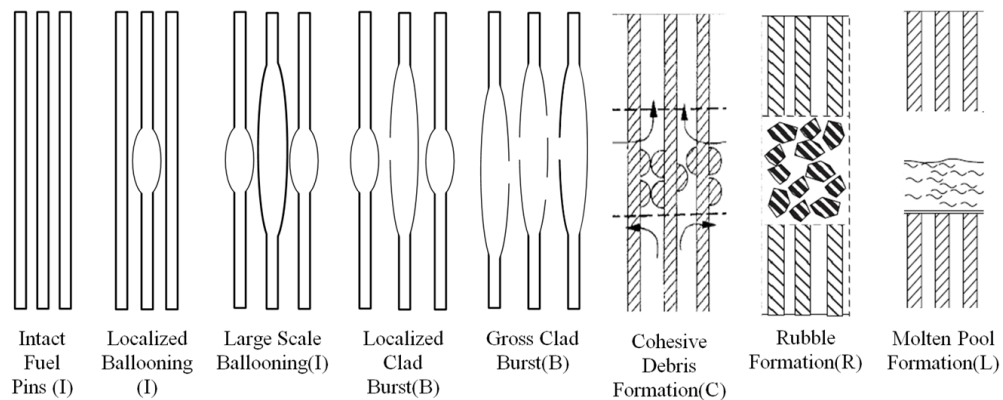


Figure 4.2: Stages of Core Degradation [1]

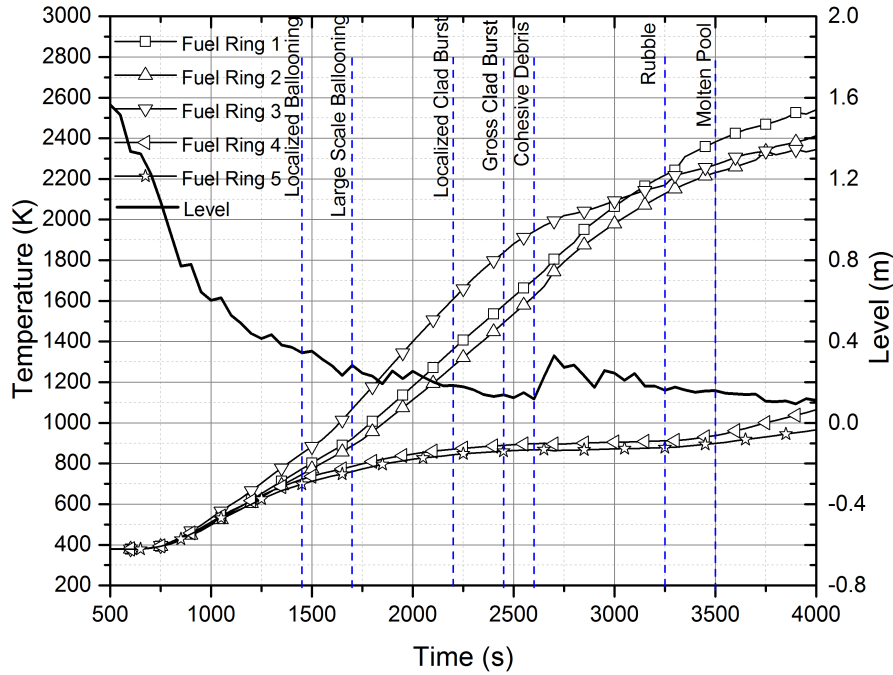


Figure 4.3: Evolution of VVER Core Degradation under LOCA Conditions

Localized ballooning is observed to begin at the highest temperature locations of the highest power fuel pins. Ballooning is observed to occur in the exposed location owing to high temperatures at this location.

Further heat-up of the core causes the ballooned portions of the respective fuel pins to spread axially causing *Large Scale Ballooning*. Ballooning is also observed in lower power pins owing to high temperatures. Higher the power higher is the extent of ballooned region length and flow blockage.

Further increase in the fuel pin temperature causes rise in the pressure within the fuel pin and the clad tends to burst. This is known as *Localized Clad Burst*. With burst of the clad the internal pressure in the fuel pin reduces and further ballooning of fuel pin is prevented. However, other axial locations of the burst fuel pins continue to get heated up. Clad burst occurs in these locations purely because of high temperatures. This state of core with clad burst at multiple locations is called *Gross Clad Burst* case.

If the heat up of the fuel pin still continues the fuel clad temperature reaches

the melting point of *Zr*. The drops of molten *Zr* formed, flow over the intact fuel rod causing complete blockages of flow area known as *Cohesive Debris*. Although the flow path gets blocked completely along the axial direction, the blockage is confined to specific axial locations. There are no blockages observed along radial flow directions and hence flow can occur in radial directions within these nodes.

Since the temperature of clad is higher than the *Zr*-melting point the fuel rod disintegrates into *Rubbles*. Formation of rubbles also causes gross blockage of the flow path in that fuel zone. Further heat up of the fuel pin increases its temperature to melting point and gross melting of fuel pin occurs. The molten mass gets relocated to lower nodes forming *Molten Pool*.

4.3 Effectiveness of SAMG Action of Water Injection into RPV

To study the effectiveness of water injection as a SAMG action under different degraded core conditions, water is injected into the core from bottom only at different stages of core degradation at a pre-defined injection rate of 200 kg/s . In this study only *bottom re-flooding* is considered and *top-reflooding* has not been simulated.

4.3.1 Injection into Localized Ballooned Core Condition

With injection into localized ballooned core condition the maximum temperature in the core at the time of injection is 1050 K as shown in Figure 4.4. Since these temperatures are lower than the threshold temperature of 980°C for Zr-clad oxidation to escalate, oxidation reaction is not significant even after water injection begins. The extent of flow blockage created due to ballooning is small and injected water is able to quench the core.

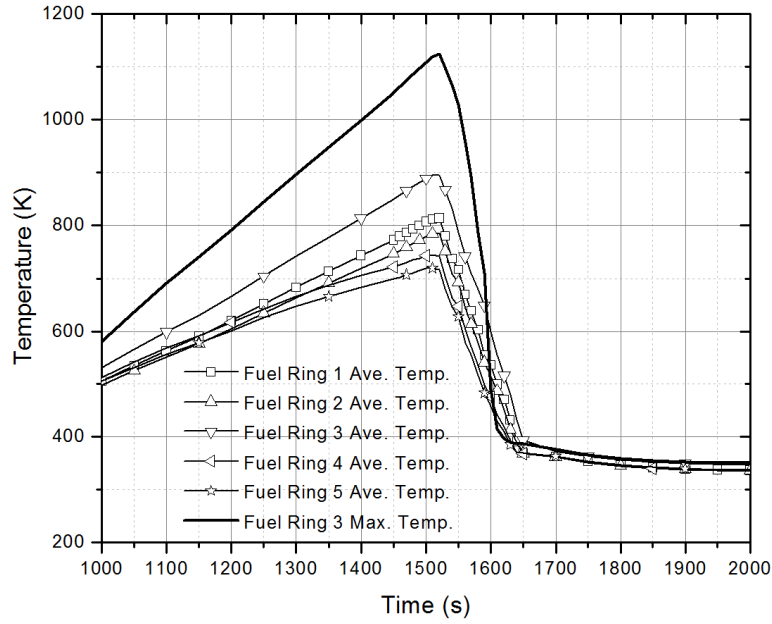


Figure 4.4: Temperature Variation of Fuel for Injection under Localized Ballooned Condition (Steam Rich Condition)

4.3.2 Injection into Large Scale Ballooned Core Condition

In this case the average temperature in fuel ring 3 at the time of injection (1700 s) is 1100 K and the temperatures of other fuel rings are within 1000 K as shown in Figure 4.5. However, the local maximum temperature in fuel ring 3 reaches 1600 K at the time of injection. Figure 4.6 shows the clad temperatures at different axial location for fuel ring 3 and the level in channel 3. It can be observed that the temperature of an axial node of the fuel pin starts decreasing when the level in that channel reaches the bottom end of that axial node. This is because, high amount of steam that is generated in the quenching of previous node, flows over this node, producing high convective cooling in this node.

Subsequently, the temperature of the node drops below T_{LF} and the node gets quenched. However, by the time level reaches half the core height, the temperature of node at that location increases to 2250 K. Convective cooling, thereafter, is able to cool the node up to 1000 K which is higher than T_{LF} . At the same time, increased heat generation due to clad oxidation prevents further cooling of the

node. Although the level in the channel rises to top of the channel, the clad does not get wetted. The node continuous to get cooled through film boiling, which is not sufficient to remove the generated heat. The temperature of the fuel rises continuously and further degradation begins. The injected water is not able to quench the core. The success of quenching in this case is governed by the clad temperature and the maximum temperature obtained in the core. Hence water injection will not be able to quench core under steam rich condition in further stages of degradation, since the clad temperature and the maximum core temperature are expected to be higher than the present case.

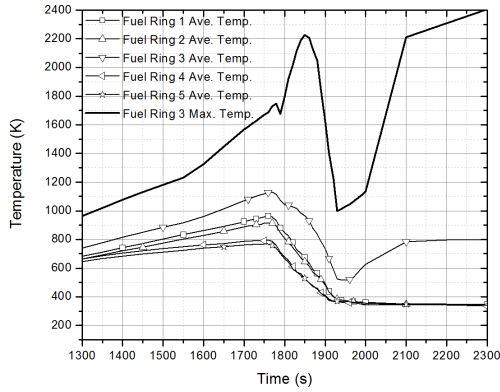


Figure 4.5: Temperature Variation of Fuel for Injection under Gross Ballooned Condition (Steam Rich Condition)

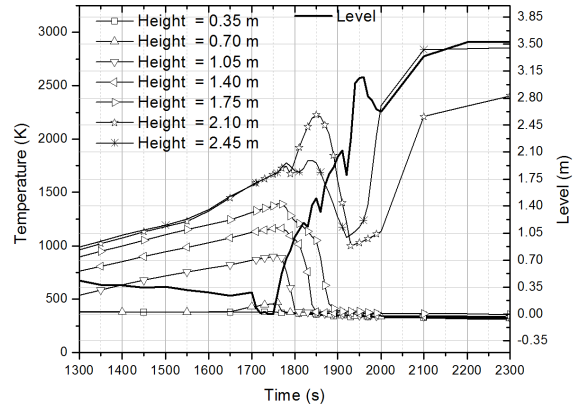


Figure 4.6: Temperature Variation of Fuel Ring 3 for Injection under Gross Ballooned Condition (Steam Rich Condition)

Figure 4.7 shows the peak cross-flow rates at different nodes along the core height for localized ballooned and gross ballooned core configuration. The magnitude of the cross-flow is higher for gross clad ballooning case than the localized clad ballooned case. Table 4.1 and Table 4.2 show the flow blockages observed at respective core states where I represents intact fuel rods.

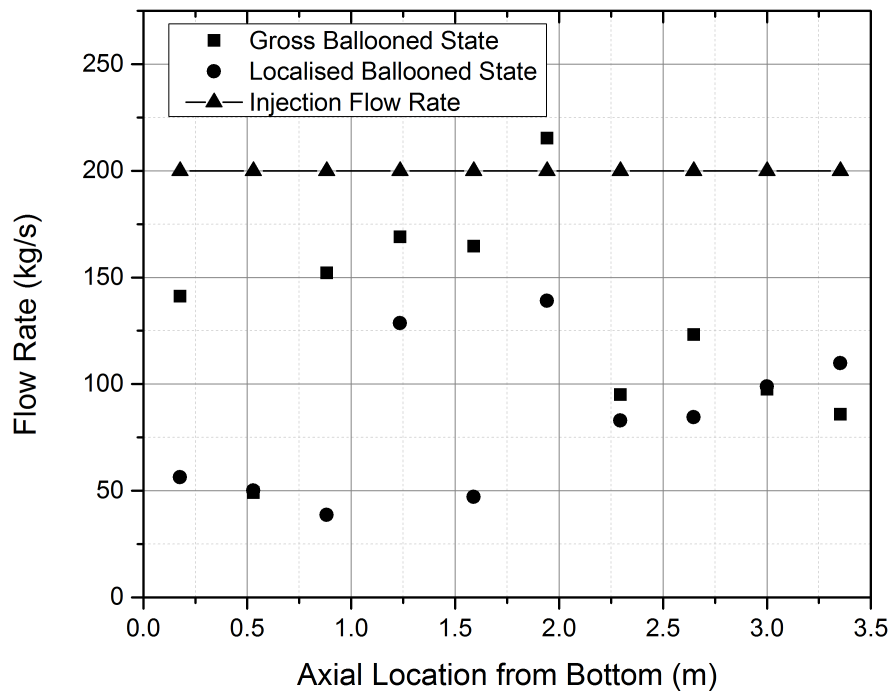


Figure 4.7: Peak Cross-Flow Rate under Different Core Configurations

Table 4.1: Core Configuration Map under Localized Clad Ballooned Condition

Axial Node	% Blockage (Damaged State)				
	Ring 1	Ring 2	Ring 3	Ring 4	Ring 5
10	0.12 (I)	0.08(I)	0.12(I)	0.08(I)	0.04(I)
9	0.37(I)	0.33(I)	0.46(I)	0.21(I)	0.08(I)
8	0.46(I)	0.41(I)	2.11(I)	0.37(I)	0.17(I)
7	0.46(I)	0.41(I)	3.52(I)	0.41(I)	0.33(I)
6	0.46(I)	0.41(I)	2.50(I)	0.41(I)	0.37(I)
5	0.41(I)	0.37(I)	0.54(I)	0.37(I)	0.37(I)
4	0.21(I)	0.17(I)	0.37(I)	0.17(I)	0.29(I)
3	0.00(I)	0.08(I)	0.12(I)	0.08(I)	0.17(I)
2	0.04(I)	0.04(I)	0.04(I)	0.04(I)	0.08(I)
1	0.04(I)	0.04(I)	0.04(I)	0.04(I)	0.04(I)

Table 4.2: Core Configuration Map under Gross Clad Ballooned Condition

Axial Node	% Blockage (Damaged State)				
	Ring 1	Ring 2	Ring 3	Ring 4	Ring 5
10	0.17 (I)	0.17(I)	0.17(I)	3.20(I)	0.08(I)
9	0.50(I)	0.46(I)	0.50(I)	3.30(I)	0.33(I)
8	5.84(I)	4.28(I)	6.22(I)	3.30(I)	0.41(I)
7	8.91(I)	7.02(I)	8.91(I)	3.30(I)	0.41(I)
6	7.36(I)	5.70(I)	7.07(I)	3.40(I)	0.41(I)
5	2.46(I)	1.30(I)	2.63(I)	3.40(I)	0.41(I)
4	0.41(I)	0.41(I)	0.41(I)	3.40(I)	0.37(I)
3	0.17(I)	0.12(I)	0.12(I)	3.30(I)	0.12(I)
2	0.04(I)	0.04(I)	0.04(I)	3.30(I)	0.04(I)
1	0.04(I)	0.04(I)	0.04(I)	3.30(I)	0.04(I)

4.3.3 Injection into Core Assuming Steam Starved Initial Condition

Similar exercise of water injection into RPV was repeated for a steam starved initial condition of RPV i.e. the RPV is assumed to be void of any steam at the beginning of the injection. The fuel temperature variation for injections at different stages of degradation is shown in Figure 4.8 through Figure 4.11. It can be seen that, due to absence of steam at initial condition, the oxidation of Zr clad is less and hence the heat production during clad oxidation is less. This helps in reducing the total heat to be removed by the injected water. The water injection is found to be successful in quenching till localized clad burst conditions.

4.4 Consequences of SAMG Action

Comparative success of water injection under different stages of accident is given in Table 4.3.

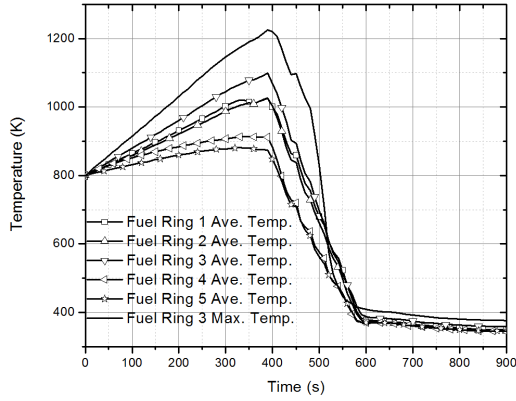


Figure 4.8: Temperature Variation of Fuel for Injection under Localized Ballooned Condition (Steam Starved Condition)

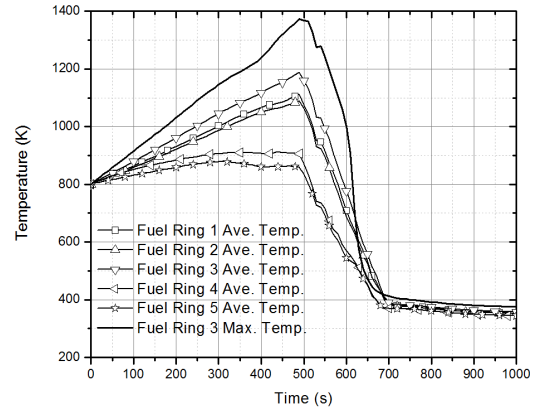


Figure 4.9: Temperature Variation of Fuel for Injection under Gross Ballooned Condition (Steam Starved Condition)

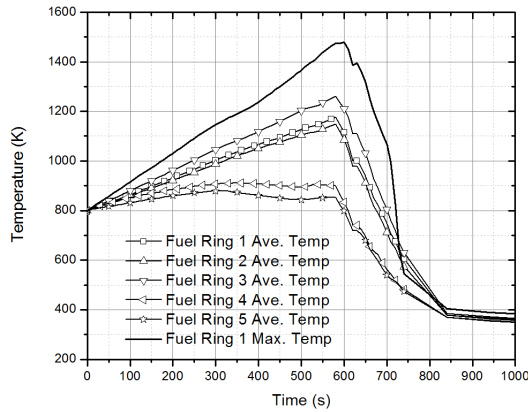


Figure 4.10: Temperature Variation of Fuel for Injection under Localized Clad Burst Condition (Steam Starved Condition)

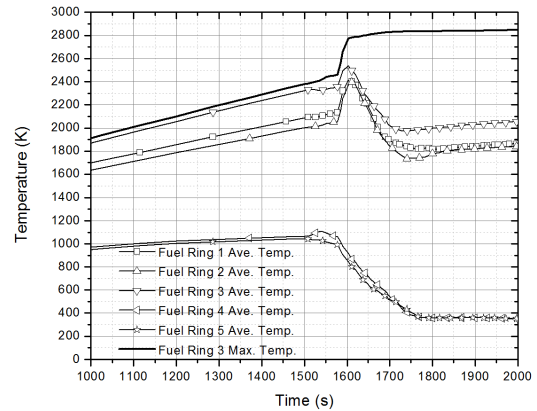


Figure 4.11: Temperature Variation of Fuel for Injection under Gross Clad Burst Condition (Steam Starved Condition)

It can be concluded that from these observations that addition of water into the RPV post dryout condition will try to quench the overheated fuel pins. However, the success of this SAMG strategy depends on several factors such as fuel clad temperature, local state of clad etc. It can be inferred from this analysis that:

- At high fuel clad temperatures, injection of water into RPV will cause se-

vere oxidation reaction between the *Zr*-clad and steam. The *Zr*-oxidation reaction is highly exothermic and thus will assist temperature escalations in the clad. This is observed in all the cases with water injection.

Table 4.3: Summary of Effectiveness of Water Injections in Degraded Core

Damaged State of Core	Steam Starved Condition		Steam Rich Condition	
	Max. Core. Temp. (K)	Success of Quenching	Max. Core. Temp. (K)	Success of Quenching
Localized Ballooned	1150	Yes	1050	Yes
Gross Ballooned	1235	Yes	1600	No
Localized Clad Burst	1355	Yes	2210	No
Gross Clad Burst	2525	No	2485	No
Rubble	2837	No	2837	No
Cohesive Debris	2837	No	2837	No
Molten Pool	2837	No	2837	No

- The temperature of the fuel pin clad goes on increasing continuously until some counter measure is taken to arrest the temperature rise. The clad temperature being higher than T_{LF} at local pressure, injected water cannot wet the surface of fuel pin clad. Wetting of surface is possible only when the clad is cooled to a temperature lower than T_{LF} . This cooling is possible essentially due to convective heat transfer to the single phase steam that is generated during quenching of the upstream nodes which forms a film over the fuel pin surfaces. However, the rate of cooling being very low as compared to rate of heat generation within the fuel pins, time taken for a given node to cool down to LF Temperature and wet the surface is high. This time period is long enough for the heat up of downstream nodes to a

temperature where core degradation begins.

- During early phase of the core degradation, ballooned fuel pins cause blockage in the flow paths reducing the fluid flow rate through the nodes. At the same time there may be local fluid acceleration through the reduced flow area. Cooling may be enhanced or reduced depending on which of these phenomena is dominant. However, the simulation shows that local fluid acceleration is not sufficient to enhance the heat transfer and the hot spot are not quenched. During late phase of core degradation, some of the flow paths may get completely blocked due to formation of rubble or cohesive debris or gross melting of fuel pins.

4.5 Estimation of Scaled Injection Rates for Experimental Setup

As seen in the earlier sections the maximum injection flow rate prescribed under SAMG for VVER is 200 kg/s . Hence for 1% decay heat of the VVER reactor core the power to injection rate ratio is found to be 150 kW.s/kg . A power to injection rate ratio lower than this value may not be practically possible due to constraint on availability of pumping power. This sets a lower limit on the ratio to be used for the experimental setup. As such there is no higher limit for the ratio, since lower is the flow rate requirement for successful quenching, the better it is from engineering point of view. The higher limit can be set by lowering the injection to such a value that it is just sufficient to remove the decay heat thermodynamically. That is:

$$W_{TH} = \dot{m}H_{fg} \tag{4.1}$$

The value can be calculated to be close to 2 MW.s/kg . It will be discussed in

subsequent chapters that the power to flow rate used for the experiments is indeed within these values. In fact, the possible range of the ratio further narrows down due to scaling constraints which will be discussed in Chapter 5.

4.6 Conclusions of Feasibility Analysis

The feasibility analysis carried out for VVER with RELAP/SCDAP concludes that under gross clad ballooning state of core degradation, the blockages in the core ranges up to 9%. Whereas, in an extended clad ballooned state (just prior to clad burst), the blockages are found to be in the range of 40-50%. Although magnitude of cross-flow velocities are not significant, the effects on quenching are prominently visible. The range for power to injection ratio is identified to be 150-2000 kW-s/kg. The same ratio needs to be maintained for experiments to replicate quenching behavior under partially degraded core conditions. Although, VVER has the option of bottom and top reflooding, the scope of present study is restricted to bottom reflooding only. Nevertheless, efforts are required to assess effectiveness of top flooding under accident conditions.

Chapter 5

Non-Dimensionalization and Pre-Test Analysis for the Experimental Setup

5.1 Introduction

In order to simulate actual systems, experiments are often performed at reduced scales, with materials and fluids other than the actual materials and fluids used in the system. Since the objective of experiments is to capture the phenomena important for understanding of full scale systems, scaling analysis is essential for the design of the smaller size experimental setups to verify the performance of actual systems. A Top-Down scaling approach, proposed by Zuber et al. [40], has been used for the design of the experimental setup for Degraded Reactor Core Reflood Experiment (DRCRE) Facility. Such an approach has been used previously for the design of Rod Bundle Heat Transfer Test Facility [41]. This approach involves obtaining non-dimensional groups for each transfer process obtained from the conservation equations. The non-dimensional groups are ratios of rates of different processes that occur in the system and are also known as Π -terms. The non-dimensional Π -terms are then analyzed to determine their relative importance.

The important Π -terms that evolve from this analysis are conserved while scaling from a typical PWR configuration to the experimental setup design.

5.2 Non-Dimensionalization of Governing Equations

The following assumptions have been made for non-dimensionalization of the conservation equations:

1. The inlet liquid velocity to the domain is constant.
2. No radial temperature gradient in the fluid domain is considered.
3. No radial velocity gradients are considered in the fluid domain.
4. There is no heat transfer to or from the quenched heat structure (i.e., cooling in the quenched regions is sufficient to remove internally generated heat).
5. Fluid is single-phase liquid below the quench front and single-phase vapor above the quench front.

Three conservation equations, namely, the fluid energy equation, the fuel energy equation, and the clad energy equation are considered for non-dimensionalization. The momentum conservation equations are not used for non-dimensionalization because the velocities across the cross-section of the setup are not expected to be uniform. Further, because of cross-flow effects the velocities can change with respect to time and location in the setup. Hence reference velocities for non-dimensionalization are not available.

5.2.1 Non-Dimensionalization of Fluid Energy Equation

Figure 5.1 represents a single fuel pin getting quenched under bottom re-flooding. The quench front is expected to be slightly above the water level for the low injection rate condition. The overall length of the quench front region is very

small as compared to the length of the quenched region below the water level and un-quenched region ahead of the water level. The fluid domain adjacent to the quenched region of the fuel pin is filled with water, whereas the fluid domain adjacent to the un-quenched region of fuel pin is filled with steam and water droplets.

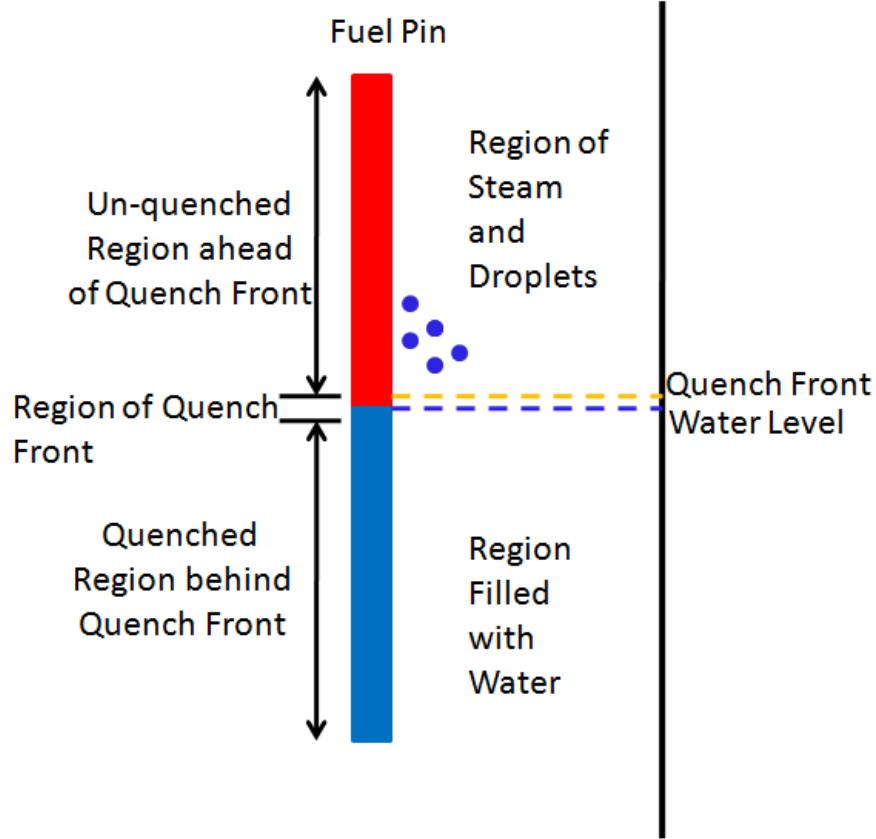


Figure 5.1: Representation of Zones under Quenching Process

The fluid energy equation can be written as:

$$V_{1\phi} \frac{\partial (\rho C_p T)}{\partial t} + V_{2\phi} \frac{\partial (\rho_g e_g)}{\partial t} = Q_{fuel,q} + Q_{hous,q} + Q_{dum,q} + Q_{ud,q} - Q_{fuel,loss} - Q_{hous,loss} - Q_{dum,loss} + \dot{m}_i H_i - \dot{m}_o H_o \quad (5.1)$$

Each term of the fluid energy equation is explained below.

Term 1: Rate of energy change in single phase region.

Term 2: Rate of energy change in the two phase region. Since the quantity of vapour in this region is large as compared to the water droplets, only the rate of energy change of vapour is considered.

Term 3: Energy release to fluid due to heated pin quenching.

$$Q_{fuel,q} = \rho_{fuel} C_{p,fuel} V_{fuel} \frac{\partial T_{fuel,q}}{\partial t} \quad (5.2)$$

Term 4: Energy release to fluid due to housing quenching.

$$Q_{hous,q} = \rho_{hous} C_{p,hous} V_{hous} \frac{\partial T_{hous,q}}{\partial t} \quad (5.3)$$

Term 5: Energy release to fluid due to dummy pin quenching.

$$Q_{dum,q} = \rho_{dum} C_{p,dum} V_{dum} \frac{\partial T_{dum,q}}{\partial t} \quad (5.4)$$

Terms 3, 4 and 5 represent the rate of release of stored energy from the heat structures. Since cooling of the heat structures is prominent in the region at or below the quench front, these terms are significant only at or below the quench front.

Term 6: Energy release to the fluid above and below the quench front region. This is apart from the release of stored heat. Since the thickness of the quench front region along the axial direction is negligible as compared to the total length of the setup, the energy released to the fluid above and below the quench front is assumed to be the total energy input to the system.

$$Q_{ud,q} = W_{in} \quad (5.5)$$

In the un-quenched region above the quench front, the steam and the carryover droplets can have temperature higher than the heat structures. Hence the fluid (steam and water droplets) can lose energy to the heat structures. These terms are prominent only in the un-quenched region ahead of the quench front and are considered only when the fluid temperature is higher than the heat structure temperature. These loss terms are expressed in 7th, 8th and 9th term as follows:

Term 7: Energy loss to heated pins. The energy loss to a heat structure in general can be divided into three components, namely, convective heat transfer from the fluid to the structure, radiative heat transfer from the vapour to the structure and radiative heat transfer from the entrained droplets to the structure.

$$Q_{fuel,loss} = Q_{fuel,conv} + Q_{fuel,g,rad} + Q_{fuel,dr,rad} \quad (5.6)$$

$$\begin{aligned} Q_{fuel,loss} = & h_{fuel,conv} A_{fuel} (T_{sat} - T_{max,fuel}) \\ & + h_{fuel,g,rad} A_{fuel} (T_g - T_{max,fuel}) + h_{fuel,dr,rad} A_{dr} (T_{sat} - T_{max,fuel}) \end{aligned} \quad (5.7)$$

Term 8: Energy loss to housing.

$$Q_{hous,loss} = Q_{hous,conv} + Q_{hous,g,rad} + Q_{hous,dr,rad} \quad (5.8)$$

$$\begin{aligned} Q_{hous,loss} = & h_{hous,conv} A_{fuel} (T_{sat} - T_{max,hous}) + \\ & h_{hous,g,rad} A_{hous} (T_g - T_{max,hous}) + h_{hous,dr,rad} A_{dr} (T_{sat} - T_{max,hous}) \end{aligned} \quad (5.9)$$

Term 9: Energy loss to dummy pins.

$$Q_{dum,loss} = Q_{dum,conv} + Q_{dum,g,rad} + Q_{dum,dr,rad} \quad (5.10)$$

$$\begin{aligned} Q_{dum,loss} = & h_{dum,conv} A_{dum} (T_{sat} - T_{max,dum}) + \\ & h_{dum,g,rad} A_{dum} (T_g - T_{max,dum}) + h_{dum,dr,rad} A_{dr} (T_{sat} - T_{max,dum}) \end{aligned} \quad (5.11)$$

Term 10: Energy flow into test section at inlet.

Term 11: Energy flow out of the test section at outlet.

The terms of the equation can be written in terms of non-dimensional parameters as:

Term 1:

$$V_{1\phi} \frac{\partial (\rho C_p T)}{\partial t} = \dot{m}_i C_{p,1\phi} (T_f - T_i) V_{1\phi}^* \frac{\partial (\rho^* C_{p,1\phi}^* \Delta T^*)_{1\phi}}{\partial t^*} \quad (5.12)$$

Term 2:

$$V_{2\phi} \frac{\partial (\rho_g e_g)}{\partial t} = \dot{m}_i C_{p,g} (T_g - T_{sat}) V_{2\phi}^* \frac{\partial (\rho_g^* C_{p,g}^* \Delta T_g^*)_{2\phi}}{\partial t^*} \quad (5.13)$$

Term 3:

$$Q_{fuel,q} = \rho_{fuel} C_{p,fuel} V_{fuel} \frac{\partial T_{fuel,q}}{\partial t} \quad (5.14)$$

$$= \frac{\rho_{fuel} C_{p,fuel} V_{fuel} (T_{fuel,max} - T_{sat})}{\tau_{fuel}} \rho_{fuel}^* C_{p,fuel}^* V_{fuel}^* \frac{\partial T_{fuel,q}^*}{\partial t^*} \quad (5.15)$$

Term 4:

$$Q_{hous,q} = \rho_{hous} C_{p,hous} V_{hous} \frac{\partial T_{hous,q}}{\partial t} \quad (5.16)$$

$$= \frac{\rho_{hous} C_{p,hous} V_{hous} (T_{hous,max} - T_{sat})}{\tau_{hous}} \rho_{hous}^* C_{p,hous}^* V_{hous}^* \frac{\partial T_{hous,q}^*}{\partial t^*} \quad (5.17)$$

Term 5:

$$Q_{dum,q} = \rho_{dum} C_{p,dum} V_{dum} \frac{\partial T_{dum,q}}{\partial t} \quad (5.18)$$

$$= \frac{\rho_{dum} C_{p,dum} V_{dum} (T_{dum,max} - T_{sat})}{\tau_{dum}} \rho_{dum}^* C_{p,dum}^* V_{dum}^* \frac{\partial T_{dum,q}^*}{\partial t^*} \quad (5.19)$$

Term 7:

$$\begin{aligned} Q_{fuel,loss} = & h_{fuel,conv} A_{fuel} (T_{sat} - T_{max,fuel}) h_{fuel,conv}^* A_{fuel}^* (T_{sat}^* - T_{max,fuel}^*) \\ & + h_{fuel,g,rad} A_{fuel} (T_g - T_{max,fuel}) h_{fuel,g,rad}^* A_{fuel}^* (T_g^* - T_{max,fuel}^*) \\ & + h_{fuel,dr,rad} A_{dr} (T_{sat} - T_{max,fuel}) h_{fuel,dr,rad}^* A_{dr}^* (T_{sat}^* - T_{max,fuel}^*) \end{aligned} \quad (5.20)$$

Term 8:

$$\begin{aligned} Q_{hous,loss} = & h_{hous,conv} A_{fuel} (T_{sat} - T_{max,hous}) h_{hous,conv}^* A_{fuel}^* (T_{sat}^* - T_{max,hous}^*) \\ & + h_{hous,g,rad} A_{hous} (T_g - T_{max,hous}) h_{hous,g,rad}^* A_{hous}^* (T_g^* - T_{max,hous}^*) \\ & + h_{hous,dr,rad} A_{dr} (T_{sat} - T_{max,hous}) h_{hous,dr,rad}^* A_{dr}^* (T_{sat}^* - T_{max,hous}^*) \end{aligned} \quad (5.21)$$

Term 9:

$$\begin{aligned}
 Q_{dum,loss} = & \\
 & h_{dum,conv} A_{dum} (T_{sat} - T_{max,dum}) h_{dum,conv}^* A_{dum}^* (T_{sat}^* - T_{max,dum}^*) \\
 & + h_{dum,g,rad} A_{dum} (T_g - T_{max,dum}) h_{dum,g,rad}^* A_{dum}^* (T_g^* - T_{max,dum}^*) \\
 & + h_{dum,dr,rad} A_{dr} (T_{sat} - T_{max,dum}) h_{dum,dr,rad}^* A_{dr}^* (T_{sat}^* - T_{max,dum}^*)
 \end{aligned} \tag{5.22}$$

Term 10:

$$\dot{m}_i H_i = \dot{m}_i (H_f - H_i) \dot{m}_i^* H_i^* \tag{5.23}$$

Term 11:

$$\dot{m}_o H_o = \dot{m}_o (H_g - H_{sat}) \dot{m}_o^* H_o^* \tag{5.24}$$

The normalizing parameters used for non-dimensionalization are given below:

$$\rho^* = \frac{\rho}{\rho_i} \tag{5.25}$$

$$C_p^* = \frac{C_p}{C_{p,i}} \tag{5.26}$$

$$V^* = \frac{V}{V_i} \tag{5.27}$$

$$T_i^* - T_{sat}^* = \frac{T_i - T_{sat}}{T_{i,max} - T_{sat}} \tag{5.28}$$

$$A^* = \frac{A}{A_i} \tag{5.29}$$

$$H^* = \frac{H}{H_i} \tag{5.30}$$

Dividing all terms of Eq. (5.1) by power input to the test section W_{in} the equation reduces to:

$$\begin{aligned}
\Pi_1 V \frac{\partial (\rho^* C_p^* \Delta T^*)_{1\phi}}{\partial t^*} + \Pi_2 V_{2\phi}^* \frac{\partial (\rho_g^* C_{p,g}^* \Delta T_g^*)_{2\phi}}{\partial t^*} = \Pi_3 \rho_{fuel}^* C_{p,fuel}^* V_{fuel}^* \frac{\partial T_{fuel,q}^*}{\partial t^*} + \\
\Pi_4 \rho_{hous}^* C_{p,hous}^* V_{hous}^* \frac{\partial T_{hous,q}^*}{\partial t^*} + \Pi_5 \rho_{dum}^* C_{p,dum}^* V_{dum}^* \frac{\partial T_{dum,q}^*}{\partial t^*} + \Pi_6 \\
- \Pi_7 h_{fuel,conv}^* A_{fuel}^* (T_{sat}^* - T_{max,fuel}^*) - \Pi_8 h_{uel,g,rad}^* A_{fuel}^* (T_g^* - T_{max,fuel}^*) \\
- \Pi_9 h_{fuel,dr,rad}^* A_{dr}^* (T_{sat}^* - T_{max,fuel}^*) - \Pi_{10} h_{hous,conv}^* A_{fuel}^* (T_{sat}^* - T_{max,hous}^*) \\
- \Pi_{11} h_{hous,g,rad}^* A_{hous}^* (T_g^* - T_{max,hous}^*) - \Pi_{12} h_{hous,dr,rad}^* A_{dr}^* (T_{sat}^* - T_{max,hous}^*) \\
- \Pi_{13} h_{dum,conv}^* A_{dum}^* (T_{sat}^* - T_{max,dum}^*) - \Pi_{14} h_{dum,g,rad}^* A_{dum}^* (T_g^* - T_{max,dum}^*) \\
- \Pi_{15} h_{dum,dr,rad}^* A_{dr}^* (T_{sat}^* - T_{max,dum}^*) + \Pi_{16} \dot{m}_i^* H_i^* - \Pi_{17} \dot{m}_o^* H_o^* \quad (5.31)
\end{aligned}$$

The Π terms in Eq. (5.31) are explained in Table 5.1.

Table 5.1: List of Π Terms for Fluid Energy Equation

Π Term	Expression	Physical Meaning
Π_1	$\frac{\dot{m}_i C_{p,\phi} (T_f - T_i)}{W_{in}}$	Ratio of Single Phase Liquid Sensible Energy change rate to Input Power
Π_2	$\frac{\dot{m}_i C_{p,g} (T_g - T_{sat})}{W_{in}}$	Ratio of Single Phase Vapor Sensible Energy change rate to Input Power
Π_3	$\frac{\rho_{fuel} C_{p,fuel} V_{fuel} (T_{fuel,max} - T_{sat})}{\tau_2 W_{in}}$	Ratio of Fuel Rod Quench Energy Release rate to Input Power
Π_4	$\frac{\rho_{hous} C_{p,hous} V_{hous} (T_{hous,max} - T_{sat})}{\tau_3 W_{in}}$	Ratio of Housing Quench Energy Release rate to Input Power

Π Term	Expression	Physical Meaning
Π_5	$\frac{\rho_{dum} C_{p,dum} V_{dum} (T_{dum,max} - T_{sat})}{\tau_4 W_{in}}$	Ratio of Dummy Rod Quench Energy Release rate to Input Power
Π_6	$\frac{Q_{ud}}{W_{in}} \approx 1$	Ratio of Energy Release rate to Single Phase Upward and Downward of Quench Front to Input Power
Π_7	$\frac{h_{fuel,conv} A_{fuel} (T_{sat} - T_{max,fuel})}{W_{in}}$	Ratio of Convective Heat Transfer rate from Fuel to Fluid to Input Power
Π_8	$\frac{h_{fuel,g,rad} A_{fuel} (T_g - T_{max,fuel})}{W_{in}}$	Ratio of Radiative Heat Transfer rate from Fuel to Fluid to Input Power
Π_9	$\frac{h_{fuel,dr,rad} A_{dr} (T_{sat} - T_{max,fuel})}{W_{in}}$	Ratio of Radiative Heat Transfer rate from Fuel to Entrained Droplets to Input Power
Π_{10}	$\frac{h_{hous,conv} A_{fuel} (T_{sat} - T_{max,hous})}{W_{in}}$	Ratio of Convective Heat Transfer rate from Housing to Fluid to Input Power
Π_{11}	$\frac{h_{hous,g,rad} A_{hous} (T_g - T_{max,hous})}{W_{in}}$	Ratio of Radiative Heat Transfer rate from Housing to Fluid to Input Power
Π_{12}	$\frac{h_{hous,dr,rad} A_{dr} (T_{sat} - T_{max,hous})}{W_{in}}$	Ratio of Radiative Heat Transfer rate from Housing to Entrained Droplets to Input Power
Π_{13}	$\frac{h_{dum,conv} A_{dum} (T_{sat} - T_{max,dum})}{W_{in}}$	Ratio of Convective Heat Transfer rate from Dummy Rod to Fluid to Input Power

Π Term	Expression	Physical Meaning
Π_{14}	$\frac{h_{dum,g,rad} A_{dum} (T_g - T_{max,dum})}{W_{in}}$	Ratio of Radiative Heat Transfer rate from Dummy Rod to Fluid to Input Power
Π_{15}	$\frac{h_{dum,dr,rad} A_{dr} (T_{sat} - T_{max,dum})}{W_{in}}$	Ratio of Radiative Heat Transfer rate from Dummy Rod to Entrained Droplets to Input Power
Π_{16}	$\frac{\dot{m}_i (H_f - H_i)}{W_{in}}$	Ratio of Single Phase Liquid Sensible Energy change rate to Input Power same as Π_1
Π_{17}	$\frac{\dot{m}_o (H_g - H_{sat})}{W_{in}}$	Ratio of Single Phase Vapor Sensible Energy change rate to Input Power same as Π_2

5.2.2 Non-Dimensionalization of Fuel Energy Equation

The radial heat conduction equation for the fuel element can be written as:

$$\rho_{fuel} C_{p,fuel} V_{fuel} \frac{\partial T_{fuel}}{\partial t} - \frac{1}{r} \frac{\partial}{\partial r} \left(k_{fuel} r \frac{\partial T_{fuel}}{\partial r} \right) V_{fuel} = q_{fuel}''' V_{fuel} - h_{gap} A_{int} (T_s - T_{c,i}) \quad (5.32)$$

Each terms of the Fuel Energy Equation is explained below:

Term 1: Rate of change of fuel stored energy.

Term 2: Radial heat conduction within the fuel element.

Term 3: Heat generation within the fuel element.

Term 4: Rate of heat removal from the pellet clad gap.

The terms of the equation can be written in terms of non-dimensional parameters as:

Term 1:

$$\rho_{fuel} C_{p,fuel} V_{fuel} \frac{\partial T_{fuel}}{\partial t} = \frac{\rho_{fuel} C_{p,fuel} V_{fuel} (T_{fuel,cl} - T_s)}{\tau_{fuel}} \rho_{fuel}^* C_{p,fuel}^* V_{fuel}^* \frac{\partial T_{fuel}^*}{\partial t^*} \quad (5.33)$$

Term 2:

$$\frac{1}{r} \frac{\partial}{\partial r} \left(k_{fuel} r \frac{\partial T_{fuel}}{\partial r} \right) V_{fuel} = \frac{k_{fuel}}{R_{fuel}^2} (T_{fuel,cl} - T_s) \frac{1}{r^*} \frac{\partial}{\partial r^*} \left(k_{fuel}^* r^* \frac{\partial T_{fuel}^*}{\partial r^*} \right) V_{fuel}^* \quad (5.34)$$

Term 3:

$$q_{fuel}''' V_{fuel} = q_{fuel,i}''' V_{fuel,i} q_{fuel}^{*''' } V_{fuel}^* \quad (5.35)$$

Term 4:

$$h_{gap} A_{int} (T_s - T_{c,int}) = h_{gap,i} A_{int,i} (T_{s,i} - T_{c,int,i}) h_{gap}^* A_{int}^* (T_s - T_{c,int})^* \quad (5.36)$$

Dividing all terms of Eq. (5.32) by power input to the test section W_{in} the fuel energy equation reduces to:

$$\begin{aligned} \Pi_{21} \rho_{1fuel}^* C_{p,fuel}^* V_{fuel}^* \frac{\partial T_{fuel}^*}{\partial t^*} - \Pi_{22} \frac{1}{r^*} \frac{\partial}{\partial r^*} \left(k_{fuel}^* r^* \frac{\partial T_{fuel}^*}{\partial r^*} \right) V_{fuel}^* \\ = \Pi_{23} q_{fuel}^{*''' } V_{fuel}^* - \Pi_{24} h_{gap}^* A_{int}^* (T_s - T_{c,int})^* \end{aligned} \quad (5.37)$$

The Π terms of Eq. (5.37) are explained in Table 5.2

5.2.3 Non-Dimensionalization of Clad Energy Equation

The heat conduction equation for the cladding can be written as:

$$\begin{aligned}
 \rho_c C_{p,c} V_c \frac{\partial T_c}{\partial t} - \frac{1}{r} \frac{\partial}{\partial r} \left(k_c r \frac{\partial T_c}{\partial r} \right) V_c = & \\
 & h_{gap} A_{c,int} (T_s - T_{c,int}) - h_{c,conv,f} A_{c,ext} (T_{c,ext} - T_g) \\
 & - h_{c,rad,c} A_{c,ext} (T_{c,ext} - T_{c,other}) - h_{c,rad,hous} A_{c,ext} (T_{c,ext} - T_{hous}) \\
 & - h_{c,rad,dum} A_{c,ext} (T_{c,ext} - T_{c,dum}) - h_{c,conv,f} A_{c,ext} (T_{c,ext} - T_{sat}) \\
 & - h_{c,rad,g} A_{c,ext} (T_{c,ext} - T_g) - h_{c,rad,dr} A_{dr} (T_{c,ext} - T_{sat}) \quad (5.38)
 \end{aligned}$$

Each terms of the Clad Energy Equation is explained below:

- Term 1: Rate of change of clad stored energy.
- Term 2: Radial heat conduction rate within clad element.
- Term 3: Heat received from fuel element through gap conduction.
- Term 4: Convective heat transfer rate to vapor.
- Term 5: Radiative heat transfer rate to other clads.
- Term 6: Radiative heat transfer rate to housing.
- Term 7: Radiative heat transfer rate to dummy fuel clad.
- Term 8: Convective heat transfer rate to fluid (water).
- Term 9: Radiative heat transfer rate to vapor.
- Term 10: Radiative heat transfer rate to entrained droplets.

Table 5.2: List of Π Terms for Fuel Energy Equation

Π Term	Expression	Physical Meaning
Π_{21}	$\frac{\rho_{fuel} C_{p,fuel} V_{fuel} (T_{fuel,cl} - T_s)}{\tau_{fuel} W_{in}}$	Ratio of Fuel Stored Energy change rate to Input Power
Π_{22}	$\frac{k_{fuel}}{R_{in fuel}^2 W_{in}} (T_{fuel,cl} - T_s)$	Ratio of Fuel Heat Conduction rate to Input Power
Π_{23}	$\frac{q_{fuel,i}''' V_{fuel,i}}{W_{in}}$	Ratio of Fuel Heat Generation rate to Input Power
Π_{24}	$\frac{h_{gap,i} A_{c,int,i} (T_{s,i} - T_{c,int,i})}{W_{in}}$	Ratio of Heat Transfer rate from Pellet to Clad to Input Power

The terms of the equation can be written in terms of non-dimensional parameters as:

Term 1:

$$\rho_c C_{p,c} V_c \frac{\partial T_c}{\partial t} = \frac{\rho_{c,i} C_{p,c,i} V_{c,i} (T_{c,int} - T_{c,ext})}{\tau_c} \rho_c^* C_{p,c}^* V_c^* \frac{\partial T_c^*}{\partial t^*} \quad (5.39)$$

Term 2:

$$\frac{1}{r} \frac{\partial}{\partial r} \left(k_c r \frac{\partial T_c}{\partial r} \right) V_c = \frac{1}{R^2} k_{c,i} (T_{c,int} - T_{c,ext}) V_{c,i} \frac{1}{r^*} \frac{\partial}{\partial r^*} \left(k_c^* r^* \frac{\partial T_c^*}{\partial r^*} \right) V_c^* \quad (5.40)$$

Term 3:

$$h_{gap} A_{c,int} (T_s - T_{c,int}) = h_{gap,i} A_{c,int,i} (T_s - T_{c,int,i}) h_{gap}^* A_{c,int}^* (T_s - T_{c,int})^* \quad (5.41)$$

Term 4:

$$h_{c,conv,f} A_{c,ext} (T_{c,ext} - T_g) = h_{c,conv,f,i} A_{c,ext,i} (T_{c,ext} - T_g)_i$$

$$h_{c,conv,f}^* A_{c,ext}^* (T_{c,ext} - T_g)^* \quad (5.42)$$

Term 5:

$$h_{c,rad,c} A_{c,ext} (T_{c,ext} - T_{c,other}) = h_{c,rad,c,i} A_{c,ext,i} (T_{c,ext} - T_{c,other})_i$$

$$h_{c,rad,c}^* A_{c,ext}^* (T_{c,ext} - T_{c,other})^* \quad (5.43)$$

Term 6:

$$h_{c,rad,hous} A_{c,ext} (T_{c,ext} - T_{hous}) = h_{c,rad,hous,i} A_{c,ext,i} (T_{c,ext} - T_{hous})_i$$

$$h_{c,rad,hous}^* A_{c,ext}^* (T_{c,ext} - T_{hous})^* \quad (5.44)$$

Term 7:

$$h_{c,rad,dum} A_{c,ext} (T_{c,ext} - T_{c,dum}) = h_{c,rad,dum,i} A_{c,ext,i} (T_{c,ext} - T_{c,dum})_i$$

$$h_{c,rad,dum}^* A_{c,ext}^* (T_{c,ext} - T_{c,dum})^* \quad (5.45)$$

Term 8:

$$h_{c,conv,f} A_{c,ext} (T_{c,ext} - T_{sat}) = h_{c,conv,f,i} A_{c,ext,i} (T_{c,ext} - T_{sat})_i$$

$$h_{c,conv,f}^* A_{c,ext}^* (T_{c,ext} - T_{sat})^* \quad (5.46)$$

Term 9:

$$h_{c,rad,g}A_{c,ext}(T_{c,ext} - T_g) = h_{c,rad,g,i}A_{c,ext,i}(T_{c,ext} - T_g)_i$$

$$h_{c,rad,g}^*A_{c,ext}^*(T_{c,ext} - T_g)^* \quad (5.47)$$

Term 10:

$$h_{c,rad,dr}A_{dr}(T_{c,ext} - T_{sat}) = h_{c,rad,dr,i}A_{dr,i}(T_{c,ext} - T_{sat})_i$$

$$h_{c,rad,dr}^*A_{dr}^*(T_{c,ext} - T_{sat})^* \quad (5.48)$$

Dividing all terms of Eq. (5.38) by power input to the test section W_{in} the clad energy equation reduces to:

$$\begin{aligned} & \Pi_{31}\rho_c^*C_{p,c}^*V_c^*\frac{\partial T_c^*}{\partial t^*} - \Pi_{32}\frac{1}{r^*}\frac{\partial}{\partial r^*}\left(h_c^*r^*\frac{\partial T_c^*}{\partial r^*}\right)V_c^* \\ &= \Pi_{33}h_{gap}^*A_{c,int}^*(T_s - T_{c,int})^* - \Pi_{34}h_{c,conv,f}^*A_{c,ext}^*(T_{c,ext} - T_g)^* \\ & - \Pi_{35}h_{c,rad,c}^*A_{c,ext}^*(T_{c,ext} - T_{c,other})^* - \Pi_{36}h_{c,rad,hous}^*A_{c,ext}^*(T_{c,ext} - T_{hous})^* \\ & - \Pi_{37}h_{c,rad,dum}^*A_{c,ext}^*(T_{c,ext} - T_{c,dum})^* - \Pi_{38}h_{c,conv,f}^*A_{c,ext}^*(T_{c,ext} - T_{sat})^* \\ & - \Pi_{39}h_{c,rad,g}^*A_{c,ext}^*(T_{c,ext} - T_g)^* - \Pi_{40}h_{c,rad,dr}^*A_{dr}^*(T_{c,ext} - T_{sat})^* \quad (5.49) \end{aligned}$$

The Π terms of Eq. (5.49) are explained in Table 5.3.

Table 5.3: List of Π Terms for Clad Energy Equation

Π Term	Expression	Physical Meaning
Π_{31}	$\frac{\rho_{c,i}C_{p,c,i}V_{c,i}(T_{c,int}-T_{c,ext})}{\tau_c W_{in}}$	Ratio of Clad Stored Energy change rate to Input Power

Π Term	Expression	Physical Meaning
Π_{32}	$\frac{k_{c,i}}{R^2 W_{in}} (T_{c,int} - T_{c,ext}) V_{c,i}$	Ratio of Clad Heat Conduction Rate to Input Power
Π_{33}	$\frac{h_{gap,i} A_{c,int,i} (T_s - T_{c,int})_i}{W_{in}}$	Ratio of Gap Heat Transfer rate from Fuel Pellet to Clad to Input Power
Π_{34}	$\frac{h_{c,conv,f,i} A_{c,ext,i} (T_{c,ext} - T_g)_i}{W_{in}}$	Ratio of Convective Heat Transfer rate from Clad to Vapour to Input Power
Π_{35}	$\frac{h_{c,rad,c,i} A_{c,ext,i} (T_{c,ext} - T_{c,other})_i}{W_{in}}$	Ratio of Radiative Heat Transfer rate from Clad to other Clads to Input Power
Π_{36}	$\frac{h_{c,rad,hous,i} A_{c,ext,i} (T_{c,ext} - T_{hous})_i}{W_{in}}$	Ratio of Radiative Heat Transfer rate from Clad to Housing to Input Power
Π_{37}	$\frac{h_{c,rad,dum,i} A_{c,ext,i} (T_{c,ext} - T_{c,dum})_i}{W_{in}}$	Ratio of Radiative Heat Transfer rate from Clad to Dummy Clads to Input Power
Π_{38}	$\frac{h_{c,conv,f,i} A_{c,ext,i} (T_{c,ext} - T_{sat})_i}{W_{in}}$	Ratio of Convective Heat Transfer rate from Clad to Fluid to Input Power
Π_{39}	$\frac{h_{c,rad,g,i} A_{c,ext,i} (T_{c,ext} - T_g)_i}{W_{in}}$	Ratio of Radiative Heat Transfer rate from Clad to Vapour to Input Power
Π_{40}	$\frac{h_{c,rad,dr,i} A_{dr,i} (T_{c,ext} - T_{sat})_i}{W_{in}}$	Ratio of Radiative Heat Transfer rate from Clad to Entrained Droplets to Input Power

5.3 Conservation of Non-Dimensional Π Terms

In order to obtain similar system behavior in a scaled down experimental setup as that of the actual system, the non-dimensional parameters obtained from normalizing of conservation equations should be conserved to the extent possible. However, it may not be possible to conserve all Π terms because of the differences in the properties of materials and imposed boundary conditions in the setup as against the evolved conditions in the actual system. Keeping in mind the practical difficulties in maintaining the Π terms, an experimental setup is designed to simulate behavior of moderately degraded core under quenching conditions.

The design parameters of the setup used for comparing the non-dimensional terms and the design of the experimental setup are described in the subsequent chapter. The non-dimensional parameters evolved in the scaling analysis have been compared numerically with the values of the parameters for actual PWR systems [41]. The parameters for PWR with postulated ballooned core condition have been calculated with ballooned fuel pin geometrical values keeping other parameters same as typical PWR.

The minimum injection flow rate required for removal of heat input to the test section can be obtained from Eq. (4.1). The ratio of energy input to the test section to the injection flow rate translates into injection flow rate of 6 g/s . The comparison has been done for three different injection flow rates of 10 g/s , 15 g/s and 35 g/s at injection temperature of 303 K with the experimental setup initially heated to clad surface temperature of 973 K . The injection rate range translates into power to injection ratio range of $0.3 - 1.2\text{ MWs/kg}$, which is well within the range $0.15 - 2.0\text{ MWs/kg}$ obtained from plant scale and thermodynamics as mentioned in Section 4.5. The basis for the design of the experimental setup is to maintain the power-to-volume ratio equal to a typical PWR case. The power and thus the number of heated pins have been scaled according to the volume of the experimental setup. A comparison of Π terms for actual PWR with the Π terms

of experimental setup is given in Table 5.4.

The following sections provide a discussion on the comparative values of the non-dimensional terms.

5.3.1 Fluid Energy Π Terms

The water injection rate has been scaled depending on the power-to-volume ratio to obtain similar re-flood velocities as those in the typical PWR case. Three different injection rates are considered. The Π_1 term, which represents single-phase convective heat transfer to liquid, is governed by the water injection rates. As shown in Table 5.4 the Π_1 values for the ballooned case (case A) and the non-ballooned case (case B) match the respective PWR values at an injection rate of 10 g/s. The dimensions of the heated pins (both ballooned and non-ballooned) in the experimental setup are higher than the actual PWR values. Consequently, the heated pins of the experimental setup store more energy than the corresponding pins of a typical PWR. The amount of energy released during quenching of heater pins is thus higher than that of a PWR, leading to higher Π_3 values. Because of the absence of housing for a typical PWR assembly and very low dummy mass per PWR assembly, the Π terms related to housing and dummy rods are absent in case of actual PWR while having non-zero values for the experimental setup. Also the Π terms for the experimental setup related to radiative heat transfer show large variation in comparison to the PWR values because of changes in geometrical parameters of fuel rods, dummy rods and housing.

Table 5.4: Comparison of Π Terms for the Experimental Setup with Typical PWR

Π	Description (Ratio of)	Values of Typical PWR		Values Obtained from Scaling Analysis for Experimental Setup					
		Ballooned Configuration	Non- ballooned Configuration	Ballooned Case (Case A)			Non Ballooned Case (Case B)		
				10 g/s	15 g/s	35 g/s	10 g/s	15 g/s	35 g/s
Π_1	Single Phase Liquid Sensible Energy Change rate to Input Power	0.141	0.144	0.148	0.22	0.518	0.148	0.22	0.518
Π_2	Single Phase Vapor Sensible Energy Change rate to Input Power	0	0	0.0	0.0	0.0	0.0	0.0	0.0
Π_3	Fuel Rod Quench Energy Release rate to Input Power	0.0059	0.066	0.008	0.18	0.232	0.19	0.207	0.289
Π_4	Housing Quench Energy Release rate to Input Power	0	0	0.116	0.154	0.198	0.098	0.131	0.199

Π_5	Dummy Rod Quench Energy Release rate to Input Power	0.001	0.001	0.043	0.099	0.141	0.032	0.051	0.141
Π_6	Energy Release rate to Single Phase Upward and Downward of Quench Front to Input Power	1	1	1.0	1.0	1.0	1.0	1.0	1.0
Π_7	Convective Heat Transfer rate from Fuel to Fluid to Input Power	1.76	0.567	1.54	3.906	30.807	0.059	1.152	17.953
Π_8	Radiative Heat Transfer rate from Fuel to Fluid to Input Power	0	0	6.8e-11	7.9e-11	9.8e-11	6.1e-11	7.7e-11	9.5e-11
Π_9	Radiative Heat Transfer rate from Fuel to Entrained Droplets to Input Power	0.086	0.074	0.007	0.017	0.291	0.001	0.008	0.206
Π_{10}	Convective Heat Transfer rate from Housing to Fluid to Input Power	0	0	0.155	0.206	0.265	0.131	0.109	0.266
Π_{11}	Radiative Heat Transfer rate from Housing to Fluid to Input Power	0	0	0	0	0	0	0	0

Π_{12}	Radiative Heat Transfer rate from Housing to Entrained Droplets to Input Power	0	0	0.627	1.061	1.851	0.507	0.329	1.732
Π_{13}	Convective Heat Transfer rate from Dummy Rod to Fluid to Input Power	0.023	0.019	11.857	6.757	4.345	11.906	2.87	17.253
Π_{14}	Radiative Heat Transfer rate from Dummy Rod to Fluid to Input Power	0	0	0	0	0	0	0	0
Π_{15}	Radiative Heat Transfer rate from Dummy Rod to Entrained Droplets to Input Power	0	0	0.001	0.06	0.129	0.001	0.002	0.168
Π_{16}	Single Phase Liquid Sensible Energy Change rate to Input Power	0.141	0.144	0.148	0.22	0.518	0.148	0.22	0.518
Π_{17}	Single Phase Vapor Sensible Energy Change rate to Input Power	0	0	0.0	0.0	0.0	0.0	0.0	0.0
Π_{21}	Fuel Stored Energy Change rate to Input Power	33.94	1.18	1.749	4.353	32.944	0.424	1.455	21.922
Π_{22}	Fuel Heat Conduction Rate to Input Power	0.558	0.121	15.522	38.63	292.35	3.764	12.91	194.54

Π_{23}	Fuel Heat Generation Rate to Input Power	1.0	1.0	1.0	1.0	1.0	1.0	1.0	1.0
Π_{24}	Heat Transfer Rate from Pellet to Clad to Input Power	0.67	0.73	0.72	0.83	0.92	0.73	0.86	0.99
Π_{31}	Clad Stored Energy Change rate to Input Power	0.0025	0.04	1.655	4.185	31.984	0.384	1.397	21.504
Π_{32}	Clad Heat Conduction Rate to Input Power	0.051	0.016	13.071	33.055	252.63	3.031	11.031	168.85
Π_{33}	Heat Transfer Rate from Pellet to Clad to Input Power	0.67	0.73	0.72	0.83	0.92	0.73	0.86	0.99
Π_{34}	Convective Heat Transfer rate from Clad to Vapour to Input Power	4.76	0.73	3.558	6.247	35.45	0.834	2.882	21.584
Π_{35}	Convective Heat Transfer rate from Clad to Fluid to Input Power	1.76	0.567	1.54	3.906	30.807	0.059	1.152	17.953
Π_{40}	Ratio of Radiative Heat Transfer rate from Clad to Entrained Droplets to Input Power	0.086	0.074	0.007	0.017	0.291	0.001	0.008	0.206

5.3.2 Fuel Energy Π Terms

The heated fuel pins of the experimental setup have higher dimensions and store more energy than the PWR fuel pins. Since the water injection rate has been scaled to maintain re-flood velocities close to the PWR value, the rate of removal of energy from the heated pins is close to an actual PWR. This is reflected in the Π_7 and Π_8 values. Consequently, the rate of change of stored energy in the fuel is much smaller than the actual PWR values, leading to the Π_{21} term being much smaller for the experimental setup than the PWR. As a consequence, quenching will occur more slowly in the case of the experimental setup as compared to the actual PWR. The temperature difference between the centerline and the surface of fuel pellets is also higher in the case of the experimental setup due to larger dimensions of the heated pin. This is reflected in a higher Π_{22} value. The Π_{23} value is unity for the setup and PWR. Since the heat transfer through the gap between the fuel and the clad plays an important role in quenching behavior, the Π_{24} value has been maintained close to PWR value by selection of appropriate pellet diameter.

5.3.3 Clad Energy Π Terms

Similar to the case for fuel pins, the clad used in the experimental setup has a greater diameter and thickness and stores more energy as compared to the PWR. However, the larger thickness of the clad along with higher thermal conductivity of the clad material enables strong axial conduction along the length of the clad. Typically, axial conduction is the controlling phenomenon in quenching phenomena with slow injection rates. For a particular node of the fuel to get quenched, the temperature has to be brought to a value lower than the minimum film boiling temperature. The stored heat as well as the heat being generated within the node needs to be removed to achieve this. However, as soon as the temperature of the node starts decreasing, heat starts flowing from the adjacent high-temperature

unquenched node, through conduction in the axial direction. The rate of change of stored energy for the clad is thus higher for the experimental setup as depicted by higher Π_{31} values. The larger thickness of the clad also leads to a higher temperature difference across the clad thickness leading to higher Π_{31} values than that for the PWR. The quench behavior is affected by the rate of release of quench energy to the fluid (Π_3) and the rate of change of stored energy in the fuel (Π_{21}) and clad (Π_{31}). Since the Π_3 term has higher magnitude than the corresponding value for a typical PWR, the quench front propagation will be slower in the experimental setup than in the actual PWR conditions. At the same time, the gap between the cladding and the fuel pellets leads to higher Π_{31} values and lower Π_{21} values for the experimental setup. This will speed up the quenching of the clad. The actual quench front velocity will be governed by these two opposing phenomena. The gap between the clad and fuel helps overcome the shortcomings of direct heated experiments [41], wherein significantly low quench front velocities are obtained due to participation of the entire energy of the fuel pin (fuel and clad both) in the quenching. Higher thickness of the clad also causes significant heat conduction in the axial direction through the clad as represented by Π_{32} value and reduces the quench front velocity. The terms Π_{36} to Π_{37} are not compared with PWR values because of absence of housing and small dummy mass present and the terms Π_{38} to Π_{39} are negligibly small.

5.3.4 Selection of Π Terms for Conservation

Since it is not possible to conserve all non-dimensional terms due to limitations on material and geometrical parameters, only the terms important for quenching have been conserved. These include the ratios of fuel or clad stored heat release rate (Π_{21}, Π_{31}), rate of heat transfer to single phase liquid (Π_1), rate of heat transfer through the pellet clad gap (Π_{33}), convective heat transfer from fuel to fluid (Π_7) and radiative heat transfer from clad to entrained droplets (Π_9). In an actual

reactor system the mass of dummy rods is negligibly small as compared to the mass of fuel pins. The core barrel, which represented by the housing in the experimental setup is sufficiently away from the central fuel pins and hence does not affect the heat transfer of central pins. Hence, the non-dimensional terms related to dummy pins and housing (Π_{10} to Π_{15} and Π_{36} to Π_{39}) do not have a reference value of PWR or the values are in-significant for comparison and are not conserved. This will not affect the quenching results because the energy release or transfer represented by these terms is negligibly small as compared to the magnitude of stored heat release represented by terms such as Π_{21} or Π_{31} .

5.4 Pre-test Analysis of the Experimental Setup

To study the effect of ballooned heated fuel pins on the quenching patterns under re-flood conditions, simulations are carried out in the RELAP5 (mod 3.2) thermal-hydraulic code. A RELAP5 specific model is developed for the experimental setup. The experimental test section is divided into two parallel channels, one containing the heated fuel pins and the other containing dummy fuel pins. The fuel pins are represented with RELAP heat structures. The fluid channels and the contained heat structures are divided into six axial nodes as shown in the nodalization in Figure 5.2. The fluid channels are connected with cross-flow junctions at each axial node to facilitate cross-flow between the two channels.

The experimental setup is initially assumed to be filled with saturated steam at atmospheric pressure. The heated fuel pins are then heated to an average temperature of 1000 K with 11 kW of total power (decay power of 1% of normal operating power of 14 kW/m per pin for a typical PWR, considered for 45 pins with 1.75 m length). Water injection is then started at an injection rate of 10 g/s . Two test cases are studied: case A, with a ballooned central zone with 40% of flow blockage over 600 mm length, and case B, with a non-ballooned central zone. The re-flood model of RELAP5 was invoked with ten subdivisions in each axial

node. The quench timings of the axial nodes in the central zone as well as in the peripheral zone for both cases are given in Table 5.5.

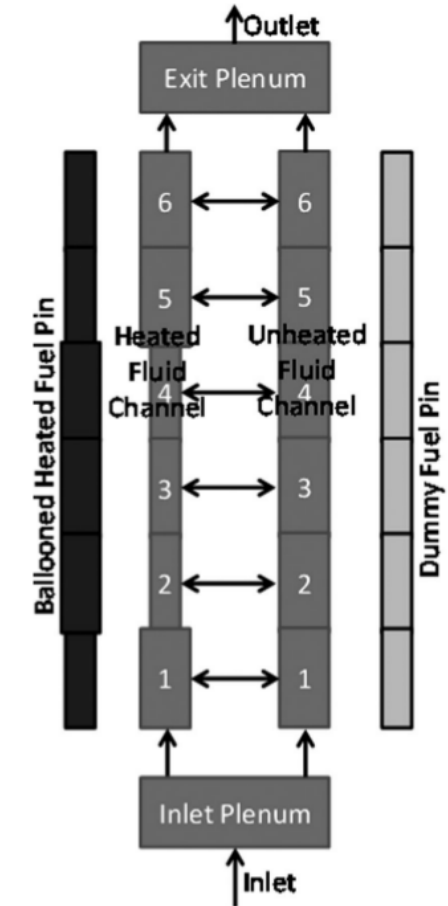


Figure 5.2: Nodalization of Model of Experimental Setup developed in RELAP5

Table 5.5: Time of Quenching for Central and Peripheral Zones for Case A and Case B

Node	Case A		Case B	
	Central Heated (Ballooned) zone	Peripheral Unheated Zone	Central Heated Zone	Peripheral Unheated Zone
1	13688	13724	13439	13500

2	14214	14410	14409	14426
3	14790	14922	14886	14895
4	15734	15858	15368	15420
5	15996	16120	15825	15885
6	16664	17230	16335	16405

5.4.1 Quenching of Upstream Non-ballooned Region (Node 1)

The total pressure drop across the length of the test setup is governed by flow blockages. Since case A has more flow blockage than case B, the pressure drop for case A is higher than that in case B. Thus, injected water requires more time to reach the upstream non-ballooned region (node 1) in case A than in case B, as shown in Table 5.5. In the peripheral fuel pins, although unheated, the quenching begins simultaneously along with the central zone. However, quenching occurs later in the central zone than the peripheral zone for case A as well as for case B. This is due to the large amount of energy released into the fluid due to quenching of the stainless steel shroud encompassing the test section. Figure 5.3 shows that quenching in both zones occurs much earlier for the case without shroud (a case wherein heat released due to quenching of shroud is neglected).

5.4.2 Quenching of Ballooned Region (Nodes 2, 3, and 4)

The temperature transients of nodes 2 and 4 for both cases are shown in Figure 5.4 and Figure 5.5, respectively.

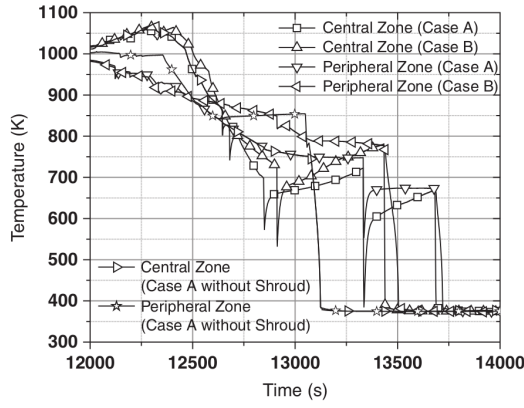


Figure 5.3: Temperature Variation of Node 1

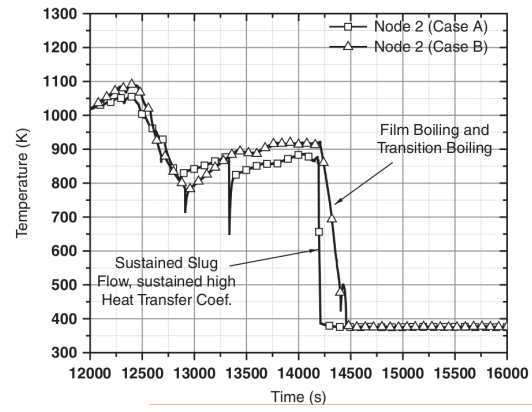


Figure 5.4: Temperature Variation of Node 2

Unlike node 1, node 2 for the central zone of ballooned case A gets quenched earlier than node 2 of case B. Entry of fluid into the node, accompanied by large steam generation near the heater pin surface, causes the flow regime to change from mist flow to slug flow. Because of the availability of a higher heat transfer area in node 2 of the central zone of case A, a larger amount of energy is transferred to the fluid entering the node as compared to the heat transferred in case B. The local steam generation is thus higher in case A than in case B. This enables a sustained slug flow pattern in the node, and the mode of heat transfer changes from single-phase steam convection to saturated nucleate boiling very quickly for case A. In contrast, for case B, the amount of steam generation is smaller than in case A, and hence, film boiling and transition boiling prevail for longer time before quenching occurs in the nucleate boiling region. This causes a delay in quenching of node 2 of the central zone of case B as compared to case A. As the quench front progresses, the amount of energy received by the fluid is higher in case A than case B owing to the higher heat transfer area availability in case A. This causes delayed quenching in subsequent nodes of case A as compared to case B as depicted by the quench timings in Table 5.5.

5.4.3 Quenching of Downstream Non-ballooned Region (Nodes 5 and 6)

As the ballooned portion ends at node 5 in case A, a sudden reduction in the blockage area in the central heated zone allows more fluid to flow into the central zone from the peripheral unheated zone in node 5 and becomes prominent in node 6. This causes sudden quenching in the central heated zone as shown in Figure 5.6.

The peripheral zone quenching follows. This phenomenon of flow redistribution is not significant in the non-ballooned case B. The times of quenching of the central heated zone and the peripheral unheated zone in case B are close to each other for the downstream region.

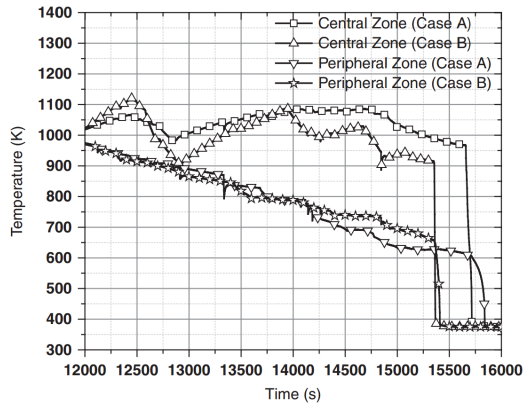


Figure 5.5: Temperature Variation of Node 4

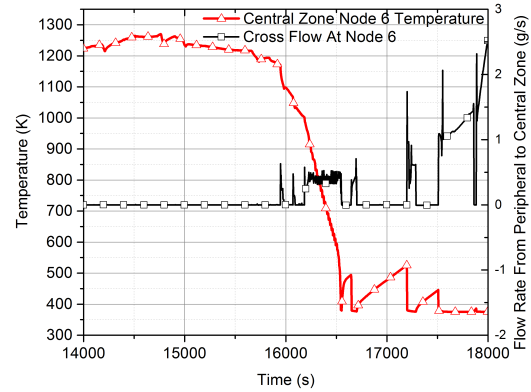


Figure 5.6: Temperature Variation of Node 6

5.5 Conclusions of Pre-Test Analysis

The following conclusions are drawn from the pre-test analysis:

- The conservations equations have been non-dimensionalized to obtain non-

dimensional Π terms for fuel, clad and injected fluid. The Π terms important for the quenching behavior have been conserved with respect to the actual PWR values to preserve the characteristics of the prototype in the experiental setup.

- Although, the RELAP5 cross-flow models do not solve complete momentum equation in the cross-flow direction, the simulations show that significant flow re-distribution takes place, particularly in the vicinity of transition between the ballooned and non-ballooned regions for the ratio of blockages considered. These effects are expected to be more pronounced in the actual experiment. The experimental setup is well instrumented with thermocouples at 70 locations to capture these cross-flow effects. The locations are selected based on the magnitude of cross flow velocities predicted by RELAP simulation for the test setup. Details of the thermocouple locations is provided in subsequent chapters.

Chapter 6

Design and Fabrication of Experimental Setup

To study the quenching behavior of a partially degraded core, Degraded Reactor Core Re-flood Experimental Facility (DRCRE) is designed and fabricated. The objective of the experiment is to obtain quench patterns for a cluster of ballooned Fuel Pin Simulators (FPS) with extended ballooned lengths. The number of FPS modeled, the extent of ballooning and the span of ballooned region are optimized, within the limits of machining capacity and material availability, to simulate the partially degraded core conditions reported in literature. The DRCRE facility is capable of using FPS of different extent of ballooning and different lengths of ballooned portions.

6.1 Approach for Scaling

The experimental setup simulates a scaled down portion of a reactor core under a partially degraded core condition. A detailed scaling analysis has been performed to conserve the quenching characteristics of the core as discussed in detail in the previous chapter. In general the approach conserves the power-to-volume ratio of the reactor core. The ballooned FPS simulates 45% ballooning spanning over 60%

of the total length. The linear heat rate of the FPS is conserved to match the decay heat condition equivalent to 1% of the full power.

6.2 Description of Experimental Setup

The experimental setup consists of a cluster of FPS having a combination of heated and unheated FPS, enclosed in a Stainless Steel (SS) shroud. The schematic of the test setup is shown in Figure 6.1. The FPS are electrically heated. The setup has provision for inlet/outlet of steam/water into the shroud, temperature measurements at different locations on various FPS as well as on the shroud, measurement of inlet flow rate and water level within the shroud, measurement of pressure in the shroud and carryover flow measurement. Detailed description of various components of the experimental setup is provided in following sections.

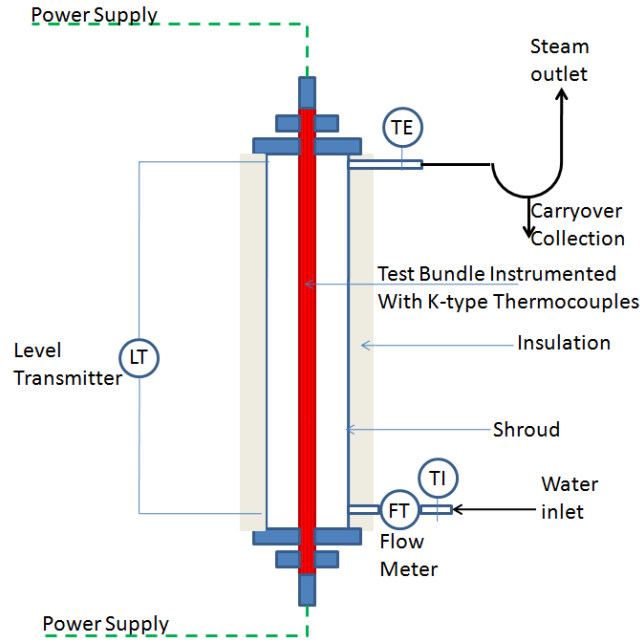


Figure 6.1: Schematic of the Experimental Setup

6.2.1 Fuel Pin Simulator (FPS)

Three different types of FPS, Straights FPS, Ballooned FPS and Dummy FPS are used in this experimental setup. The Straight FPS and the Ballooned FPS can

be electrically heated by passing electric current through the Tungsten rod kept along the centerline of the FPS. The tungsten rods run throughout the length of these pins and protrude out from either ends to facilitate connection with electrical copper bus bars. Alumina annular sleeves of various dimensions are slid over the central tungsten rod of each FPS. Each FPS uses SS tube as clad throughout the length of FPS. Grooves of 1 mm width and 1 mm depth are cut over the SS clad, along the length of the clad at four equi-spaced azimuthal locations for each FPS. Thermocouples are mounted within these grooves at required axial locations such that they do not protrude out of the clad surface. The disturbances caused by the thermocouples on fluid flow, thus, remain minimal.

The Dummy FPS are exactly the same as the Straight FPS, except for the absence of Tungsten Rod. Dummy FPS can not be heated electrically and are used only to provide necessary flow blockages in the peripheral region to simulate degraded core condition. Approximate Engineering Drawings of the Straight FPS and Ballooned FPS are shown in Figure 6.2. The dimensional details of FPS are tabulated in Table 6.1.

Table 6.1: Dimensional Details of FPS

Description	Straight FPS	Ballooned FPS	Dummy FPS
Number of Pins	20	25	12
Heated / Unheated	Heated	Heated	Unheated
Heater Material	Tungsten	Tungsten	-
Heater Rod OD	3 mm	3 mm	-
Length of Heater Rod	2000 mm	2000 mm	-
Pellet Material	Alumina	Alumina	Alumina

Description	Straight FPS	Ballooned FPS	Dummy FPS
Pellet ID	$3\text{ mm}^{+0.15}_{-0.00}$	$3\text{ mm}^{+0.15}_{-0.00}$	$3\text{ mm}^{+0.15}_{-0.00}$
Pellet OD	$7\text{ mm}^{+0.00}_{-0.15}$	$10\text{ mm}^{+0.00}_{-0.15}$ (Ballooned Region)	$7\text{ mm}^{+0.00}_{-0.15}$
Pellet Length	25 mm	25 mm	25 mm
Clad Material	SS	SS	SS
Clad ID	$7\text{ mm}^{+0.15}_{-0.00}$	$10\text{ mm}^{+0.15}_{-0.00}$ (Ballooned Region)	$7\text{ mm}^{+0.15}_{-0.00}$
Clad OD	$11\text{ mm}^{+0.15}_{-0.00}$	$14\text{ mm}^{+0.15}_{-0.00}$ (Ballooned Region)	$11\text{ mm}^{+0.15}_{-0.00}$
Clad Length	1150 mm	1150 mm 600 mm (Ballooned) 550 mm (Un-ballooned)	1150 mm
Length of Upper End Segment	350 mm	350 mm	300 mm
Length of Lower End Segment	500 mm	500 mm	450 mm

Each FPS is divided into three regions viz., the Lower End Segment, the Upper End Segment and Central Segment, as shown in Figure 6.2. The thermocouples

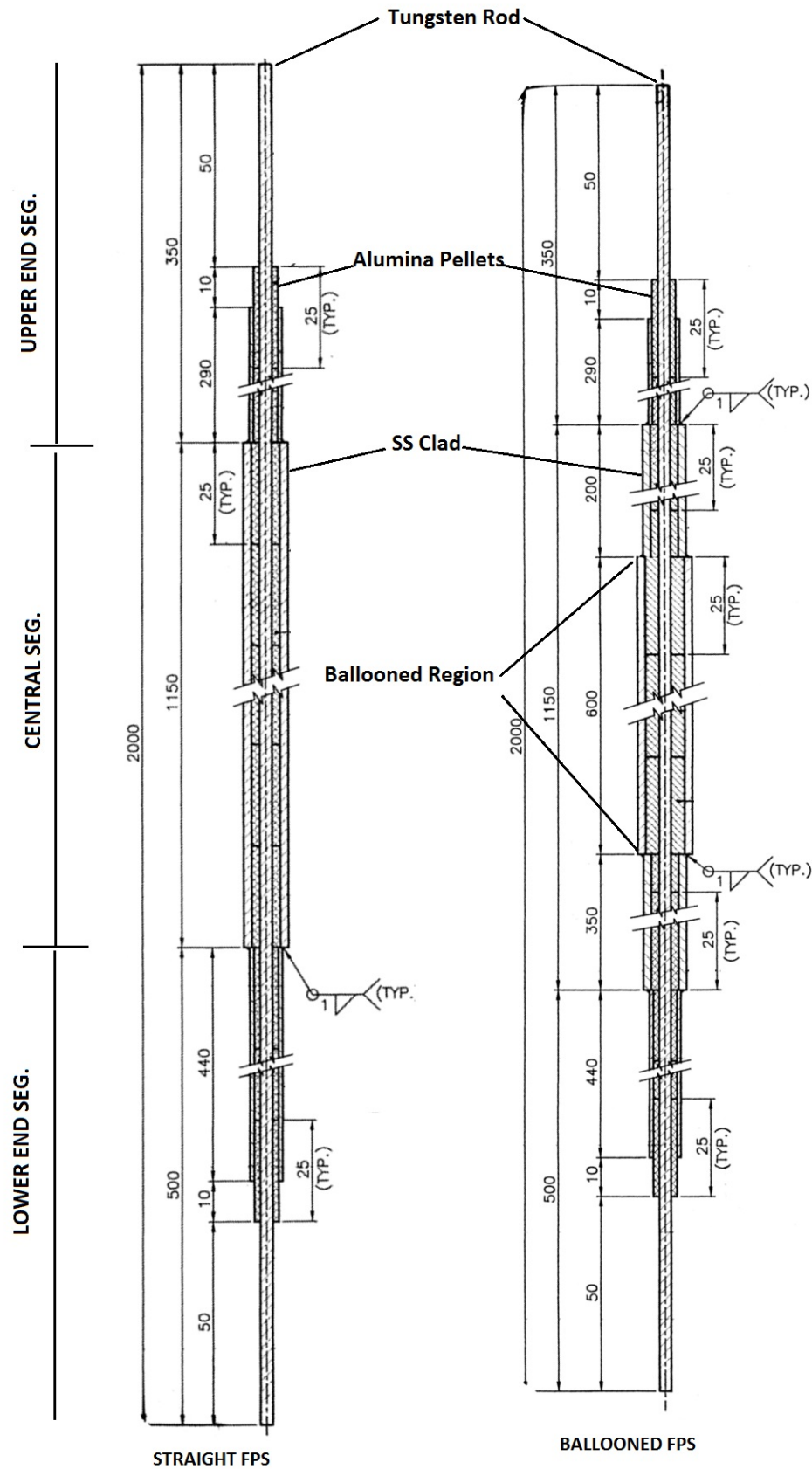


Figure 6.2: Straight FPS and Ballooned FPS

are mounted only in the Central Segment of the FPS and this is the region under experimental observation. The Upper End Segment and Lower End Segment facilitate lowering of FPS outer diameters. This increases the gap between neighboring FPS and is required for easy mounting of FPS. Long lengths and lower diameters of the End Segments help towards reducing the end effects and restricting the effects only to the End Segments.

6.2.1.1 Reason for Tungsten-Alumina-SS Combination

Table 6.2: Details of FPS Material

Material	Density kg/m^3	Specific Heat $J/kg.K$	Thermal Con- ductiv- ity $W/m.K$	Thermal Capac- ity $J/m^3.K$	Effective Thermal Conduc- tivity $W/m.K$	Thermal Diffusiv- ity m^2/s
UO ₂ [42]	10730	311.4	3.26	3.34e6	7.442	2.23e-6
Zr	6560	278	22.7	1.82e6		
Tungsten [43]	19250	145.53	112	3.75e6	10.81	2.76e-6
Alumina [44]	3950	1225	10.5			
SS	7800	500	25	3.9e6		

SS has been chosen as the clad material due to its better workability. It also facilitates easy mounting of SS sheathed thermocouples by spot welding technique. Alumina has been considered suitable due to its high melting temperature. Table

6.2 enlists the thermo-physical properties of actual fuel material and the material used for FPS construction around the re-wetting temperature (600°C). It can be seen that combination of Tungsten heater rod and Alumina pellets has 12% more thermal capacity than that of the UO₂ pellets. The calculated thermal diffusivity values for the actual fuel and simulator pins are close to each other.

The arrangement of coaxial tungsten heater, alumina sleeves and SS clad provides indirect way of heating the FPS, i.e., the heater element (tungsten) does not contact the clad (SS) and hence selective heating of heater rod, simulating internal heat generation in actual fuel, can be achieved. As can be seen from Table 6.1, the tolerances on the alumina sleeve outer diameter and SS clad internal diameter are so selected that the gap between the fuel pellets and clad is maintained. This simulates the gas gap between the fuel pellets and clad in actual fuel pins. Provision of gas gap between pellets and clad also enables simulation of conductive decoupling between clad and pellets. The quenching patterns are strongly governed by this gap and hence, simulation of this is necessary for study of quenching patterns.

6.2.2 Fuel Pin Simulator Assembly

The FPS Assembly consists of a combination of 25 ballooned FPS, 20 straight FPS and 12 dummy FPS arranged in a square pitch. The cross-section view of FPS Assembly is shown in Figure 6.3.

The FPS are held in their respective positions with the help of spacer on either ends of the FPS assembly. The spacer are located in the Upper and Lower End Segments of the FPS and do not obstruct or affect the flow of fluid in the Central Segment under experimental observation.

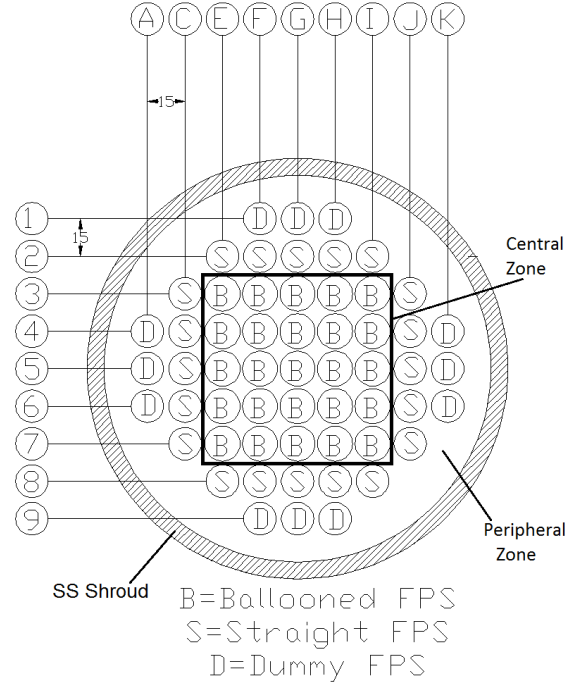


Figure 6.3: FPS Assembly Configuration Map

6.2.3 Test Section

The FPS Assembly is enclosed in a test section made up of SS pipe 150 mm in diameter. The Test Section is closed on either ends with a Sealing Flange Sliding Pin Assembly. This assembly facilitates sealing of the test section on either ends to ensure no leakages and at the same time allows FPS to move freely due to thermal expansion of the pins. This prevents the pins from bowing due to thermal expansion.

The test section has provisions for entry of steam or water into the test section through four inlet ports from bottom flange at equi-spaced azimuthal locations. The steam water mixture can flow out of the test section through two outlet ports located in the top flange. The connecting wires of thermocouples are taken out from the side flange provided in the lower portion of the test section. The test section wall has thermocouples mounted on the outer surface of the wall at specific axial locations. This facilitates measurement of the wall surface temperatures

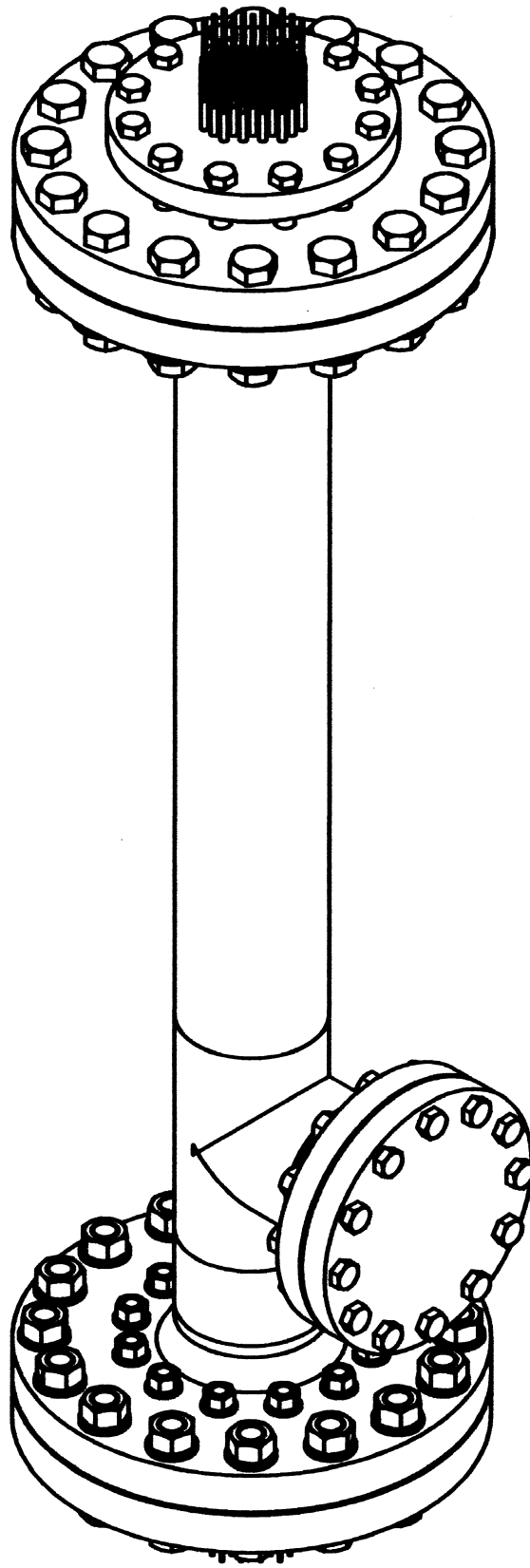


Figure 6.4: 3D Schematic of the Test Section

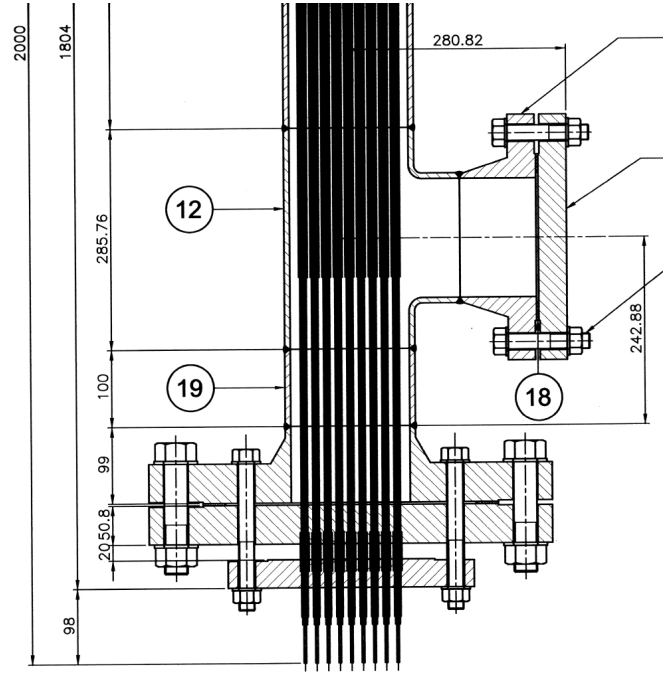


Figure 6.5: Drawing of Sealing Flange Sliding Pin Assembly

which can be used to calculate the heat loss through the test section to the environment. The test section is clad with a 5mm thick layer of Glass-wool to minimize the heat loss to the environment. A three-dimensional drawing of the test section is shown in Figure 6.4.

6.2.4 Sealing Flange Sliding Pin Assembly

The Sealing Flange Sliding Pin Assembly provides leak tightness on either ends of the test section and facilitates free sliding of FPS, if required, due to thermal expansion. The Drawing of the Assembly is shown in Figure 6.5.

The assembly consists of a set of three flanges and a sealing stud. The Weld-Neck Flange is welded to the end of the test section pipe. The Closing Flange is a blind flange that closes the Weld-Neck Flange. Holes are drilled through the Closing Flange according to the FPS locations for the FPS to come out. The Sealing Studs are then slid over the protruding portions of FPS. The Sealing Studs are pressed against the counter bores in the Closing Flange by means of the Sealing Flange. Graph-oil is added to the counter bores of Sealing as well as

Closing Flanges to ensure leak tightness.

6.2.5 Steam Supply Assembly

The steam supply assembly consists of a table top steam generator, a pump and a water storage tank. The steam generator is capable of delivering steam at atmospheric pressure with $40^{\circ}C$ superheat at a fixed flow rate of 4 g/s . The temperature of the steam entering into the test section is measured with a thermocouple.

6.2.6 Water Supply Assembly

The water supply assembly consists of a water storage tank, a low flow high head centrifugal pump and a flow meter. Water is injected into the test section through the flow meter. The assembly is capable of supplying water at a maximum flow rate of 50 g/s . The temperature of water flowing into the test section is measured using a thermocouple near the inlet of the test section.

6.2.7 Exhaust Assembly

The steam/water mixture that flows out of the test section is collected into an outlet header. The mixture flows through a U-seal that separates entrained water droplets from steam. The separated steam is dumped into a tank filled with water to prevent steam discharge into the atmosphere. The dump tank has a provision to drain and replenish the inventory to cater to the heat load. The entrained water droplets are collected in a measuring flask for carryover flow measurement.

6.2.8 Power Supply Assembly

The power supply assembly consists of a high current low voltage AC power supply of 60 kW capacity capable of supplying maximum of 2000 A current and a set of aluminium bus bars and copper connecting cables. The Tungsten rods protruding

through the Sealing Flange Sliding Pin assembly are inserted into copper discs with holes corresponding to heater pin locations. Tungsten rods are silver brazed to the copper discs to achieve proper electrical contact. The configuration of copper discs on both the sides is shown in Figure 6.6. The copper discs are connected to aluminium bus bars through copper connecting cables. Fans are provided in the vicinity of copper discs to ensure sufficient cooling through forced air circulation to maintain the copper discs temperature below $50^{\circ} C$.

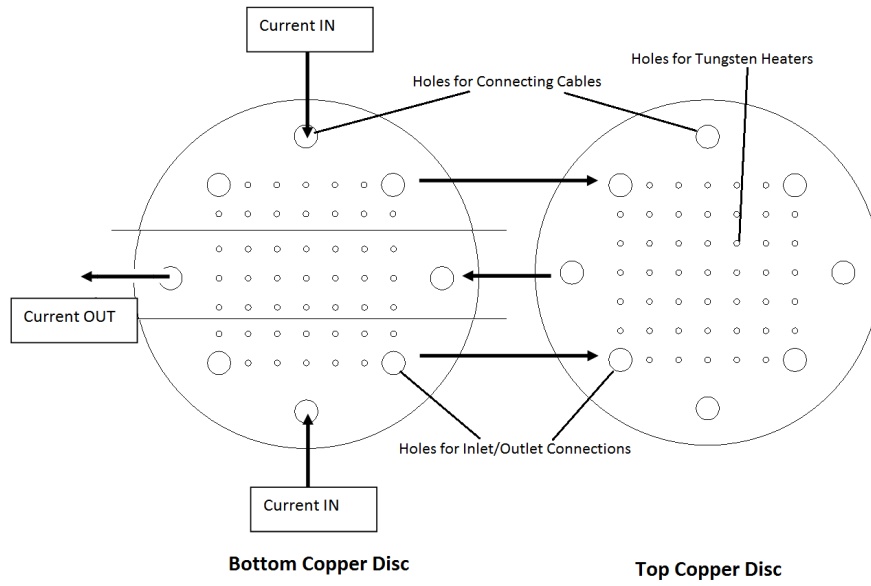


Figure 6.6: Configuration of Copper Discs used as Connecting Bus Bars indicating Current Flow Direction

6.2.8.1 Evaluation of Power Supply Parameters

Nominal power rating for a typical PWR fuel pin is $14 kW/m$. For FPS of 2m in length the nominal power rating is $28 kW$; 1% of the nominal power has been assumed for decay heat simulation in the test setup. Hence power requirement for a FPS is $280 W$. 45 out of the 57 FPS are heated FPS. Hence total power requirement of the test setup is $12.6 kW$. Considering 50% extra power capacity to account for losses, the maximum power requirement of the test setup is $19 kW$. The configuration of heated pins has been shown in Figure 6.7.

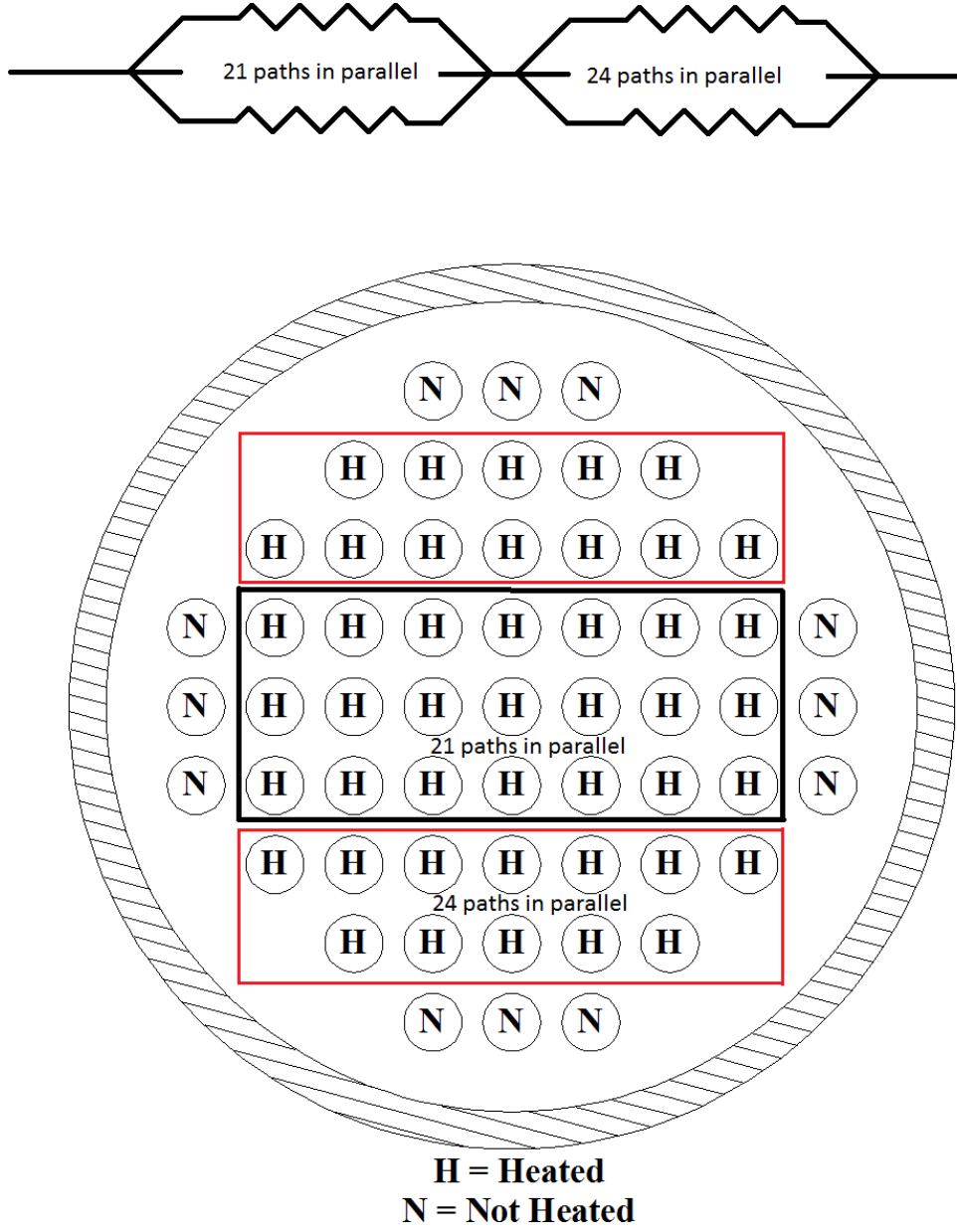


Figure 6.7: Electrical Configuration of Heated FPS

Theoretical resistance of single heater pin at room temperature:

$$R = \frac{\rho l}{A} \quad (6.1)$$

$$R = \frac{5.6e - 8X2}{7.068e - 6} \quad (6.2)$$

$$R = 15.8m\Omega \quad (6.3)$$

However, the actual resistance of single heater pin was found to be $10\text{ m}\Omega$. The effective resistance for the network of pins is $0.892\text{ m}\Omega$ at 30^0 C . The heater pins are expected to reach 1000^0 C during the experiment. The effective resistance is calculated to be $5.35\text{ m}\Omega$ at 1000^0 C . Hence the current and voltage requirement for the setup at different temperatures are as shown in Table 6.3.

Table 6.3: Power Supply Parameters

Temperature	Effective Resistance	Current	Voltage
30^0 C	$0.892\text{ m}\Omega$	4615 A	4.11 V
1000^0 C	$5.35\text{ m}\Omega$	1884 A	10.08 V

The power supply used for the experiments can provide 2000A maximum current. Hence the setup is heated at low power to start with and power is increased as the heater rod resistance increases due to rise in temperature.

6.2.9 Instrumentation

The test setup is instrumented with several instruments for measuring various parameters. The list of the instruments used, range, accuracy and their purpose are given in Table 6.4. The details of calibration of instruments are provided in Appendix A and the uncertainties in calculated quantities are mentioned in

Appendix B

6.2.9.1 Thermocouple Location Maps

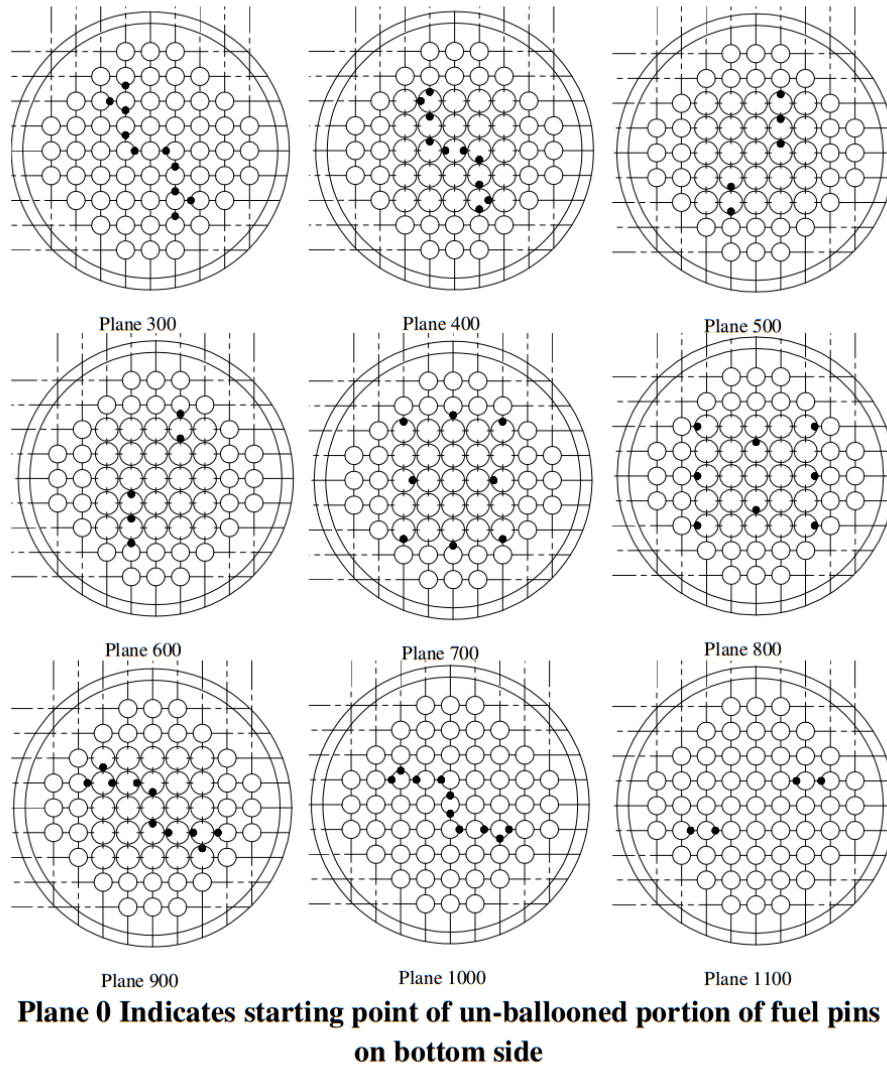


Figure 6.8: Thermocouple Locations Map

Thermocouples are mounted at several locations on the straight as well as ballooned FPS to facilitate measurement of temperature. K-type thermocouples with 0.5 mm diameter SS clad have been used. The thermocouples have been fixed by spot-welding technique so that they remain welded to the surface at

temperatures of the order of 800°C . The locations of thermocouples have been chosen to be spanning entire cross-section of the test setup. Figure 6.8 shows the thermocouple location maps at different elevation planes and locations of these planes have been shown in Figure 6.9. Plane XXX corresponds to a plane at a distance of XXX mm from the non-ballooned portion on the bottom side of straight FPS. The planes span ballooned as well as non-ballooned region of the Central Segment of the FPS.

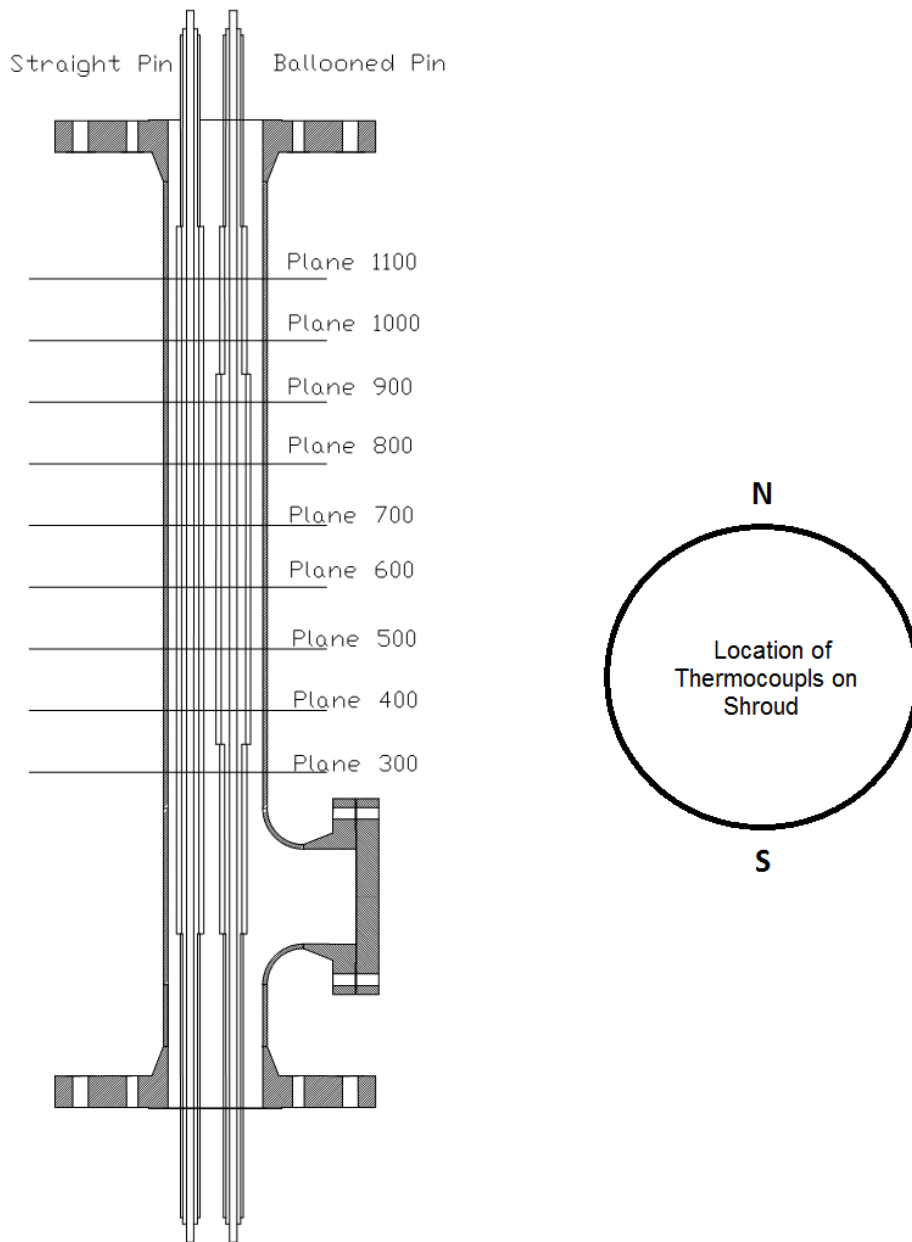


Figure 6.9: Thermocouple Location Planes

Table 6.4: List of Instruments

Measurement of	Location	Instrument/ Sensor	Make/ Model	Range	Accuracy
Water Level within the Test Section	On the Test Section	Level Transmitter	Siemens SITRANS P DS III	0 – 5m	0.001m
Inlet Water Flow Rate	At water inlet to inlet manifold	Glass Tube Flow meter	Tansa GTR-Tx	0 – 50g/s	1g/s
Temperature of Inlet Water	At inlet manifold	K-type Thermocouples	Balmer Make	0 – 1300°C	+/-1%
Temperature of Exit Fluid	At exit manifold	K-type Thermocouples			
Clad Surface Temperature	In the grooves over FPS surface	K-type Thermocouples			
Shroud Surface Temperature	Outer surface of shroud	K-type Thermocouples			

The thermocouple ends are taken out from the side flange assembly. The side flange assembly houses a number of thermocouple plugs. Figure 6.10 shows drawing of the thermocouple plug. Each of these plugs can accommodate 8 to 9 thermocouples. These thermocouple plugs are sealed to these plugs by brazing. Thermocouple locations details are provided in Appendix C.

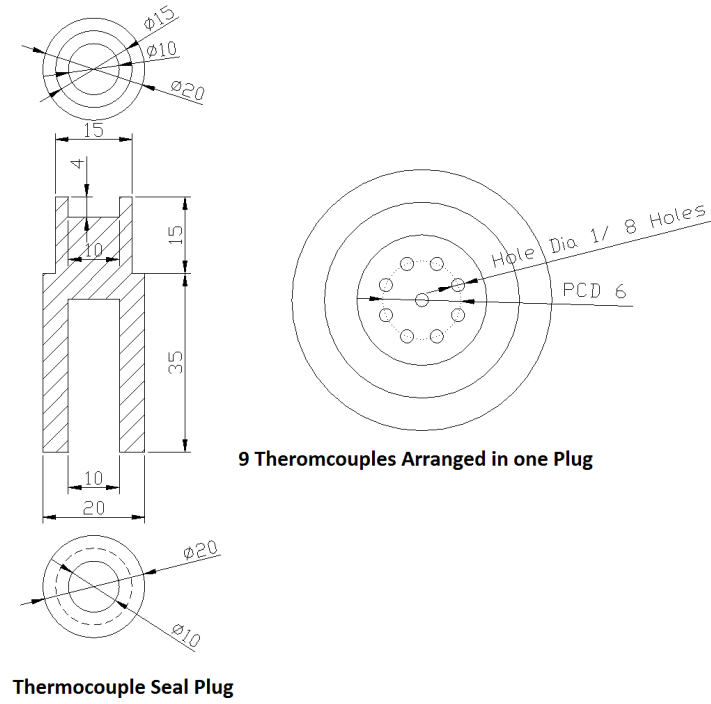


Figure 6.10: Thermocouple Plug

6.3 Fabrication of the Experimental Setup

The SS clads are cut to required lengths and longitudinal grooves are cut on the clads to facilitate mounting of thermocouples. The FPS are assembled by inserting alumina sleeves of appropriate dimensions over the tungsten rods. The assembly is then inserted into SS clad. Steps in the SS clad at the locations of change in diameter are welded together with overlapping joint to prevent any ingress of coolant into the FPS. These weld joints are tested by Dye Penetration test to detect any surface flaws in the joints.

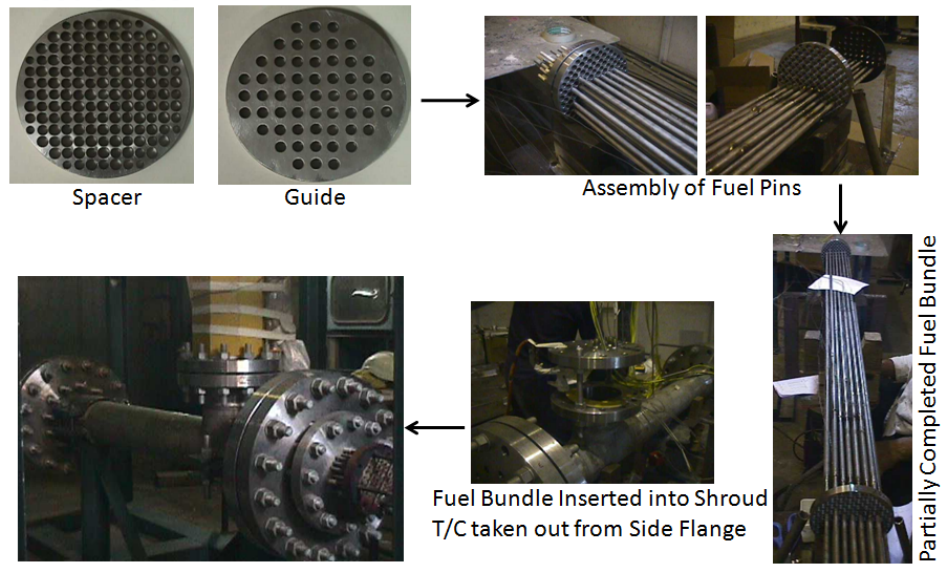


Figure 6.11: Stages of Test Section Fabrication

The FPS are then arranged in a matrix bound together at either end with the help of Spacer Disc and Guider pair. FPS are inserted one by one into the matrix and thermocouples are spot welded at appropriate location on the FPS. The guider discs are then removed. The test section is prepared by welding together weld-neck flanges to the ends of 150 mm SS pipe. The assembled FPS matrix is then inserted into the pre-fabricated test section. The thermocouple ends are taken out through the seal plugs on the side flange. The test section is then closed on both sides with the help of closing flange, such that the FPS ends protrude out through the closing flange. Seal studs are then inserted over each FPS at both ends. Sealing flange is then inserted over the seal studs to make the assembly leak tight. Copper bus bars are then brazed to the tungsten rod ends. The thermocouples are checked at every step of assembly for possible damages. The test section is mounted on a stand that can support its transportation in horizontal position as well as its erection in vertical position for experiments. Various stages of fabrication are delineated in Figure 6.11. Figure 6.12 shows the erected experimental setup.



Figure 6.12: Photograph of the DRCRE Test Section

Chapter 7

Experimental Results and Discussion

Several experiments are performed to study the quenching behavior of a partially degraded core. The parameters selected for the experiments, the experimental procedure, salient results of the experiments, discussion on effect of each parameter and the development of correlations from the experiments are presented in this chapter.

7.1 Matrix of Experimental Parameters

To study the quenching patterns for partially degraded core three parameters are selected, namely, the initial average FPS temperature, water injection rate and the input power. Table 7.1 shows the range of values considered for these parameters.

The initial average FPS temperature is varied from $260^{\circ}C$ to $650^{\circ}C$. The lower value of the range is selected to be higher than the Leidenfrost Temperature. Since the thermocouples as well as the FPS clad are made up of SS, temperatures higher than $650^{\circ}C$ are detrimental for the thermocouple and FPS clad. This limits the upper-most value for initial average FPS temperature.

Under severe accident conditions the amount of water actually reaching the

reactor core is uncertain and is expected to be lower than the SAMG injection rates. Moreover, several studies have been reported in literature for higher injection rates. Hence a range of lower injection flow rates is selected. The lowermost injection rate is selected to be higher than that derived from thermodynamics as explained in Section 5.2.

Table 7.1: Matrix of Experimental Parameters

Water Injection Rate (g/s)	Initial FPS Average Temperature									
	260 ⁰ C			325 ⁰ C			390 ⁰ C		650 ⁰ C	
	Input Power (% of Full Power)									
10	0	0.5	1.0	0	0.5	1.0	0	0.5	1.0	1.0
16	0	0.5	1.0	0	0.5	1.0	0	0.5	1.0	1.0
25	0	0.5	1.0	0	0.5	1.0	0	0.5	1.0	1.0
40	0	0.5	1.0	0	0.5	1.0	0	0.5	1.0	1.0

The experiments with 0% power are performed to study the effect of stored heat on the quenching patterns. The higher limit on input power is based on the decay heat expected at the time of injection.

7.2 Experimental Procedure

The following experimental procedure is adopted for all experiments:

1. The power supply to the instruments and the data logger is switched on.
2. Venting of Level Transmitter and filling of cold leg is carried out to ensure zero level in the level transmitter.
3. The power supply to the FPS heaters is switched on.

4. The test section is heated to about 140°C by passing superheated steam through the test section. This also helps in driving out air from the test section.
5. Power is increased in steps till required steady state with initial average FPS temperature as per the test matrix is achieved.
6. The power is increased in single step to pre-selected value as per the test matrix. The water injection to the test section is started simultaneously and the flow rate is regulated at a pre-selected value as per the test matrix.
7. The power to the test section is switched off when the injected water flows out through the exit line ensuring complete filling of the test section. It is ensured that all thermocouples show completion of quenching before the power is switched off.
8. The water injection to the test section is stopped and the test section is allowed to cool down.

7.3 Characterization Experiments

7.3.1 Heat Loss Experiments

Heat loss experiments are carried out to estimate the heat loss from the test section through the insulation. The experimental setup is heated with a constant power input till a steady state FPS average temperature is obtained. Table 7.2 details the power input to the test section, the FPS average temperature, Shroud average temperature and estimated natural convection heat transfer coefficient obtained during the experiment.

Table 7.2: Estimation of Heat Loss from DRCRE Setup

Test No.	Avg. FPS Temp. ($^{\circ}C$)	Avg. Shroud Temp. ($^{\circ}C$)	Input Power(W)	Estimated HTC (W/m^2K)
1	260	135	996	6.52
2	325	224	1256	6.64
3	390	281	1813	7.75
4	500	407	2673	8.57
5	600	510	3849	10.17
6	650	538	5575	13.40

Using Churchill and Chu's correlation, natural convection heat transfer can be evaluated as:

$$h_{natconv} = \left[0.824 + Ra^{1/6} \left(\frac{\left[1 + \left(\frac{0.5}{Pr} \right)^{9/16} \right]^{-16/9}}{300} \right)^{1/6} \right]^2 \frac{k}{L} \quad (7.1)$$

where the characteristics length L is the height of the cylindrical portion of the experimental setup. The heat transfer coefficient of $18.73W/m^2K$ is obtained from above equation. Using the insulation thickness of 5 mm over 150 mm shell and thermal conductivity of $0.04W/mK$, the overall heat transfer coefficient can be calculated as:

$$\frac{1}{h} = \frac{1}{h_{natconv}} + \frac{r_2 \ln(r_2/r_1)}{K_{insulation}} \quad (7.2)$$

The calculated overall heat transfer coefficient for test no. 1 is 6.27 which is very close to the estimated heat transfer coefficient in Table 7.2.

7.3.2 FPS Characterization Experiments

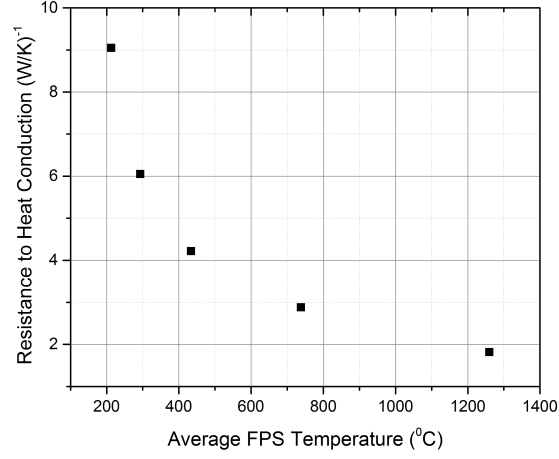


Figure 7.1: Internal Resistance to Heat Conduction within FPS

The characterization of FPS is carried out to estimate the resistance to heat conduction from the tungsten heater rod to the SS clad through alumina pellets as a function of FPS average temperature. A single FPS is heated in ambient conditions till pseudo steady-state is achieved. The tungsten rod temperature as well as FPS clad temperatures were measured using thermocouples at three different axial locations. The total heat generation within the FPS is then used to calculate the resistance to heat conduction within the FPS. Figure 7.1 shows the variation of average FPS internal resistance to heat conduction as a function of FPS average temperature.

7.4 Initial Conditions for Experiments

Table 7.3 enlists the input parameters used for the DRCRE experiments.

Table 7.3: Input Parameters for DRCRE Experiments

Sr. No.	Test No.	Initial Avg. FPS Temp. ($^{\circ}C$)	Water Injection Rate (g/s)	Input Power (% of Full Power)
1	21	260	40	0
2	47	260	25	0
3	20	260	16	0
4	19	260	10	0
5	9	325	40	0
6	10	325	25	0
7	46	325	16	0
8	11	325	10	0
9	16	390	40	0
10	17	390	25	0
11	45	390	16	0
12	18	390	10	0
13	25	260	40	0.5
14	26	260	25	0.5
15	24	260	16	0.5
16	27	260	10	0.5
17	12	325	40	0.5
18	7	325	25	0.5
19	23	325	16	0.5
20	38	325	10	0.5

21	13	390	40	0.5
22	14	390	25	0.5
23	22	390	16	0.5
24	37	390	10	0.5
25	28	260	40	1.0
26	29	260	25	1.0
27	30	260	16	1.0
28	36	260	10	1.0
29	33	325	40	1.0
30	31	325	25	1.0
31	39	325	16	1.0
32	57	325	10	1.0
33	41	390	40	1.0
34	50	390	25	1.0
35	52	390	16	1.0
36	53	390	10	1.0
37	59	650	40	1.0
38	60	650	25	1.0
39	61	650	16	1.0
40	62	650	10	1.0

7.5 Discussion of a typical Quenching Experiment

A typical quenching experiment (Test no. 31 in Table 7.3) with initial average FPS temperature of 325°C , injection flow rate of 25g/s and input power of 1% is selected for discussion. The power input to the test section is shown in Figure 7.2. It can be seen that the power input required for achieving steady state average FPS temperature of 325°C is about 1.3 kW. The radial and axial temperature profiles in the DRCRE setup are shown in Figure 7.3 and Figure 7.4 respectively. The initial average FPS temperature is above the Leidenfrost temperature. The input power is increased to 11kW at $t = 0\text{ s}$ after achieving steady state average FPS temperature. Injection of water is also initiated simultaneously at an injection flow rate of 25g/s (1.5 lpm) as shown in Figure 7.5.

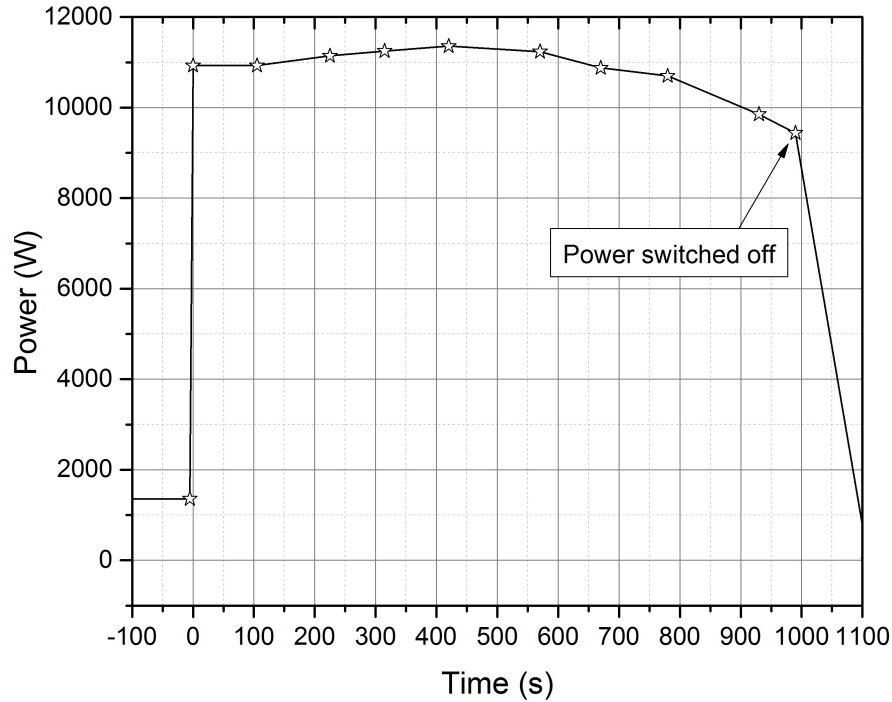


Figure 7.2: Power Input to the Test Section
(P = 1% Full power, Injection Rate = 25 g/s , Initial avg. FPS T = 325°C)

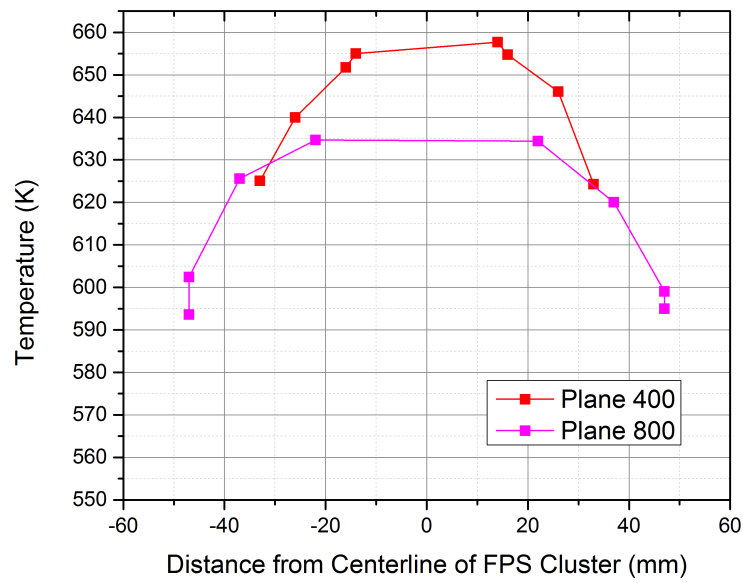


Figure 7.3: Radial Temperature Profile
(P = 1% Full power, Injection Rate = 25 g/s, Initial avg. FPS T = 325°C)

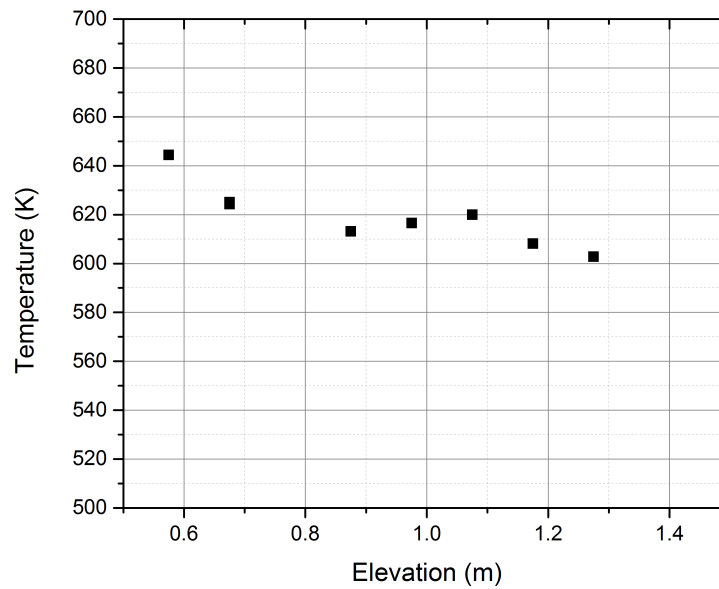


Figure 7.4: Axial Temperature Profile
(P = 1% Full power, Injection Rate = 25 g/s, Initial avg. FPS T = 325°C)

The temperature transient as measured by thermocouples located at different planes is shown in Figure 7.6. The region of the test setup instrumented with thermocouples is located 575 mm from the inlet of the test section. Hence it takes sufficient time for the injected water to reach the instrumented region within the test setup. As the water injection is started, the injected water comes in contact with hot and dry external surface of FPS as well as the internal surface of shroud in the lower end segment region. Because of the heat received from these surfaces, water temperature increases to saturation temperature and boiling starts. Steam generated in this process flows over the FPS, in the upward direction towards the exit of test section. However, cooling caused by this steam flow is not sufficient to remove the simulated decay heat. Thus, the temperature of the instrumented portion of FPS continuous to rise.

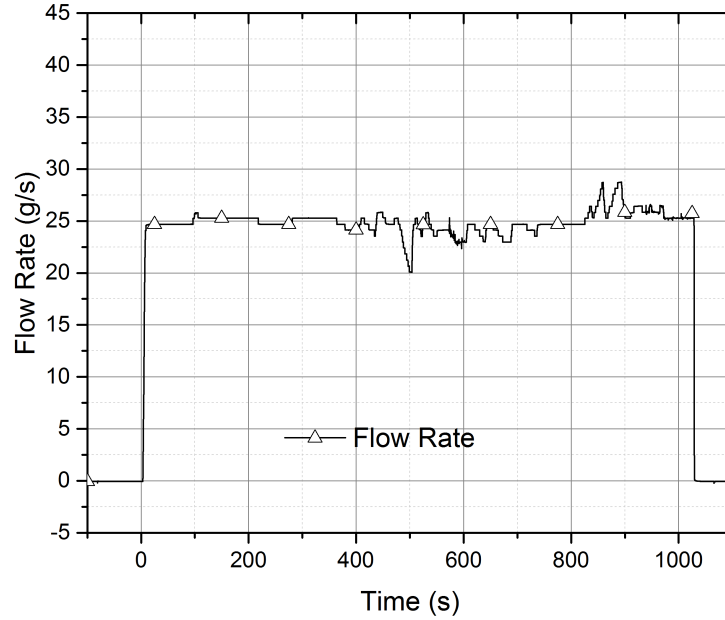
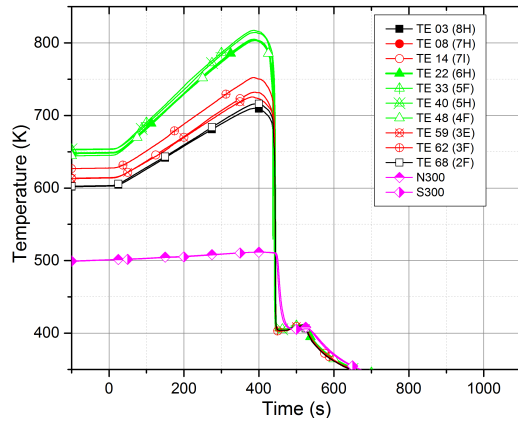
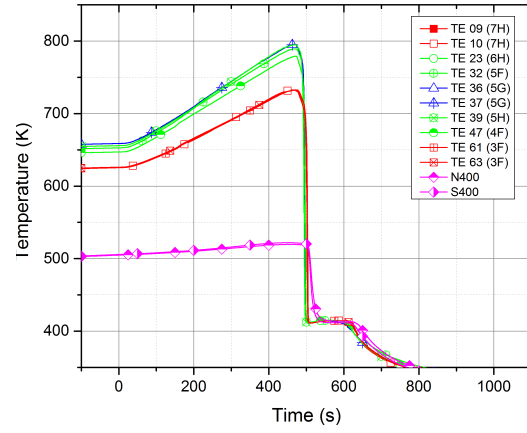


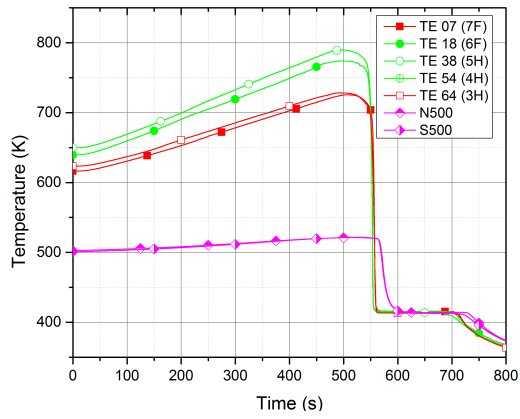
Figure 7.5: Water Injection Rate
(P = 1% Full power , Injection Rate = 25 g/s, Initial avg. FPS T = 325°C)



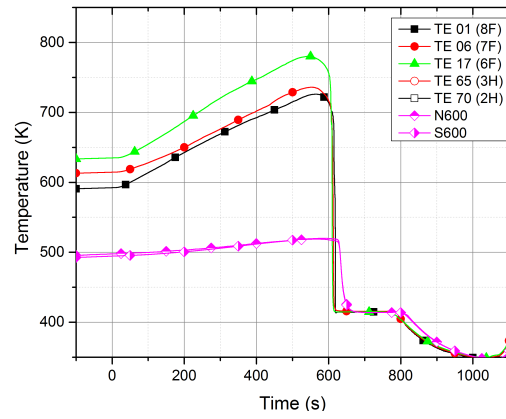
(a) Plane 300



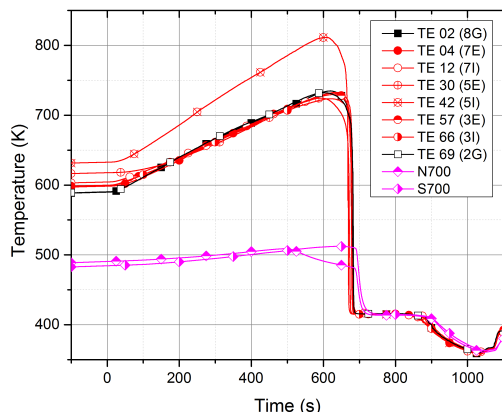
(b) Plane 400



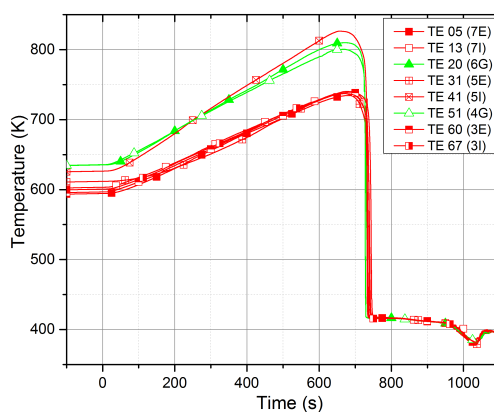
(c) Plane 500



(d) Plane 600



(e) Plane 700



(f) Plane 800

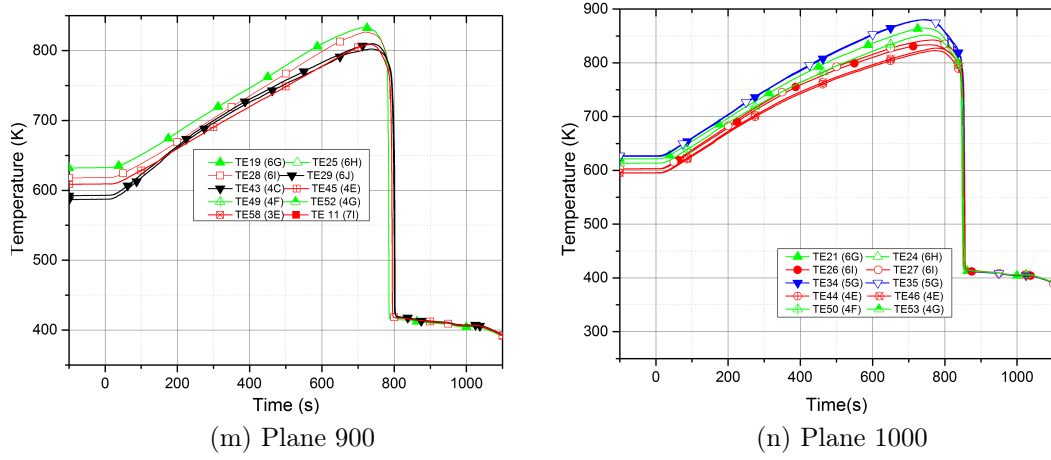


Figure 7.6: Temperature Transient at Different Planes along the Test Section Length

As the water level in the test section approaches the central segment of FPS, the rate of rise of FPS temperature reduces, suggesting improvement in heat transfer coefficient. The clad temperatures at this moment are significantly higher than the Leidenfrost temperature. Further rise in the water level causes initiation of quenching, resulting in sharp fall in the temperatures. Quenching starts at a later time for upper elevations as indicated by the thermocouple measurement. The FPS temperature just before the initiation of quenching is thus higher at upper elevations. Successful initiation of quenching even at higher temperature suggests that the contact between the FPS clad and liquid coolant is established. This is possible only if the axial conduction through the FPS clad is able to reduce the FPS temperature below the Leidenfrost temperature. Presence of axial conduction also indicates that this is a case of “Conduction controlled” re-wetting.

It can be observed that at a given axial location, the quenching of FPS in the central as well as peripheral region happens within a time span of 20-25 s from each other. This suggests that cross-flow created by blockages does not significantly affect the time of quenching of central and peripheral FPS, for the injection rate of 25 g/s. It is shown in the later sections that the cross-flow effects are more pronounced for lower injection rates and tend to affect the quenching of

central and peripheral FPS. The quenching of shroud at that axial location also takes place simultaneously. The test pressure transient is shown in Figure 7.7. Sharp rise in the pressure is seen starting from 375 s. At this time of the transient, the quench front moves from the lower non-ballooned segment into the central ballooned segment as shown in Figure 7.6(a)-(b). The central ballooned segment has higher stored energy and higher heat transfer area due to larger FPS diameter. This causes rise in the total energy being transferred to the coolant, resulting in pressure rise. Since the test setup has four nozzle of 6.35 mm diameter at the exit, continuous heat addition to the fluid causes pressurization of the test setup.

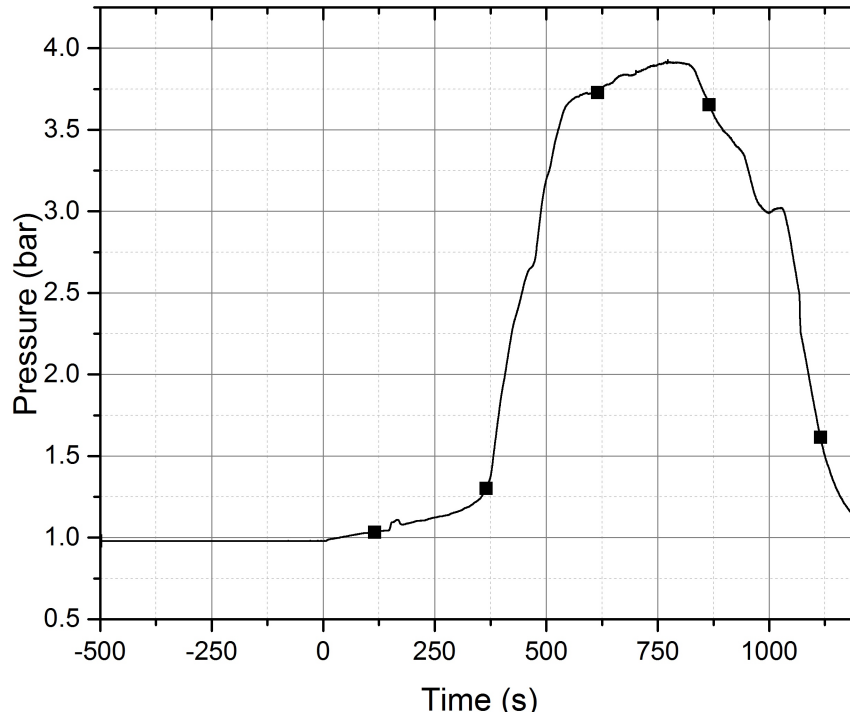


Figure 7.7: Pressure Transient ($P = 1\%$ Full power , Injection Rate = 25 g/s, Initial avg. FPS $T = 325^{\circ}C$)

The stored heat as well as decay heat content of the heater pins causes injected water to start boiling and the water eventually gets converted to superheated steam towards the exit of the test setup. The temperature measurements at the exit of the setup shown in Figure 7.8 suggest significant superheating of steam. However, not all injected water is converted to steam. The amount of water droplets collected

at the exit, also called as carryover, is shown in Figure 7.9.

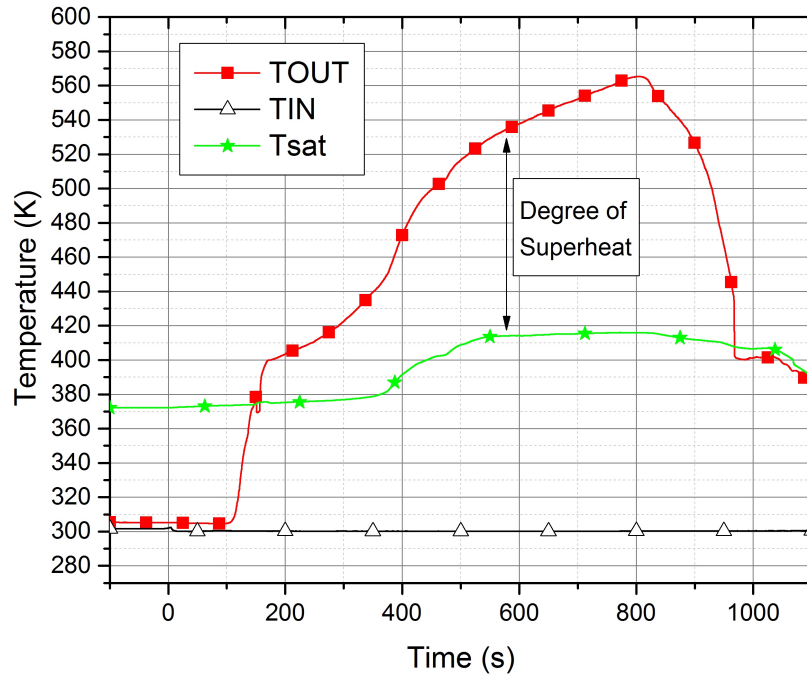


Figure 7.8: Inlet and Outlet Fluid Temperature Transient ($P = 1\%$ Full power, Injection Rate = 25 g/s, Initial avg. FPS $T = 325^{\circ}C$)

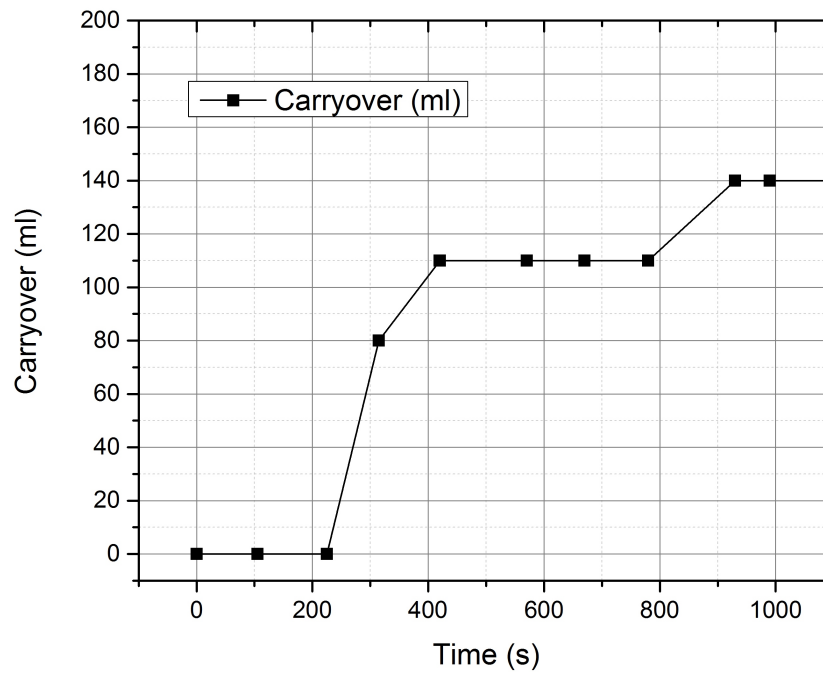


Figure 7.9: Carryover Measured at the Exit of the Setup ($P = 1\%$ Full power, Injection Rate = 25 g/s, Initial avg. FPS $T = 325^{\circ}C$)

Due to high velocity of the generated steam, small droplets of water are carried along with the steam. The droplets continue to receive heat from the nearby heated surfaces by radiation and due to convection from steam in contact. Some droplets also come in contact with the heat FPS clad surface and undergo evaporation. However, the amount of heat received is not sufficient for evaporation of all droplets. Some droplets escape the test section without getting evaporated, resulting in carryover.

It can be seen that the amount of carryover is high towards the beginning and end of the transient, i.e., when the water level is within the non-ballooned region of the test setup. The water droplets traveling through the ballooned region have more proximity with the FPS due to less flow area availability.

Hence these water droplets are more likely to come in contact with the FPS surface and receive more heat from FPS resulting in evaporation. This results in lesser carryover in the ballooned region as compared to that in the non-ballooned region.

7.5.1 Assessment of Heat Transfer Coefficient

The water injected into the test setup receives heat from the heater pins under different heat transfer regimes along the length of the heater pins. Figure 7.10 shows the behaviour of heat transfer coefficient calculated at plane 400. The heat transfer coefficient is calculated by equating the rate of change of stored energy of the SS clad to the difference of heat received from the tungsten heater rod through alumina pellets and heat transferred to coolant. This heat transfer process is represented by energy conservation equation for clad as shown in Eq. (7.3).

$$m_c C_p \frac{\partial T_c}{\partial t} = \frac{(T_{cl} - T_c)}{R_i} - h_e A_e (T_c - T_{sat}) \quad (7.3)$$

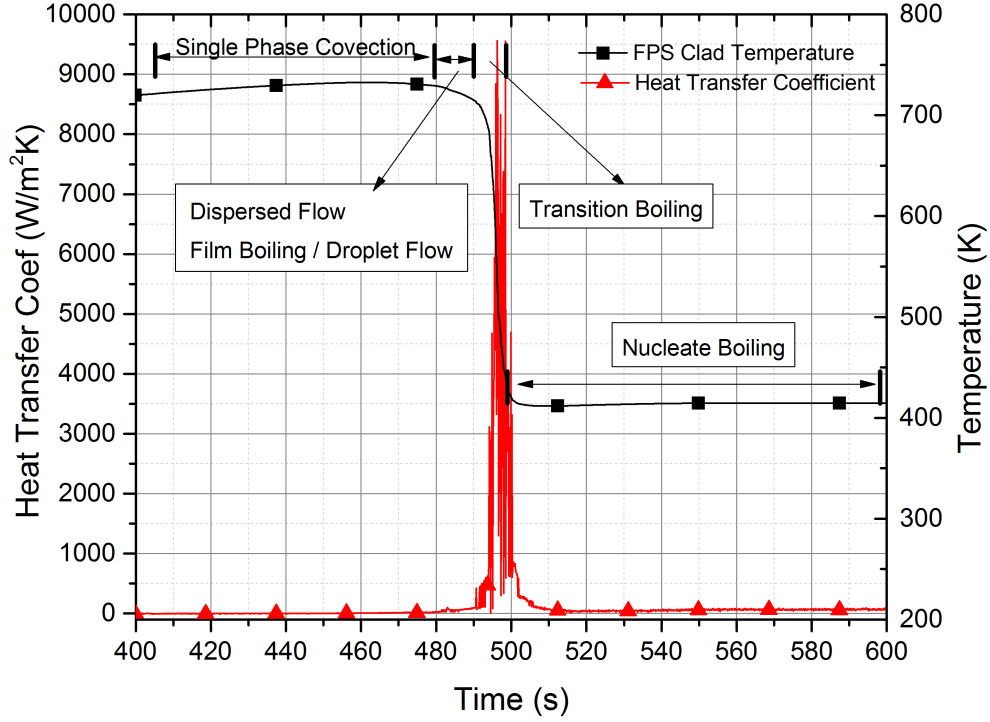


Figure 7.10: Variation of Heat Transfer Coefficient with Time at Plane 400 ($P = 1\%$ Full power, Injection Rate = 25 g/s, Initial avg. FPS $T = 325^{\circ}\text{C}$)

The resistance to heat conduction R_i from central tungsten rod to the FPS clad is obtained from the FPS characterization experiments discussed in Section 7.3.2. Hence, heat transfer from the FPS internal structures to the SS clad (first term on right hand side of Eq. (7.3)) is calculated.

Figure 7.11 shows the variation of peak heat transfer coefficient along the length of the FPS for central and peripheral regions. The peak heat transfer coefficient in the central region reduces at the entry of ballooned region length. Decrease in the available flow area at the entry of the ballooned region results in re-distribution of flow leading to reduction of fluid entering in the central ballooned region. Reduction in the amount of fluid entering in this region results in reduction of heat removal capacity during quenching. The rate of cooling of FPS is thus reduced. This causes reduction in the peak heat transfer coefficient at that location. As the quench front moves further into the ballooned region, the fluid velocity increases

due to continuous addition of heat from nearby FPS ballooned portion. This causes more and more carryover as discussed in next section. The heat transfer coefficient thus increases monotonically. In the peripheral region, the heat transfer coefficient increases at the entry of ballooned region because of increase in local fluid velocity. Thereafter, the heat transfer coefficient increases monotonically because of increase in fluid velocity due to heat addition, similar to the central region.

Near the end of ballooned region, the heat transfer coefficient reduces in the peripheral region and increases in the central region. This is because more fluid is diverted from the peripheral region into the central region causing changes in the local fluid velocities.

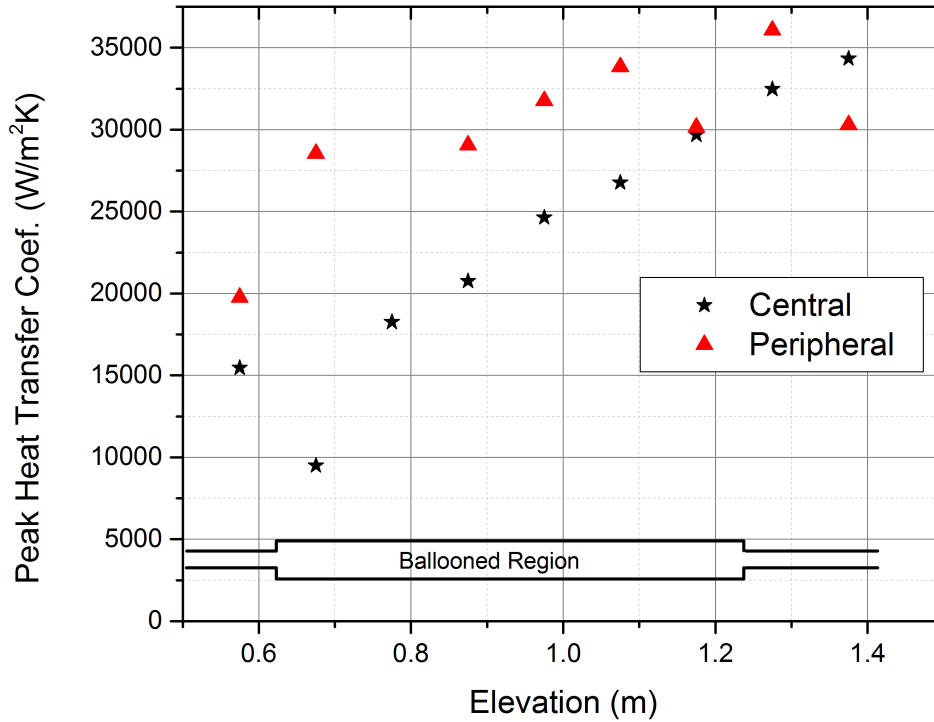


Figure 7.11: Variation of Peak Heat Transfer Coefficient along the length of FPS (P = 1% Full power, Injection Rate = 25 g/s, Initial avg. FPS T = 325°C)

7.5.2 Assessment of Quench Front Location and Quench Front Velocity

Figure 7.12 shows the collapsed water level evolution along with location of quench front. The location of the quench front is calculated based on criterion of rate of fall of clad temperature (>200 K/s) reported in literature [11]. It can be seen that the quench front is ahead of the actual water level during the entire transient, suggesting that this is a case of "Conduction Controlled" re-wetting.

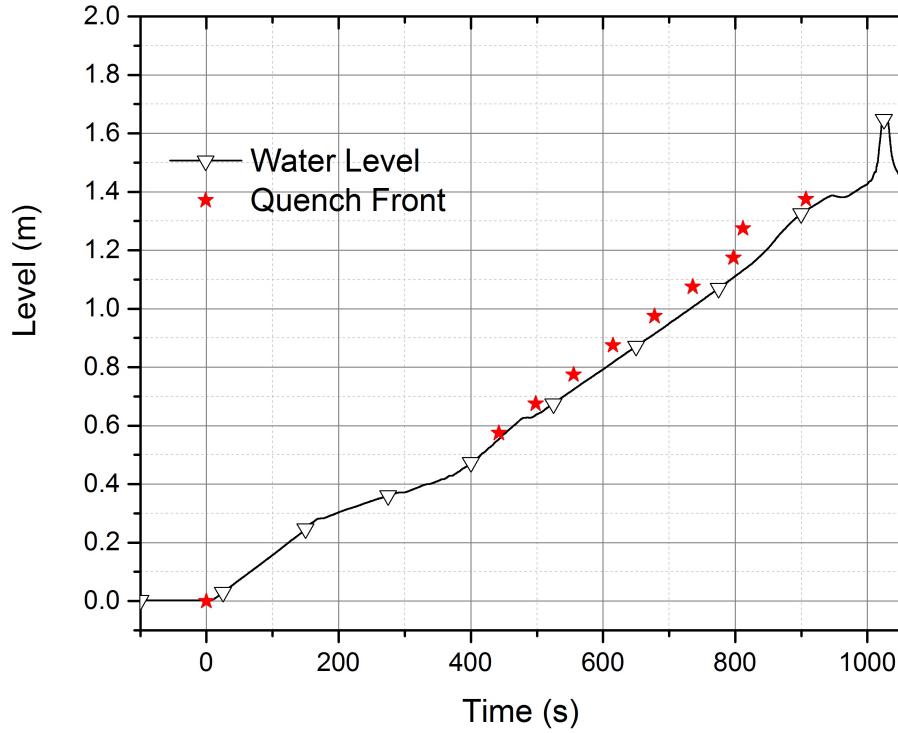


Figure 7.12: Water Level and Quench Front Location Transient (P = 1% Full power, Injection Rate = 25 g/s, Initial avg. FPS T = 325°C)

The quench front velocity is calculated by dividing the axial distance between two thermocouples by the difference in the time of arrival of quench front at that location. Thus, the quench front velocity plotted at elevation of 0.575 m is actually average quench front velocity between the elevation 0.575 m and 0.675 m. Figure 7.13 shows the variation of the quench front velocity along the length of the FPS. The quench front velocity is low in the non-ballooned region of FPS near the

entry.

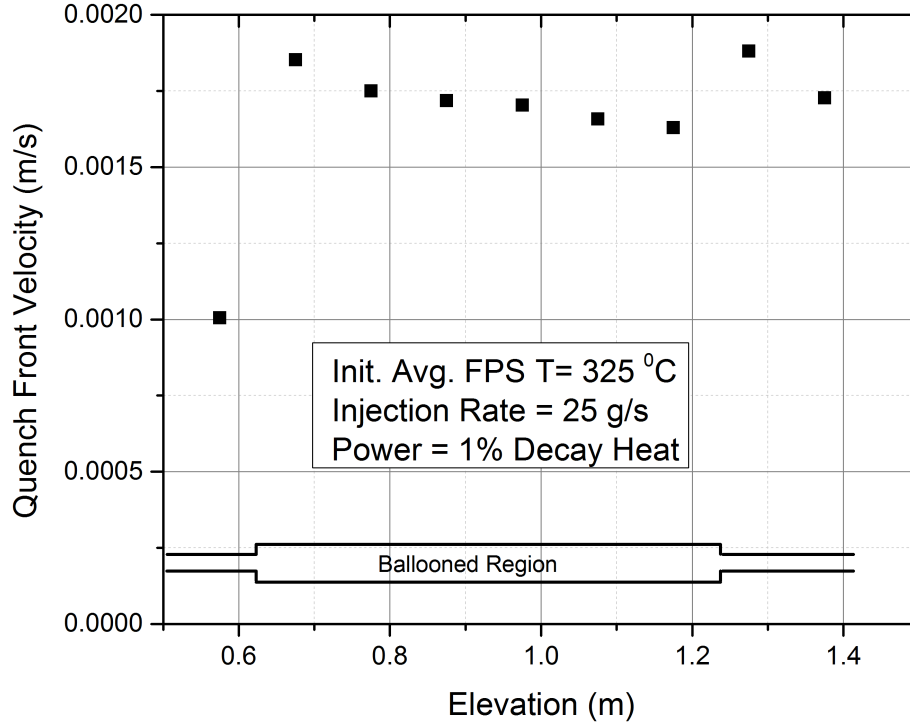


Figure 7.13: Quench Front Velocity along the Test Section ($P = 1\%$ Full power, Injection Rate = 25 g/s, Initial avg. FPS $T = 325^\circ\text{C}$)

The quench front velocity is low while entering into the ballooned region because of flow re-distribution taking place at the entry of ballooned region. As the quench front enters into the ballooned region, the quench front velocity increases. Along the ballooned length of FPS, the quench front velocity decreases continuously. As the water front travels through the ballooned region, the steam velocity ahead of the water front goes on increasing owing to continuous addition of heat. This causes an increase in the amount of droplet carryover as it is proportional to steam velocity [45] as given in Eq. (7.4).

$$E = 0.015 + 0.44 \log_{10} \left[0.9245 \left(\frac{\frac{j_g \mu_g}{\sigma} \sqrt{\frac{\rho_g}{\rho_f}}}{2.46e^{-4}} \right) \right] \quad (7.4)$$

Thus, the water front velocity and hence the quench front velocity decreases in the

ballooned region. The changes in the quench front velocity are not significant near the exit of ballooned segment. As the quench front travels out of the ballooned region, the steam velocity decreases causing reduction in carryover droplets. At the same time decrease in liquid velocity also reduces. Thus the quench front velocity is not significantly affected.

7.5.3 Effect of Initial Average FPS Temperature

Figure 7.14 shows the quenching transients obtained with different initial average FPS temperatures. Higher the average initial temperature, higher is the heat stored within the heater pins. Thus, quenching with higher average initial FPS temperature is delayed as compared to quenching with lower average initial temperature as shown in Figure 7.14.

At plane 300, the non-ballooned portion towards the entry of test setup, the quenching of central and peripheral pins happens simultaneously. As the water level rises into the ballooned region, the quenching of central pins is found to be earlier than the peripheral pins. The effect becomes pronounced at locations further up into the ballooned region. However, in the non-ballooned region towards the exit of the test setup, peripheral pins get quenched earlier than the central pins.

Taking into consideration the amount of carryover observed during quenching (Figure 7.9), when the water level is within the non-ballooned region of the test setup, more flow area is available in the central region. This facilitates easy path for the carryover droplets to escape to test setup exit without making any contact with FPS surface. As explained in the earlier section the carryover droplets tend to evaporate and enhance cooling of FPS in the ballooned region. Hence, for the duration for which the quench front is traveling through the ballooned region, carryover measurement shows reduction in amount and corresponding central zone pins are quenched earlier than the peripheral region.

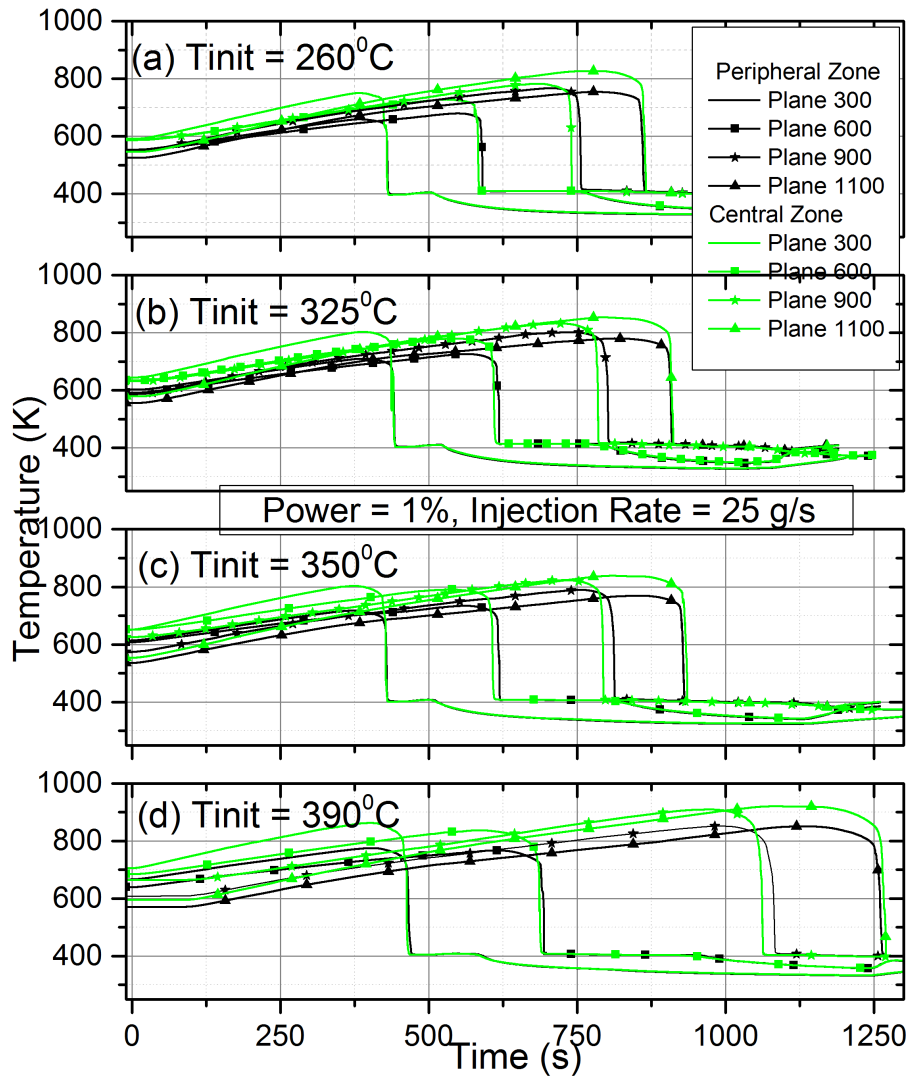


Figure 7.14: Temperature Transient at different planes with different init. Avg. FPS Temperature

Figure 7.15 shows the variation of the quench front velocity along the length of the test section for different initial average FPS temperatures. The quench front velocity is higher for the lower initial average FPS temperature case, as expected. The enhancement of quench front velocity in the ballooned region is also higher for the low temperature case due to low content of stored heat. At the exit of the ballooned region, the quench front velocity increases due to flow re-distribution.

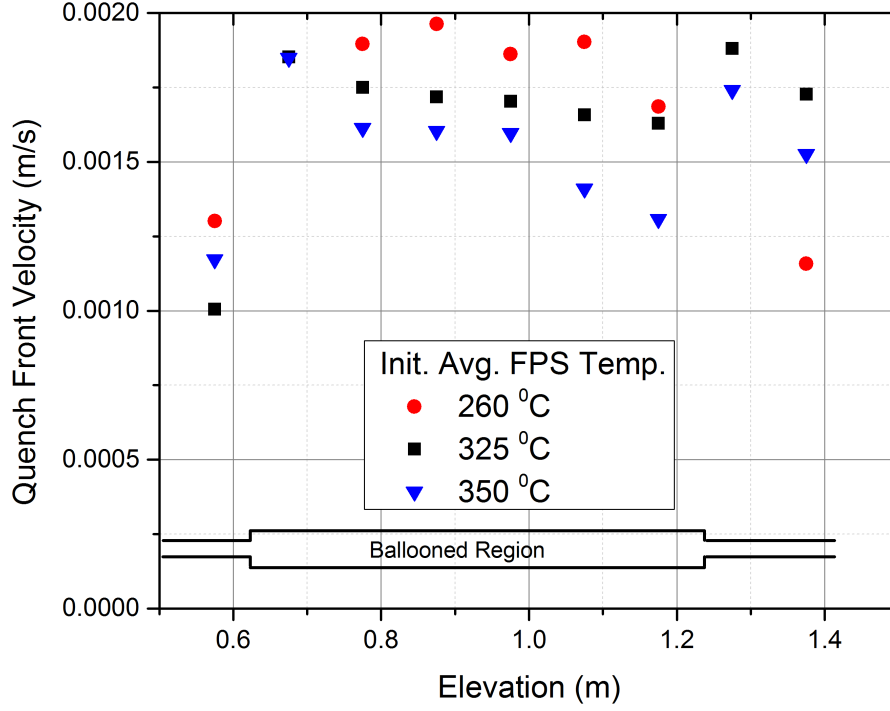


Figure 7.15: Quench Front Velocity for different Initial Avg. FPS Temperature ($P = 1\%$, Injection Rate = 25 g/s)

7.5.4 Effect of Water Injection Flow Rate

Figure 7.16 shows the quenching behavior observed with initial average clad temperature of 260°C , 1% decay power and different injection flow rates. It can be seen that as the injection flow rate reduces, the time required for quenching increases. The difference in time of quenching observed in the central and peripheral region of the core is more pronounced within the ballooned length of the FPS at lower flow rate condition and diminishes at higher flow rates. For low flow rate, the water front velocity below the quench front level as well as the steam velocity above the quench front level is lower than for the high flow rates. Hence, the water droplets flowing with steam as carryover remain in the ballooned region for longer duration. The cooling effect due to evaporation of these carryover droplets is enhanced as compared to the high flow rate condition. This results in pronounced difference in time of quenching in of central and peripheral region for low flow rate.

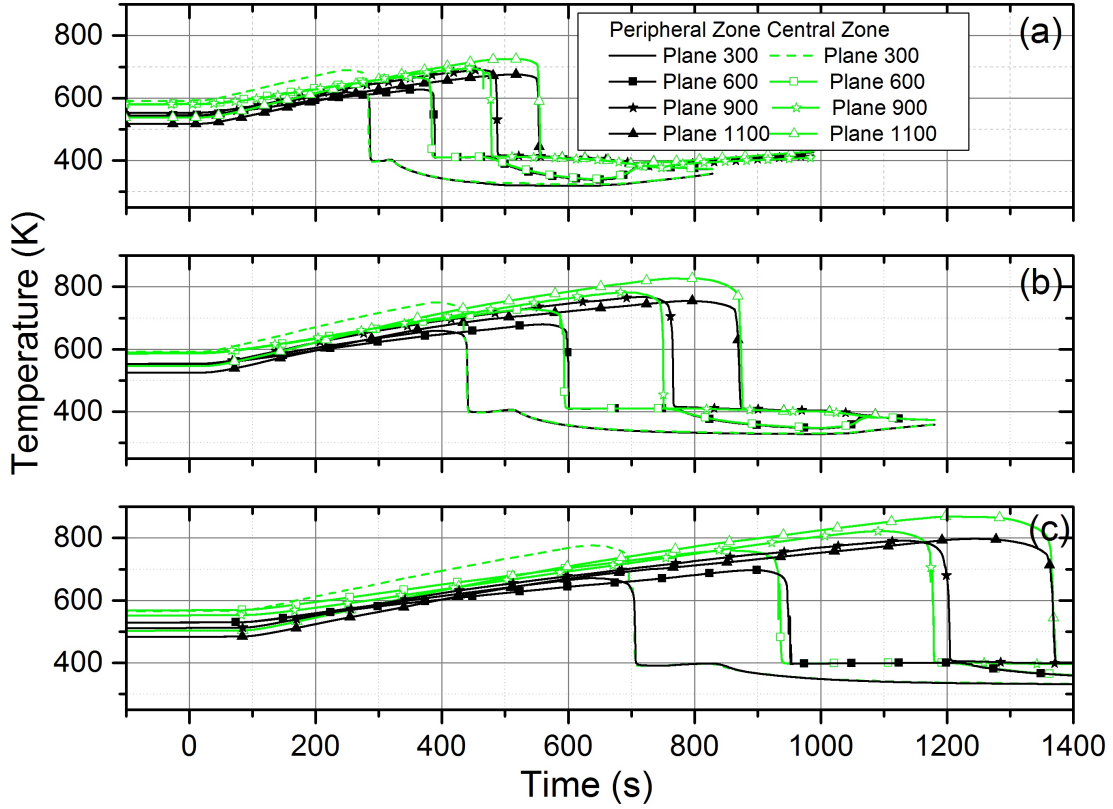


Figure 7.16: Temperature Transient at Different Planes with different Water Injection Rates (a) 40 g/s (b) 25 g/s and (c) 16 g/s ($P = 1\%$ Full power, Initial Avg. FPS Temperature 260°C)

Figure 7.17 shows the shape of the quench front across the cross-section of the test section at different axial levels for experiments with different injection rates. It can be seen in the ballooned region the quench front is ahead of that in the peripheral region. The acceleration of the quench front in the central ballooned region as compared to that in the peripheral region is prominent for lower flow rate conditions.

Figure 7.18 shows the evolution of water level and location of quench front obtained for different injection flow rates. For the lower injection flow rate viz. 10 g/s and 20 g/s, the quench front location is ahead of the water level, suggesting conduction controlled re-wetting. On the other hand, for the high injection flow rate of 40 g/s, the quench front location is at the water level.

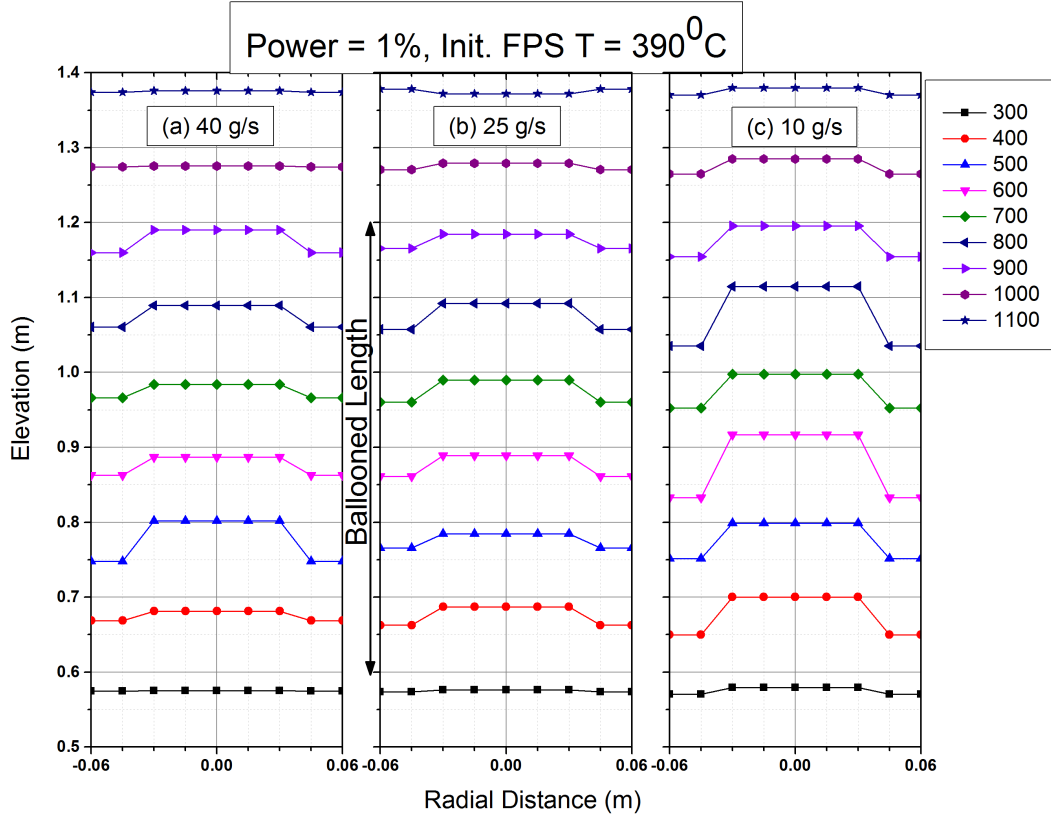


Figure 7.17: Quench Front at Different Planes with Different Water Injection Rates (a) 40 g/s (b) 25 g/s and (c) 10 g/s (P = 1% Full power, Initial Avg. FPS Temperature 260⁰C)

This indicates that with an increase in the injection flow rate, there is a tendency to move from conduction controlled re-wetting to fluid controlled re-wetting.

Figure 7.19 and 7.20 show the change in the quench front velocity with injection flow rate for experiments performed with 1% and 0.5 % decay power, respectively. The inverse of quench front velocity is plotted on the y-axis. The cold re-flood line indicates inverse of water front velocity with respect to different injection flow rates in a cold setup and without power input.

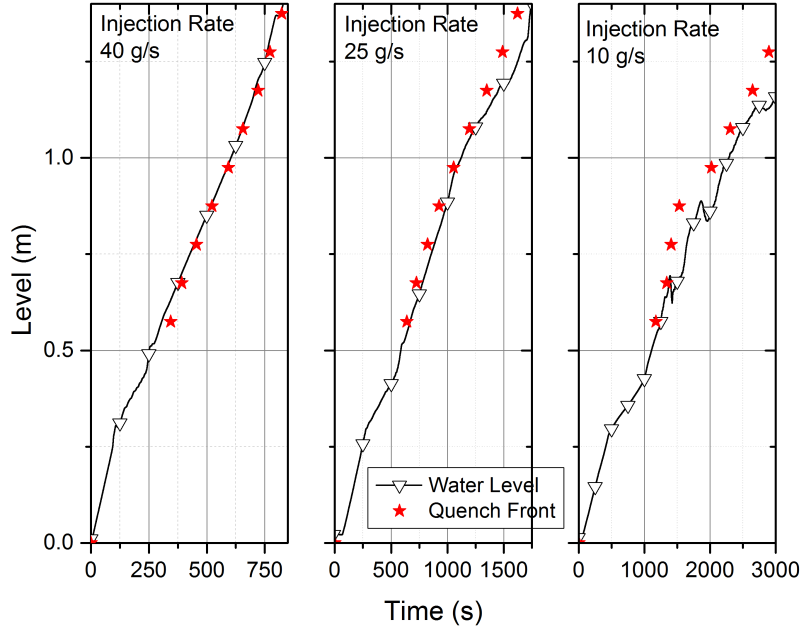


Figure 7.18: Evolution of Water Level and Location of Quench Front for different Water Injection Rates
($P = 1\%$ Full power, Initial Avg. FPS Temperature $260^{\circ}C$)

For low initial temperature conditions, the quench front velocity is found to be close to the cold re-flood condition. As the initial temperature increases, the quench front velocity reduces in comparison to the cold re-flood case. Addition of heat to the injected water causes heat up and evaporation. This is expected to result in lesser water front velocity and hence the quench front velocity as well. As we move away from the minimum injection line, towards higher injection flow rates, the conduction controlled re-wetting prevails. Figure 7.19 indicates that, with an increase in the injection flow rate the quench front velocity approaches the cold re-flood line in the conduction controlled region. However, for further rise in injection flow rate, the re-wetting pattern tends to change from conduction controlled re-wetting to fluid controlled re-wetting.

The quench front now lags behind or is at the water front, and hence the quench front velocity diverges from the cold re-flood condition. In this region as the injection flow rate increases, the quench front velocity diverges from the cold re-flood line.

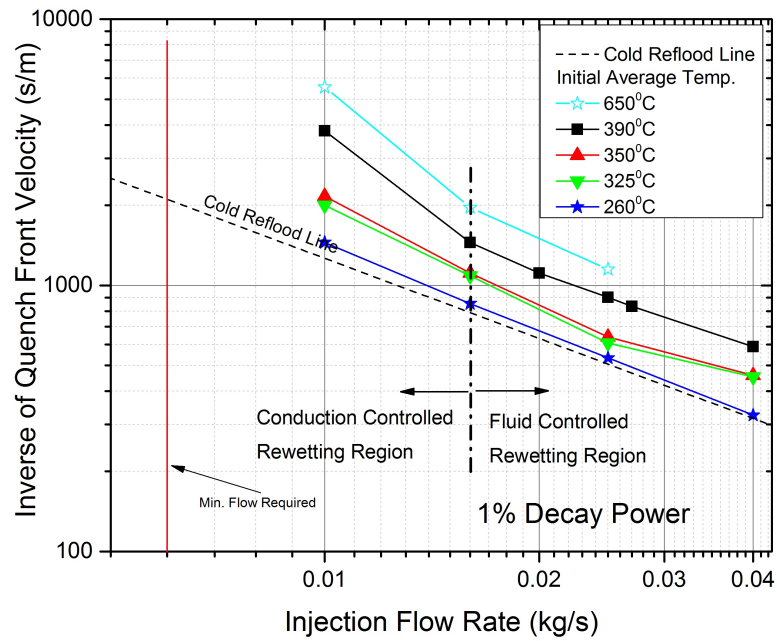


Figure 7.19: Variation of Quench Front Velocity with Injection Rate at 1% Decay Power

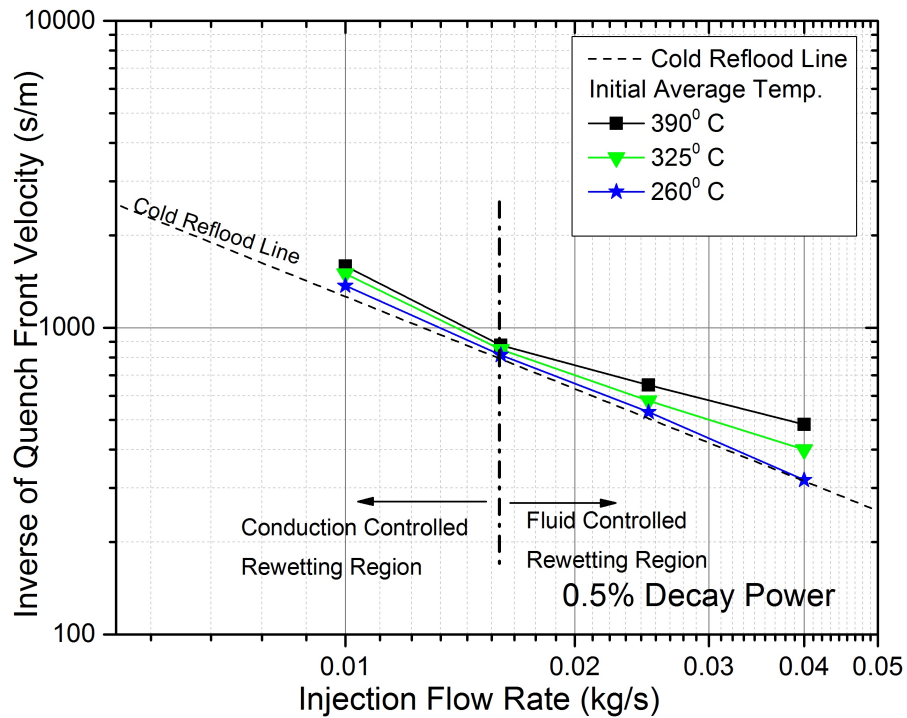


Figure 7.20: Variation of Quench Front Velocity with Injection Rate at 0.5% Decay Power

This is because in the conduction controlled region, quenching takes places from Leidenfost temperature, which is lower than the Minimum Film Boiling temperature. In the fluid controlled region, quenching takes place from the Minimum Film Boiling temperature. Hence, as the re-wetting pattern tends to change with rise in flow rate, the temperature at the start of quenching also increases. Thus, the quench front velocity tends to reduce.

Figure 7.21 shows comparison of carryover measured for different injection flow rates. The total amount of carryover is observed to be maximum for the lowest injection flow rate condition. The fraction of injection flow rate that appears as carryover is directly proportional to steam velocity [45] as given in Eq. (7.4).

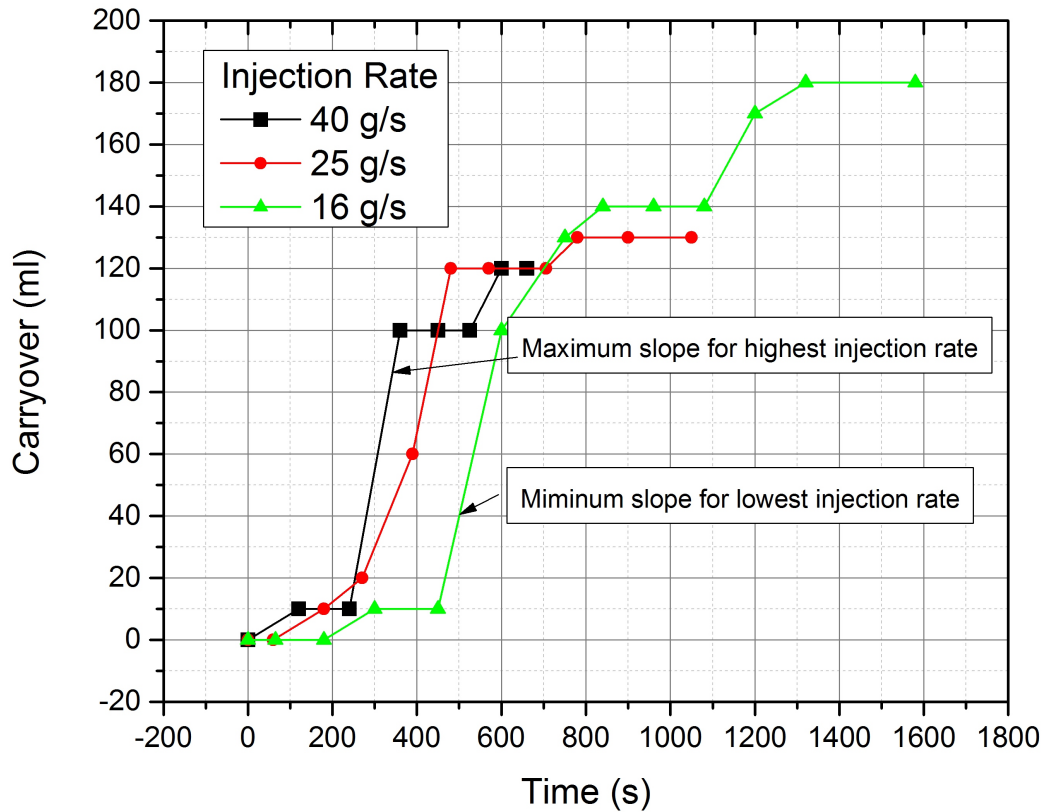


Figure 7.21: Comparative Carryover Measurements for Experiments with different Water Injection Rates

It is evident from the slope of the first rise in the carryover amount that highest slope is observed for maximum injection rate of 40 g/s. However, for the low flow

rate condition, the total time required for complete quenching of entire length of the FPS is more than that of high injection rate condition. Hence, the total carryover accumulated over the entire duration of the transient is higher for the low injection rate condition.

7.5.5 Effect of Input Power

Figure 7.22 shows the comparative behavior of FPS under quenching for different levels of input power (simulating decay heat). Figure 7.22 (a) shows the quenching pattern under zero input power. Since there is no power input to the FPS during quenching, only the stored heat is removed due to water injection.

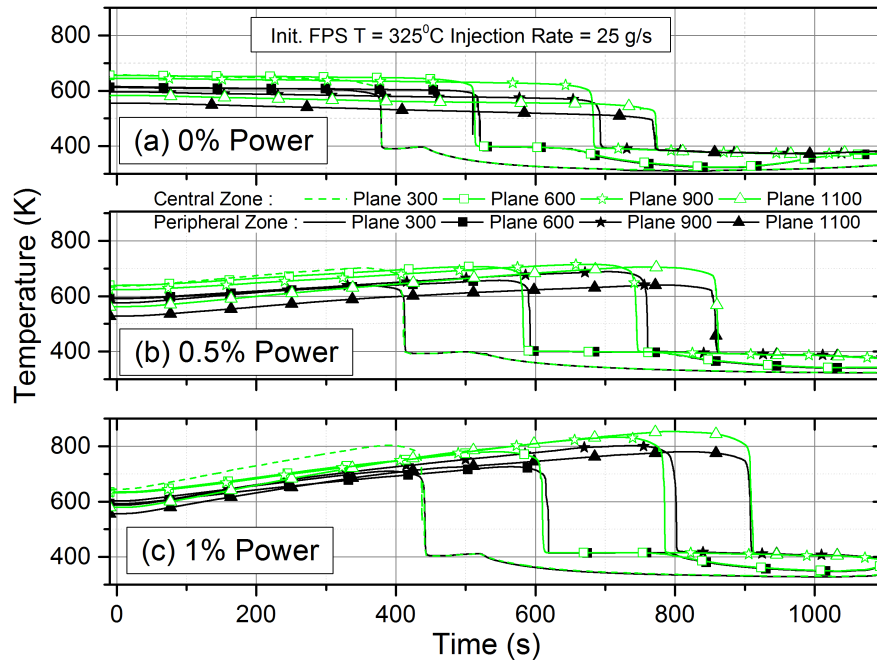


Figure 7.22: Temperature Transient at different planes with different Input Power (a) 0% Full Power (b) 0.5% Full Power and (c) 1% Full Power (Injection Rate = 25 g/s, Initial Avg. FPS Temperature 260°C)

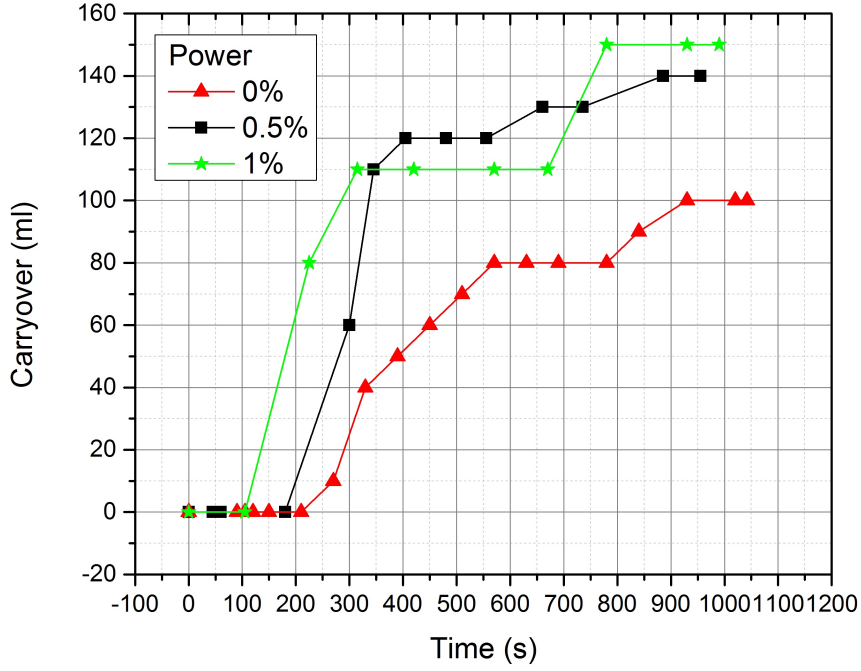


Figure 7.23: Comparative Carryover measurements for experiments with different power input

For the locations towards the exit of test setup (plane 1100), significant pre-cooling is observed prior to the water level reaching this position, owing to steam flow. As expected, the total time for quenching increases with increase in power input to the test section. Figure 7.23 indicates that carryover increases with increase in the power input to the FPS. Higher input power causes higher steam generation rate for a given water injection flow rate. This leads to higher velocities of steam within the test setup causing more droplets carryover.

7.6 Discussion on High Temperature Experiment

Typically for PWRs, the SAMG actions are invoked when the upper plenum temperature reaches 650°C . Hence, experiments are performed with 650°C as initial average FPS temperature with different injection flow rates. The objective of these experiments is to identify the minimum flow rate requirement below which the FPS temperature crosses 1000°C (threshold temperature for accelerated Zr-oxidation)

during the transient.

Figure 7.24 shows the temperature transients for different injection rates. Only the thermocouples showing maximum temperatures are selected for the sake of clarity. The maximum temperature in all three experiments is found to occur at plane 900, located just before the end of the ballooned section. It can be seen that as the injection flow rate decreases the maximum temperature increases, as expected. For the injection rate of 25g/s the temperature is limited to 1000°C, whereas, for lower injection rates the FPS temperature crosses this limit. Figure 7.25 shows the water level and the quench front locations for different injection flow rates. In all the three cases, the quench fronts are above the water level, suggesting conduction controlled re-wetting.

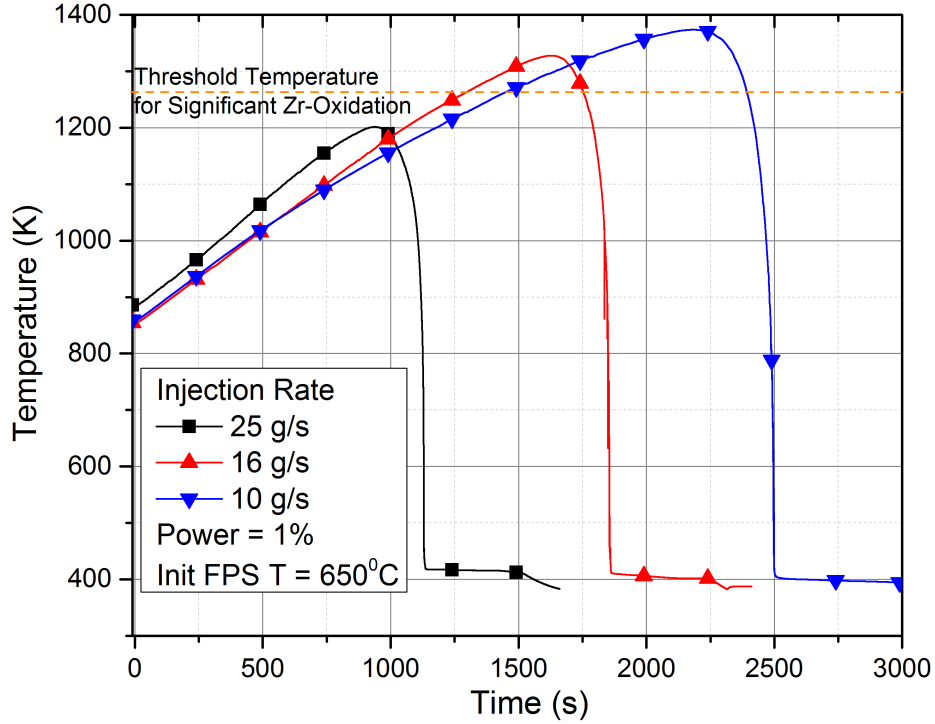


Figure 7.24: Maximum Temperature Transient for different Injection Rates

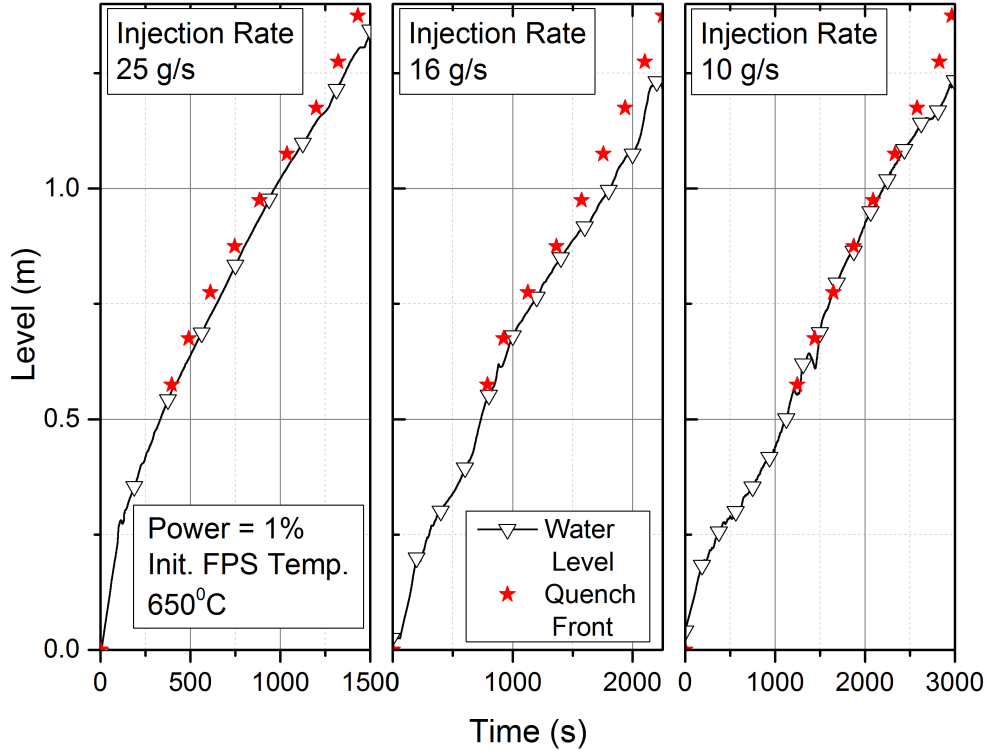


Figure 7.25: Water Level and Quench Front Location for different Injection Rates

Figure 7.26 shows FPS temperature along the length of the setup, at the time instance of 1000 s. The temperatures at bottom six locations are equal to or less than T_{ONB} temperature indicating completion of re-wetting. For the top three locations, the temperatures are much higher than the T_{MFB} suggesting that quenching has not started yet. The water level is located below the top four locations. The lowest location above the water level has cooled down significantly as compared to the top three locations. This indicates that a combined effect of accelerated steam flow above the water level and impinging carryover droplets is efficient in providing significant pre-cooling at this location. The location of T_{MFB} temperature is above the water level, confirming that the quench front location is above the water level and conduction controlled re-wetting prevails.

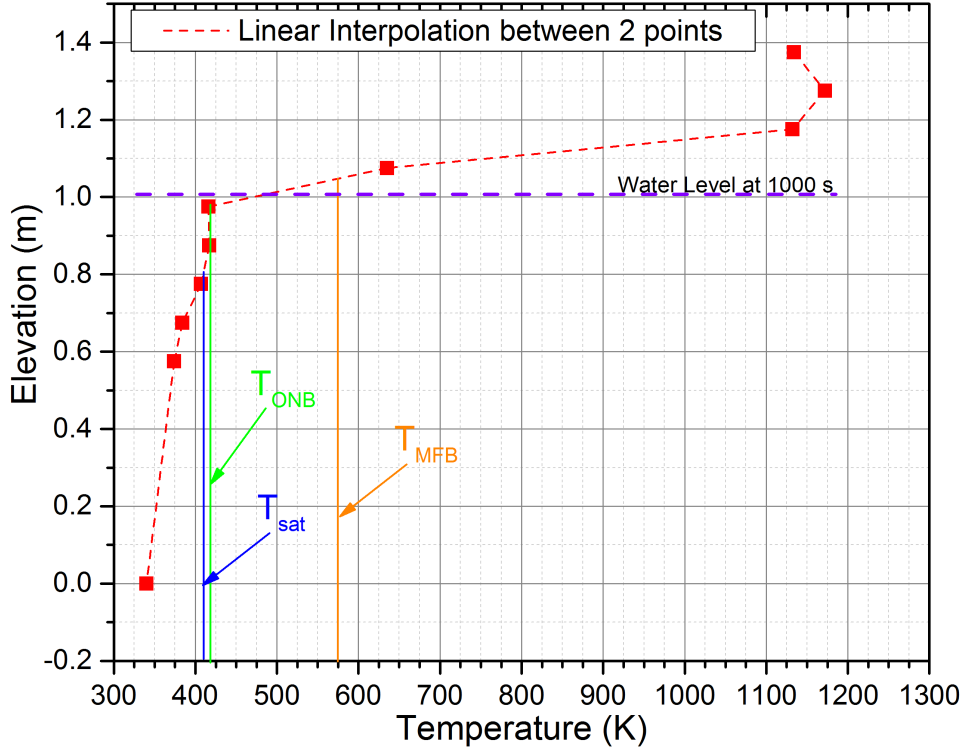


Figure 7.26: FPS Axial Temperature Variation (Power = 1%, Injection Rate = 25 g/s, Init. FPS T = 650°C, time = 1000s)

7.7 Development of Correlations

The experimental data generated from the DRCRE facility have been used to develop empirical correlations for the peak heat transfer coefficient and average quench front velocity. Since standard correlations are available in literature for estimating heat transfer coefficient and quench front velocity for flow through fuel bundles in intact core configuration, the present correlations predict only the enhancement of heat transfer coefficient and quench front velocity observed in case of partially degraded core condition.

7.7.1 Correlation for Peak Heat Transfer Coefficient

Because of flow re-distribution taking place in the ballooned region of FPS assembly, the heat transfer coefficient in the ballooned region reduces near the entry

point of the ballooned region and increases monotonically thereafter. The peak FPS temperature, input power and injection flow rate are used as parameters for predicting enhancement of heat transfer coefficient empirically. The parameters have been non-dimensionalized with the help of respective reference values. The correlation is given in Eq. (7.5).

$$\frac{h_{\text{ballooned}}}{h_{\text{non-ballooned}}} = 0.7767 \left(\frac{P}{\dot{m} H_{fg}} \right)^{0.1298} \left(\frac{T_{s,\text{peak}} - T_{\text{sat}}}{T_{LF} - T_{\text{sat}}} \right)^{-0.2777} \left(\left[4 + \frac{z}{D_h} \right] \frac{z}{D_h} \right)^{0.2345} \quad (7.5)$$

It can be seen from the correlation that higher the input power or lower the water injection flow rate, the enhancement or reduction of heat transfer coefficient is pronounced. The heat transfer coefficient also reduces with increase in peak clad temperature owing to higher stored energy of the clad. Figure 7.27 shows comparison of heat transfer coefficient ratio predicted by the correlation and observed in experiments. The prediction of correlation is accurate with 10% variation on either side. The correlation is applicable only for 45% radial blockages extending over 60% of total length for the flow rate range of $0.11 - 0.45 \text{ g/s/m/pin}$ and for input power ranging from 0-1% of typical full linear heat rating per pin used for typical PWRs (14 kW/m).

The heat transfer coefficient in the non-ballooned configuration $h_{\text{non-ballooned}}$ in Eq. (7.5) can be obtained from available correlations such as the correlation suggested by Murao and Sugimoto [46] as Eq. (7.6).

$$h_{\text{non-ballooned}} = 0.94 \left(\frac{k_g^3 \rho_g \rho_l H_{fg} g}{z \mu_g \Delta T_{\text{sat}}} \right)^{0.25} (1 - \alpha)^{0.25} + \sigma e (1 - \alpha)^{0.5} \frac{(T_s^4 - T_{\text{sat}}^4)}{\Delta T_{\text{sat}}} \quad (7.6)$$

7.7.2 Correlation for Average Quench Front Velocity

The average quench front velocity has been correlated based on the quench front velocity in a non-ballooned geometry. Injection flow rate, input power and average initial FPS temperature are used as parameter in non-dimensional form. The correlation has been shown in Eq. (7.7).

$$\frac{V_{q,ballooned}}{V_{q,non-ballooned}} = 1.9061 \left(\frac{P}{\dot{m}H_{fg}} \right)^{0.1320} \left(\frac{T_{FPS,average} - T_{sat}}{T_{LF} - T_{sat}} \right)^{-0.2196} \quad (7.7)$$

The quench front velocity enhancement increases with increase in power and reduction in injection flow rate. At higher clad temperatures the velocity enhancement is found to be lower. Figure 7.28 shows comparison of quench front velocity ratio predicted by the correlation and observed in experiments. The prediction of correlation is accurate with 10% deviation. The correlation is applicable only for 45% radial blockages extending over 60% of total length for the flow rate range of $0.11 - 0.45 \text{ g/s/m/pin}$ and for input power ranging from 0-1% of typical full linear heat rating per pin used for typical PWRs (14 kW/m). The quench front velocity in the non-ballooned configuration $V_{q,non-ballooned}$ in Eq. (7.7) can be calculated from available correlations such as the correlation for location of the quench front developed from FLECHT-SEASET experimental data [36] shown in Eq. (7.8).

$$z_q = \left(1 + 50 \left(\frac{T_q - T_{init}}{T_{init} - T_{sat}} \right) \right) tV_{in} \frac{1}{50 \left(\frac{T_q - T_{init}}{T_{init} - T_{sat}} \right) + \left(\frac{t_{peak} V_{in}}{z_q} \right) (Q_r + 0.5Q_r e^{-9Q_r^2})} \quad (7.8)$$

where Q_r is the fraction of total power released in the length covered with liquid domain and t_q is the time at which quench front attains location of peak power.

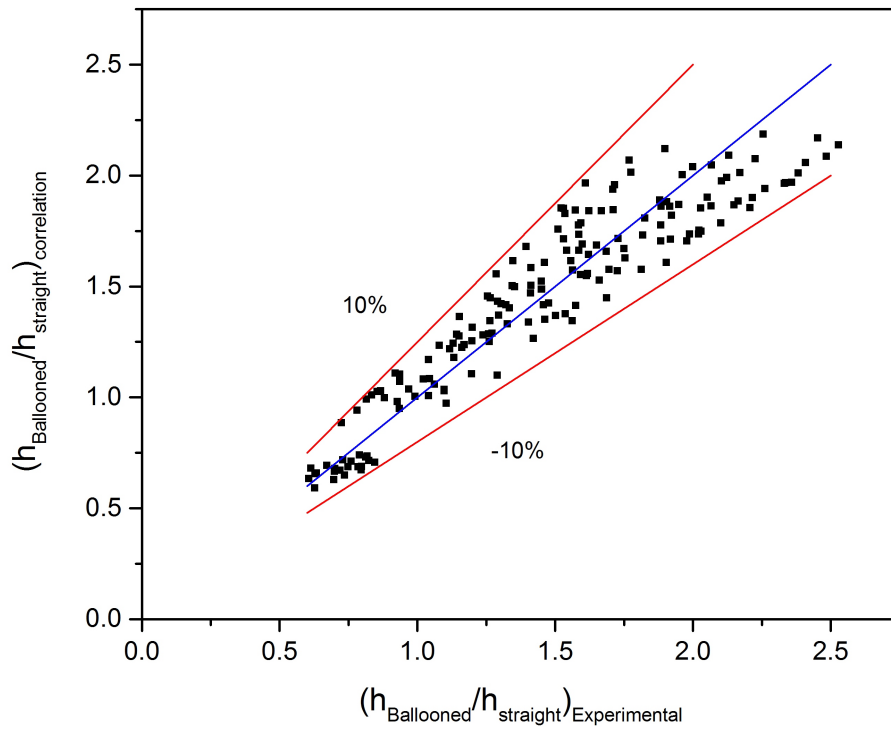


Figure 7.27: Peak Heat Transfer Correlation

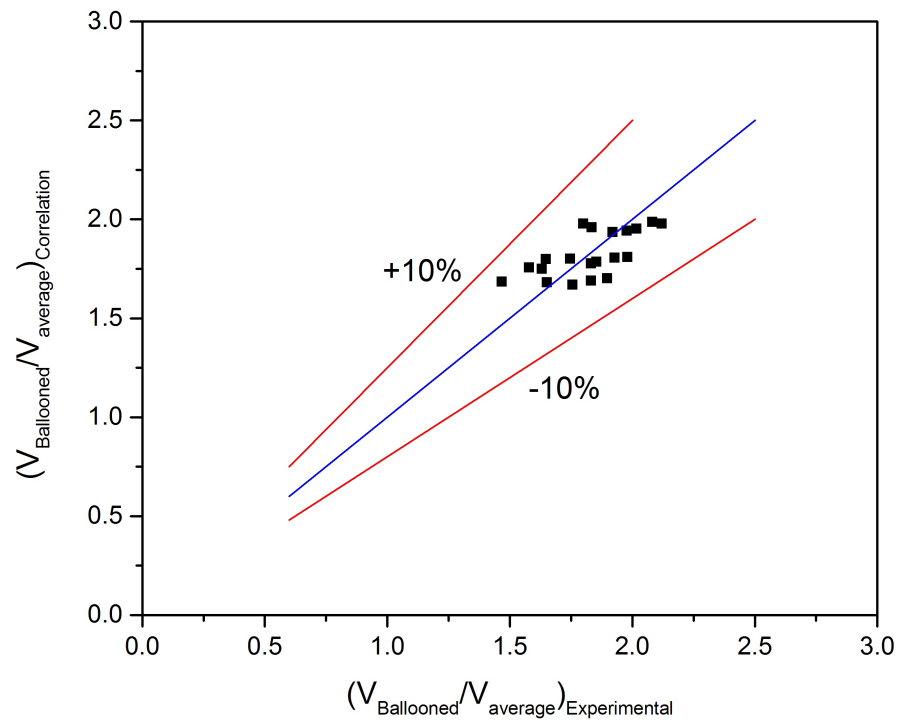


Figure 7.28: Quench Front Velocity Correlation

7.8 Salient Observations from Experiments

Salient observations from the experimental study are enlisted below:

1. Water injection into the DRCRE setup is found to be successful in quenching the FPS for the range of decay power levels, injection flow rates and initial average FPS temperature considered in this study.
2. Quenching behaviour of ballooned FPS is largely controlled by the injection flow rates. Conduction controlled rewetting pattern is observed for lower flow rates upto 0.25 g/s/m/pin beyond which, there is a tendency to change from conduction controlled rewetting to fluid controlled rewetting.
3. A sudden reduction in HTC is observed at the entry of ballooned region owing to significant flow re-distribution. The HTC improves thereon with monotonous rise in the peak HTC along the length of the test section.
4. The quench front is found to be accelerating in the ballooned central zone as compared to non-ballooned peripheral zone, causing earlier quenching in the central zone than the peripheral zone.
5. Correlation developed for the peak heat transfer coefficient is able to predict within $\pm 10\%$ of accuracy. The peak heat transfer coefficient in the ballooned region is found to be upto 2 times higher than that in the non-ballooned region.
6. Correlation developed for ratio of quench front velocity is able to predict within $\pm 10\%$ of accuracy. The quench front velocity in the ballooned region is found to be upto 2 times higher than the quench front velocity in the non-ballooned region.

Chapter 8

Development of Numeric Tool and Validation

8.1 Introduction to the code PDRCR

A thermal-hydraulics code, Partially Degraded Reactor Core Re-flood (PDRCR), is developed to simulate quenching behavior of moderately degraded reactor core. The code is based on finite volume approach and uses explicit formulation. The salient features of PDRCR distinct from existing codes are as follows:

- Pressure-enthalpy formulation for fluid conservation equations.
- Incorporation of complete steam-water property tables based on IAWPS-97 formulation.
- Incorporation of complete momentum conservation equation in the cross-flow direction that enables simulation of cross-flow between two parallel channels.
- Use of a novel water packing mitigation scheme for low flow flux conditions.

8.2 PDRCR Architecture and Modules

PDRCR has been developed in a modular approach that facilitates modification or up-gradation of any of the modules, without disturbing the other modules. Several modules have been developed to cater to simulation of different physical processes in reactor core re-flood simulation, such as fluid flow, fuel heat conduction. PDRCR solves for two-dimensional heat conduction equation within the fuel elements (module FUEL) and conservation equations for the fluid flow with two fluid six equation model (module FLOW) and uses heat transfer correlations for various flow regimes (module HTC). Figure 8.1 represents PDRCR code structure and also indicates information exchange between various modules of PDRCR. The formulation of PDRCR is presented in the following section.

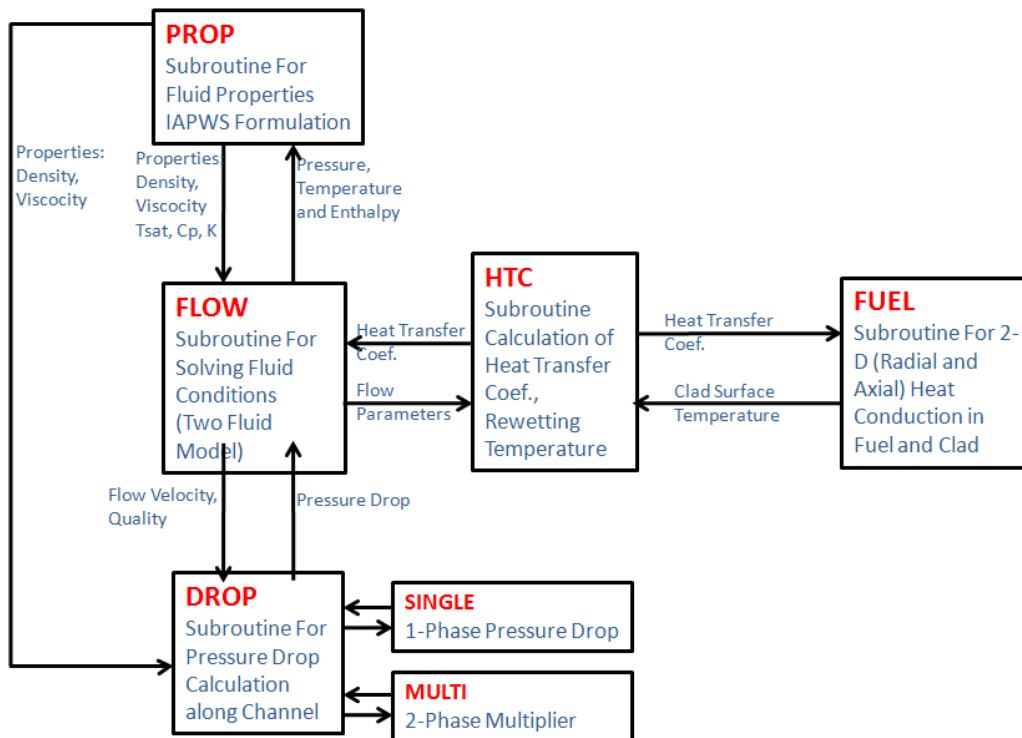


Figure 8.1: PDRCR Code Structure

8.2.1 Discretization of Fluid Flow path (Module FLOW)

The one-dimensional fluid flow path considered in FLOW for evaluation is discretized into several control volumes along the length as shown in Figure 8.2. A staggered node approach is used for the evaluation variable. The velocities are calculated on the boundary of the control volume, called FACE, represented by letters $i - 1$, i , $i + 1$ and the pressure, enthalpy and void fraction are calculated at the control volume (called CELL) center, represented by points W and E . The mass and energy equations are integrated with respect to the spatial variable z from z_i to z_{i+1} to obtain the pressure and internal energy values at the cell centers. And the momentum equation is integrated from cell center to cell center to obtain the velocity values at the faces. The positive flow direction is assumed to be from cell W to cell E . The parameters at the cell faces are obtained from the neighboring cells based on the First Order Upwind Scheme of Advection as follows:

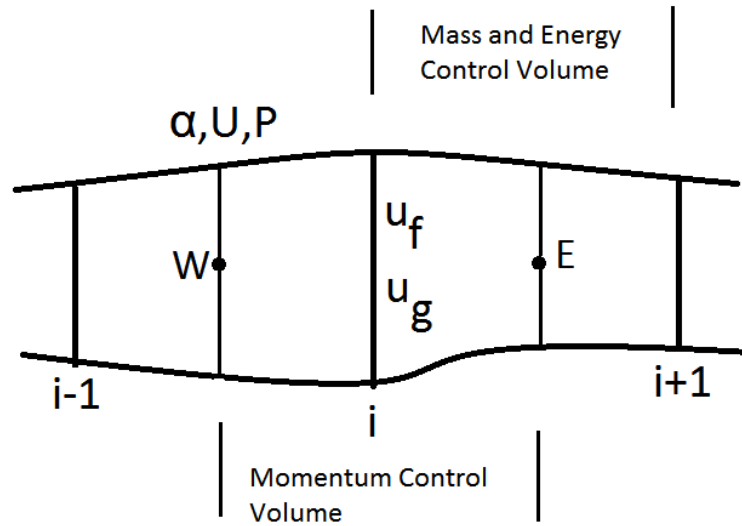


Figure 8.2: Flow Path discretized into Control Volumes

$$\begin{aligned}
 \phi_i &= \phi_W \quad \text{if } u_i > 0 \\
 &= \phi_E \quad \text{if } u_i < 0 \\
 &= \phi_W \quad \text{if } u_i = 0 \ \& \ P_W > P_E \\
 &= \phi_E \quad \text{if } u_i = 0 \ \& \ P_W < P_E \\
 &= \frac{\rho_E \phi_E + \rho_W \phi_W}{\rho_E + \rho_W} \quad \text{if } u_i = 0 \ \& \ P_W = P_E
 \end{aligned} \tag{8.1}$$

8.2.2 Conservation Equations for Fluid Flow

The two fluid six-equation model used for the simulation of fluid flow solves mass, momentum and energy conservation equations of liquid and gaseous phases in an explicit manner. A combination of addition or differences of these conservation equations is used to obtain a convenient set of equations to solve for. The energy conservation equations of liquid and gaseous phase are solved to obtain the enthalpy of individual phases, momentum equations yield the phasic velocities on cell faces and mass conservation equations are used for the calculation of pressure and void fraction at the cell centers. The evolution of the conservation equations and algebraic modifications to obtain the unknown parameters are described in following sections:

8.2.2.1 Mass Conservation Equation

Consider a flow path of varying flow cross-section as shown in Figure 8.2. The mass conservation equations for gaseous phase through the flow path can be written as:

$$\frac{\partial (\alpha_g \rho_g)}{\partial t} + \frac{1}{A} \frac{\partial (\alpha_g \rho_g u_g A)}{\partial z} = \Gamma_g \tag{8.2}$$

Similarly for liquid phase:

$$\frac{\partial (\alpha_f \rho_f)}{\partial t} + \frac{1}{A} \frac{\partial (\alpha_f \rho_f u_f A)}{\partial z} = \Gamma_f \quad (8.3)$$

Expanding the time derivative terms in Eq. (8.2) and Eq. (8.3), we get:

$$\alpha_g \frac{\partial (\rho_g)}{\partial t} + \rho_g \frac{\partial (\alpha_g)}{\partial t} + \frac{1}{A} \frac{\partial (\alpha_g \rho_g u_g A)}{\partial z} = \Gamma_g \quad (8.4)$$

$$\alpha_f \frac{\partial (\rho_f)}{\partial t} + \rho_f \frac{\partial (\alpha_f)}{\partial t} + \frac{1}{A} \frac{\partial (\alpha_f \rho_f u_f A)}{\partial z} = \Gamma_f \quad (8.5)$$

Assuming the two phase mixture to be of single component, the mass generation terms in Eq. (8.4) and Eq. (8.5) are merely transformation from one phase to other. Hence, we have:

$$\Gamma_g = -\Gamma_f \quad (8.6)$$

$$\alpha_g + \alpha_f = 1 \quad (8.7)$$

Differentiating Eq. (8.7) with respect to time we get:

$$\frac{\partial \alpha_g}{\partial t} = -\frac{\partial \alpha_f}{\partial t} \quad (8.8)$$

The specific enthalpy can be expressed as a function of internal energy, pressure and density as:

$$H = e + \frac{P}{\rho} \quad (8.9)$$

For the sake of clarity, symbol h is used for Heat Transfer Coefficient and symbol H is used for Specific Enthalpy. Differentiating Eq. (8.9) with respect to time, we get:

$$\frac{\partial H}{\partial t} = \frac{\partial e}{\partial t} + \frac{\rho \frac{\partial P}{\partial t} - P \frac{\partial \rho}{\partial t}}{\rho^2} \quad (8.10)$$

Hence, the time derivative of internal energy can be obtained as:

$$\frac{\partial e}{\partial t} = \frac{\partial H}{\partial t} - \frac{1}{\rho} \frac{\partial P}{\partial t} + \frac{P}{\rho^2} \frac{\partial \rho}{\partial t} \quad (8.11)$$

The fluid density can be expressed as a function of pressure and internal energy as:

$$\rho = f(P, e) \quad (8.12)$$

Thus the time derivative of density by product rule is:

$$\frac{\partial \rho}{\partial t} = \left. \frac{\partial \rho}{\partial P} \right|_e \frac{\partial P}{\partial t} + \left. \frac{\partial \rho}{\partial e} \right|_P \left(\frac{\partial H}{\partial t} - \frac{1}{\rho} \frac{\partial P}{\partial t} + \frac{P}{\rho^2} \frac{\partial \rho}{\partial t} \right) \quad (8.13)$$

Thus,

$$\frac{\partial \rho}{\partial t} = \frac{1}{\left(1 - \frac{P}{\rho^2} \frac{\partial \rho}{\partial e}\right)} \left[\left(\frac{\partial \rho}{\partial P} \Big|_e - \frac{1}{\rho} \frac{\partial \rho}{\partial e} \Big|_P \right) \frac{\partial P}{\partial t} + \frac{\partial \rho}{\partial e} \Big|_P \frac{\partial H}{\partial t} \right] \quad (8.14)$$

The addition of mass conservation equations for gaseous (Eq. (8.4)) and liquid (Eq. (8.5)) yields Sum-Mass conservation equation as:

$$\alpha_g \frac{\partial (\rho_g)}{\partial t} + \alpha_f \frac{\partial (\rho_f)}{\partial t} + \rho_g \frac{\partial (\alpha_g)}{\partial t} + \rho_f \frac{\partial (\alpha_f)}{\partial t} + \frac{1}{A} \frac{\partial (\alpha_g \rho_g u_g A + \alpha_f \rho_f u_f A)}{\partial z} = \Gamma_g + \Gamma_f \quad (8.15)$$

Using Eq. (8.6) and Eq. (8.7) in Eq. (8.15), we get:

$$\alpha_g \frac{\partial (\rho_g)}{\partial t} + \alpha_f \frac{\partial (\rho_f)}{\partial t} + (\rho_g - \rho_f) \frac{\partial (\alpha_g)}{\partial t} + \frac{1}{A} \frac{\partial (\alpha_g \rho_g u_g A + \alpha_f \rho_f u_f A)}{\partial z} = 0 \quad (8.16)$$

Substituting the derivative of density from Eq. (8.14) in Eq. (8.16), we get:

$$\begin{aligned} & \alpha_g \frac{1}{\left(1 - \frac{P}{\rho_g^2} \frac{\partial \rho_g}{\partial e_g}\right)} \left[\left(\frac{\partial \rho_g}{\partial P} - \frac{1}{\rho_g} \frac{\partial \rho_g}{\partial e_g} \right) \frac{\partial P}{\partial t} + \frac{\partial \rho_g}{\partial e_g} \frac{\partial H_g}{\partial t} \right] \\ & + \alpha_f \frac{1}{\left(1 - \frac{P}{\rho_f^2} \frac{\partial \rho_f}{\partial e_f}\right)} \left[\left(\frac{\partial \rho_f}{\partial P} - \frac{1}{\rho_f} \frac{\partial \rho_f}{\partial e_f} \right) \frac{\partial P}{\partial t} + \frac{\partial \rho_f}{\partial e_f} \frac{\partial H_f}{\partial t} \right] \\ & + (\rho_g - \rho_f) \frac{\partial (\alpha_g)}{\partial t} + \frac{1}{A} \frac{\partial (\alpha_g \rho_g u_g A + \alpha_f \rho_f u_f A)}{\partial z} = 0 \end{aligned} \quad (8.17)$$

Let,

$$M_k = \frac{\partial \rho_k}{\partial P} - \frac{1}{\rho} \frac{\partial \rho_k}{\partial e_k} \quad (8.18)$$

and

$$N_k = 1 - \frac{P}{\rho_k^2} \frac{\partial \rho_k}{\partial e_k} \quad (8.19)$$

where k represents liquid phase (f) or gaseous phase (g). Putting Eq. (8.18) and Eq. (8.19) in Eq. (8.17), we get:

$$\begin{aligned} \alpha_g \frac{1}{N_g} \left[M_g \frac{\partial P}{\partial t} + \frac{\partial \rho_g}{\partial e_g} \frac{\partial H_g}{\partial t} \right] + \alpha_f \frac{1}{N_f} \left[M_f \frac{\partial P}{\partial t} + \frac{\partial \rho_f}{\partial e_f} \frac{\partial H_f}{\partial t} \right] \\ + (\rho_g - \rho_f) \frac{\partial (\alpha_g)}{\partial t} + \frac{1}{A} \frac{\partial (\alpha_g \rho_g u_g A + \alpha_f \rho_f u_f A)}{\partial z} = 0 \end{aligned} \quad (8.20)$$

Rearranging the above equation we get:

$$\begin{aligned} \frac{\partial P}{\partial t} \left(\alpha_g \frac{M_g}{N_g} + \alpha_f \frac{M_f}{N_f} \right) + \frac{\partial H_f}{\partial t} \left(\frac{\alpha_f}{N_f} \frac{\partial \rho_f}{\partial e_f} \right) + \frac{\partial H_g}{\partial t} \left(\frac{\alpha_g}{N_g} \frac{\partial \rho_g}{\partial e_g} \right) \\ + (\rho_g - \rho_f) \frac{\partial (\alpha_g)}{\partial t} + \frac{1}{A} \frac{\partial (\alpha_g \rho_g u_g A + \alpha_f \rho_f u_f A)}{\partial z} = 0 \end{aligned} \quad (8.21)$$

Integrating Eq. (8.21) with respect to time and space, over the control volume shown in Figure (8.2), the integrated Sum-Mass Conservation equation can be obtained as:

$$\begin{aligned} (P^{n+1} - P^n) V \left(\alpha_g \frac{M_g}{N_g} + \alpha_f \frac{M_f}{N_f} \right) + (H_f^{n+1} - H_f^n) V \left(\frac{\alpha_f}{N_f} \frac{\partial \rho_f}{\partial e_f} \right) \\ + (H_g^{n+1} - H_g^n) V \left(\frac{\alpha_g}{N_g} \frac{\partial \rho_g}{\partial e_g} \right) + (\rho_g - \rho_f) V (\alpha_g^{n+1} - \alpha_g^n) \\ + \Delta t (\dot{\alpha}_g \dot{\rho}_g u_g A + \dot{\alpha}_f \dot{\rho}_f u_f A)_i^{i+1} = 0 \end{aligned} \quad (8.22)$$

Similarly, subtracting Eq. (8.3) from Eq. (8.2) to obtain the Difference-Mass

conservation equation, we get:

$$\alpha_g \frac{\partial (\rho_g)}{\partial t} - \alpha_f \frac{\partial (\rho_f)}{\partial t} + \rho_g \frac{\partial (\alpha_g)}{\partial t} - \rho_f \frac{\partial (\alpha_f)}{\partial t} + \frac{1}{A} \frac{\partial (\alpha_g \rho_g u_g A - \alpha_f \rho_f u_f A)}{\partial z} = \Gamma_g - \Gamma_f \quad (8.23)$$

Using Eq. (8.6), Eq. (8.7), Eq. (8.14), Eq. (8.18) and Eq. (8.19) in Eq. (8.23) and rearranging, we get:

$$\begin{aligned} \frac{\partial P}{\partial t} \left(\alpha_g \frac{M_g}{N_g} - \alpha_f \frac{M_f}{N_f} \right) - \frac{\partial H_f}{\partial t} \left(\frac{\alpha_f}{N_f} \frac{\partial \rho_f}{\partial e_f} \right) + \frac{\partial H_g}{\partial t} \left(\frac{\alpha_g}{N_g} \frac{\partial \rho_g}{\partial e_g} \right) \\ + (\rho_g + \rho_f) \frac{\partial (\alpha_g)}{\partial t} + \frac{1}{A} \frac{\partial (\alpha_g \rho_g u_g A - \alpha_f \rho_f u_f A)}{\partial z} = 2\Gamma_g \end{aligned} \quad (8.24)$$

After integration the Difference-Mass conservation equation can be obtained as:

$$\begin{aligned} (P^{n+1} - P^n) V \left(\alpha_g \frac{M_g}{N_g} - \alpha_f \frac{M_f}{N_f} \right) - (H_f^{n+1} - H_f^n) V \left(\frac{\alpha_f}{N_f} \frac{\partial \rho_f}{\partial e_f} \right) \\ + (H_g^{n+1} - H_g^n) V \left(\frac{\alpha_g}{N_g} \frac{\partial \rho_g}{\partial e_g} \right) + (\rho_g + \rho_f) V (\alpha_g^{n+1} - \alpha_g^n) \\ + \Delta t (\dot{\alpha}_g \dot{\rho}_g u_g A - \dot{\alpha}_f \dot{\rho}_f u_f A)_i^{i+1} = 2\Gamma_g \end{aligned} \quad (8.25)$$

8.2.2.2 Energy Conservation Equation

The energy conservation for the gaseous phase can be written as:

$$\begin{aligned} \frac{\partial (\alpha_g \rho_g H_g)}{\partial t} + \frac{1}{A} \frac{\partial (\alpha_g \rho_g u_g H_g A)}{\partial z} - \alpha_g \frac{\partial P}{\partial t} - \frac{u_g}{A} \frac{\partial (P \alpha_g A)}{\partial z} \\ = Q_{w,g} + Q_{i,g} + Q_{\Gamma,w,g} + Q_{\Gamma,i,g} + Q_{diss,g} \end{aligned} \quad (8.26)$$

Expanding the time derivative terms in Eq. (8.26),

$$\begin{aligned} & \alpha_g \rho_g \frac{\partial H_g}{\partial t} + \alpha_g H_g \frac{\partial \rho_g}{\partial t} + \rho_g H_g \frac{\partial \alpha_g}{\partial t} - \alpha_g \frac{\partial P}{\partial t} \\ & + \frac{1}{A} \frac{\partial (\alpha_g \rho_g u_g H_g A)}{\partial z} - \frac{u_g}{A} \frac{\partial (P \alpha_g A)}{\partial z} = Q_{w,g} + Q_{i,g} + Q_{\Gamma,w,g} + Q_{\Gamma,i,g} + Q_{diss,g} \end{aligned} \quad (8.27)$$

Substituting Eq. (8.14), Eq. (8.18) and Eq. (8.19) in Eq. (8.27) we get:

$$\begin{aligned} & \alpha_g \rho_g \frac{\partial H_g}{\partial t} + \alpha_g H_g \left(\frac{M_g}{N_g} \frac{\partial P}{\partial t} + \frac{1}{N_g} \frac{\partial \rho_g}{\partial e_g} \frac{\partial H_g}{\partial t} \right) + \rho_g H_g \frac{\partial \alpha_g}{\partial t} - \alpha_g \frac{\partial P}{\partial t} \\ & + \frac{1}{A} \frac{\partial (\alpha_g \rho_g u_g H_g A)}{\partial z} - \frac{u_g}{A} \frac{\partial (P \alpha_g A)}{\partial z} = Q_{w,g} + Q_{i,g} + Q_{\Gamma,w,g} + Q_{\Gamma,i,g} + Q_{diss,g} \end{aligned} \quad (8.28)$$

Rearranging Eq. (8.27),

$$\begin{aligned} & \frac{\partial H_g}{\partial t} \left(\alpha_g \rho_g + \frac{\alpha_g H_g}{N_g} \frac{\partial \rho_g}{\partial e_g} \right) + \frac{\partial \alpha_g}{\partial t} (\rho_g H_g) + \frac{\partial P}{\partial t} \left(\alpha_g H_g \frac{M_g}{N_g} - \alpha_g \right) \\ & + \frac{1}{A} \frac{\partial (\alpha_g \rho_g u_g H_g A)}{\partial z} - \frac{u_g}{A} \frac{\partial (P \alpha_g A)}{\partial z} = Q_{w,g} + Q_{i,g} + Q_{\Gamma,w,g} + Q_{\Gamma,i,g} + Q_{diss,g} \end{aligned} \quad (8.29)$$

Integrating Eq. (8.29) with respect to time and space, we get:

$$\begin{aligned} & (H_g^{n+1} - H_g^n) V \left(\alpha_g \rho_g + \frac{\alpha_g H_g}{N_g} \frac{\partial \rho_g}{\partial e_g} \right) + (\alpha_g^{n+1} - \alpha_g^n) V (\rho_g H_g) \\ & + (P^{n+1} - P^n) V \left(\alpha_g H_g \frac{M_g}{N_g} - \alpha_g \right) + \Delta t \left(\dot{\alpha}_g \dot{\rho}_g u_g \dot{H}_g A \right)_i^{i+1} - \Delta t u_g (P \dot{\alpha}_g A)_i^{i+1} \\ & = (Q_{w,g} + Q_{i,g} + Q_{\Gamma,w,g} + Q_{\Gamma,i,g} + Q_{diss,g}) \Delta t V \end{aligned} \quad (8.30)$$

Similarly, energy equation for the liquid phase can be obtained in integrated form as:

$$\begin{aligned}
 & (H_f^{n+1} - H_f^n) V \left(\alpha_f \rho_f + \frac{\alpha_f H}{N_f} \frac{\partial \rho_f}{\partial e_f} \right) - (\alpha_g^{n+1} - \alpha_g^n) V (\rho H_f) \\
 & + (P^{n+1} - P^n) V \left(\alpha_f H_f \frac{M_f}{N_f} - \alpha_f \right) + \Delta t \left(\dot{\alpha}_f \dot{\rho}_f u_f \dot{H}_f A \right)_i^{i+1} - \Delta t u_f (P \dot{\alpha}_f A)_i^{i+1} \\
 & = (Q_{w,f} + Q_{i,f} + Q_{\Gamma,w,f} + Q_{\Gamma,i,f} + Q_{diss,f}) \Delta t V \quad (8.31)
 \end{aligned}$$

8.2.2.3 Momentum Conservation Equation

The momentum conservation equation for the gaseous phase can be written as:

$$\begin{aligned}
 \frac{\partial (\alpha_g \rho_g u_g)}{\partial t} + \frac{\partial (\alpha_g \rho_g u_g^2)}{\partial z} + \alpha_g \frac{\partial P}{\partial z} = & \alpha_g \rho_g G_z - \alpha_g \rho_g F_{w,g} u_g + \Gamma_g u_{inter} \\
 & - \alpha_g \rho_g F_{i,g} (u_g - u_f) - C \alpha_g \alpha_f \rho_m \frac{\partial (u_g - u_f)}{\partial t} \quad (8.32)
 \end{aligned}$$

where, the mixture density ρ_m is defined as:

$$\rho_m = \alpha_g \rho_g + \alpha_f \rho_f \quad (8.33)$$

Multiplying the Mass Conservation Equation for gaseous phase Eq. (8.2) by u_g and subtracting from this the gaseous phase momentum equation Eq. (8.32), we get,

$$\begin{aligned}
& \frac{\partial (\alpha_g \rho_g u_g)}{\partial t} + \frac{\partial (\alpha_g \rho_g u_g^2)}{\partial z} + \alpha_g \frac{\partial P}{\partial z} - u_g \frac{\partial (\alpha_g \rho_g)}{\partial t} - u_g \frac{\partial (\alpha_g \rho_g u_g)}{\partial z} \\
& = \alpha_g \rho_g G_z - \alpha_g \rho_g F_{w,g} u_g + \Gamma_g u_{inter} - \Gamma_g u_g \\
& \quad - \alpha_g \rho_g F_{i,g} (u_g - u_f) - C \alpha_g \alpha_f \rho_m \frac{\partial (u_g - u_f)}{\partial t} \quad (8.34)
\end{aligned}$$

Expanding the time derivative terms in Eq. (8.34):

$$\begin{aligned}
& \alpha_g \rho_g \frac{\partial u_g}{\partial t} + u_g \frac{\partial (\alpha_g \rho_g)}{\partial t} + u_g \frac{\partial (\alpha_g \rho_g u_g)}{\partial z} + \alpha_g \rho_g u_g \frac{\partial u_g}{\partial z} + \alpha_g \frac{\partial P}{\partial z} \\
& \quad - u_g \frac{\partial (\alpha_g \rho_g)}{\partial t} - u_g \frac{\partial (\alpha_g \rho_g u_g)}{\partial z} = \alpha_g \rho_g G_z - \alpha_g \rho_g F_{w,g} u_g + \Gamma_g u_{inter} - \Gamma_g u_g \\
& \quad - \alpha_g \rho_g F_{i,g} (u_g - u_f) - C \alpha_g \alpha_f \rho_m \frac{\partial (u_g - u_f)}{\partial t} \quad (8.35)
\end{aligned}$$

Rearranging, we get:

$$\begin{aligned}
& \alpha_g \rho_g \frac{\partial u_g}{\partial t} + \frac{\alpha_g \rho_g}{2} \frac{\partial u_g^2}{\partial z} + \alpha_g \frac{\partial P}{\partial z} = \alpha_g \rho_g G_z - \alpha_g \rho_g F_{w,g} u_g \\
& \quad + \Gamma_g u_{g,inter} - \Gamma_g u_g - \alpha_g \rho_g F_{inter,g} (u_g - u_f) - C \alpha_g \alpha_f \rho_m \frac{\partial (u_g - u_f)}{\partial t} \quad (8.36)
\end{aligned}$$

Similarly, the momentum equation for the liquid phase can be written as:

$$\begin{aligned}
& \alpha_f \rho_f \frac{\partial u_f}{\partial t} + \frac{\alpha_f \rho_f}{2} \frac{\partial u_f^2}{\partial z} + \alpha_f \frac{\partial P}{\partial z} = \alpha_f \rho_f G_z - \alpha_f \rho_f F_{w,f} u_f \\
& \quad + \Gamma_f u_{f,inter} - \Gamma_f u_f - \alpha_f \rho_f F_{inter,f} (u_f - u_g) - C \alpha_g \alpha_f \rho_m \frac{\partial (u_f - u_g)}{\partial t} \quad (8.37)
\end{aligned}$$

Adding Eq. (8.36) and Eq. (8.37), the Sum-Momentum Equation can be obtained as:

$$\begin{aligned}
& \alpha_g \rho_g \frac{\partial u_g}{\partial t} + \frac{\alpha_g \rho_g}{2} \frac{\partial u_g^2}{\partial z} + \alpha_g \frac{\partial P}{\partial z} + \alpha_f \rho_f \frac{\partial u_f}{\partial t} + \frac{\alpha_f \rho_f}{2} \frac{\partial u_f^2}{\partial z} + \alpha_f \frac{\partial P}{\partial z} = \\
& \alpha_g \rho_g G_z - \alpha_g \rho_g F_{w,g} u_g + \alpha_f \rho_f G_x - \alpha_f \rho_f F_{w,f} u_f \\
& + \Gamma_g u_{g,inter} - \Gamma_g u_g - \alpha_g \rho_g F_{inter,g} (u_g - u_f) - C \alpha_g \alpha_f \rho_m \frac{\partial (u_g - u_f)}{\partial t} \\
& + \Gamma_f u_{f,inter} - \Gamma_f u_f - \alpha_f \rho_f F_{inter,f} (u_f - u_g) - C \alpha_g \alpha_f \rho_m \frac{\partial (u_f - u_g)}{\partial t} \quad (8.38)
\end{aligned}$$

Applying conservation of momentum across the interface between the gaseous and liquid phases, the inter-phase terms in Eq. (8.38) should add up to zero. Thus, we have,

$$\begin{aligned}
& \Gamma_g u_{g,inter} - \Gamma_g u_g - \alpha_g \rho_g F_{inter,g} (u_g - u_f) - C \alpha_g \alpha_f \rho_m \frac{\partial (u_g - u_f)}{\partial t} \\
& + \Gamma_f u_{f,inter} - \Gamma_f u_f - \alpha_f \rho_f F_{inter,f} (u_f - u_g) - C \alpha_g \alpha_f \rho_m \frac{\partial (u_f - u_g)}{\partial t} = 0 \quad (8.39)
\end{aligned}$$

The above equation holds good when the individual contributions at interface due to mass transfer and interface friction add up to to zero. Hence we have,

$$\Gamma_g u_{g,inter} - \Gamma_g u_g = \Gamma_f u_{f,inter} - \Gamma_f u_f \quad (8.40)$$

Thus,

$$u_{f,inter} = u_{g,inter} = u_{inter} \quad (8.41)$$

$$\alpha_g \rho_g F_{inter,g} (u_g - u_f) = \alpha_f \rho_f F_{inter,f} (u_g - u_f) \quad (8.42)$$

Thus,

$$\alpha_g \rho_g F_{inter,g} = \alpha_f \rho_f F_{inter,f} = \alpha_f \rho_f \alpha_g \rho_g F_{inter} \quad (8.43)$$

The Sum-Momentum Equation reduces to:

$$\begin{aligned} \alpha_g \rho_g \frac{\partial u_g}{\partial t} + \frac{\alpha_g \rho_g}{2} \frac{\partial u_g^2}{\partial z} + \alpha_f \rho_f \frac{\partial u_f}{\partial t} + \frac{\alpha_f \rho_f}{2} \frac{\partial u_f^2}{\partial z} = -\frac{\partial P}{\partial z} \\ + \rho_m G_z - \alpha_g \rho_g F_{w,g} u_g - \alpha_f \rho_f F_{w,f} u_f - \Gamma_g (u_g - u_f) \end{aligned} \quad (8.44)$$

Similarly, the Difference-Momentum Equation is obtained by dividing Eq. (8.36) and Eq. (8.37) by $\alpha_g \rho_g$ and $\alpha_f \rho_f$ respectively and subtracting:

$$\begin{aligned} \frac{1}{\alpha_g \rho_g} \left[\alpha_g \rho_g \frac{\partial u_g}{\partial t} + \frac{\alpha_g \rho_g}{2} \frac{\partial u_g^2}{\partial z} + \alpha_g \frac{\partial P}{\partial z} \right] - \frac{1}{\alpha_f \rho_f} \left[\alpha_f \rho_f \frac{\partial u_f}{\partial t} + \frac{\alpha_f \rho_f}{2} \frac{\partial u_f^2}{\partial z} + \alpha_f \frac{\partial P}{\partial z} \right] = \\ \frac{1}{\alpha_g \rho_g} \left[\alpha_g \rho_g G_z - \alpha_g \rho_g F_{w,g} u_g + \Gamma_g u_{g,inter} - \Gamma_g u_g - \alpha_g \rho_g F_{inter,g} (u_g - u_f) - C \alpha_g \alpha_f \rho_m \frac{\partial (u_g - u_f)}{\partial t} \right] \\ - \frac{1}{\alpha_f \rho_f} \\ \left[\alpha_f \rho_f G_x - \alpha_f \rho_f F_{w,f} u_f + \Gamma_f u_{f,inter} - \Gamma_f u_f - \alpha_f \rho_f F_{inter,f} (u_f - u_g) - C \alpha_g \alpha_f \rho_m \frac{\partial (u_f - u_g)}{\partial t} \right] \end{aligned} \quad (8.45)$$

$$\begin{aligned} \frac{\partial u_g}{\partial t} + \frac{1}{2} \frac{\partial u_g^2}{\partial z} + \frac{1}{\rho_g} \frac{\partial P}{\partial z} - \frac{\partial u_f}{\partial t} - \frac{1}{2} \frac{\partial u_f^2}{\partial z} + \frac{1}{\rho_f} \frac{\partial P}{\partial z} = \\ G_z - F_{w,g} u_g + \frac{\Gamma_g u_{g,inter}}{\alpha_g \rho_g} - \frac{\Gamma_g u_g}{\alpha_g \rho_g} - F_{inter,g} (u_g - u_f) - \frac{C \alpha_f \rho_m}{\rho_g} \frac{\partial (u_g - u_f)}{\partial t} \\ - G_x + F_{w,f} u_f - \frac{\Gamma_f u_{f,inter}}{\alpha_f \rho_f} + \frac{\Gamma_f u_f}{\alpha_f \rho_f} + F_{inter,f} (u_f - u_g) + \frac{C \alpha_g \rho_m}{\rho_f} \frac{\partial (u_f - u_g)}{\partial t} \end{aligned} \quad (8.46)$$

$$\begin{aligned}
 \frac{\partial u_g}{\partial t} + \frac{1}{2} \frac{\partial u_g^2}{\partial z} - \frac{\partial u_f}{\partial t} - \frac{1}{2} \frac{\partial u_f^2}{\partial z} = \\
 - \left(\frac{1}{\rho_g} - \frac{1}{\rho_f} \right) \frac{\partial P}{\partial z} + \frac{\Gamma_g}{\alpha_g \rho_g \alpha_f \rho_f} [u_{inter} \rho_m - (\alpha_g \rho_g u_f + \alpha_f \rho_f u_g)] \\
 - F_{w,g} u_g + F_{w,f} u_f - F_{inter} (u_g - u_f) \rho_m - \frac{C \rho_m^2}{\rho_g \rho_f} \frac{\partial (u_g - u_f)}{\partial t} \quad (8.47)
 \end{aligned}$$

Integrating the Sum-Momentum Equation Eq. (8.44) and the Difference-Momentum Equation Eq. (8.47) over momentum control volume i.e. from cell center W to cell center E and over time, we get:

$$\begin{aligned}
 (\alpha_g \rho_g)_i^n (u_g^{n+1} - u_g^n) \Delta z + (\alpha_f \rho_f)_i^n (u_f^{n+1} - u_f^n) \Delta z + \frac{1}{2} (\dot{\alpha}_g \dot{\rho}_g)_i^n (u_g^{2,n})_W^E \Delta t \\
 + \frac{1}{2} (\dot{\alpha}_f \dot{\rho}_f)_i^n (u_f^{2,n})_W^E \Delta t = - (P)_W^E \Delta t + \rho_m G_z \Delta z \Delta t - (\alpha_g \rho_g)_i^n F_{w,g}^n u_g^n \Delta z \Delta t \\
 - (\alpha_f \rho_f)_i^n F_{w,f}^n u_f^n \Delta z \Delta t - \Gamma_g (u_g - u_f)^n \Delta z \Delta t \quad (8.48)
 \end{aligned}$$

$$\begin{aligned}
 \left(1 + \frac{C \rho_m^2}{\rho_g \rho_f} \right) [(u_g^{n+1} - u_g^n) - (u_f^{n+1} - u_f^n)] \Delta z + \frac{1}{2} \left(\frac{\dot{\alpha}_g \dot{\rho}_g}{\alpha_g \rho_g} \right)^n (u_g^{2,n})_W^E \Delta t \\
 - \frac{1}{2} \left(\frac{\dot{\alpha}_f \dot{\rho}_f}{\alpha_f \rho_f} \right)^n (u_f^{2,n})_W^E \Delta t = - \left(\frac{1}{\rho_g} - \frac{1}{\rho_f} \right)_i^n (P^{n+1})_W^E \Delta t - F_{w,g}^n u_g^n \Delta z \Delta t \\
 + F_{w,f}^n u_f^n \Delta x \Delta t - (\rho_m F_{inter})_i^n (u_g^n - u_f^n) \Delta z \Delta t \\
 + \left(\frac{\Gamma_g}{\alpha_g \rho_g \alpha_f \rho_f} \right)_i^n [u_{inter}^n \rho_m^n - (\alpha_g^n \rho_g^n u_f^n + \alpha_f^n \rho_f^n u_g^n)]_i \Delta z \Delta t \quad (8.49)
 \end{aligned}$$

8.2.3 Solution of Conservation Equations for Fluid Flow (Module FLOW)

The mass, momentum and energy conservation for gaseous and liquid phases constitute a set of six equations which are solved for six unknowns, namely, the phasic

velocities u_g, u_f , the phasic enthalpies H_g, H_f , pressure P and void fraction α_g .

The Sum-Mass conservation Equation Eq. (8.22), Difference-Mass conservation Equation Eq. (8.25) and Energy conservation Equations Eq. (8.30) and Eq. (8.31) involve four unknown parameters, namely, $(H_g^{n+1} - H_g^n)$, $(H_f^{n+1} - H_f^n)$, $(P^{n+1} - P^n)$ and $(\alpha_g^{n+1} - \alpha_g^n)$. These equations can be solved simultaneously by arranging them in matrix as:

$$\begin{bmatrix} C_{11} & C_{12} & C_{13} & C_{14} \\ C_{21} & C_{22} & C_{23} & C_{24} \\ C_{31} & C_{32} & C_{33} & C_{34} \\ C_{41} & C_{42} & C_{43} & C_{44} \end{bmatrix} \begin{bmatrix} (H_g^{n+1} - H_g^n) \\ (H_f^{n+1} - H_f^n) \\ (\alpha_g^{n+1} - \alpha_g^n) \\ (P^{n+1} - P^n) \end{bmatrix} = \begin{bmatrix} R_1 \\ R_2 \\ R_3 \\ R_4 \end{bmatrix} \quad (8.50)$$

where

$$\begin{aligned} C_{11} &= \left(\alpha_g \rho_g + \frac{\alpha_g H_g}{N_g} \frac{\partial \rho_g}{\partial e_g} \right) V & C_{12} &= 0 \\ C_{13} &= (\rho_g H_g) V & C_{14} &= \left(\alpha_g H_g \frac{M_g}{N_g} - \alpha_g \right) V \\ C_{21} &= 0 & C_{22} &= \left(\alpha_f \rho_f + \frac{\alpha_f H_f}{N_f} \frac{\partial \rho_f}{\partial e_f} \right) V \\ C_{23} &= (\rho H_f) V & C_{24} &= \left(\alpha_f H_f \frac{M_f}{N_f} - \alpha_f \right) V \\ C_{31} &= \left(\frac{\alpha_g}{N_g} \frac{\partial \rho_g}{\partial e_g} \right) V & C_{32} &= \left(-\frac{\alpha_f}{N_f} \frac{\partial \rho_f}{\partial e_f} \right) V \\ C_{33} &= (\rho_g + \rho_f) V & C_{34} &= \left(\alpha_g \frac{M_g}{N_g} - \alpha_f \frac{M_f}{N_f} \right) V \\ C_{41} &= \left(\frac{\alpha_g}{N_g} \frac{\partial \rho_g}{\partial e_g} \right) V & C_{42} &= \left(\frac{\alpha_f}{N_f} \frac{\partial \rho_f}{\partial e_f} \right) V \\ C_{43} &= (\rho_g - \rho_f) V & C_{44} &= \left(\alpha_g \frac{M_g}{N_g} + \alpha_f \frac{M_f}{N_f} \right) V \end{aligned} \quad (8.51)$$

and

$$\begin{aligned} R_1 &= \Delta t \left(\dot{\alpha}_g \dot{\rho}_g u_g \dot{H}_g A \right)_i^{i+1} - \Delta t u_g (P \dot{\alpha}_g A)_i^{i+1} \\ &\quad + (Q_{w,g} + Q_{i,g} + Q_{\Gamma,w,g} + Q_{\Gamma,i,g} + Q_{diss,g}) \Delta t V \end{aligned} \quad (8.52)$$

$$R_2 = \Delta t \left(\dot{\alpha}_f \dot{\rho}_f u_f \dot{H}_f A \right)_i^{i+1} - \Delta t u_f (P \dot{\alpha}_f A)_i^{i+1} + (Q_{w,f} + Q_{i,f} + Q_{\Gamma,w,f} + Q_{\Gamma,i,f} + Q_{diss,f}) \Delta t V \quad (8.53)$$

$$R_3 = -\Delta t (\dot{\alpha}_g \dot{\rho}_g u_g A - \dot{\alpha}_f \dot{\rho}_f u_f A)_i^{i+1} + 2\Gamma_g \quad (8.54)$$

$$R_4 = -\Delta t (\dot{\alpha}_g \dot{\rho}_g u_g A + \dot{\alpha}_f \dot{\rho}_f u_f A)_i^{i+1} \quad (8.55)$$

The Eq. (8.50) is multiplied by inverse of C to solve for the unknown parameters.

Similarly the Sum-Momentum equation Eq. (8.48) and Difference-Momentum equation Eq. (8.49) are solved simultaneously by arranging them in matrix form as:

$$\begin{bmatrix} M_{11} & M_{12} \\ M_{21} & M_{22} \end{bmatrix} \begin{bmatrix} (u_g^{n+1} - u_g^n) \\ (u_f^{n+1} - u_f^n) \end{bmatrix} = \begin{bmatrix} S_1 \\ S_2 \end{bmatrix} \quad (8.56)$$

where

$$M_{11} = \Delta z (\alpha_g \rho_g)_i^n \quad (8.57)$$

$$M_{12} = \Delta z (\alpha_f \rho_f)_i^n \quad (8.58)$$

$$M_{21} = \Delta z \left(1 + \frac{C \rho_m^2}{\rho_g \rho_f} \right)_i \quad (8.59)$$

$$M_{22} = -\Delta z \left(1 + \frac{C \rho_m^2}{\rho_g \rho_f} \right)_i \quad (8.60)$$

and

$$\begin{aligned} S_1 = & -\frac{1}{2} (\dot{\alpha}_g \dot{\rho}_g)_i^n (u_g^{2,n})_W^E \Delta t - \frac{1}{2} (\dot{\alpha}_f \dot{\rho}_f)_i^n (u_f^{2,n})_W^E \Delta t - (P)_W^E \Delta t \\ & + \rho_m G_z \Delta z \Delta t - (\alpha_g \rho_g)_i^n F_{w,g}^n u_g^n \Delta x \Delta t - (\alpha_f \rho_f)_i^n F_{w,f}^n u_f^n \Delta z \Delta t - \Gamma_g (u_g - u_f)^n \Delta z \Delta t \end{aligned} \quad (8.61)$$

$$\begin{aligned} S_2 = & -\frac{1}{2} \left(\frac{\dot{\alpha}_g \dot{\rho}_g}{\alpha_g \rho_g} \right)_i^n (u_g^{2,n})_W^E \Delta t + \frac{1}{2} \left(\frac{\dot{\alpha}_f \dot{\rho}_f}{\alpha_f \rho_f} \right)_i^n (u_f^{2,n})_W^E \Delta t \\ & - \left(\frac{1}{\rho_g} - \frac{1}{\rho_f} \right)_i^n (P^{n+1})_W^E \Delta t - F_{w,g}^n u_g^n \Delta z \Delta t + F_{w,f}^n u_f^n \Delta z \Delta t - (\rho_m F_{inter})_i^n (u_g^n - u_f^n) \Delta z \Delta t \\ & + \left(\frac{\Gamma_g}{\alpha_g \rho_g \alpha_f \rho_f} \right)_i^n [u_{inter}^n \rho_m^n - (\alpha_g^n \rho_g^n u_f^n + \alpha_f^n \rho_f^n u_g^n)]_i \Delta z \Delta t \end{aligned} \quad (8.62)$$

Figure 8.3 shows the process of obtaining new solution from the previous time step solution. For each control volume of the computational domain, the momentum conservation equation is solved first to obtain the updated velocity field. The mass and energy conservation equations are then solved using the updated velocity field values. The momentum equation is solved again with the new values

of Pressure field.

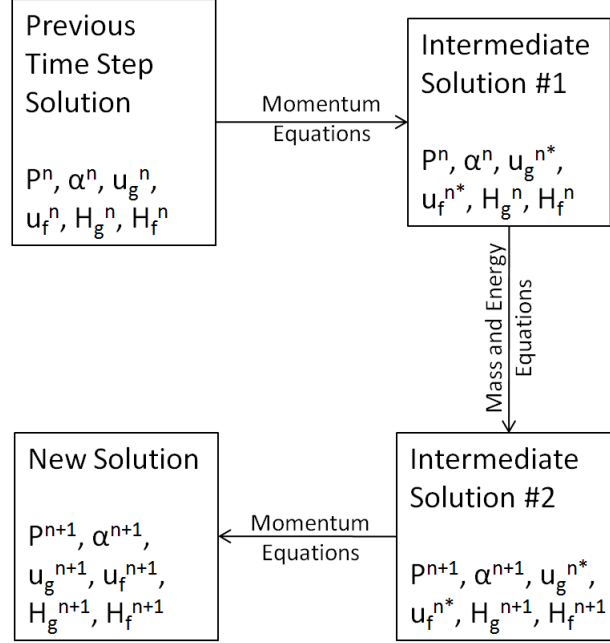


Figure 8.3: Solution Process for FLOW Module

8.2.4 Solution of Conservation Equation for Fuel (Module FUEL)

The energy conservation equation for the Fuel element is essentially the heat conduction equation. The FUEL module solves for heat conduction within the fuel in radial as well as axial direction. Variation in the azimuthal direction is not considered. The module employs a finite volume approach and uses a fully explicit scheme of solution.

Figure 8.4 shows a fuel element discretized using finite volume approach.

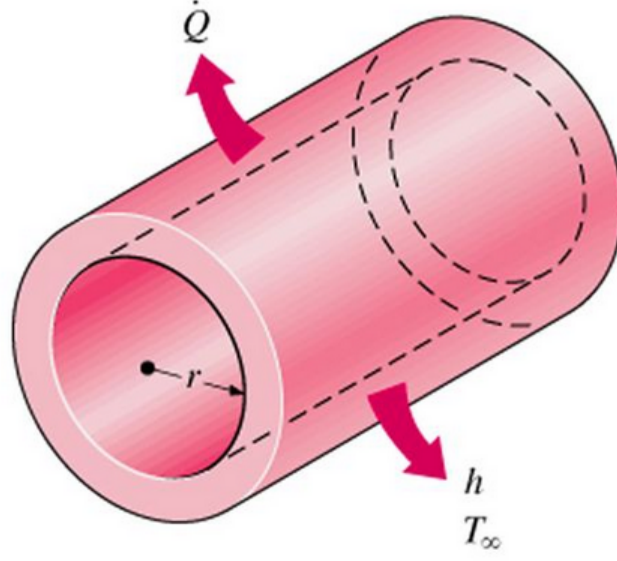


Figure 8.4: Heat Conduction in Radial Direction

Assuming no variation along the azimuthal direction the heat conduction equation in radial coordinate for the element can be written as:

$$Q_{r,W} - Q_{r,E} + Q_{z,S} - Q_{z,N} + Q_{generation} = mC_p \frac{\partial T}{\partial t} \quad (8.63)$$

$$\begin{aligned} -K(2\pi r_i dz) \left(\frac{\partial T}{\partial r} \right)_i + K(2\pi r_{i+1} dz) \left(\frac{\partial T}{\partial r} \right)_{i+1} - K(2\pi r_P dr) \left(\frac{\partial T}{\partial z} \right)_j \\ + K(2\pi r_P dr) \left(\frac{\partial T}{\partial z} \right)_{j+1} \\ + q_{generation}''' (2\pi r_P dr dz) = (2\pi r_P dr dz) C_p \frac{\partial T}{\partial t} \end{aligned} \quad (8.64)$$

Eq. (8.64) can be written in discretized form as:

$$\begin{aligned}
& -K(2\pi r_i)(z_{j+1} - z_j) \left(\frac{T_P^n - T_W^n}{r_P - r_W} \right) + K(2\pi r_{i+1})(z_{j+1} - z_j) \left(\frac{T_E^n - T_P^n}{r_E - r_P} \right) \\
& -K(2\pi r_P)(r_{i+1} - r_i) \left(\frac{T_P^n - T_S^n}{z_P - z_S} \right) + K(2\pi r_P)(r_{i+1} - r_i) \left(\frac{T_N^n - T_P^n}{z_N - z_P} \right) \\
& + q_{generation}''' (2\pi r_P)(z_{j+1} - z_j)(r_{i+1} - r_i) \\
& = (2\pi r_P)(z_{j+1} - z_j)(r_{i+1} - r_i) C_p \left(\frac{T_P^{n+1} - T_P^n}{t^{n+1} - t^n} \right) \quad (8.65)
\end{aligned}$$

Eq. (8.65) can be rearranged to get:

$$T_P^{n+1} = PT_P^n + ST_S^n + NT_N^n + WT_W^n + ET_E^n + C \quad (8.66)$$

where,

$$P = \frac{\frac{r_P(r_{i+1}-r_i)(z_{j+1}-z_j)\rho C_p}{(t^{n+1}-t^n)} - \frac{Kr_i(z_{j+1}-z_j)}{(r_P-r_W)} - \frac{Kr_{i+1}(z_{j+1}-z_j)}{(r_E-r_P)} - \frac{Kr_P(r_{i+1}-r_i)}{(z_P-z_S)} - \frac{Kr_P(r_{i+1}-r_i)}{(z_N-z_P)}}{\frac{r_P(r_{i+1}-r_i)(z_{j+1}-z_j)\rho C_p}{(t^{n+1}-t^n)}} \quad (8.67)$$

$$S = \frac{-\frac{K}{(z_P-z_S)}}{\frac{(z_{j+1}-z_j)\rho C_p}{(t^{n+1}-t^n)}} \quad (8.68)$$

$$N = \frac{-\frac{K}{(z_N-z_P)}}{\frac{(z_{j+1}-z_j)\rho C_p}{(t^{n+1}-t^n)}} \quad (8.69)$$

$$E = \frac{-\frac{Kr_{i+1}}{(r_E-r_P)}}{\frac{r_P(r_{i+1}-r_i)\rho C_p}{(t^{n+1}-t^n)}} \quad (8.70)$$

$$W = \frac{-\frac{Kr_i}{(r_P - r_W)}}{\frac{r_P(r_{i+1} - r_i)\rho C_P}{(t^{n+1} - t^n)}} \quad (8.71)$$

Thus the new time step temperatures T^{n+1} can be obtained using the old time step temperature T^n and Eq. (8.66) through Eq. (8.71).

8.2.5 Module for Heat Transfer Coefficients (Module HTC)

As mentioned in Section 8.2, a set of correlations for the heat transfer coefficients are used as closure relations between the fluid flow solution obtained from FLOW and fuel conduction solution in FUEL. A Heat Transfer Coefficient Module HTC has been developed which takes inputs from the FLOW and FUEL module, such as the fuel surface temperature, the fluid and gaseous phase temperatures in the fluid cell, the phasic velocities, void fraction coefficients and flow regimes. An appropriate correlations is then selected based on the heat transfer regime determined from the inputs and flow boiling model. Calculated values of heat fluxes from the fuel surface to the individual phase of flow are then fetched to FUEL and FLOW subroutines for the next step of calculation.

A flow boiling model based on the Steiner's Boiling model [47] is used. This model facilitates modifications or replacement of any of the correlations used, keeping the rest of the code structure intact. The set of conditions used for the determination of the heat transfer regime are expressed as an algorithm in Figure 8.5.

Table 8.1 gives the details of heat transfer regime and the corresponding correlation used for the estimation of heat transfer coefficient. The entrainment of water particles within the steam domain is modeled with modified entrainment model of Steen and Wallis [48, 49] as used in code TRACE (a version of RELAP code maintained by USNRC) [45]. The correlation for fraction of water entrained

is given as:

$$E = 0.015 + 0.44 \log_{10} \left[0.9245 \left(\frac{v_{g,dimensionless}}{v_{g,dimensionless,crit}} \right)^2 \right] \quad (8.72)$$

where the non-dimensional steam velocity is obtained as:

$$v_{g,dimensionless} = \frac{\dot{j}_g \mu_g}{\sigma} \sqrt{\frac{\rho_g}{\rho_f}} \quad (8.73)$$

and the critical dimensionless steam velocity is:

$$v_{g,dimensionless,crit} = 2.46e - 4 \quad (8.74)$$

The calculation of radiative heat exchanges between different structures modeled in PDRCR is performed based on pre-calculated view factors. The radiative heat flux is applied as an additional boundary source on the participating structures.

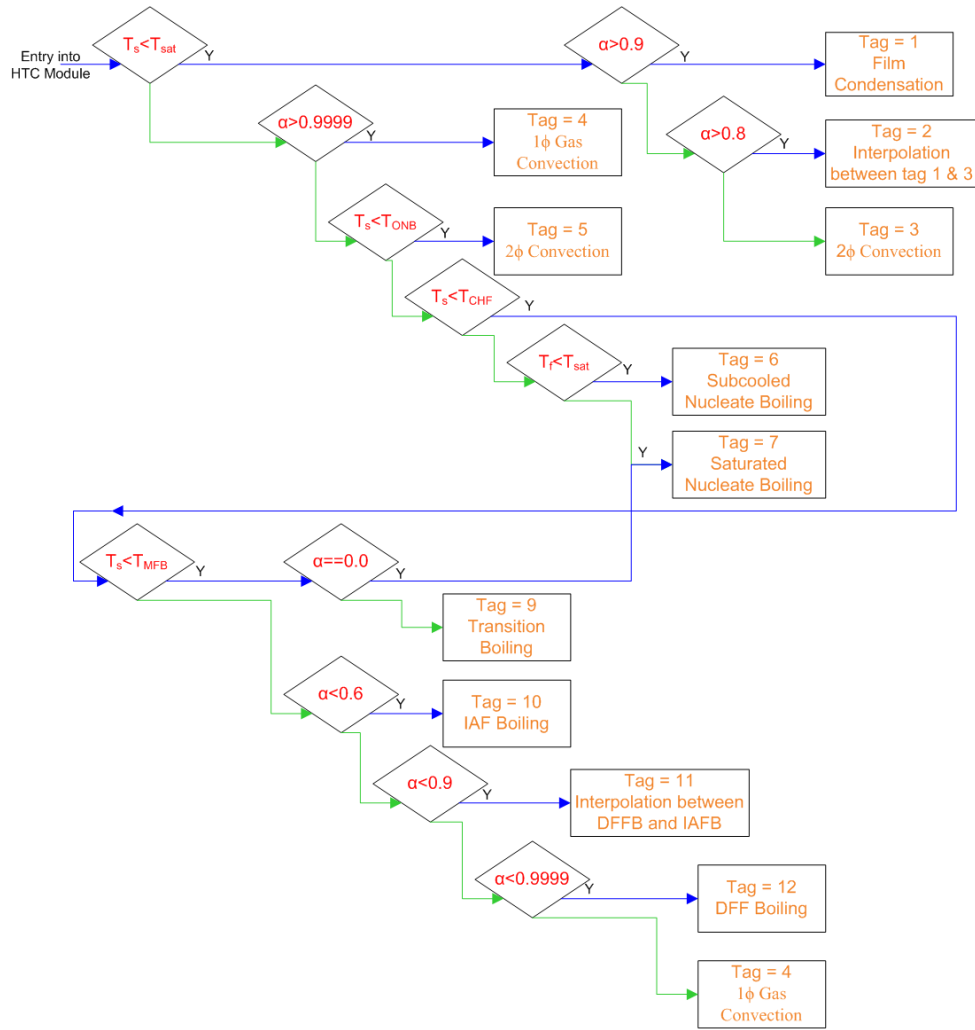


Figure 8.5: Heat Transfer Regime Identification Map

Table 8.1: Heat Transfer Regimes and Correlations used in PDRCR

Regime Tag	Heat Transfer Regime	Correlation Used
4	Single Phase Forced Convection	Gnielinski Correlation $h = \frac{K}{D} \left(\frac{(f/s)(Re-1000)Pr}{1+12.7(f/s)^{1/2}(Pr^{2/3}-1)} \right)$ $f = (0.7904 \ln(Re) - 1.64)^{-2}$

Regime Tag	Heat Transfer Regime	Correlation Used
3	Two Phase Forced Convection	<p>Aggour's Correlation</p> $h_{2\phi} = (1 - \alpha)^{-0.83} h_f$ $Nu_f = 0.0155 Re_f^{0.83} Pr_f^{0.5} \left(\frac{\mu_{bulk}}{\mu_{wall}} \right)^{0.33}$
6, 7	Pool Boiling	<p>Gorenflo Correlation</p> $h_{PB} = h_0 F_{PB} (q''/q_0'')^n$ $h_0 = 5600 \text{ W/m}^2 \text{ K}$ $q_0'' = 20000 \text{ W/m}^2$ $F_{PB} = 1.73 P_r^{0.27} + \left(6.1 + \frac{0.68}{1 - P_r} \right) P_r^2$ $P_r = \frac{P}{P_{crit}}$ $n = 0.9 - 0.3 P_r^{0.15}$ $h_{PB} = [h_0 (F_p/q_0'')^n]^{\frac{1}{1-n}} (T_w - T_{sat})^{\frac{n}{1-n}}$
6, 7	Sub-cooled / Saturated Nucleate Boiling (with flow)	$q_{FB}'' = [q_{FC}'' + (q_{PB}'' - q_{BI}'')^3]^{1/3}$ $q_{BI}'' = q_{PB}'' (T_{ONB})$
10	Inverted Annular Film Boiling	$h_{f,conv} = \frac{K_f}{D_h} \max(0.0, 1.3 (0.268 \delta^{0.77} - 0.34))$ $\delta = \frac{D_h}{2} \left\{ \left[1 + \alpha \left(\frac{4}{\pi} \left(\frac{Pitch}{D_{fuel}} \right)^2 - 1 \right) \right]^{1/2} - 1 \right\}$ $h_g = \frac{K_g}{\delta}$ $q_{f,rad}'' = \frac{\sigma(T_w^4 - T_f^4)}{\frac{1}{\sqrt{1-\alpha}}}$
9	Transition Regime	$q_{TB}'' = F_{TB} q_{CHF}'' + (1 - F_{TB}) q_{MFB}''$ $F_{TB} = \sqrt{1 - \alpha} \left(\frac{T_w - T_{MFB}}{T_{CHF} - T_{MFB}} \right)^2$
-	Critical Heat Flux	$T_{CHF} = 385.25 - 1.1446 P^2 + 22.751 P$ <p>(Pressure in bar)</p>

Regime Tag	Heat Transfer Regime	Correlation Used
-	Minimum Film Boiling Temperature	$T_{MFB} = T_{MFB,sat} + \left(\frac{h_{f,sat} - h_f}{h_{fg}} \right) \frac{10^4}{(2.82 + 1.22P)}$ $T_{MFB,sat} = 557.85 + 44.1P - 3.72P^2$ (Pressure in MPa and Temperature in K)
-	Temperature at Onset of Nucleate Boiling	$T_{ONB} =$ $T_f + \left(\frac{1}{4} \right) \left[\sqrt{\Delta T_{ONB,sat}} + \sqrt{\Delta T_{ONB,sat} + 4\Delta T_{sub}} \right]^2$ $T_{ONB,sat} = \frac{2h_{FC}\sigma T_{sat}}{F^2 \rho_g h_{fg} K_f}$ $F = 1 - \exp(-\phi^3 - 0.5\phi)$

8.2.6 Module for Steam Water Properties (Module PROP)

Since the properties of steam and water vary significantly with pressure as well as enthalpy, it is essential to account for the property changes along the flow channel. A property subroutine is thus developed with IAPWS Formulation of Steam and Water Properties [50]. The module takes pressure and phasic enthalpy of each cell as input and calculates thermodynamic properties including derivatives of some of the properties required by the conservation equations.

The formulation is valid in the entire stable fluid region of H_2O from the melting-pressure curve to 1873 K at pressures up to 1000 MPa, the lowest temperature on the melting pressure curve being 251.165 K (at 208.566 MPa).

8.3 Solution Algorithm

The algorithm followed by PDRCR is shown in Figure 8.6. The input file is read to generate discretized domains for FLOW and FUEL modules. As the time spepping begins, the thermodynamic properties are calculated for each discretized cell based

on the pressure and enthalpy value. The advected quantities are then calculated at face centers using first order upwinding scheme. The modules for pressure drop (DROP) and heat transfer (HTC) calculations are then invoked. Based on the fluxes evaluated by HTC module, the FUEL domain is solved first followed by the FLOW domain. While solving the FLOW equations, the momentum equation is solved first to obtain new time step velocities followed by solution of mass and energy conservation equations in fully-explicit manner. Once all the modules are solved, the variables are updated to new time step quantities.

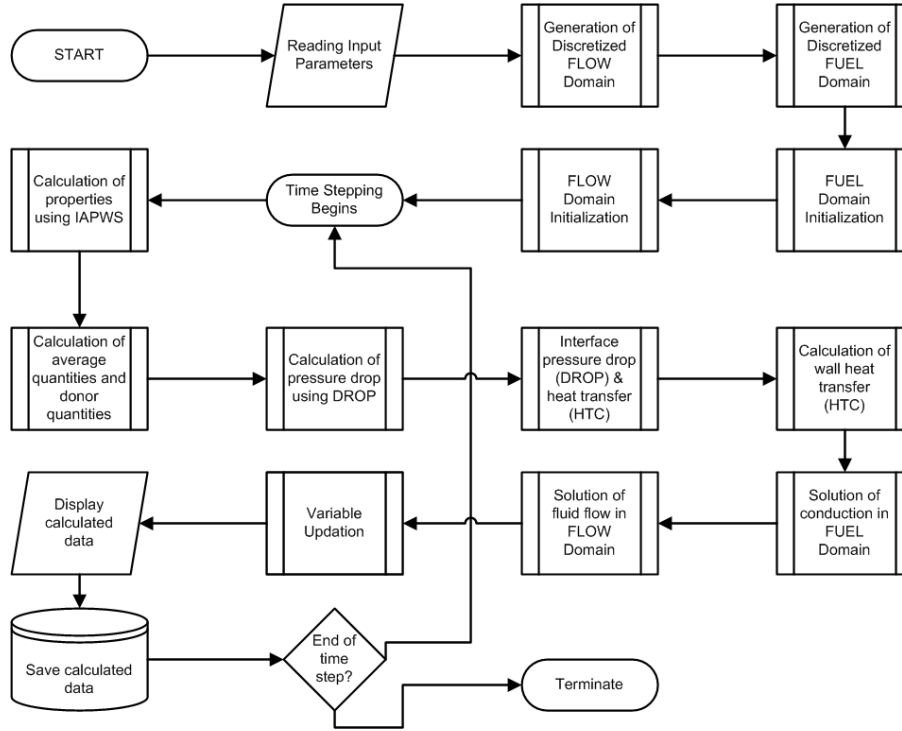


Figure 8.6: PDRCR Algorithm

8.4 New Water Packing Mitigation Scheme

Water packing is defined as artificial spikes observed in the pressure solution of two phase flow when a cell nearly filled with liquid gets filled completely [45]. Till the time the cell is not completely filled with liquid, the compressibility of the cell is large, owing to the presence of some steam. As soon as the cell gets completely

filled with liquid, the compressibility of the cell reduces drastically. The inlet flow rate of water at this time step is finite, however outlet flow rate has not increased from zero. This leads to a sudden pressure rise in the cell. In the next time step, this pressure rise produces significant outflow velocity of liquid, much higher than the inflow velocity. This leads to sudden drop in the pressure of this cell. This numerical phenomena is called water packing.

In existing system codes such as RELAP5, TRACE, water packing is avoided by multiplying the coefficient of pressure change term in the momentum solution of the liquid phase with a large number (as shown in Eq. (8.75)) , when the cell is near filling condition.

$$V_{f,i}^{n+1} = 0.01 - (VFDP)_i^n (P_B^{n+1} - P_B^n) + (VFDP)_j^n (FACTOR) (P_A^{n+1} - P_A^n) \quad (8.75)$$

where the terms VFDP represent pressure drop terms and FACTOR represents the multiplier used for mitigating water packing. This leads to artificial rise in the outflow velocity of liquid even before the cell is completely filled with liquid, so that, the cell pressure does not rise. The multiplication factor is chosen arbitrarily based on experience. It is also reported in the code manual of RELAP5, that, such a scheme of water packing works fine for flows with large flow velocities and is not as efficient at low flow velocities. A new water packing mitigation scheme is thus proposed for low flow velocities.

The phenomena of water packing is purely artificial and comes into existence because of artificial cell boundary that has been created to discretize the domain. Hence a new scheme is developed to eliminate water packing, which creates a Dummy Cell at the earlier existing cell boundary such that the Dummy Cell now involves some part of cells on either side of the boundary (i.e., cells A and B). The original cell A and cell B are thus modified to cell A' and cell B' as shown in Figure

8.7. The water front now lies near the center of this newly created Dummy Cell which is nearly half filled. The compressibility of this Dummy Cell is high owing to presence of steam. When the Dummy Cell is created, the outflow velocity of the modified cell A' is set to the inlet flow velocity, because the water front has already moved past the cell boundary of cell A', and A' is completely filled with water. The pressure spikes in A' are eliminated as the inflow and outflow of water are nearly the same in subsequent time steps. The Dummy Cell is used for calculations only till the water front crosses the originally defined cell boundary between cell A and cell B into the next cell (cell B). The Dummy Cell is subsequently deleted and the momentum solution is solved for the original cell boundary.

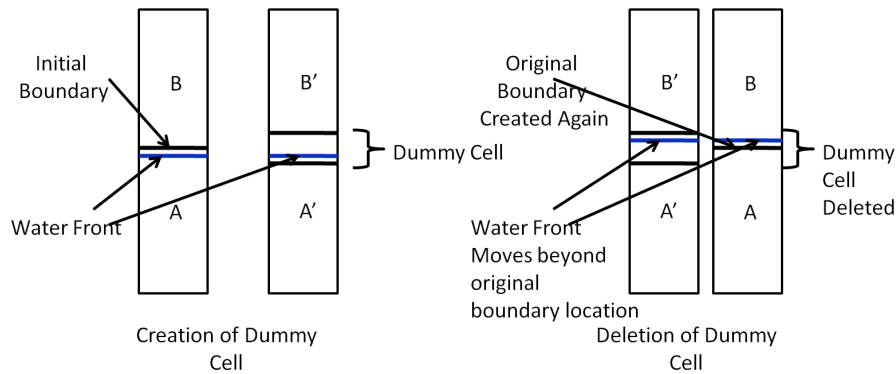


Figure 8.7: Creation and Deletion of Dummy Cell

The effectiveness of this water packing scheme over the water packing schemes used in present system analysis codes such as TRACE is discussed in Section 8.8.

8.5 Treatment of Cross-Flow

As mentioned in Chapter 3, the system codes used for simulation of severe accidents do not consider the momentum flux terms in the cross-flow direction. As pointed out in the feasibility analysis, which has been carried out with the RELAP5 tool, the effect of cross-flow is significant even when the momentum flux terms are not considered. For the case of quenching of partially degraded core with ballooned

region, the quenching water front is expected to be at different axial locations along the cross-section of the core. An exaggerated expression of this is shown in Figure 8.8.

Under such condition, the fluid densities for two neighboring cells of different flow paths are expected to be significantly different. Since the momentum flux term is a product of donor cell momentum (which is function of fluid density) and cross-flow velocity, the momentum flux terms are significant in magnitude. To account for the momentum flux terms in the cross-flow direction, the momentum conservation equations for gaseous phase Eq. (8.32) and for liquid phase Eq. (8.37) are modified to incorporate cross-flow terms as shown in Eq. (8.76) and Eq. (8.77).

$$\begin{aligned} \frac{\partial (\alpha_g \rho_g u_g)}{\partial t} + \frac{\partial (\alpha_g \rho_g u_g^2)}{\partial z} + \frac{\partial (\alpha_g \rho_g u_g v_g)}{\partial z} + \alpha_g \frac{\partial P}{\partial z} = & \alpha_g \rho_g G_z - \alpha_g \rho_g F_{w,g} u_g + \Gamma_g u_{inter} \\ & - \alpha_g \rho_g F_{i,g} (u_g - u_f) - C \alpha_g \alpha_f \rho_m \frac{\partial (u_g - u_f)}{\partial t} \end{aligned} \quad (8.76)$$

$$\begin{aligned} \frac{\partial (\alpha_f \rho_f u_f)}{\partial t} + \frac{\partial (\alpha_f \rho_f u_f^2)}{\partial z} + \frac{\partial (\alpha_f \rho_f u_f v_f)}{\partial z} + \alpha_f \frac{\partial P}{\partial z} = & \alpha_f \rho_f G_z - \alpha_f \rho_f F_{w,f} u_f + \Gamma_f u_{inter} \\ & - \alpha_f \rho_f F_{i,f} (u_f - u_g) - C \alpha_g \alpha_f \rho_m \frac{\partial (u_f - u_g)}{\partial t} \end{aligned} \quad (8.77)$$

where v_g and v_f are the cross-flow velocities for gaseous and liquid phase, respectively. The phasic velocities in the cross-flow direction are calculated at the face i as shown in Figure 8.9 by solving the momentum equation in cross-flow direction given by Eq. (8.78) and Eq. (8.79).

$$\begin{aligned} \frac{\partial (\alpha_g \rho_g v_g)}{\partial t} + \frac{\partial (\alpha_g \rho_g v_g^2)}{\partial y} + \alpha_g \frac{\partial P}{\partial y} = & -\alpha_g \rho_g F_{w,g} v_g + \Gamma_g v_{inter} \\ & - \alpha_g \rho_g F_{i,g} (v_g - v_f) - C \alpha_g \alpha_f \rho_m \frac{\partial (v_g - v_f)}{\partial t} \end{aligned} \quad (8.78)$$

$$\begin{aligned} \frac{\partial (\alpha_f \rho_f v_f)}{\partial t} + \frac{\partial (\alpha_f \rho_f v_f^2)}{\partial y} + \alpha_f \frac{\partial P}{\partial y} = & -\alpha_f \rho_f F_{w,f} v_f + \Gamma_f v_{inter} \\ & - \alpha_f \rho_f F_{i,f} (v_f - v_g) - C \alpha_g \alpha_f \rho_m \frac{\partial (v_f - v_g)}{\partial t} \end{aligned} \quad (8.79)$$

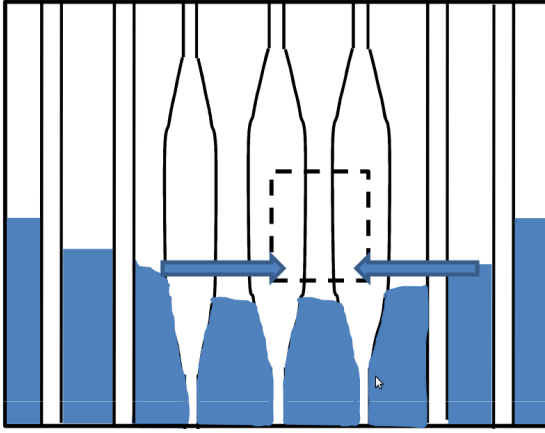


Figure 8.8: Conceptual Representation of Cross-Flow

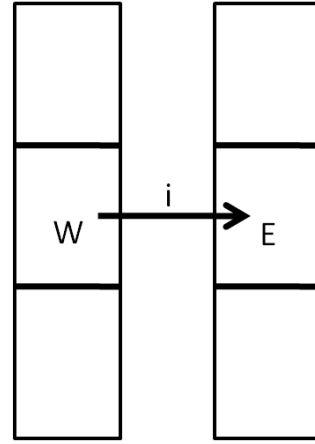


Figure 8.9: Discretization of Cross-Flow Path

The conservation equations in the axial direction are solved first to obtain the pressures in cell W and cell E. The frictional pressure drops are calculated based on the velocities v_f and v_g from the older time step. The new time step velocities are then calculated using Eq. (8.78) and Eq. (8.79). Hence, these equations can be solved to obtain cross-flow velocities.

8.6 Treatment of Heat Transfer with Cross-Flow

As discussed in Section 8.2.5, the heat transfer coefficient is calculated with a correlation selected from a set of correlations based on various parameters such as flow regime and void fraction. The quality (and the void fraction) at a given axial location for two parallel channels can differ significantly depending on the

geometry of the channel and total energy deposited by the fuel. A cross-flow across the two channels would therefore inject fluid of significantly different quality and velocity from one channels to other. Since the heat transfer coefficient is a function of Re and Pr which are fluid properties, the heat transfer coefficient due to cross-flow will differ significantly from the axial flow case. The heat transfer due to axial and cross-flow has been treated separately such that

$$q_{total} = q_{cross} + q_{axial} \quad (8.80)$$

Here it has been assumed that the fluid flowing in the radial direction is able to contact the heat transfer surfaces in the other channel. This assumption is acceptable since the length of the fluid volume in the radial direction is very small as compared to the axial direction and hence the fluid can easily traverse the distance in radial direction to establish a contact. The heat transfer area apportionment has been done based on the net fluxes of fluid moving in axial and radial direction. The calculation of heat transfer coefficient for the cross-flow is also carried out with HTC Module. An appropriate correlation is selected for the cross-flow.

8.7 Treatment of Large Axial Temperature Gradients in FUEL

Due to presence of sharp temperature gradients in the fuel pin in the axial direction (high temperature in the non-quenched region and near saturation temperature in quenched region), finer discretization is required in the fuel domain. In the Fluid domain, however, use of fine discretization restricts the time step used by FLOW module considerably. Hence, an adaptive discretization technique is used in PDRCR code. A coarse discretization is used by FLOW module and the FUEL

module in the region away from the water level. Each cell in the FLOW discretization corresponds to a single FUEL cell. However, in the vicinity of the water level, the single FUEL cell associated with the FLOW cell containing water level is discretized into 10 sub-cells such that multiple sub-cells of FUEL mesh correspond to a single cell in FLOW as shown in Figure 8.10. The apportionment of heat transfer between the liquid and gaseous phases is done with respect to the area of surface occupied by each phase.

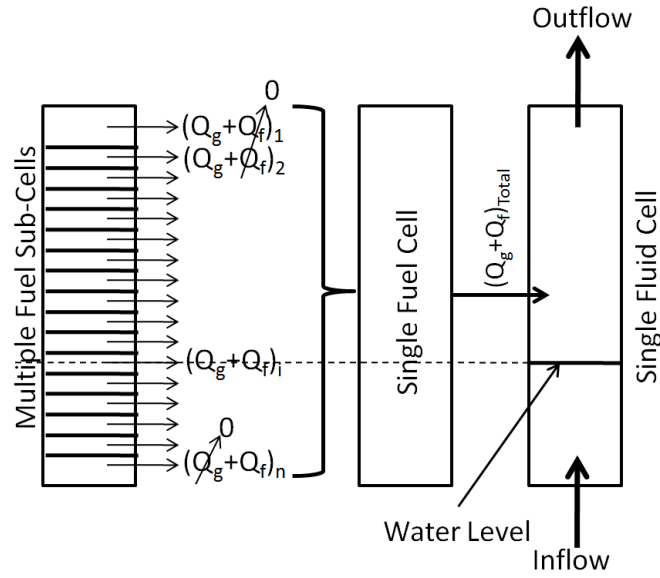


Figure 8.10: FUEL and FLOW Nodalization

8.8 Validation Results for PDRCR

To assess the performance of different modules, several test cases are considered and the performance is compared against analytical solution or available numerical codes or CFD calculations in commercial softwares. The test cases considered have been tabulated in Table 8.2.

Table 8.2: Test Cases for PDRCR Modules Validation

Test Case No.	Test Case	Modules Tested	Reference for Comparison	Details
1	Radial Heat Transfer with Internal Heat Generation	FUEL	Analytical Solution	Compares solution of Heat Conduction Equation
2	Axial Heat Transfer with Internal Heat Generation	FUEL	Analytical Solution	Compares solution of Heat Conduction Equation
3	1D Single Phase Water Flow (Isothermal Condition)	FLOW	RELAP5	Compares pressure drop calculation
4	1D Single Phase Water Flow (Non-Isothermal Condition)	FLOW	RELAP5	Compares solution of Energy Equation
5	1D Single Phase Steam Flow (Isothermal Condition)	FLOW	RELAP5	Compares pressure drop calculation

Test Case No.	Test Case	Modules Tested	Reference for Comparison	Details
6	1D Single Phase Steam Flow (Non-Isothermal Condition)	FLOW	RELAP5	Compares solution of Energy Equation
7	1D Water Fill Test for Pipe filled with Superheated Steam	FLOW	RELAP5	Compares inter-phase heat and mass transfer calculation
8	2D Single Phase Water Flow with Cross-Flow	FLOW	COMSOL CFD Simulations	Testing of treatment of cross-flow
9	Property Values at Different Pressure and Temperatures	PROP	IAPWS Steam Tables	Testing of property prediction
10	Performance of New Water Packing Mitigation Scheme	FLOW	TRACE scheme	Compares performance of new scheme with existing schemes

8.8.1 Test Case 01: Radial Heat Conduction with Internal Heat Generation

To assess the performance of FUEL Heat Conduction Module a test case with only radial heat conduction is considered. The fuel pin radius is taken to be 4.0 mm and the volumetric heat generation rate is 10^7 W/m^3 . A fixed temperature boundary condition of 972 K is imposed on the outer surface of fuel. Figure 8.11 shows the comparison with analytical solution for different grids.

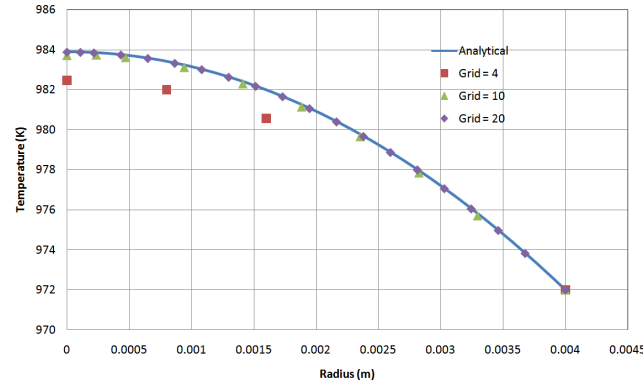


Figure 8.11: Temperature Profile for Radial Heat Conduction

8.8.2 Test Case 02: Axial Heat Conduction with Internal Heat Generation

To assess the performance of FUEL Heat Conduction Module a test case with only axial heat conduction is considered. A fuel pin of length 1000 mm and diameter 20 mm is heated uniformly with constant the volumetric heat generation rate of 10^5 W/m^3 . A fixed temperature boundary condition of 972 K is imposed on either ends of the fuel pin. The fuel surface is assumed to be insulated. Figure 8.12 shows the comparison with analytical solution.

8.8.3 Test Case 03: 1D Single Phase Water Flow (Isothermal Condition)

A vertical pipe is initially assumed to be filled with water at 295.5 K . Water injection is then started from the bottom at a fixed flow rate at the same temperature. The evolution of pressure at different cells is compared with RELAP5 results as shown in Figure 8.13.

8.8.4 Test Case 04: 1D Single Phase Water Flow (Non-Isothermal Condition)

A vertical pipe is initially assumed to be filled with water at 295.5 K . Water injection is then started from the bottom at a fixed flow rate at a specified temperature. The water injection velocity is maintained constant at 0.1 m/s . The evolution of temperature at different cells is compared with the predictions of RELAP5. Figure 8.14 shows the evolution of temperature of nodes for injection water temperature higher than the initial water temperature and the comparison with the results obtained with RELAP5. Similarly Figure 8.15 shows the evolution of temperature of cells for injection water temperature lower than the initial water temperature.

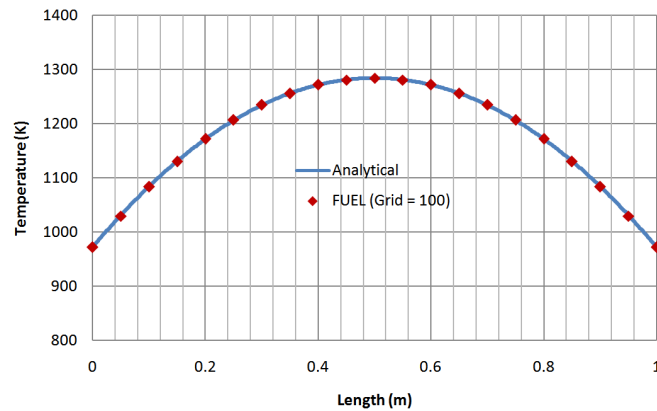


Figure 8.12: Temperature Profile for Axial Heat Conduction

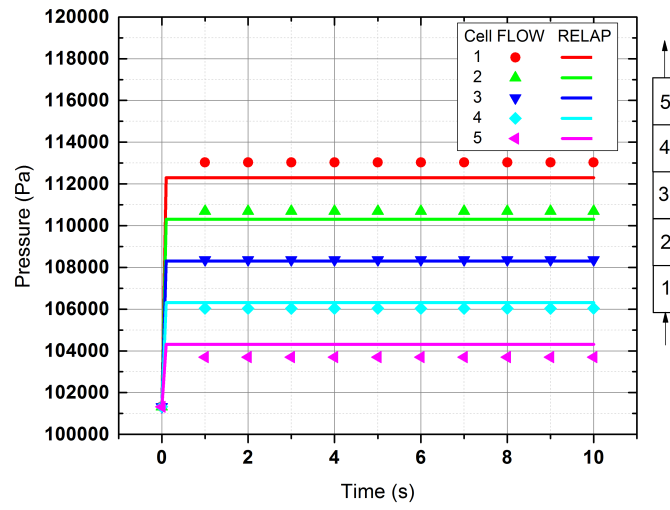


Figure 8.13: Fluid Pressure Transient for Isothermal Water Injection

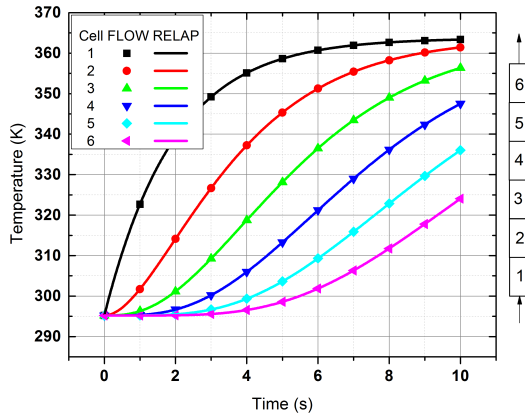


Figure 8.14: Fluid Temperature Transient for Water Injection at 363 K at 0.1m/s

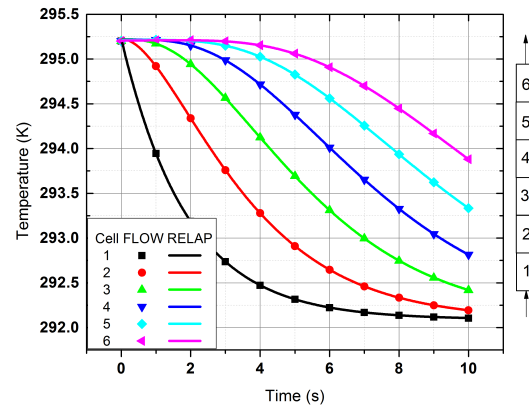


Figure 8.15: Fluid Temperature Transient for Water Injection at 292.2 K at 0.1m/s

8.8.5 Test Case 05: 1D Single Phase Steam Flow (Isothermal Condition)

A vertical pipe is initially assumed to be filled with steam at 430.0 K. Steam injection is then started from the bottom at a fixed flow rate at the same temperature. The evolution of pressure at different cells is compared with RELAP5 as shown in Figure 8.16.

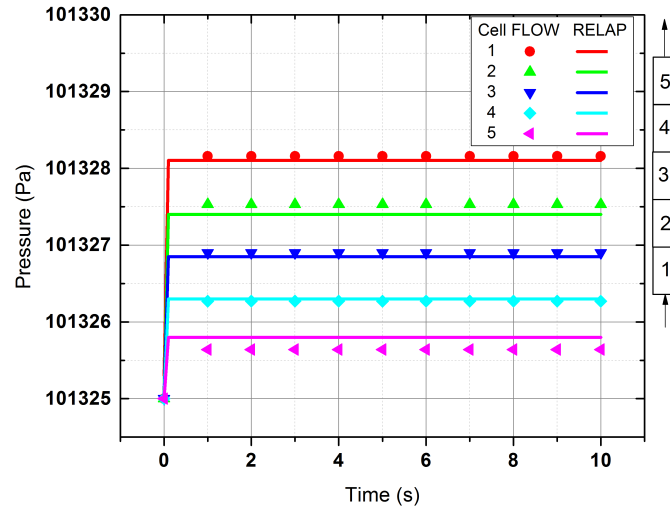


Figure 8.16: Fluid Pressure Transient for Isothermal Steam Injection

8.8.6 Test Case 06: 1D Single Phase Steam Flow (Non-Isothermal Condition)

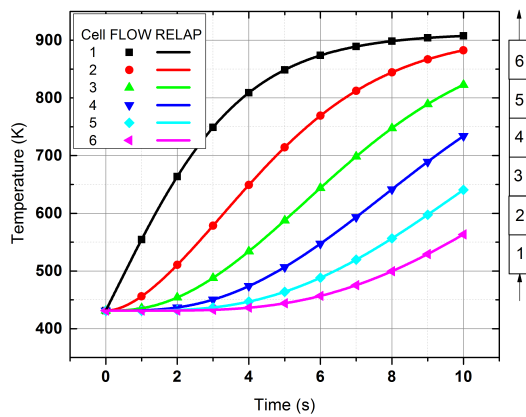


Figure 8.17: Fluid Temperature Transient for Water Injection at 930 K at 0.1m/s

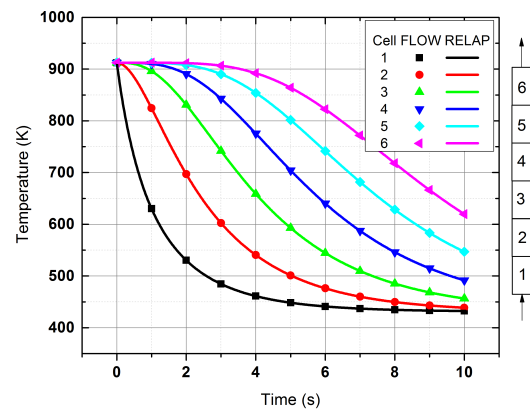


Figure 8.18: Fluid Temperature Transient for Water Injection at 430 K at 0.1m/s

The Single Phase Steam Flow case is validated by considering a vertical pipe to be initially filled with steam at 430 K. Steam injection is then started from the bottom at a fixed flow rate at 930 K. The injection velocity is maintained constant at 0.1 m/s. The evolution of temperature at different cells is shown in

Figure 8.17. Similarly the evolution of temperature at cells for the injection of low temperature steam at 430 K into high temperature steam at 915 K is shown in Figure 8.18.

8.8.7 Test Case 07: Water Fill Test

To validate the two phase heat and mass transfer at the interface between the two phases Two Phase Pipe Fill test was considered. The pipe is initially filled with superheated steam with 10^0C superheat at atmospheric pressure. Water injection is then started from the bottom of the pipe with a fixed flow velocity of 0.1 m/s and with a sub-cooling of 20^0C . The effect of heat transfer at the interface between the superheated steam and sub-cooled water has been considered. The evolution of the void fraction at different cells of the pipe is compared with the prediction of RELAP5 simulations as shown in Figure 8.19. The evolution of void fraction matches well with the RELAP5 predictions. Similarly to validate the two phase pressure drop models used in FLOW Module the pressure variation along the length of the pipe is compared with the RELAP5 results as shown in Figure 8.20.

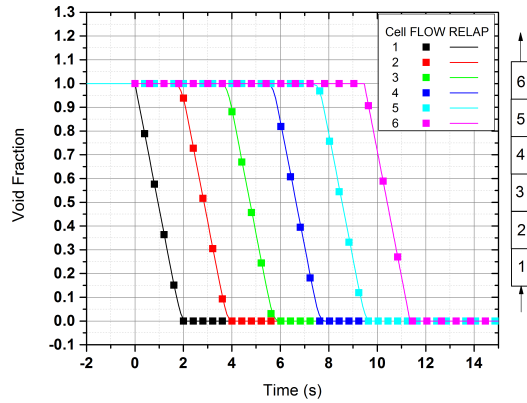


Figure 8.19: Void Fraction Transient for Water Injection into Steam Filled Pipe

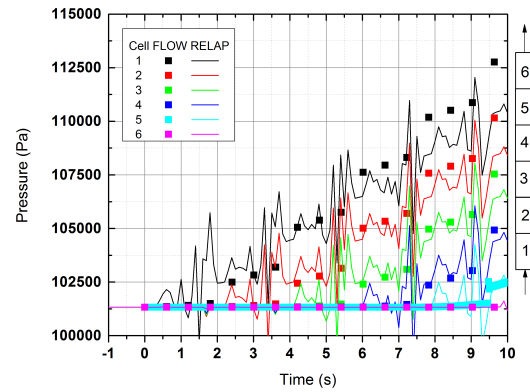


Figure 8.20: Pressure Transient for Water Injection into Steam Filled Pipe

8.8.8 Test Case 08: 2D Single Phase Water Flow with Cross-Flow

Two parallel channels of 1.2 m length, each with 0.0316 m^2 flow area, divided into 6 control cells along the length are considered. The adjacent volumes of the parallel channels are connected through cross-flow junctions to facilitate flow across the channels. One of the channels has reduced flow area in the second, third and fourth control volume as shown in Figure 8.21.

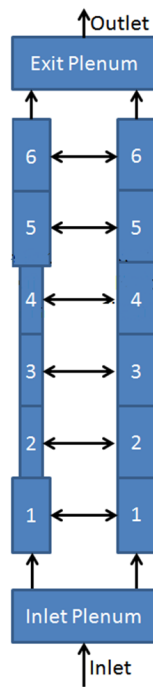


Figure 8.21: Nodalization of Flow Path for Cross-Flow of Water (Simulation with FLOW)

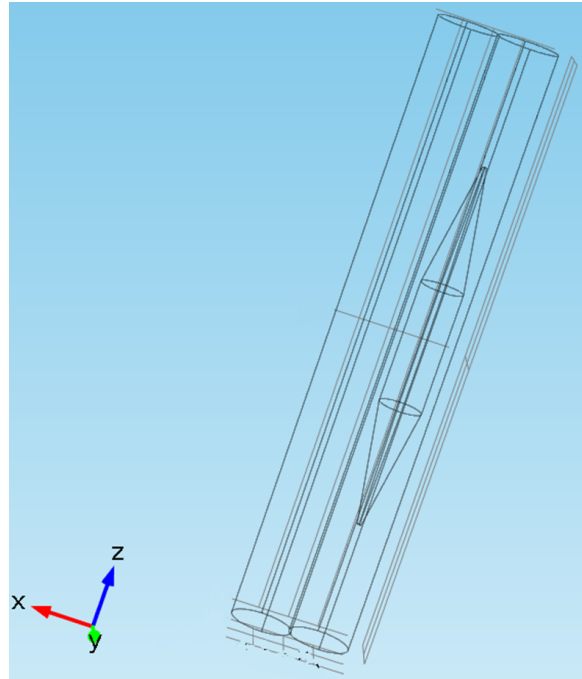


Figure 8.22: COMSOL Domain for Simulation of Cross-Flow of Water

Three-dimensional (3D) simulations are carried out in COMSOL for comparison. The domain considered for the 3D simulation is shown in Figure 8.22. Flow area reduction is created by inserting a solid object within one of the channels. To estimate extent of cross-flow taking place, the channels are initially considered to be filled with water at 290 K and water injection is started at 0.05 m/s through

both channels. Figure 8.23 shows the cross-flow velocity at the cross-flow junctions of FLOW module and comparison with the velocity at corresponding points in the 3D domain of COMSOL. The velocities are found to be very close to each other. The velocities are also significant in magnitude as compared to the axial inlet velocity suggesting that significant radial flow exists.

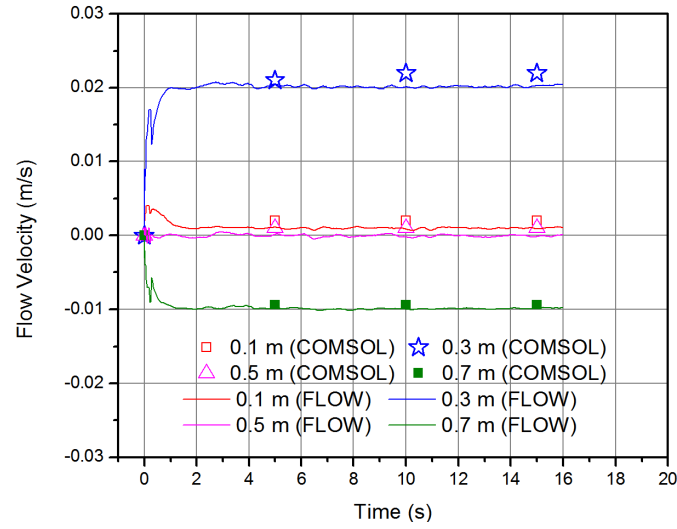


Figure 8.23: Velocities at Cross-Flow Junctions in FLOW and comparison with COMSOL

8.8.9 Test Case 09: Property Values at Different States of System

The property subroutine is validated against a set of property values given in the IAPWS Data sheets. Some of the values are shown in Table 8.3. The property values predicted by the subroutine are found to be accurate up to 6th decimal place.

Table 8.3: Comparison of Properties cCalculated by PROP Subroutine with Reference Values in IAPWS Tables

Temperature (K)	Pressure (kPa)	State	Reference Density (kg/m ³)	Density (PROP) (kg/m ³)	Reference Enthalpy (kJ/kg)	Enthalpy (PROP) (kJ/kg)
275	0.6984	L	999.887	999.887	7.7597	7.7597
275	0.6984	V	0.0551	0.0551	2504.29	2504.29
450	932.2035	L	890.341	890.341	749.1616	749.1616
450	932.2035	V	4.8120	4.8120	2774.41	2774.41
625	16908.2693	L	567.09	567.09	1686.27	1686.27
625	16908.2693	V	118.29	118.29	2550.71	2550.71

8.8.10 Test Case 10: Performance of New Water Packing Mitigation Scheme

As discussed in Section 8.2, the numerical phenomena of water packing causes artificial spikes in the prediction of pressure for a cell which is approaching null void condition. This is shown in Figure 8.24, depicting pressure variation of few cells of a vertical pipe (divided in 8 cells) which is being filled with water. The artificial pressure spikes are an order of magnitude higher, reaching up to 2500kPa , than the system pressure of 400kPa . The pressure spike, which is numerically generated only in the cell that is approaching null void condition, also gets propagated to the connected cells. In a network of large number of cells connected to each other, a pressure disturbance of such a magnitude can cause artificial pressure oscillations

through all the cells.

The water packing mitigation scheme used in RELAP and TRACE (a version of RELAP maintained by USNRC) is based on use of an artificial multiplier for reducing the magnitude of pressure spike. The above test case of water filling, when simulated using RELAP shows significant reduction in the pressure spikes as shown in Figure 8.25. The magnitude of pressure spikes is still 20 % of the system pressure.

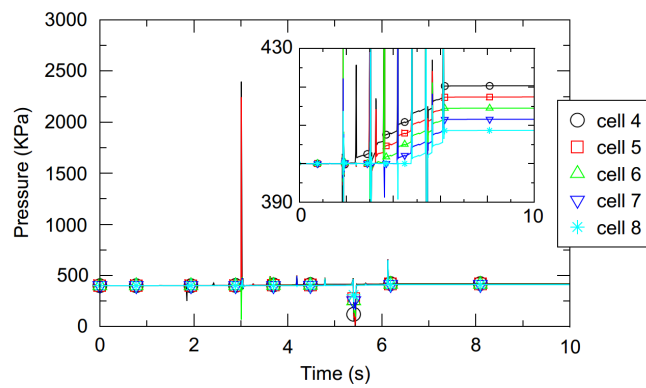


Figure 8.24: Pressure Prediction without any Water Packing Mitigation Scheme [45]

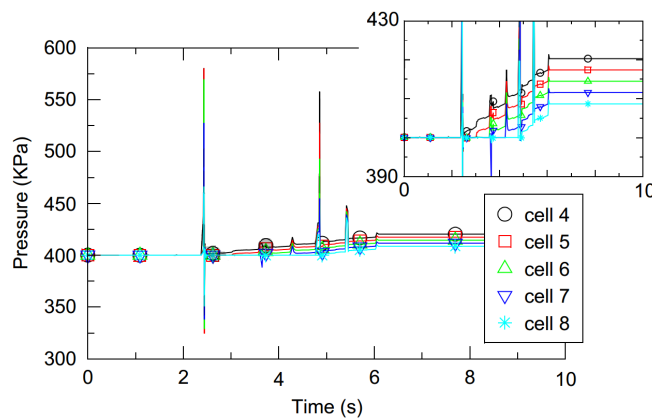


Figure 8.25: Pressure Prediction with Water Packing Mitigation Scheme of TRACE (RELAP) [45]

Figure 8.26 shows the variation of pressure with new water packing mitigation scheme for a pipe fill test case and its comparison with RELAP5 prediction. It

can be seen that the pressure spikes are altogether eliminated with the use of new water packing mitigation scheme.

8.9 Simulations of Reactor Core Quenching Experiments

As discussed in Chapter 3, several experiments have been performed by various researchers to study the quenching of a reactor core. For most of these experiments, the experimental data are well documented and are available in open literature. These experimental investigations are used for benchmarking of the PDRCR code. The experiments are divided into two categories, viz. Experiments with Intact Rod Geometry and Experiments with Ballooned Rod Geometry. SEFLEX Series of experiments have been chosen for assessment of PDRCR prediction because of their simplicity to model and availability of sufficient data. SEFLEX encompasses experiments with Intact Rod Geometry as well as experiments with Ballooned Rod Geometry.

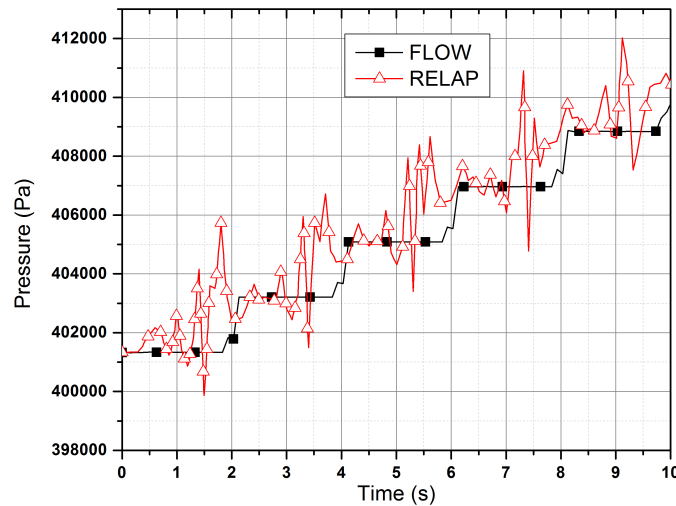


Figure 8.26: Pressure Prediction with New Water Packing Mitigation Scheme of PDRCR

8.9.1 Comparison with Intact Rod Experiments - Single Flow Path simulation in PDRCR

For the case of experiments with intact rod geometry, the blockages throughout the flow cross-section are uniform. Hence, the velocities in the cross-flow directions are expected to be small. Thus, the experimental test setup can be modeled as a single flow path in PDRCR. The models for cross-flow in FLOW and subsequently the heat transfer calculation due to cross-flow in HTC are switched off.

8.9.1.1 SEFLEX Series I Experiments

SEFLEX Series I experiments consist of a set of tests performed on a 5 X 5 fuel pin matrix with straight, non-ballooned, indirectly heated fuel pins [30]. The matrix is enclosed in square SS shroud of 6.5 mm thickness. The fuel pins are electrically heated to specified surface temperature and quenching at specific pressure is started with specific water injection rate. The initial condition of the setup, water injection rate, axial power profile, geometry of the test section as well as the material of construction used for the fuel pins are simulated in the PDRCR Code. The process parameters used for the SEFLEX Series I Tests are tabulated in Table 8.4. Geometrical details used in PDRCR code and details of discretization are provided in Table 8.5. The results obtained for Test 4 are compared with the predictions of PDRCR code and a detailed discussion is provided in following section.

Comparative Results for SEFLEX Series I Test 4

Figure 8.27 shows the input power curve used for Test 4 and its comparison with power curve used by PDRCR. The PDRCR code is run initially for 150 s to achieve steady-state temperature distribution same as that used in Test 4. The initial temperature distribution along the length of fuel pin is compared in Figure 8.28. Figure 8.29 shows the inlet flow rate for Test 4 and its comparison with the

PDRCR simulation. With injection of water into the test section, the nodes of fuel clad get cooled one by one. Figure 8.30 shows the comparison between the clad temperatures as measured in the experiment and the calculated clad temperatures obtained from PDRCR. The quench time prediction of PDRCR is found to be in good agreement with the experimental data within 7.5% error. Figure 8.31 shows the temperature variation of a single point on the clad. The clad temperature shows intermediate spikes as the PDRCR code switches from one heat transfer regime to other. Such spikes are also observed in simulation with RELAP5 (refer Figure 5.3 to Figure 5.6) are attributed to transition between heat transfer regimes. As the point gets cooled the variation of heat transfer coefficients to steam and water pertaining to different heat transfer regimes are shown in Figure 8.32. Figure 8.33 shows the axial temperature distribution in Fuel and Clad at a particular time instant. Sharp temperature gradient exists near the quench front. This is also evident from Figure 8.34 showing the temperature distribution along the radius of fuel at different axial locations in the vicinity of the quench front location. The radial temperature distribution within the FPS shows large temperature drop across the fuel-clad gap as expected. The temperature gradient within the fuel pellet is low as expected for low heat rate (simulating decay heat). Figure 8.35 shows the evolution of radial temperature profile for the axial location at 2000 mm from top. The quenching of Shroud and its comparison with experimental data are shown in Figure 8.36.

General trend of fuel clad quenching and the time of quenching are well captured by PDRCR. The comparison of various experimental results from different tests of SEFLEX Series with PDRCR prediction is shown in Figure 8.37 through Figure 8.42.

Table 8.4: Process Parameters for SEFLEX Series I Tests

Test No.	Downstream Pressure (bar)	Injection Velocity (mm/s)
3	4.1	38
4	4.1	58
5	2.1	38
6	2.1	58

Table 8.5: Geometrical Parameters and Discretization Details for Simulation with PDRCR

Parameter	Unit	Value
Fuel Pellet OD	mm	9.2
Clad ID	mm	9.3
Clad OD	mm	10.75
Radial Nodes in Fuel	-	7
Radial Nodes in Clad	-	2
Axial Nodes	-	100
No of Fuel Pins	-	1 (representing all 25 pins)
Shroud Width	mm	78.5
Shroud Thickness	mm	6.5

Parameter	Unit	Value
Radial Nodes in Shroud	-	2

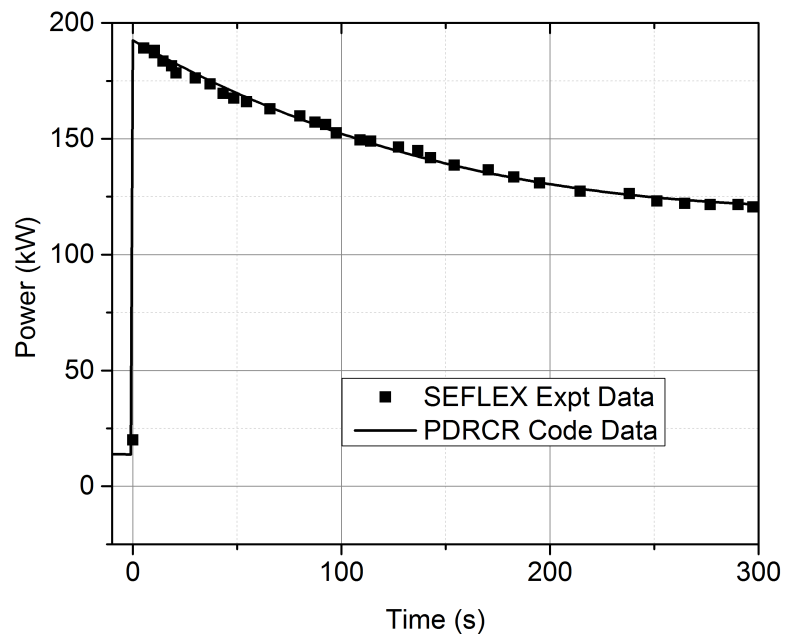


Figure 8.27: Input Power Curve (Comparison of SEFLEX Series I Test 4 and PDRCR Code)

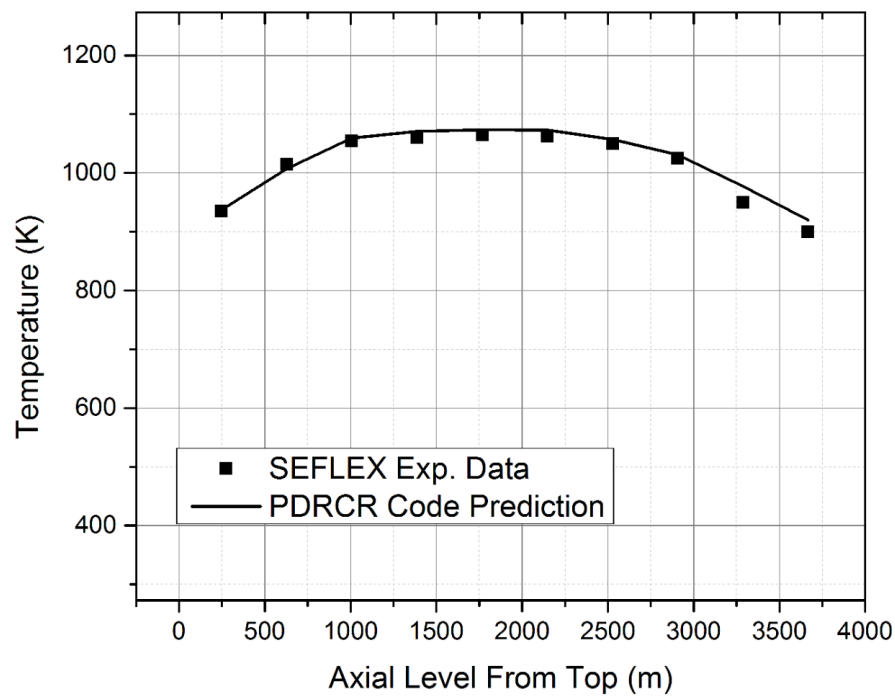


Figure 8.28: Initial Axial Temperature Distribution (Comparison of SEFLEX Series I Test 4 and PDRCR Code)

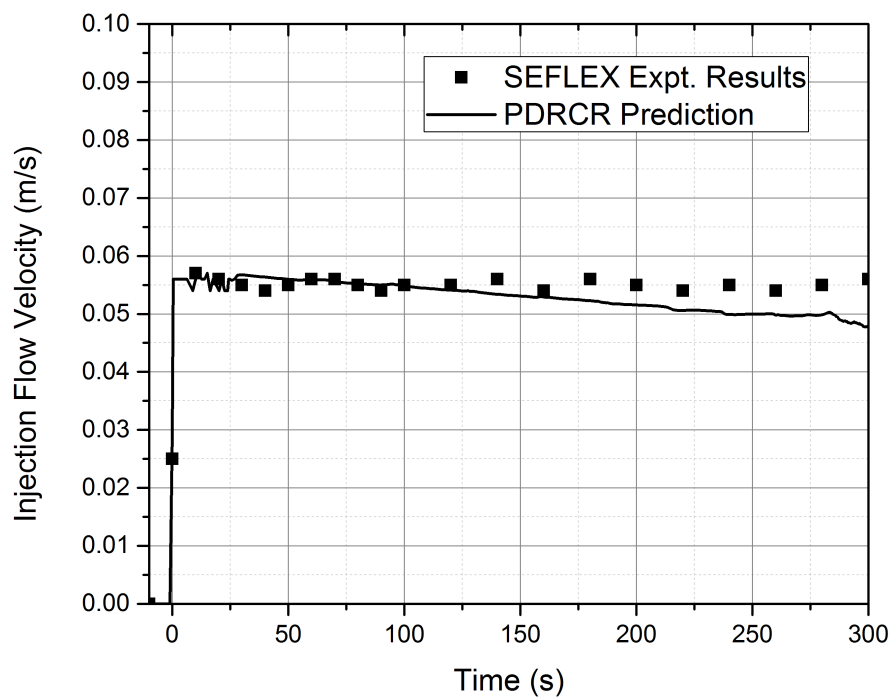


Figure 8.29: Inlet Flow Rate (Comparison of SEFLEX Series I Test 4 and PDRCR Code)

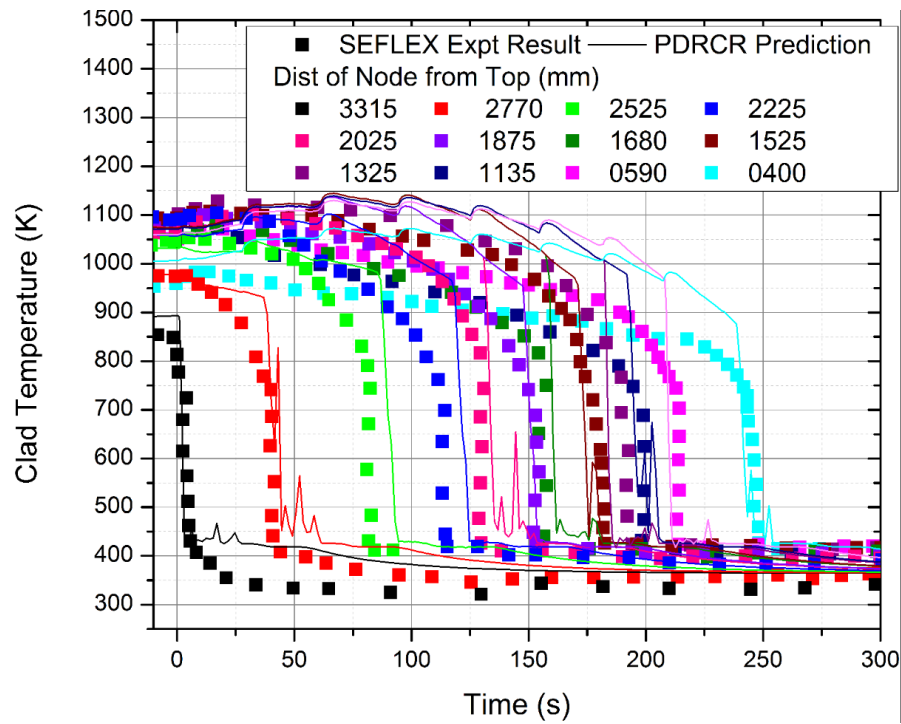


Figure 8.30: Clad Temperature at various Axial Locations
(Comparison of SEFLEX Series I Test 4 and PDRCR Code)

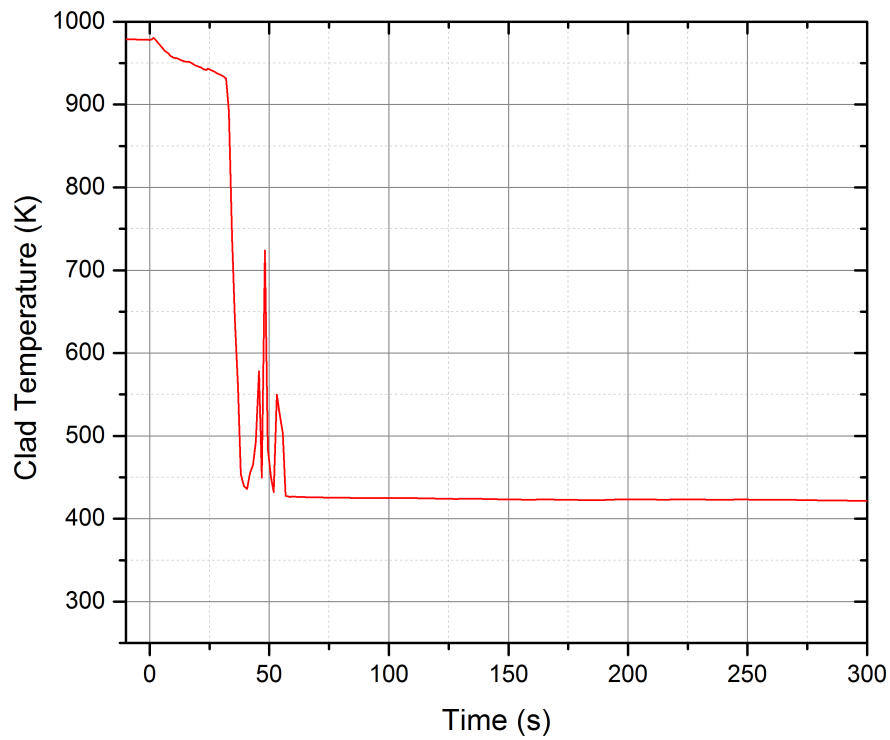


Figure 8.31: Clad Temperature Variation at axial location of 2270 mm

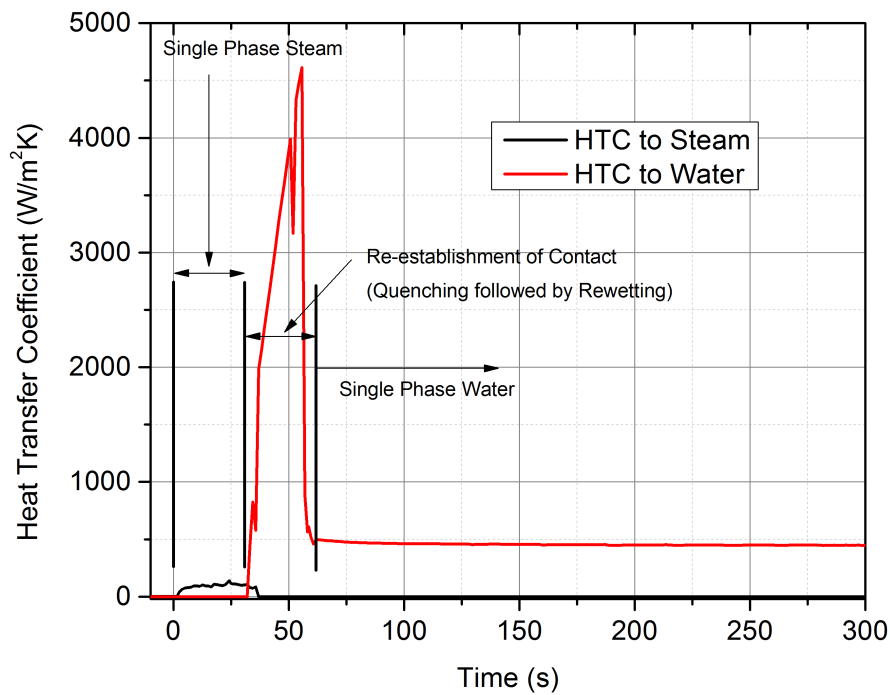


Figure 8.32: Variation of Heat Transfer Coefficients at axial location of 2270 mm

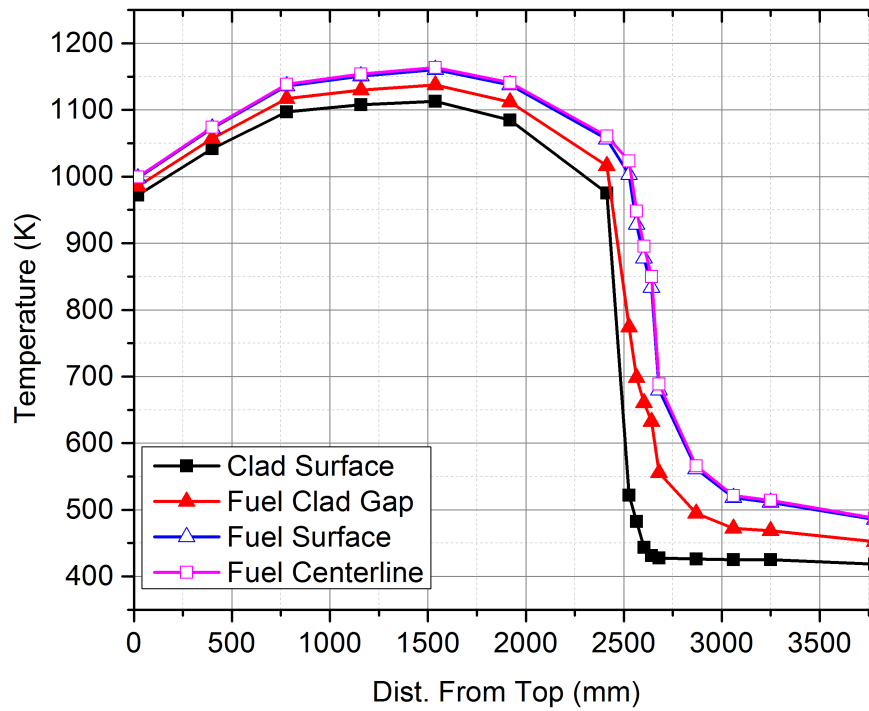


Figure 8.33: Axial Clad Temperature Distribution at $t = 100$ s

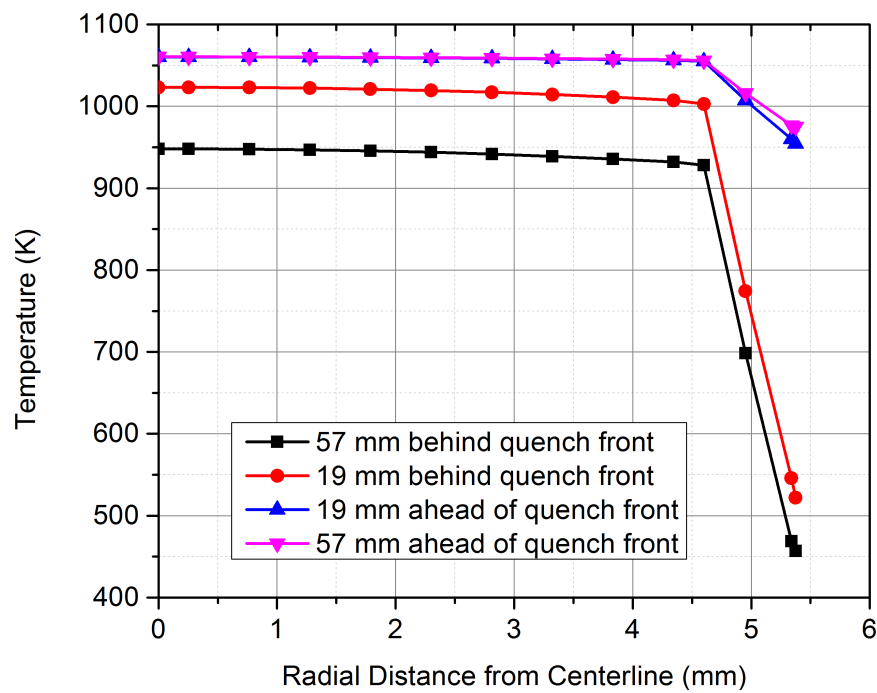


Figure 8.34: Radial Temperature Distribution at $t = 100$ s

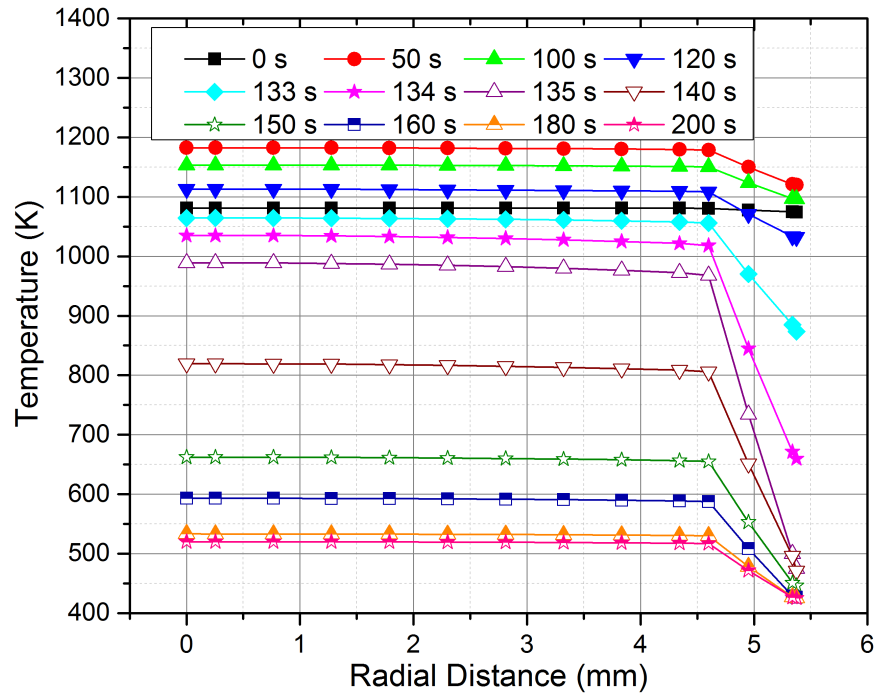


Figure 8.35: Evolution of Radial Temperature Distribution

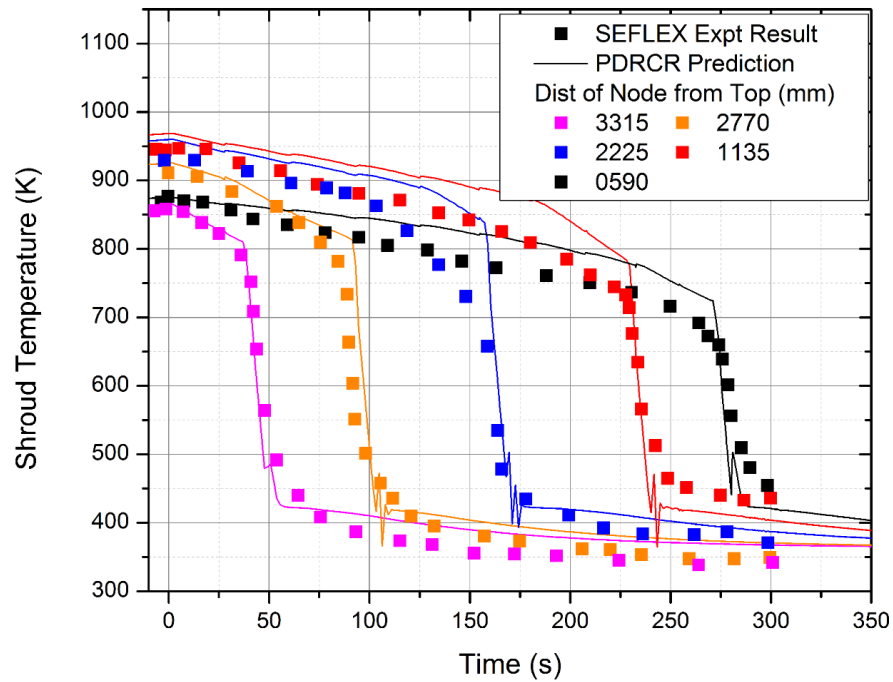


Figure 8.36: Shroud Temperature at various Axial Locations (Comparison of SEFLEX Series I Test 4 and PDRCR Code)

Comparative Results for SEFLEX Series I Test 3

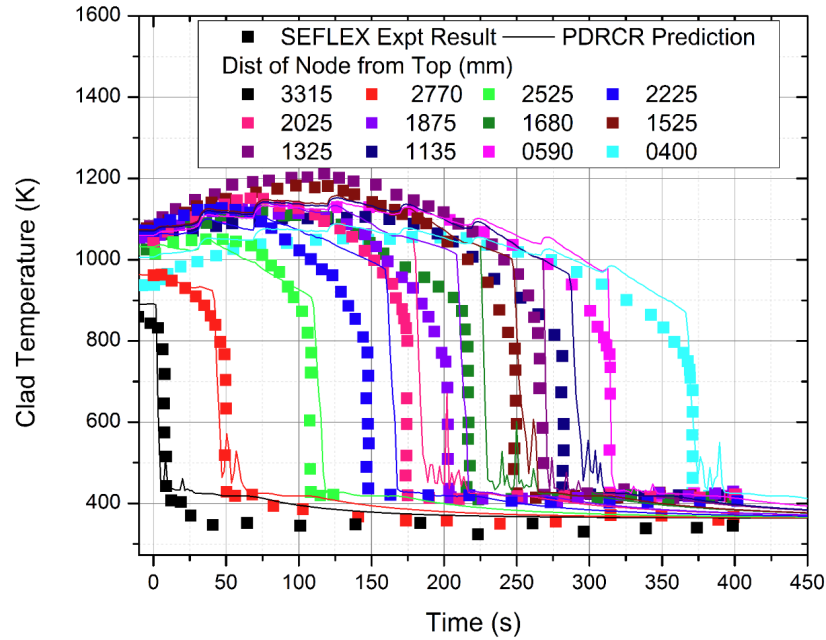


Figure 8.37: Clad Temperature at various Axial Locations
(Comparison of SEFLEX Series I Test 3 and PDRCR Code)

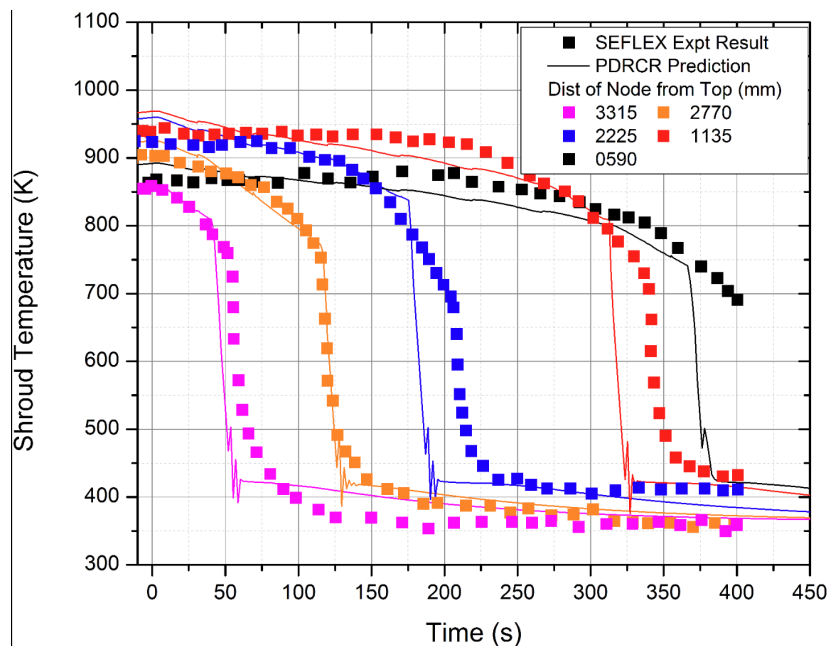


Figure 8.38: Shroud Temperature at various Axial Locations
(Comparison of SEFLEX Series I Test 3 and PDRCR Code)

Comparative Results for SEFLEX Series I Test 5

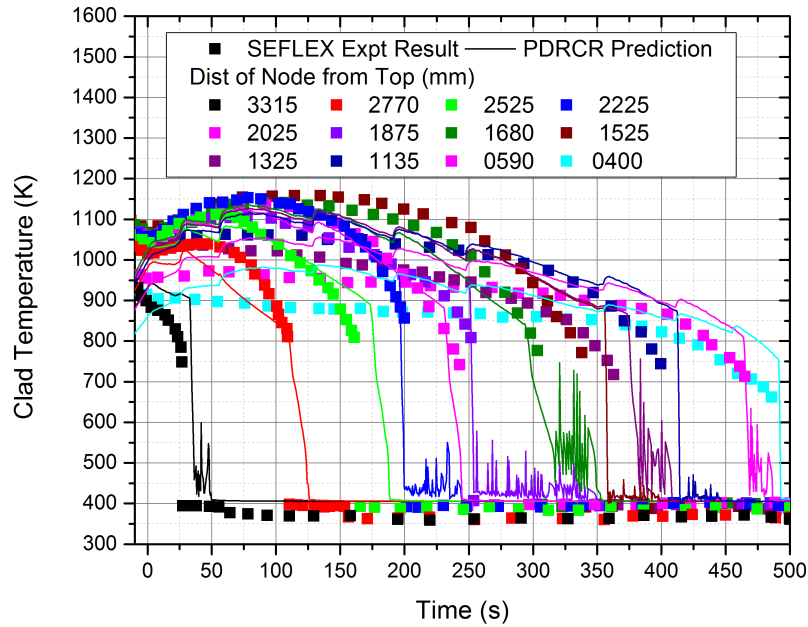


Figure 8.39: Clad Temperature at various Axial Locations
(Comparison of SEFLEX Series I Test 5 and PDRCR Code)

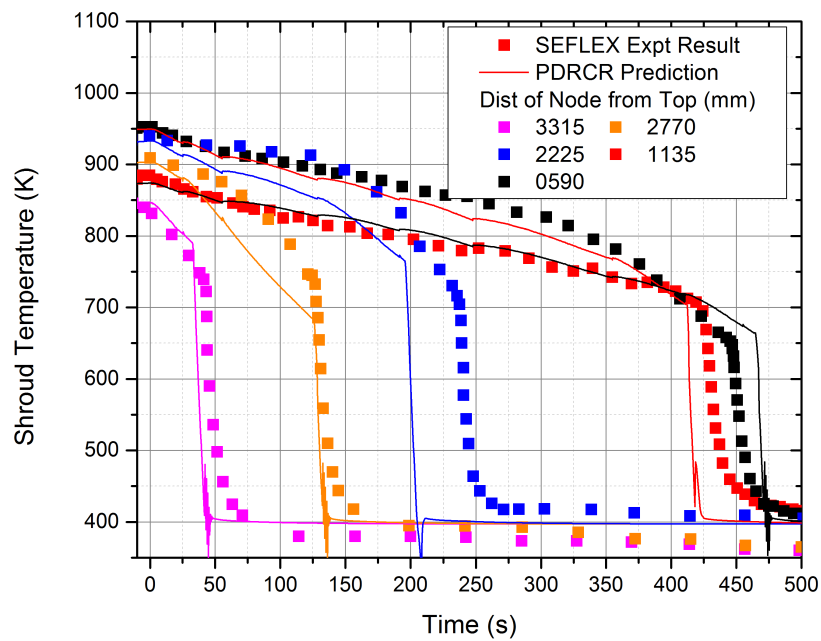


Figure 8.40: Shroud Temperature at various Axial Locations
(Comparison of SEFLEX Series I Test 5 and PDRCR Code)

Comparative Results for SEFLEX Series I Test 6

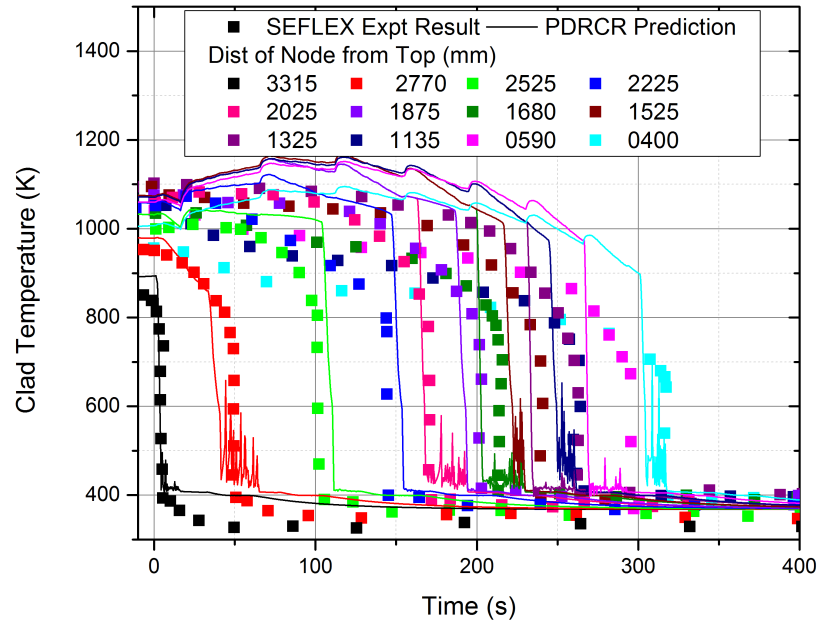


Figure 8.41: Clad Temperature at various Axial Locations
(Comparison of SEFLEX Series I Test 6 and PDRCR Code)

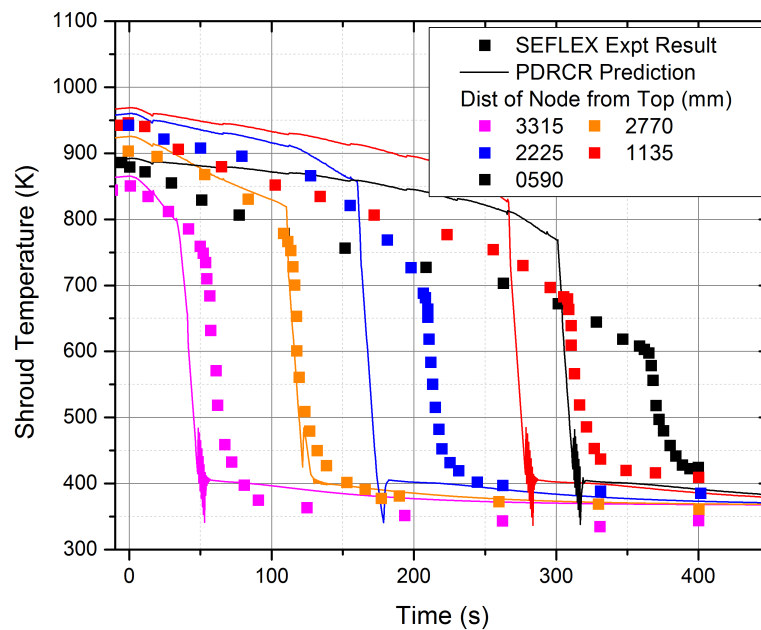


Figure 8.42: Shroud Temperature at various Axial Locations
(Comparison of SEFLEX Series I Test 6 and PDRCR Code)

8.9.2 Comparison with Intact Rod Experiments - Parallel Flow Path Simulation in PDRCR

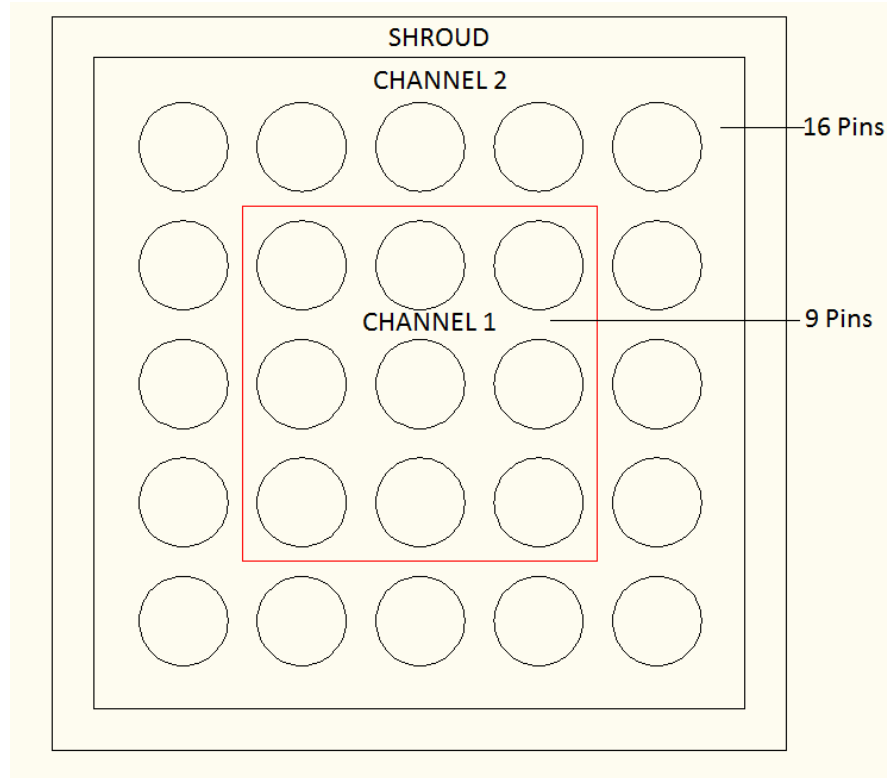


Figure 8.43: Selection of Channels for SEFLEX Simulation

To assess the magnitude of the cross-flow velocities in Intact Rod experiments and its effect on quench patterns, the SEFLEX Series I Test 4 is further modeled with two parallel channels configuration in PDRCR. Figure 8.43 shows the cross-section of SEFLEX Series I Test 4 experimental setup and selection of flow areas for modeling in PDRCR. The geometrical parameters and details of simulation in PDRCR are given in Table 8.6.

Table 8.6: Geometrical Parameters and Discretization Details for Simulation of SEFLEX with 2 Channels in PDRCR

Parameter	Unit	Channel 1	Channel 2
Fuel Pellet OD	mm	9.2	9.2
Clad ID	mm	9.3	9.3
Clad OD	mm	10.75	10.75
Radial Nodes in Fuel	-	7	7
Radial Nodes in Clad	-	2	2
Axial Nodes in Fuel	-	100	100
Axial Nodes in Fluid	-	10	10
No of Fuel Pins	-	1 (representing 9 pins)	1 (representing 16 pins)
Flow Area	sq mm	1020.6	2869.7
Hydraulic Diameter	mm	13.4	13.4
Shroud Width	mm	78.5	
Shroud Thickness	mm	6.5	
Radial Nodes in Shroud	-	2	

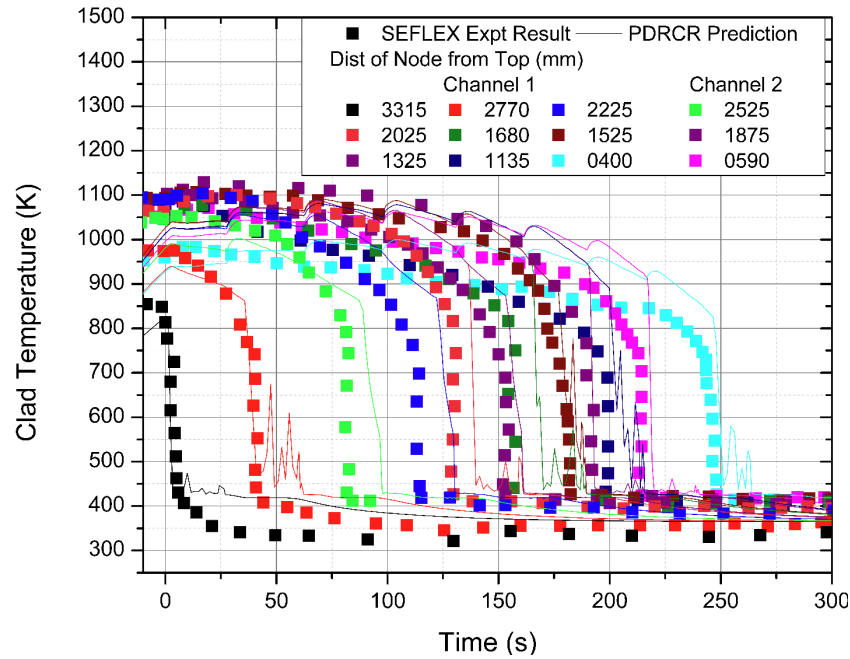


Figure 8.44: Clad Temperature at various Axial Locations
(Comparison of SEFLEX Series I Test 4 and PDRCR Code with two channels)

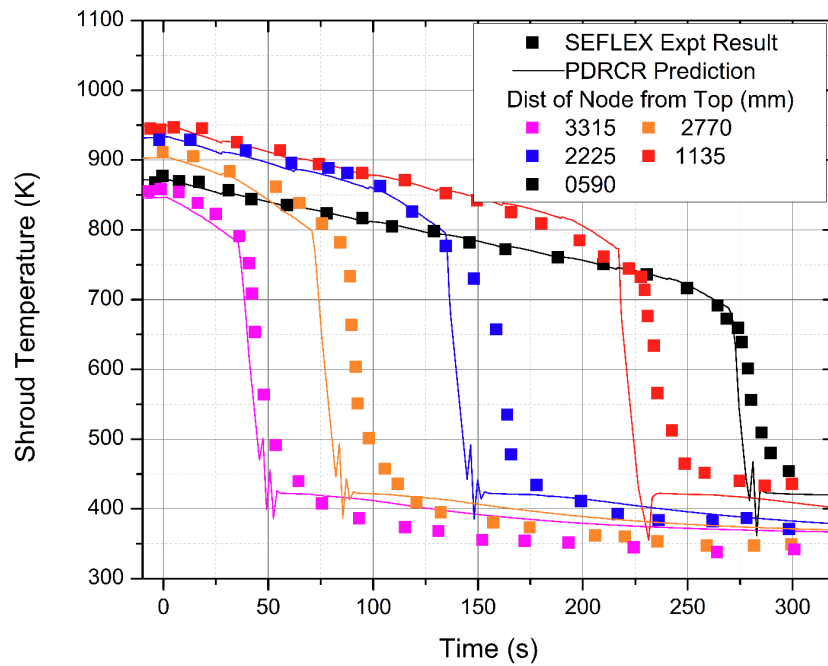


Figure 8.45: Shroud Temperature at various Axial Locations
(Comparison of SEFLEX Series I Test 4 and PDRCR Code with two channels)

Figure 8.44 and Figure 8.45 show the variation of Clad temperature and Shroud Temperature at various locations. It can be observed from Figure 8.44 that the clad prediction matches well for fuel pins in Channel 1 as well as those in Channel 2. The quenching of shroud is found to be earlier than observed in the experiments as shown in Figure 8.45. The representative pins of channel 1 and channel 2 and the shroud are modeled as three individual structure in PDRCR as against single channel configuration explained in Section 8.9.1.1 where only a single pin and a shroud are modeled as structures. Because of the changes in view factors and average temperatures of representative pins, the radiative heat flux received by the shroud (which is the only heat source for the shroud) is slightly lower than the single-channel-configuration. Hence, the shroud is predicted to get quenched earlier than the prediction for single-channel-configuration case.

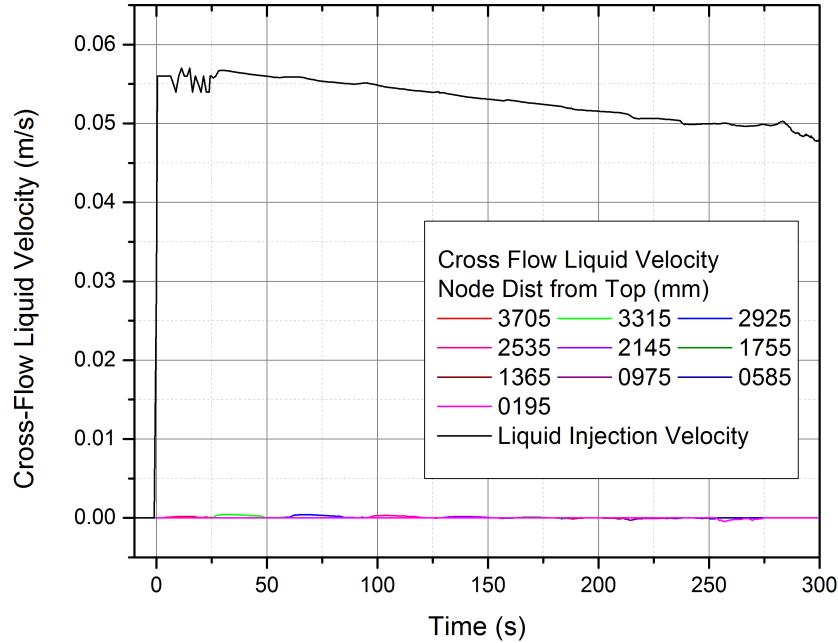


Figure 8.46: Cross-Flow Water Velocity at various Axial Locations (PDRCR with two channels)

The cross-flow velocities of Water and Steam at all the nodes are shown in Figure 8.46 and Figure 8.47, respectively. It can be seen that the magnitudes of water velocities at the cross-flow junctions are much smaller as compared to the

water injection velocity at the inlet of the test section.

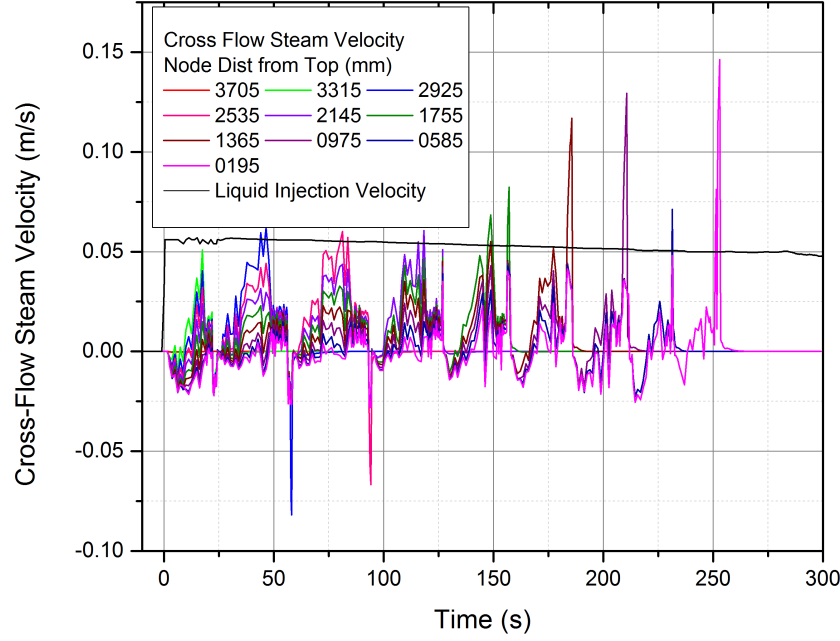


Figure 8.47: Cross-Flow Steam Velocity at various Axial Locations (PDRCR with two channels)

The steam flow velocity magnitudes are comparable to the water injection velocity and hence, the mass flux at cross-flow junctions because of steam flow is negligible as compared to inlet mass flux. Thus it can be inferred that the cross-flow effects are indeed negligible in experiments with intact rod geometry (without ballooning).

8.9.3 Comparison with Ballooned Rod Experiments

Since in these experiments, the flow blockages are not uniform through the flow cross-section, the cross-flow is expected to be significant. The experiments are thus modeled in PDRCR as two parallel channels. The cross-flow models are switched on in FLOW to simulate the cross-flow between the two flow paths. The HTC module takes care of the heat transfer due to cross-flow. SEFLEX Series III Test 35 has been selected for comparison. The geometrical parameters and discretization details are as given in Table 8.6, except that in Channels 1 reduction in flow area

equivalent to 92% flow blockage is used for node 6.

Figure 8.48 and Figure 8.49 show the variation of Clad and Shroud Temperature respectively along with PDRCR prediction. The predictions match well with the SEFLEX experimental results.

The cross-flow steam velocities are shown in Figure 8.50. It can be seen that the steam velocities are comparable with injection fluid velocity. Hence the mass flux because of steam velocity is negligible as compared to inlet mass flux. However, the liquid velocity at the cross-flow junction is comparable with the injection velocity as shown in Figure 8.51. The mass flux at the cross-flow junction because of liquid is comparable with the inlet mass flux.

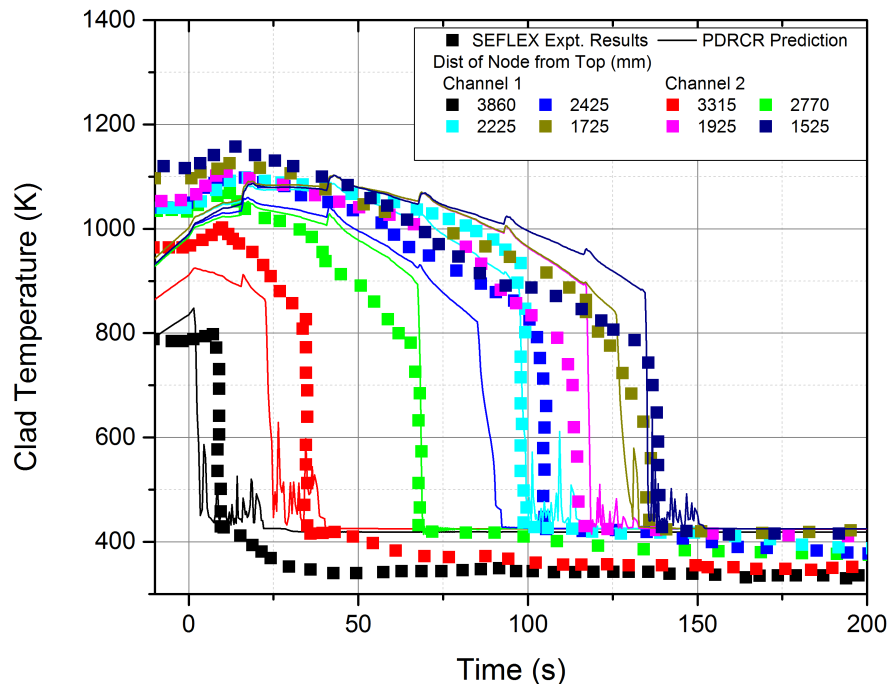


Figure 8.48: Clad Temperature at various Axial Locations
(Comparison of SEFLEX Series III Test 35 and PDRCR Code with
two channels)

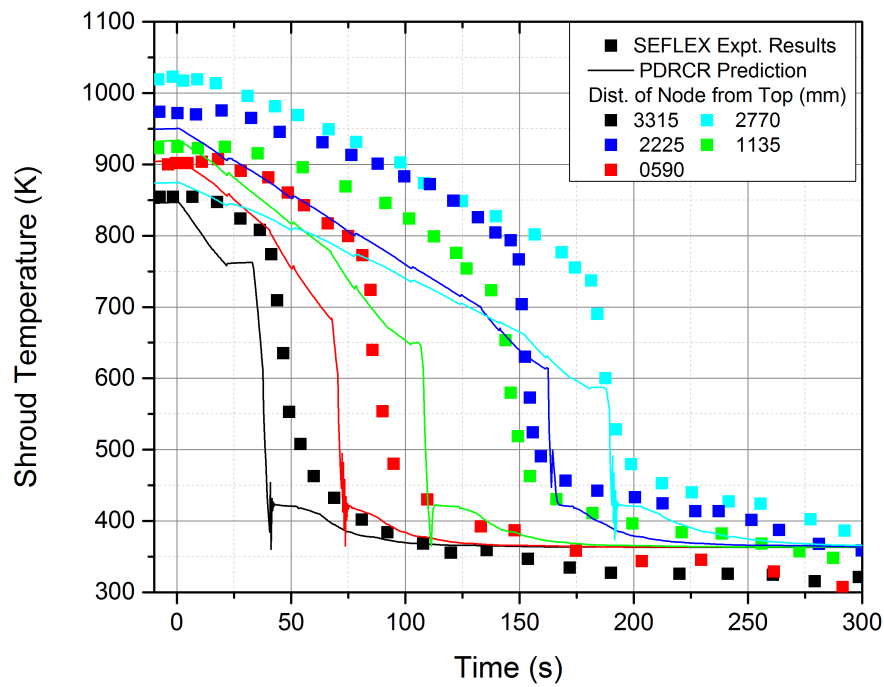


Figure 8.49: Shroud Temperature at various Axial Locations
(Comparison of SEFLEX Series III Test 35 and PDCRCR Code with two channels)

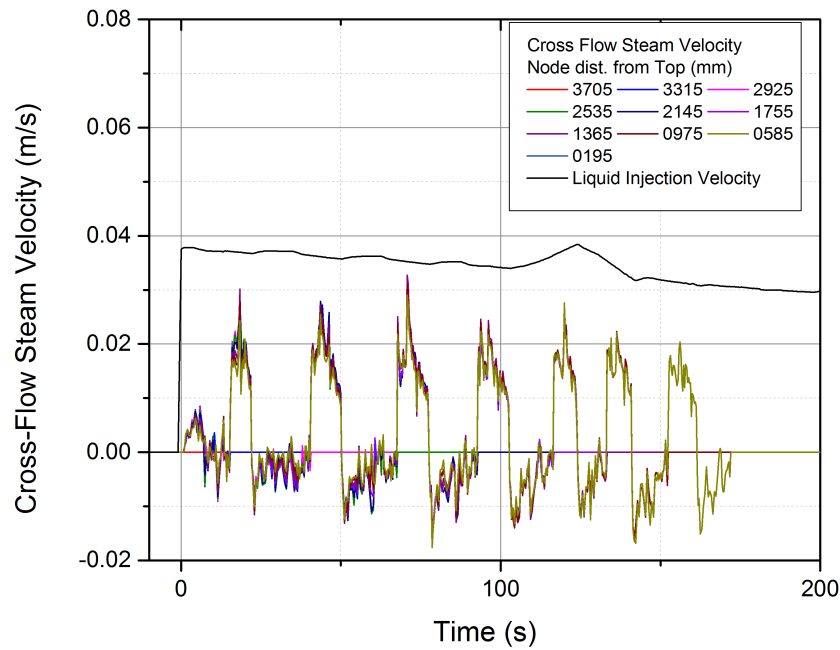


Figure 8.50: Cross-Flow Steam Velocity at various Axial Locations
(Comparison of SEFLEX Series III Test 35 and PDCRCR Code with two channels)

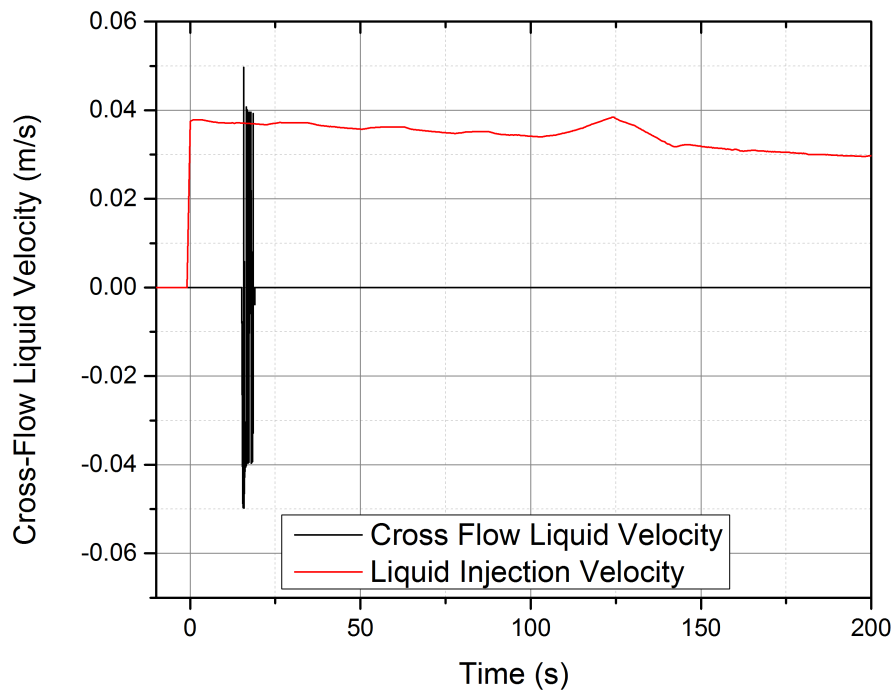


Figure 8.51: Cross-Flow Liquid Velocity at various Axial Locations (Comparison of SEFLEX Series III Test 35 and PDRCR Code with two channels)

8.10 Comparison of DRCRE Experimental Results with PDRCR Predictions

Table 8.7: Geometrical Parameters and Discretization Details for Simulation of DRCRE with 2 Channels in PDRCR

Parameter	Unit	Channel 1	Channel 2
Fuel Pellet OD	mm	6.95	6.95
Clad ID	mm	7.0	7.0
Clad OD	mm	11.0	11.0
Fuel Pellet OD (Ballooned FPS)	mm	14.0	-

Parameter	Unit	Channel 1	Channel 2
Clad ID (Ballooned FPS)	mm	10.0	-
Clad OD (Ballooned FPS)	mm	9.95.0	-
Radial Nodes in Fuel	-	7	7
Radial Nodes in Clad	-	2	2
Axial Nodes in Fuel	-	100	100
Axial Nodes in Fluid	-	10	10
No of Fuel Pins	-	1 (representing 25 pins)	1 (representing 32 pins)
Flow Area	sq mm	3249.6	9939.2
Hydraulic Diameter	mm	15.0	24.9
Shroud ID	mm	154.6	
Shroud Thickness	mm	6.8	
Radial Nodes in Shroud	-	2	

The test section of DRCRE experimental facility is modeled using PDRCR with 2 parallel channel configuration. The central region of 25 ballooned FPS is modeled as channel 1 and the peripheral region of 32 FPS is modeled as channel 2. Figure 8.52 shows the cross-section of the DRCRE test section and selection of flow areas for modeling in PDRCR. The geometrical parameters and details of simulation in PDRCR is given in Table 8.7.

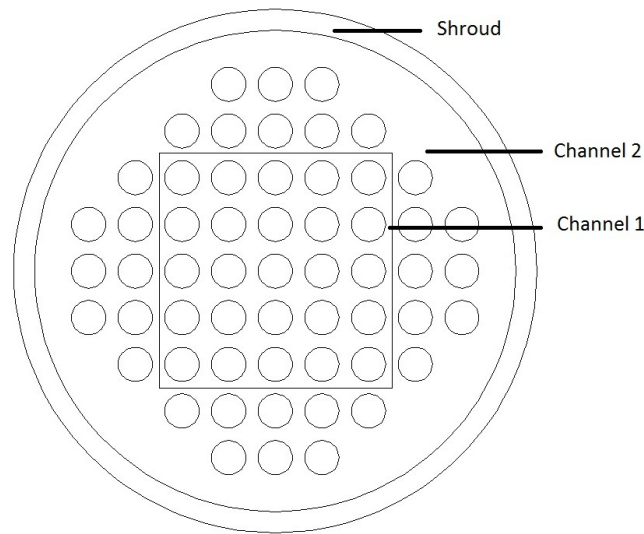
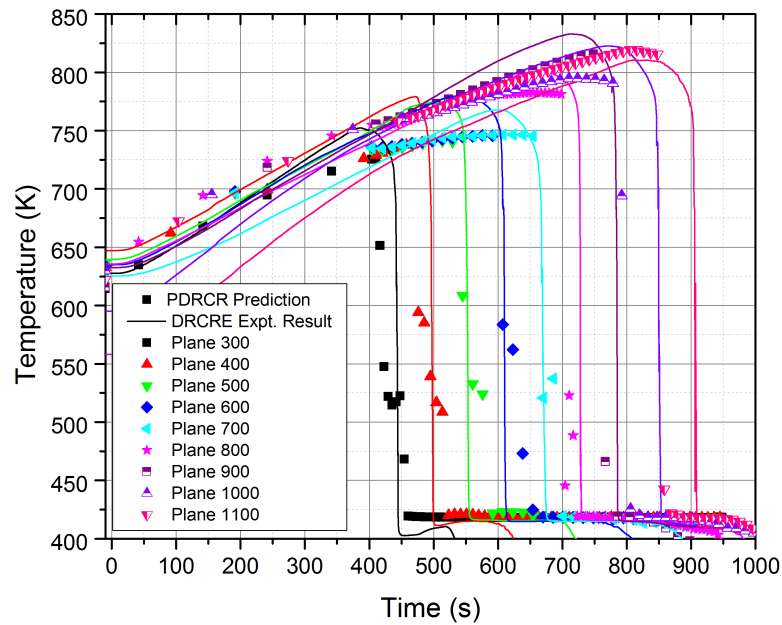
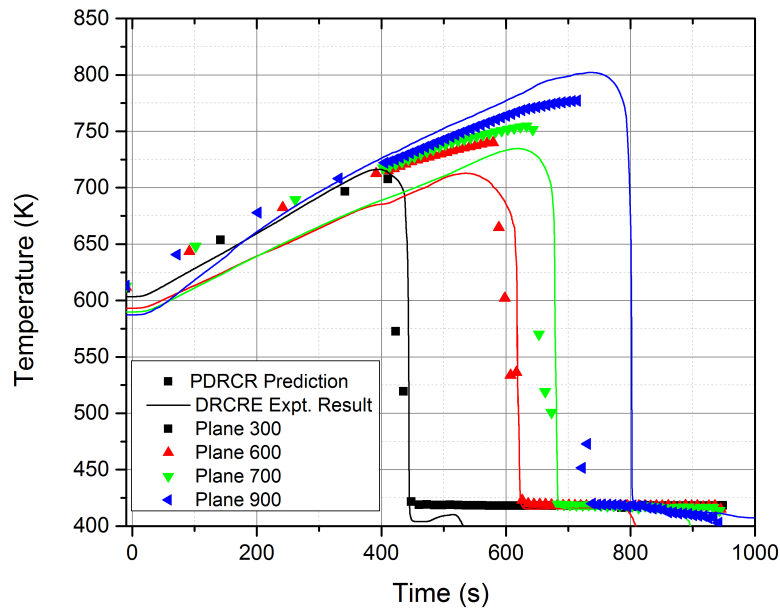


Figure 8.52: Selection of Channels for DRCRE Simulation

Figure 8.53 and Figure 8.54 show the comparison of DRCRE experimental results with PDRCR prediction for FPS clad and shroud, respectively. The predictions match well with the DRCRE results.



**Figure 8.53: Clad Temperature at various Axial Locations
(Comparison of DRCRE Test 31 and PDRCR Code with 2 channels)**



**Figure 8.54: Shroud Temperature at various Axial Locations
(Comparison of DRCRE Test 31 and PDRCR Code with 2 channels)**

Figure 8.55 shows the comparison of predicted cross-flow rate with injection flow rate at various elevations.

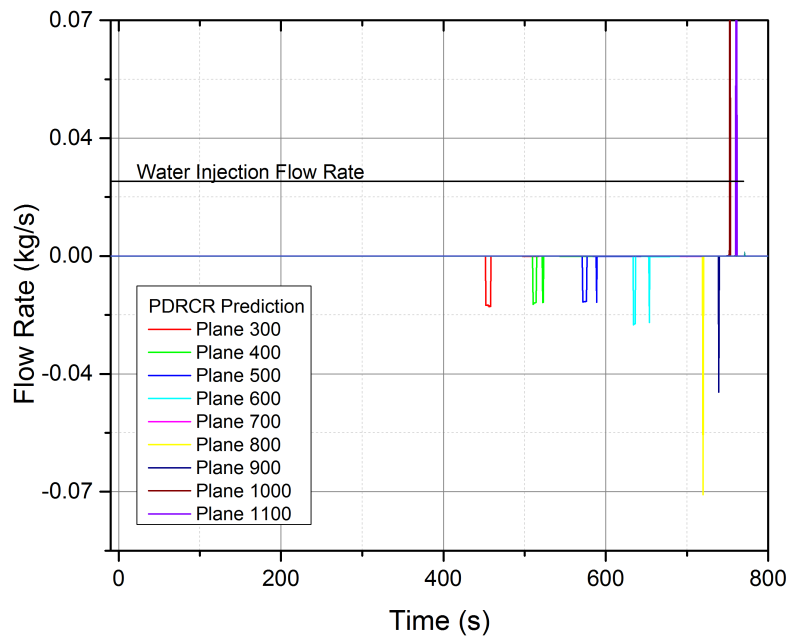


Figure 8.55: PDRCR Prediction of Cross-flow at various Axial Locations

8.11 Development of Quenching Map

As discussed in the previous chapter, in most of the experiments performed in the DRCRE facility, the peak FPS temperature is limited to 980°C , which is the threshold temperature for accelerated Zr-steam oxidation reaction. However, for experiments performed with initial average FPS temperature of 650°C , the peak FPS temperature was observed to cross the oxidation threshold temperature, as discussed in Section 7.6. Such high temperatures are detrimental for the DRCRE test setup. Hence, the benchmarked PDRCR code is used to simulate several cases of different initial average FPS temperature and injection rates at 1% decay power to assess whether the FPS peak temperature is limited to the threshold oxidation temperature. Figure 8.56 shows initial average FPS temperature and injection rates considered for DRCRE experiments as well for simulations performed in PDRCR code.

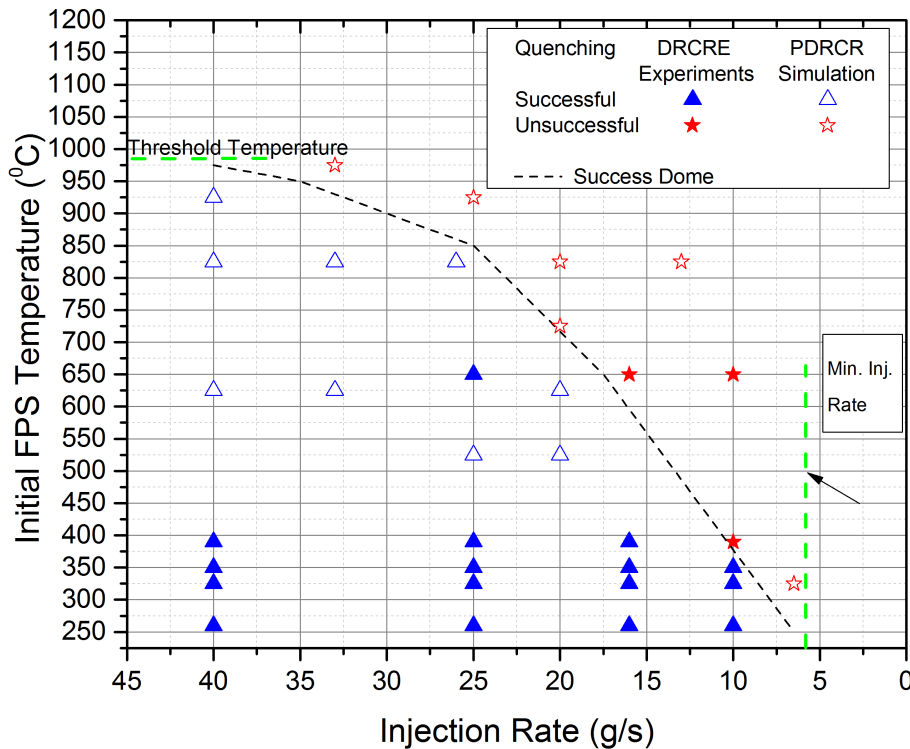


Figure 8.56: Quenching Map

The results for successful quenching (peak FPS temperature limited to threshold oxidation temperature) and unsuccessful quenching are clearly segregated from each other. Success of quenching is found to be limited to a dome delineated by minimum injection rate required and maximum initial average FPS temperature. It can be seen from Figure 8.56 that even for initial average temperature higher than 650°C and injection rate of the order of 40 g/s (which is less than half of the SAMG prescribed rate) the FPS temperature is limited to the oxidation threshold and successful quenching can be ascertained.

Chapter 9

Conclusions

Success of water injection into a reactor core under accident conditions depends largely on the injection rate and state of core at the time of injection. The knowledge gap area was identified to understand the effect of water injection under low injection rate conditions into a partially degraded reactor core condition. Such a core configuration consists of fuel pins ballooned over significant length, and is found to exist in the early stages of severe accident for a typical PWR. Feasibility analysis carried out with RELAP5 brought out the injection rate ranges and typical core temperatures under which quenching due to water injection was found to be successful. An experimental facility DRCRE was developed based on non-dimensional numbers obtained from non-dimensionalization of governing equations. Non-dimensional parameters obtained from scaling of governing equations were conserved with respect to plant scale values. Several experiments were carried out in the DRCRE facility to understand the effect of parameters such as injection rate, initial temperature of FPS and input power.

9.1 Conclusions of Present Study

Following salient conclusions can be drawn from the experimental study:

1. The SAMG action of water injection into partially degraded reactor core

configuration with 45% flow blockages extending over 60% of fuel pin is found to be successful for decay power levels up to 1% of full power and injection flow rates of 0.11-0.45 g/s per unit length of single FPS for all initial average FPS temperatures up to 650°C .

2. A sudden reduction in the heat transfer coefficient is observed at the entry of the ballooned region of FPS owing to significant flow re-distribution. The heat transfer coefficient improves thereon with a monotonous rise in the peak heat transfer coefficient along the length of the test section.
3. The adverse of effects of flow re-distribution such as lesser flow in the ballooned region as compared to that in the non-ballooned region are overcome by the heat transfer enhancement due to carryover droplets contacting FPS surface in the ballooned region. In effect the degradation of the fuel pins (simulated with 45% flow blockages extending over 60% length of FPS) causes accelerated quenching as compared to that of the intact fuel pins. Extended ballooning of fuel pins expected in a partially degraded core condition is not detrimental to the quenching of the fuel pins.
4. Quenching behavior of the ballooned FPS is largely controlled by the injection flow rates. Conduction controlled re-wetting pattern is observed for lower flow rates up to 0.25 g/s per unit length of single FPS. With an increase in injection flow rates beyond 0.25 g/s per unit length of FPS there is a tendency to change from conduction controlled re-wetting to fluid controlled re-wetting. Quenching of fuel pins is successful even for flow rates lesser than the prescribed SAMG flow rates, provided, the temperatures remain below the threshold limit of accelerated Zr-oxidation (980°C).
5. A correlation is developed for the ratio of peak heat transfer coefficient in the ballooned region to the non-ballooned region. Peak heat transfer coefficient in the ballooned region is found to be 2 times higher than the peak heat

transfer coefficient in the non-ballooned region.

6. A correlation is developed for the ratio of quench front velocity in the ballooned region to the quench front velocity in the non-ballooned region.

A numeric tool PDRCR was developed to simulate quenching behavior of partially degraded core under low injection rate condition. PDRCR is based on six equation formulation for two phase flow and solves coupled heat transfer between fluid and fuel with help of closure correlations. Following conclusions can be drawn from the development of PDRCR:

1. The modules of PDRCR code are well validated against analytical solutions and other numeric tools.
2. The special models used for the treatment of phenomena specific to quenching of partially degraded core under low injection rate are found to be satisfactory. These models include models of water packing mitigation under low injection rates, treatment of cross-flow and heat transfer under ballooned core conditions.
3. PDRCR facilitates simulation of parallel flow paths connected with cross-flow junctions. Comparison of PDRCR simulation with SEFLEX experimental results (90% flow blockages extended over 6% of FPS length) as well as DRCRE experiments (45% flow blockages extended over 60% of FPS length) was found to be satisfactory.
4. PDRCR predictions indicate that even for initial FPS temperature higher than 650°C and injection flow rate lower than half the prescribed SAMG values, the FPS temperatures remain below the threshold temperature for Zr-oxidation.

The experimental investigation in DRCRE facility and numerical simulations with PDRCR suggest that partially degraded core condition considered in this study is

amenable to quenching even for injection rates lower than the SAMG values. In most of the cases considered for the study, the clad oxidation can be prevented. The effects of parameters such as injections rate, initial temperature and power on the quenching patterns are well understood.

9.2 Scope for Future Work

The DRCRE facility has been used to assess quenching patterns for a partially degraded core condition with 45% blockage extending over 60% of FPS length. The facility can be used further to understand quenching patterns for higher blockages of the order of 80%. The data generated will not only help in understanding the quenching behavior but it will also help in benchmarking of PDRCR code for wider range of blockage ratios.

Definitions

Bottom Re-flooding Water injection into the reactor core from bottom.

Cohesive Debris Formation Formation of mixture of molten drops of clad with cracked fuel pellets called Cohesive Debris

Design Basis Accident Accident conditions against which an NPP is designed according to established design criteria, and for which the damage to the fuel and the release of radioactive material are kept within authorized limits.

Gross Clad Burst Mechanical rupture of fuel clad under accident conditions at multiple locations spanning across the reactor core

Large Scale Ballooning Ballooning of fuel pins under accident condition at various locations spanning across the core and spanning over long lengths of fuel pin (typically more than 20% of total length)

Leidenfrost Temperature The maximum temperature at which a permanent contact can be established between an isothermal surface and infinitesimally small droplet of coolant.

Localized Ballooning Ballooning of fuel pins under accident condition restricted to few regions and spanning over short lengths of fuel pin (typically 10-20% of total length)

Localized Clad Burst Mechanical rupture of fuel clad under accident conditions restricted to few regions of the core

Minimum Film Boiling Temperature Minimum surface temperature required for sustained film boiling.

Molten Pool Formation Formation of molten pool of fuel and clad material under accident conditions

Normal Operation Operation of an NPP within specified operational limits and conditions including startup, power operation, shutting down, shutdown, maintenance, testing and refuelling.

Precursory Cooling Cooling ahead of quench front, caused due to entrained droplets or accelerated steam flow.

Rubble Formation Formation of cracked fuel pellets debris called Rubbles and clad rupture allowing the Rubble to come out of the fuel pin into the core

Quench Front The boundary between the transition region and film boiling region.

Quench Temperature The temperature at which sharp fall in surface temperature is initiated due to enhanced heat transfer.

Safety Systems Systems important to safety provided to assure safe shutdown of a reactor or residual heat removal from a core, or to limit the consequences of anticipated operational occurrences and DBAs.

Severe Accident An accident involving damage to the nuclear fuel and the reactor core in general.

Severe Accident Management Guidelines A set of guidelines containing instructions for actions in the framework of severe accident management

System Code A computer model that is capable of simulating the transient performance of a complex system like an NPP. A system code typically includes equations for thermohydraulics, neutronics and heat transfer and must be

equipped with special models to simulate the performance of components such as pumps and separators. The code should typically also simulate the control logic implemented in the plant and be able to predict the accident evolution.

Top Re-flooding Water injection into the reactor core from top.

References

- [1] MATPRO. A library of materials properties for light water reactor accident analysis. Technical report, NUREG/CR-6150-Volume-IV.
- [2] USNRC. Tmi-2 lessons learned task force final report a library of materials properties for light water reactor accident analysis. Technical report, NUREG-0585, 1979.
- [3] Wolfgang Hering and Christoph Homann. Degraded core reflooding: Present understanding and Impact on LWRs. *Nuclear Engineering and Design*, 237:2315–2321, April 2007.
- [4] Claude Grandjean. Collability of blocked regions in a rod bundle after ballooning under loca conditions : Main findings from a review of past experimental programmes. *Nuclear Engineering and Design*, 237:1872–1886, February 2007.
- [5] Alexander Sesonske Samuel Glasstone. *Nuclear Reactor Engineering*. CBS, second edition, 2004.
- [6] K.Hassmann and J.P.Hosemann. Consequences of degraded core accidents. *Nuclear Engineering and Design*, 80:285–299, March 1984.
- [7] B.R.Sehgal. Accomplishments and challenges of the severe accident research. *Nuclear Engineering and Design*, 210:79–94, August 2001.
- [8] Windberg Vimi Hozer, Nagy. Coolability of ballooned vver bundles with pellet relocation. *Proceedings of TOP FUEL*, page 2032, September 2009.

- [9] J.J.Carbajo. A study on the rewetting temperature. *Nuclear Engineering and Design*, 84:21–52, April 1985.
- [10] R.B.Duffey and D.T.C Porthouse. The physics of rewetting in water reactor emergency core cooling. *Nuclear Engineering and Design*, 25:379–394, 1973.
- [11] F. S. Gunnerson and T. R. Yackle. Quenching and rewetting of nuclear fuel rods. *Nuclear Technology*, 54:113–117, July 1981.
- [12] R. M. Thomas. Methods for calculating the conduction controlled rewetting for clad rod. *Nuclear Engineering and Design*, 110:1–16, 1988.
- [13] Hsu-Chieh Yeh. An analysis of rewetting of a nuclear fuel rod in water reactor emergency core cooling. *Nuclear Engineering and Design*, 34:317–322, 1975.
- [14] R.E.Caflisch and J.B.Keller. Quench front propagation. *Nuclear Engineering and Design*, 65:97–102, 1981.
- [15] A.C.Spencer A.W.Gurcak and T.A.Porsching. Implicit isotherm migration: A numerical method for the two-dimensional quench front problem. *Nuclear Engineering and Design*, 61:25–31, 1980.
- [16] J.J.Carbajo and A.D.Siegal. Review and comparison among the different models for rewetting in lwrs. *Nuclear Engineering and Design*, 58:33–44, 1980.
- [17] K.D.Kimball and R.P.Roy. Quench front propagation during bottom reflooding of a heated annular channel. *Nuclear Engineering and Design*, 76:79–88, 1983.
- [18] R.Viskanta and D.M.Kim. Heat transfer from a partially uncovered reactor core. *Nuclear Engineering and Design*, 85:71–82, 1985.

- [19] R.Viskanta and A.K.Mohanty. Heat-up of partially uncovered pwr fuel rod in the presense of cladding oxidation and steam dissociation. *Nuclear Engineering and Design*, 105:231–242, 1988.
- [20] R.Schutzle and H.Unger. A mathematical model for the investigation of rewetting of fuel rod. *Nuclear Engineering and Design*, 101:315–322, 1987.
- [21] N. Zuber and J. A. Findlay. Average volumetric concentration in two-phase flow systems. *Journal of Heat Transfer*, 87:453–468, 1965.
- [22] N.Tregoures C.Bechaud M.Quintard F.Fichot, F.Duval. The impact of thermal non-equilibrium and large scale 2d/3d effects on debris bed reflooding and coolability. *Nuclear Engineering and Design*, 236:2144–2163, March 2006.
- [23] Nourdine Chikhi and Florian Fichot. Reflooding model for quasi-intact rod configuration: Quench front tracking and heat transfer closure laws. *Nuclear Engineering and Design*, 240:3387–3396, July 2010.
- [24] The RELAP5 Code Development Team. Relap5/mod3 code manual: Code structure, system models, and solution methods. Technical report, NUREG/CR-5535, 1995.
- [25] F.B.Cheung D.L.Aumiller R.J.Houser M.J.Holowach, L.E.Hochreiter. Scaling of quench front and entrainment related phenomena. *Nuclear Engineering and Design*, 223:197–209, January 2003.
- [26] H. C. No F. Eltwila M.Ishii, G. Zhang. Stepwise integral scaling method for severe accident analysis and its application to corium dispersion in direct containment heating. *Nuclear Engineering and Design*, 151:223–234, 1994.
- [27] M.E.Nissley L.E.Hochreiter M.Y.Young, S.M.Bajorek. Application of code scaling applicability andvuncertainty methodology to the large break loss of coolant. *Nuclear Engineering and Design*, 186:39–52, December 1998.

- [28] Hee Cheon No and M.Ishii. Scaling study of in-core boil-off and heating process. *Nuclear Engineering and Design*, 143:265–283, April 1993.
- [29] R. van de Graff and T.H.J.J. van der Hagen. Two phase flow scaling laws for a simulated bwr assembly. *Nuclear Engineering and Design*, 148:455–462, 1994.
- [30] P.Ihle and K.Rust. Pwr reflood experiments using full length bundles of rods with zircaloy claddings and alumina pellets. *Nuclear Engineering and Design*, 99:223–237, 1987.
- [31] J. C. Chen K. Tuzla, Cetin Unal. An experimental study of bottom rewetting in a rod bundle geometry. *Nuclear Engineering and Design*, 125:189–200, 1991.
- [32] L.Sepold et. al. Severe fuel damage experiments performed in the quench facility with 21-rod bundles of lwr-type. *Nuclear Engineering and Design*, 237:2157–2164, March 2007.
- [33] P. Ihle and K. Rust. Seflex fuel rod simulator effects in flooding experiment, part 1: Evaluation report. Technical report, Kernforschungszentrum karlsruhe, 1986.
- [34] P. Ihle and K. Rust. Seflex fuel bundle simulator effects in flooding experiment, part 2: Unblocked bundle data. Technical report, Kernforschungszentrum karlsruhe, 1986.
- [35] P. Ihle and K. Rust. Seflex fuel bundle simulator effects in flooding experiment, part 3: Blocked bundle data. Technical report, Kernforschungszentrum karlsruhe, 1986.
- [36] USNRC. Pwr flecht-seaset unblocked bundle, forced and gravity reflood task. Technical report, NUREG/CR-2256, 1982.

- [37] P. D. Parsons et. al. Pwr fuel behaviour under design basis accident conditions, december 1986, csni-129. Technical report, Committee on the Safety of Nuclear Installations, OECD Nuclear Energy Agency, 1986.
- [38] Alok Mishra S. K. Agrawal, Ashok Chauhan. The vvers at kudankulam. *Nuclear Engineering and Design*, 236:812–836, 2006.
- [39] Andreeva et al. Overview of plant specific severe accident management strategies for kozloduy nuclear power plant, wwer 1000/320. *Annals of Nuclear Energy*, 35:555–564, 2008.
- [40] Novak Zuber et.al. An integrated structure and scaling methodology for severe accident technical issue resolution: Development of methodology. *Nuclear Engineering and Design*, 186:1–21, March 1998.
- [41] T.F. Lin C. Frepoli A. Sridharan D.R. Todd E.R. Rosa L.E. Hochreiter, F-B Cheung. Rod bundle heat transfer test facility test plan and design. Technical report, The Pennsylvania State University, University Park, 2010.
- [42] SG Popov. Thermophysical properties of mox and uo2 fuel including the effects of orradiation, ornl/tm-2000/351. Technical report, Oak Ridge National Lab., TN (USA), 2000.
- [43] G. K. White and S. J. Collocott. Heat capacity of reference materials: Cu and w. *Journal of Physical and Chemical Reference Data*, 13(4):1251–1257, 1984.
- [44] Y S Touloukian. *Thermophysical properties of matter*. New York, IFI/Plenum, 1970.
- [45] Division of Risk Assessment and USNRC Special Projects. The trace v5.0 theory manual. *Field Equations, Solution Methods and Physical Models*, Accession number ML120060403, January 2012.

- [46] Yoshio Murao and Jun Sugimoto. Correlation for heat transfer coefficient for saturated film boiling during reflood phase prior to quenching. *Journal of Nuclear Science and Technology*, 14:275–284, April 1981.
- [47] Dieter Steiner and Jerry Taborek. Flow boiling heat transfer in vertical tube correlated by an asymptotic model. *Heat Transfer Engineering*, 13(2):43–69, 1992.
- [48] G. B. Wallis. Letter to the editor on phenomena of liquid transfer in two phase dispersed annular flow. *Internatioal Journal of Heat and Mass Transfer*, 11:783–785, 1968.
- [49] D. A. Steen and G. B. Wallis. The transition from annular to annular-mist concurrent two phase down flow. Technical report, AECReport-NYO-3114-2, 1964.
- [50] D.G. Friend. Revised release on the iapws formulation 1995 for the thermodynamic properties of ordinary water substance for general and scientific use. *Internation Association for Properties of Water and Steam*, 2009.

Appendix A

Calibration of Measuring Instruments

A.1 Calibration of K-type Thermocouples

The thermocouples used for temperature measurement in the experiment were calibrated in constant temperature dry bath against master thermocouple of accuracy. Five randomly selected thermocouples were chosen and calibrated in the range of 30 to 1000⁰C.

Calibration table for K-type thermocouples is shown in Table A.1 and the calibration curve is shown in Figure A.1.

Table A.1: Calibration Table for K-type Thermocouples

Sr. No.	K-type Thermocouples		
	Reference Reading (⁰ C)	Thermocouple Reading (⁰ C)	% of error
1	30	29.9	0.33
2	200	199.5	0.25
3	400	401.6	0.4
4	600	602.9	0.483

Sr.	K-type Thermocouples		
No.	800	803.4	0.425
6	1000	1004.6	0.46

The maximum uncertainty in the measurement of temperature using thermocouples is found to be 3.56%.

A.2 Calibration of Flowmeter

The rotameter used for water injection flow rate measurement in the experiment was calibrated against Turbine Flow Meter.

Calibration table for rotameter is shown in Table A.2 and the calibration curve is shown in Figure A.2.

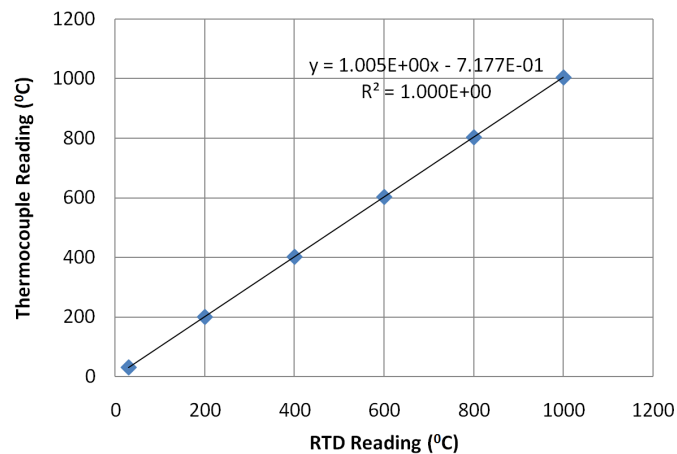


Figure A.1: Thermocouple Calibration Curve

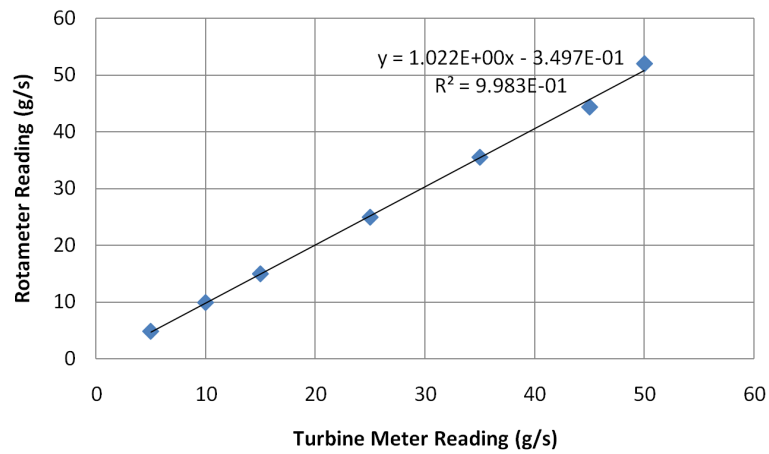


Figure A.2: Rotameter Calibration Curve

Table A.2: Calibration Table for Rotameter

Sr. No.	Glass Tube Rotameter		
	Reference Reading (g/s)	Rotameter Reading (g/s)	% of error
1	5	4.901	1.98
2	10	9.961	0.39
3	15	15.016	0.106
4	25	24.975	0.1
5	35	35.518	1.48
6	45	45.648	1.43
7	50	51.567	3.134

Maximum uncertainty in the measurement of flow is found to be 2.9%.

A.3 Calibration of Level Transmitter

The differential pressure transmitter used for measurement of water level in the test section was calibrated against calibrated DPT.

Calibration table for level transmitter is shown in Table A.3 and the calibration curve is shown in Figure A.3.

Table A.3: Calibration Table for Level Transmitter

Sr. No.	Differential Pressure Transmitter		
	Reference Reading (mm)	DPT Reading (mm)	% of error
1	100	101.1	1.1
2	300	299.9	0.033
3	500	498.12	0.376
4	700	702.15	0.307
5	900	903.16	0.351
6	1100	1098.12	0.261
7	1300	1297.34	0.204
8	1500	1502.15	0.143

Maximum uncertainty in the measurement of level is found to be 2.5%.

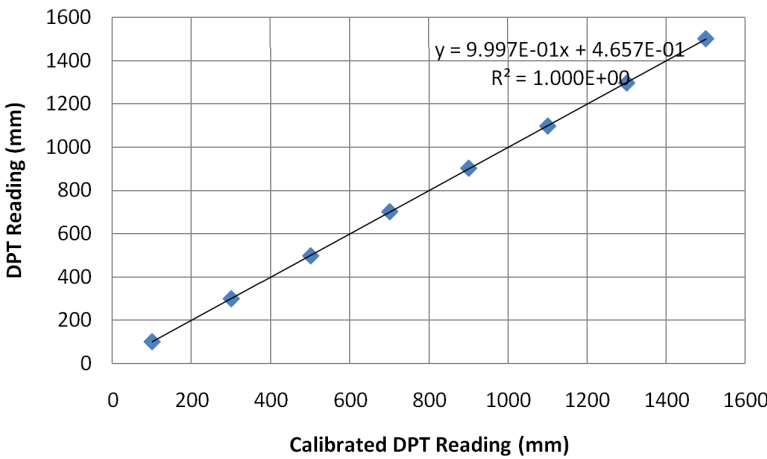


Figure A.3: Level Transmitter Calibration Curve

Appendix B

Uncertainty Analysis

B.1 Uncertainties in Measured Parameters

Sr. No.	Parameter Measures	Sensor	Range	3σ	Maximum Uncertainty
1	Clad Temperature	Thermocouple	$20 - 1300^{\circ}C$	$1.07^{\circ}C$	3.56%
2	Injection Flow Rate	Rotameter	$10 - 40g/s$	0.29 g/s	2.9%
3	Level	Level Transmitter	$0 - 1500mm$	22.5mm	1.88%
4	Input Voltage	Multimeter	2-7V	0.001V	0.05%
5	Input Current	Tong Meter	100-2000A	0.1A	0.1%

Table ?? enlists the parameters being measured in the experiments and the corresponding uncertainties in the measurement.

B.2 Uncertainties in the Derived Quantities

B.2.1 Uncertainty of Input Power Measurement

The input power is calculated using Eq.B.1

$$P = V * I \quad (B.1)$$

Hence the uncertainty in the power is calculated as

$$\frac{dP}{P} = \sqrt{\left(\frac{dV}{V}\right)^2 + \left(\frac{dI}{I}\right)^2} \quad (B.2)$$

$$\frac{dP}{P} = 0.12\% \quad (B.3)$$

B.2.2 Uncertainty in Heat Transfer Coefficient

The heat transfer coefficient is derived using Eq. B.4

$$h = \frac{P}{A (T_s - T_{sat})} \quad (B.4)$$

Hence the uncertainty in the HTC is calculated as

$$\frac{dh}{h} = \sqrt{\left(\frac{dP}{P}\right)^2 + 2 \left(\frac{dT}{T}\right)^2} \quad (B.5)$$

$$\frac{dh}{h} = 5.04\% \quad (\text{B.6})$$

B.2.3 Uncertainty in Quench Front Velocity

The heat transfer coefficient is derived using Eq. B.7

$$V_q = \frac{X}{\Delta t} \quad (\text{B.7})$$

Since the different in quenching time is obtained from the quenching sensed by thermocouple. Hence the uncertainty in the quench front velocity is calculated as

$$\frac{dV}{V} = \sqrt{\left(\frac{dX}{X}\right)^2 + 2\left(\frac{dT}{T}\right)^2} \quad (\text{B.8})$$

$$\frac{dh}{h} = 5.13\% \quad (\text{B.9})$$

Appendix C

Thermocouple Installation Details

Table C.1enlists the details and locations of thermocouples. Corresponding pin locations are shown in Figure C.1.

Table C.1: Thermocouple Location Details

Sr. No.	Thermocouple Number	Pin Loca- tion	Azimuthal Position	Distance from Inlet (mm)	Plane
1	1	8F	N	875	600
2	2	8G	N	975	700
3	3	8H	N	575	300
4	4	7E	S	975	700
5	5	7E	W	1075	800
6	6	7F	N	875	600
7	7	7F	S	775	500
8	8	7H	N	575	300
9	9	7H	S	675	400
10	10	7H	E	675	400
11	11	7I	N	1175	900

12	12	7I	S	975	700
13	13	7I	E	1075	800
14	14	7I	W	575	300
15	15	6C	E	1375	1100
16	16	6E	E	1375	1100
17	17	6F	N	875	600
18	18	6F	S	775	500
19	19	6G	N	1175	900
20	20	6G	S	1075	800
21	21	6G	E	1275	1000
22	22	6H	N	575	300
23	23	6H	S	675	400
24	24	6H	E	1275	1000
25	25	6H	W	1175	900
26	26	6I	S	1275	1000
27	27	6I	E	1275	1000
28	28	6I	W	1175	900
29	29	6J	W	1175	900
30	30	5E	E	975	700
31	31	5E	W	1075	800
32	32	5F	N	675	400
33	33	5F	E	575	300
34	34	5G	N	1275	1000
35	35	5G	S	1275	1000
36	36	5G	E	675	400

37	37	5G	W	675	400
38	38	5H	N	775	500
39	39	5H	S	675	400
40	40	5H	W	575	300
41	41	5I	E	1075	800
42	42	5I	W	975	700
43	43	4C	E	1175	900
44	44	4E	N	1275	1000
45	45	4E	E	1175	900
46	46	4E	W	1275	1000
47	47	4F	N	675	400
48	48	4F	S	575	300
49	49	4F	E	1175	900
50	50	4F	W	1275	1000
51	51	4G	N	1075	800
52	52	4G	S	1175	900
53	53	4G	W	1275	1000
54	54	4H	N	775	500
55	55	4I	W	1375	1100
56	56	4J	W	1375	1100
57	57	3E	N	975	700
58	58	3E	S	1175	900
59	59	3E	E	575	300
60	60	3E	W	1075	800
61	61	3F	N	675	400

62	62	3F	S	575	300
63	63	3F	W	675	400
64	64	3H	N	775	500
65	65	3H	S	875	600
66	66	3I	N	975	700
67	67	3I	W	1075	800
68	68	2F	S	575	300
69	69	2G	S	975	700
70	70	2H	S	875	600
71	N1	Shell	N	575	300
72	N2	Shell	N	675	400
73	N3	Shell	N	775	500
74	N4	Shell	N	875	600
75	N5	Shell	N	975	700
76	N6	Shell	N	1075	800
77	N7	Shell	N	1175	900
78	S1	Shell	S	575	300
79	S2	Shell	S	675	400
80	S3	Shell	S	775	500
81	S4	Shell	S	875	600
82	S5	Shell	S	975	700
83	S6	Shell	S	1075	800
84	S7	Shell	S	1175	900

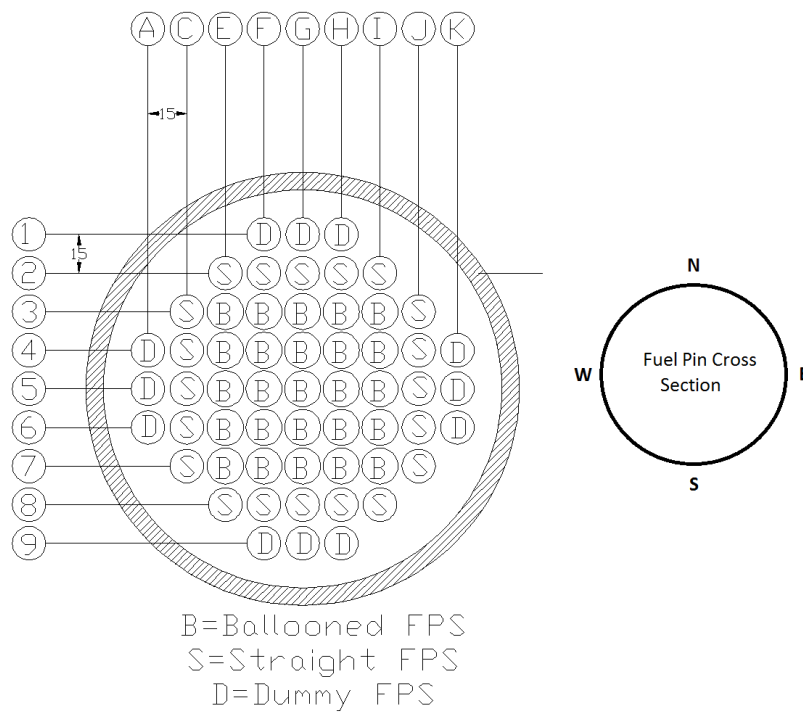


Figure C.1: Pin Location Map

Appendix D

Use of Developed Correlations

D.1 Correlation for Peak Heat Transfer Coefficient

The Peak Heat Transfer Coefficient correlations can be used as follows:

1. The heat transfer coefficient for the non-ballooned configuration can be calculated using Murao-Sugimotos correlation:

$$h_{non-ballooned} = 0.94 \left(\frac{k_g^3 \rho_g \rho_l H_{fg} g}{z \mu_g \Delta T_{sat}} \right)^{0.25} (1 - \alpha)^{0.25} + \sigma e (1 - \alpha)^{0.5} \frac{(T_s^4 - T_{sat}^4)}{\Delta T_{sat}} \quad (D.1)$$

2. The calculated temperature from the PDRCR code for the present time is used as $T_{s,peak}$. Using flow parameters and location of the node, the heat transfer coefficient can be calculated using the developed correlation:

$$\frac{h_{ballooned}}{h_{non-ballooned}} = 0.7767 \left(\frac{P}{\dot{m} H_{fg}} \right)^{0.1298} \left(\frac{T_{s,peak} - T_{sat}}{T_{LF} - T_{sat}} \right)^{-0.2777} \left(\left[4 + \frac{z}{D_h} \right] \frac{z}{D_h} \right)^{0.2345} \quad (D.2)$$

3. When the node temperature reaches point of inflation (increasing trend changes to decreasing trend because of axial conduction), the above calculated heat transfer coefficient is used.

D.2 Correlation for Average Quench Front Velocity

1. The location of the quench front for a non-ballooned configuration can be calculated using FLECHT-SEASET correlation:

$$z_q = \left(1 + 50 \left(\frac{T_q - T_{init}}{T_{init} - T_{sat}}\right)\right) t V_{in} \frac{1}{50 \left(\frac{T_q - T_{init}}{T_{init} - T_{sat}}\right) + \left(\frac{t_{peak} V_{in}}{z_q}\right) (Q_r + 0.5 Q_r e^{-9 Q_r^2})} \quad (D.3)$$

2. The velocity of the quench front can be calculated using time derivative of Eq.D.3.
3. This can be used as $V_{q,non-ballooned}$ in the average quench front velocity correlation:

$$\frac{V_{q,ballooned}}{V_{q,non-ballooned}} = 1.9061 \left(\frac{P}{\dot{m} H_{fg}}\right)^{0.1320} \left(\frac{T_{FPS,average} - T_{sat}}{T_{LF} - T_{sat}}\right)^{-0.2196} \quad (D.4)$$

and the average quench front velocity in the ballooned region can be calculated.

Appendix E

Sample Calculations for the Pi-Terms

Calculation of Π_1

The Π_1 term is defined as the ratio of sensible energy change rate for liquid phase to the total heat input

$$\Pi_1 = \frac{\dot{m}_i C_{p,1\phi} (T_f - T_i)}{W_{in}} \quad (\text{E.1})$$

For an injection flow rate of $10g/s$, fluid inlet temperature of 30^0C , the calculated value is 0.148.

Calculation of Π_3

The Π_3 term is defined as the ratio of fuel rod quench energy release rate to the total heat input

$$\Pi_3 = \frac{\rho_{fuel} C_{p,fuel} V_{fuel} (T_{fuel,max} - T_{sat})}{\tau_2 W_{in}} \quad (E.2)$$

This can be re-written as:

$$\Pi_3 = \frac{\rho_{fuel} C_{p,fuel} A_{fuel} u_{waterfront} (T_{fuel,max} - T_{sat})}{W_{in}} \quad (E.3)$$

For a weighted average density of $7382 kg/m^3$, weighted average specific heat capacity of $598.2 J/kg.K$, calculated water velocity of $0.265 mm/s$, the calculated value of Π_3 is 0.232.

Calculation of Π_4

The Π_4 term is defined as the ratio of housing quench energy release rate to the total heat input

$$\Pi_3 = \frac{\rho_{hous} C_{p,hous} V_{fuel} (T_{house} - T_{sat})}{\tau_3 W_{in}} \quad (E.4)$$

This can be re-written as:

$$\Pi_3 = \frac{\rho_{hous} C_{p,hous} A_{hous} u_{waterfront} (T_{house} - T_{sat})}{W_{in}} \quad (E.5)$$

For a density of $7800 kg/m^3$, average specific heat capacity of $500.0 J/kg.K$, calculated water velocity of $0.265 mm/s$ the calculated value of Π_3 is 0.198.

Calculation of Π_5

The Π_5 term is defined as the ratio of dummy rod quench energy release rate to the total heat input

$$\Pi_5 = \frac{\rho_{dum} C_{p,dum} V_{fuel} (T_{dum} - T_{sat})}{\tau_3 W_{in}} \quad (E.6)$$

This can be re-written as:

$$\Pi_5 = \frac{\rho_{dum} C_{p,dum} A_{dum} u_{waterfront} (T_{dum} - T_{sat})}{W_{in}} \quad (E.7)$$

For a weighted average density of $5331 kg/m^3$, weighted average specific heat capacity of $610.0 J/kg.K$, calculated water velocity of $0.265 mm/s$ the calculated value of Π_5 is 0.141.

Calculation of Π_7

The Π_7 term is defined as the ratio of dummy rod quench energy release rate to the total heat input

$$\Pi_7 = \frac{h_{fuel,conv} A_{fuel} (T_{sat} - T_{max,fuel})}{W_{in}} \quad (E.8)$$

For a heat transfer coefficient of $410 W/m^2 K$ and maximum temperature as 973 K, the calculated value of Π_7 is 30.8.

Calculation of Π_{21}

The Π_{21} term is defined as the ratio of rate of change of stored energy of fuel to the total heat input.

$$\Pi_{21} = \frac{\rho_{fuel} C_{p,fuel} V_{fuel} (T_{fuel,cl} - T_s)}{\tau_{fuel} W_{in}} \quad (E.9)$$

For a weighted average density of $7382 kg/m^3$, weighted average specific heat capacity of $598.2 J/kg.K$, calculated ΔT of 11.4 across the fuel radius and fuel thermal time constant of 13.65s, the calculated value of Π_3 is 1.75.

Appendix F

Comparison of PDRCR Prediction with DRCRE Experimental Results

Test No 07

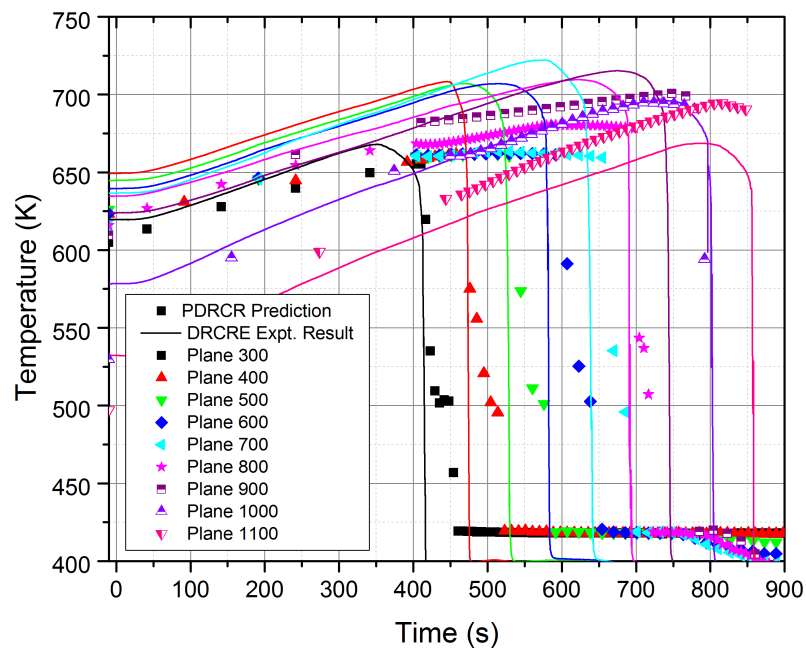


Figure F.1: Clad Temperatures at Various Axial Locations
(Comparison of DRCRE Test 07 with PDRCR Predictions)

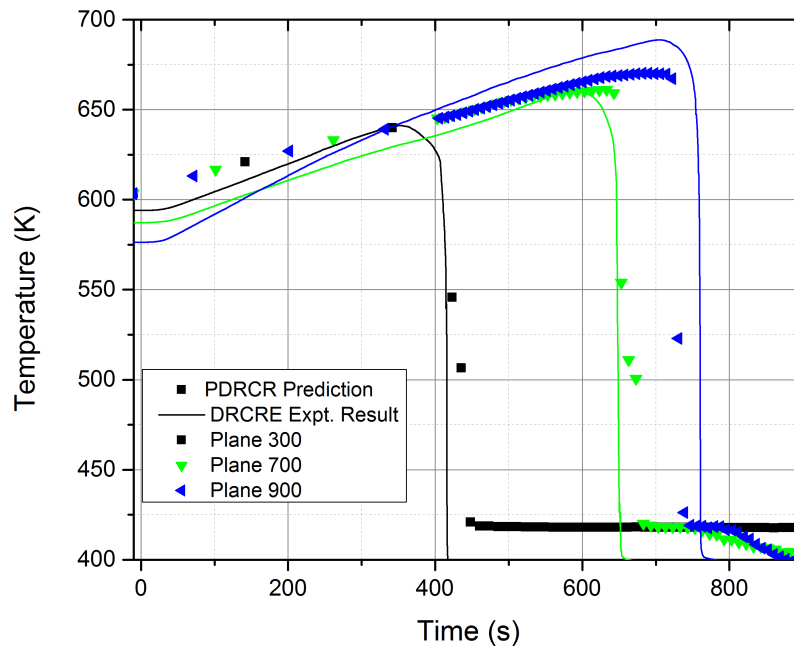


Figure F.2: Shell Temperatures at Various Axial Locations (Comparison of DRCRE Test 07 with PDRCR Predictions)

Test No 10

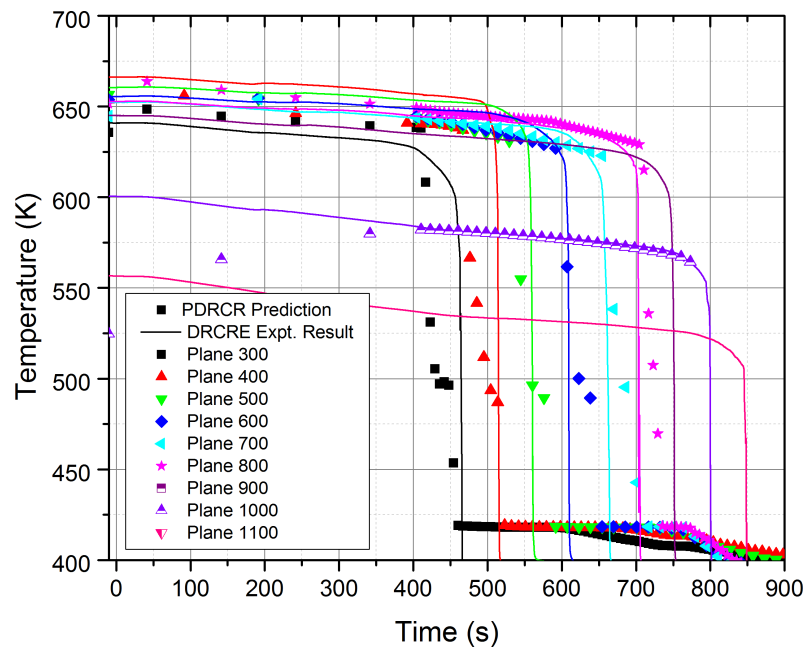


Figure F.3: Clad Temperatures at Various Axial Locations (Comparison of DRCRE Test 10 with PDRCR Predictions)

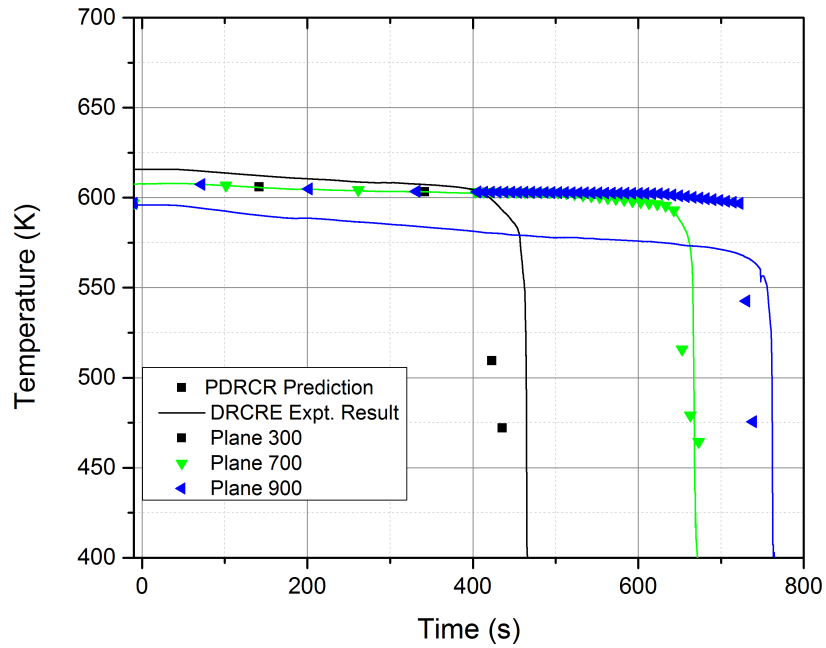


Figure F.4: Shell Temperatures at Various Axial Locations
(Comparison of DRCRE Test 10 with PDRCR Predictions)

Test No 14

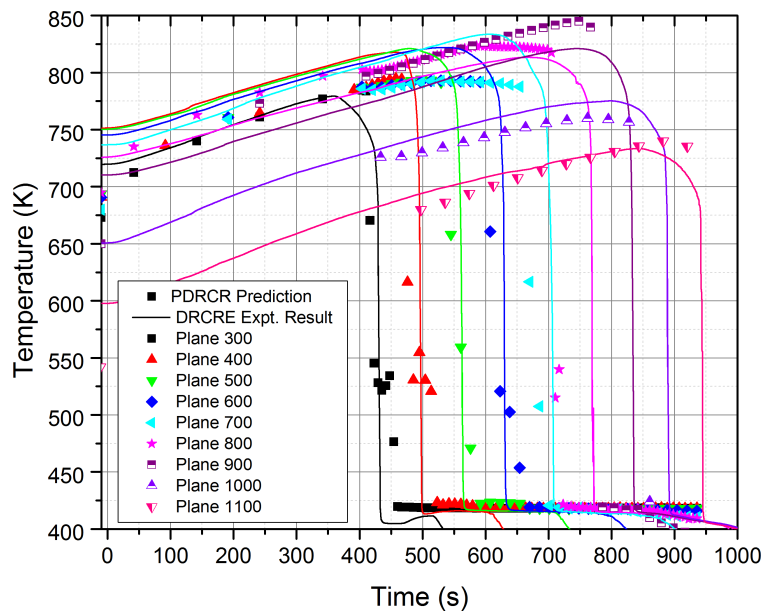


Figure F.5: Clad Temperatures at Various Axial Locations
(Comparison of DRCRE Test 14 with PDRCR Predictions)

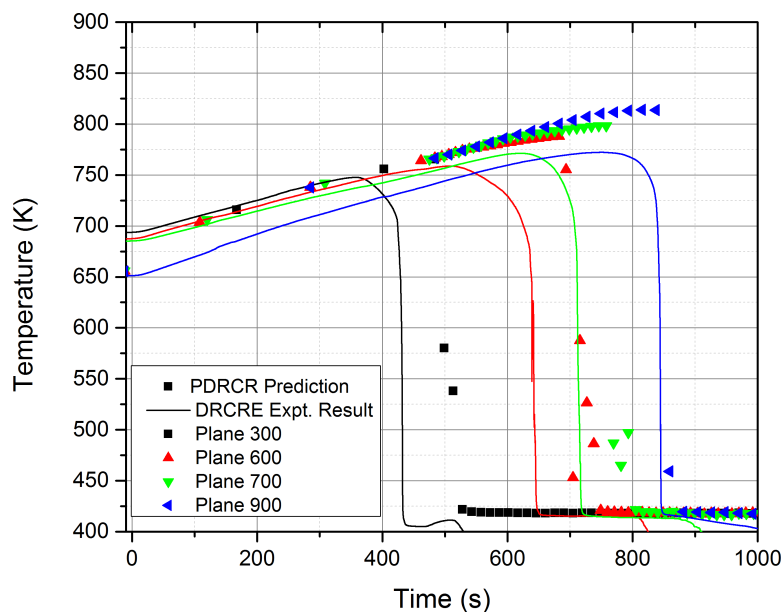


Figure F.6: Shell Temperatures at Various Axial Locations (Comparison of DRCRE Test 14 with PDRCR Predictions)

Test No 17

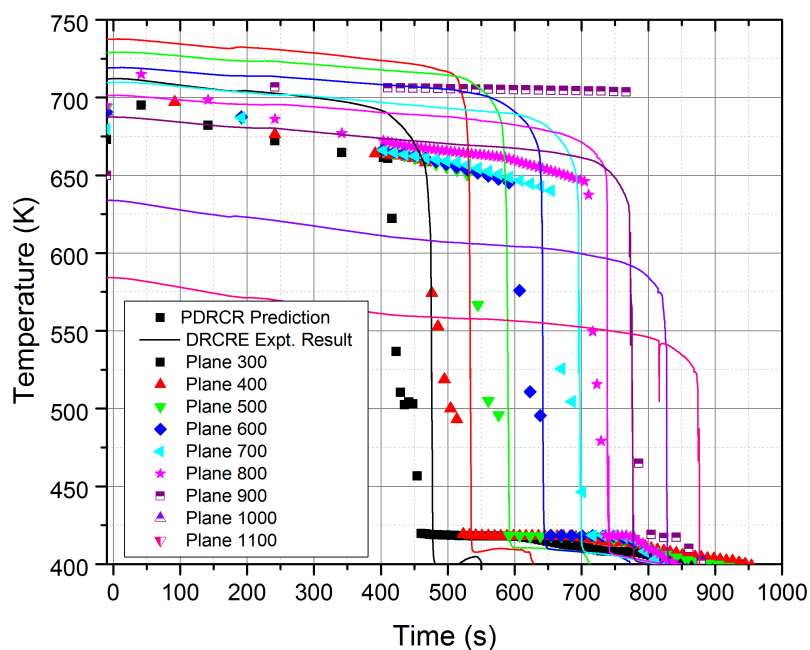


Figure F.7: Clad Temperatures at Various Axial Locations (Comparison of DRCRE Test 17 with PDRCR Predictions)

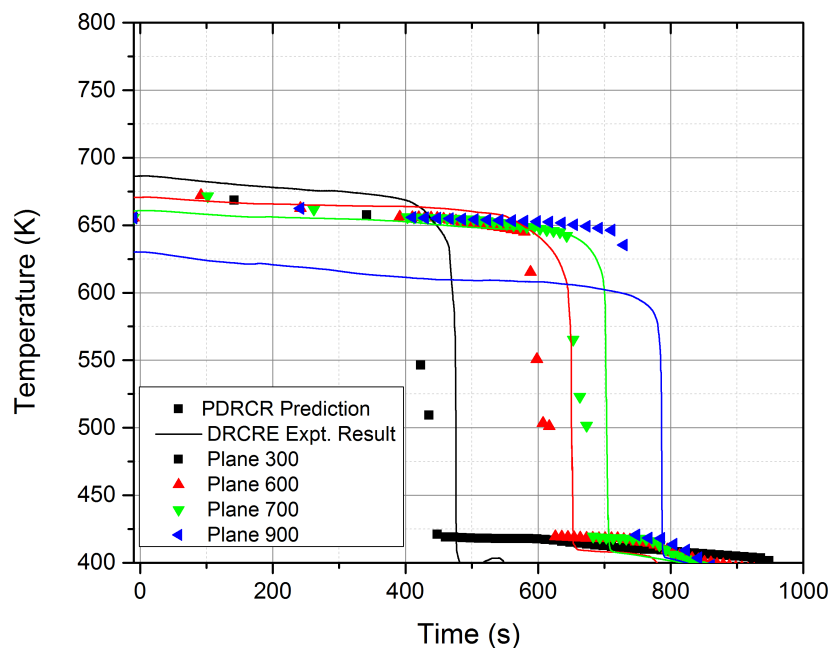


Figure F.8: Shell Temperatures at Various Axial Locations (Comparison of DRCRE Test 17 with PDRCR Predictions)

Test No 50

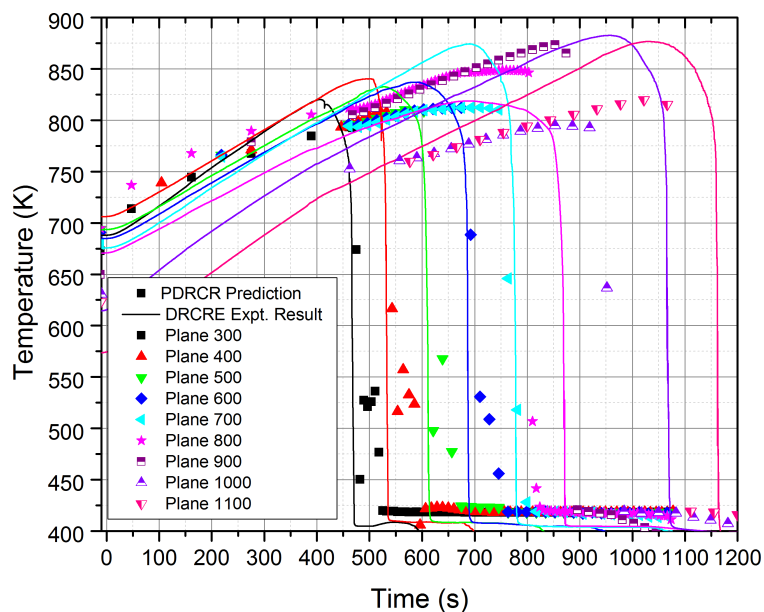


Figure F.9: Clad Temperatures at Various Axial Locations (Comparison of DRCRE Test 50 with PDRCR Predictions)

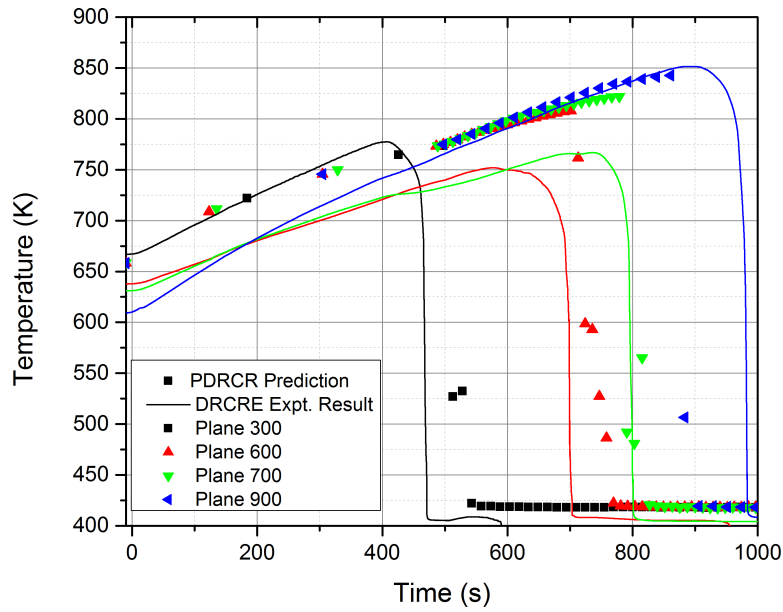


Figure F.10: Shell Temperatures at Various Axial Locations (Comparison of DRCRE Test 50 with PDRCR Predictions)

Test No 60

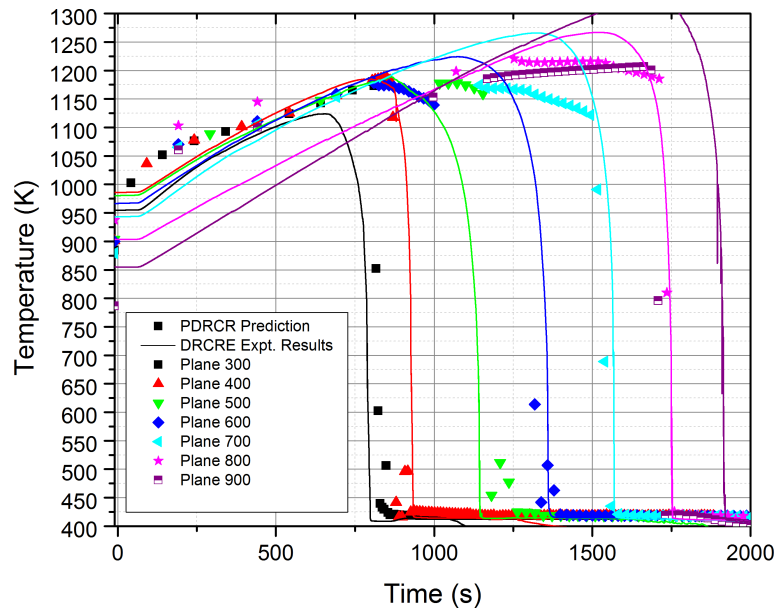


Figure F.11: Clad Temperatures at Various Axial Locations (Comparison of DRCRE Test 60 with PDRCR Predictions)

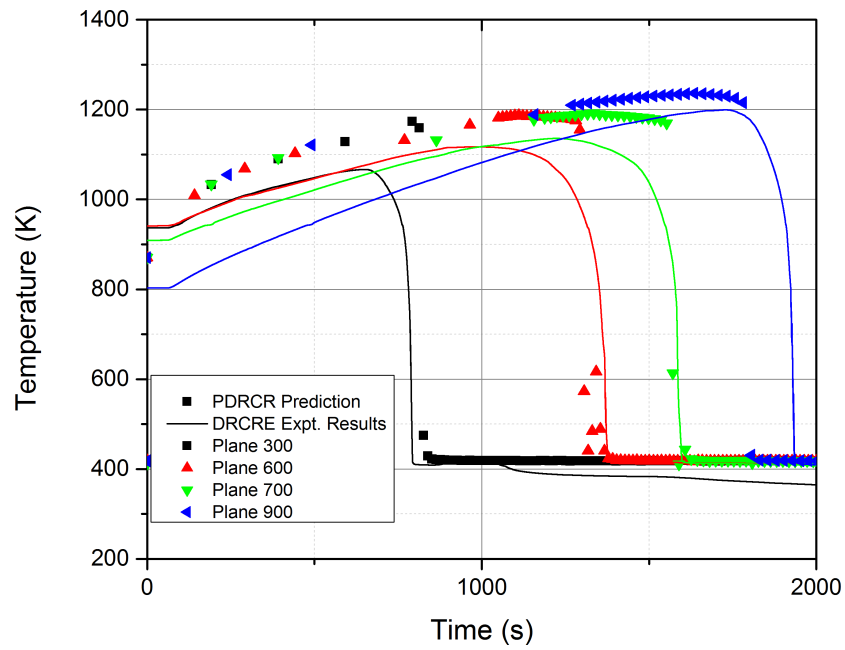


Figure F.12: Shell Temperatures at Various Axial Locations (Comparison of DRCRE Test 60 with PDRCR Predictions)